# ARTIFICIAL INTELLIGENCE, LIDAR AND CO-OPERATIVE REMOTE SENSING FOR ATMOSPHERIC OBSERVATION AND OFF-SHORE WIND ENERGY

Thesis submitted to the Universitat Politècnica de Catalunya

in partial fulfilment for the degree of

*Doctor of Philosophy*

**Andreu Salcedo Bosch**

CommSensLab – Remote Sensing Lab.

Department of Signal Theory and Communications

Doctorate program in

Signal Theory and Communications

Supervisor: Prof. Francesc Rocadenbosch Burillo

Barcelona, June 2023

Aquesta tesi és el resultat d'anys d'esforç i dedicació i d'una llarga trajectòria a la meva vida en el món acadèmic. El resultat de tot això no hagués sigut possible sense el suport i l'acompanyament de moltíssimes persones que han compartit el camí amb mi.

Primer de tot, vull agraïr al meu director de tesi, el Professor Francesc Rocadenbosch, per donar-me la oportunitat d'entrar al món de la ciència i la investigació i guiar-me amb molta dedicació durant tots aquests anys.

En segon lloc vull agraïr al Marcos Paulo haver compartit el camí del doctorat amb mi. Totes les experiències viscudes junts, tant dins com a fora de la universitat, han fet que aquest viatge no hagi sigut un viatge solitari.

En tercer lloc vull agraïr als companys de DTU per acollir-me a Dinamarca i fer-me sentir com a casa.

Reservo una dedicatoria molt especial a tots els amics de la UPC, que han fet que la universitària hagi sigut una de les etapes més felices de la meva vida.

Sobretot vull donar les gràcies a la meva família per tot el suport i haver-me permès seguir aquest camí. Aquesta és la millor herència que mai m'haguéssin pogut deixar i sense ells no seria qui sóc.

Finalment, vull agraïr i dedicar aquesta tesi a tots els amics i companys de Sant Vicenç dels Horts. Ells són els que em fan sentir que tinc casa.

# Acknowledgements

The following institutions are gratefully acknowledged for their contribution to this work:

- This research project was part of projects PID2021-126436OB-C21 and PGC2018-094132-B-I00 funded by Ministerio de Ciencia e Investigación (MCIN)/ Agencia Estatal de Investigación (AEI)/ 10.13039/501100011033/ FEDER "Una manera de hacer Europa" and MDM-2016-0600 by MCIN/AEI.
- CommSensLab-UPC was awarded María-de-Maeztu (MDM) Excellence Unit (MDM-2016-0600, 1/7/2017-30/6/2021) funded by the Agencia Estatal de Investigación, Spain.
- The work of A. Salcedo Bosch was supported by grant 2020 FISDU 00455 funded by Generalitat de Catalunya—AGAUR.
- The European Commission collaborated under projects H2020 ATMO-ACCESS (GA-101008004) and H2020 ACTRIS-IMP (GA-871115). The European Institute of Innovation and Technology (EIT), KIC InnoEnergy project NEPTUNE (Offshore Metocean Data Measuring Equipment and Wind, Wave and Current Analysis and Forecasting Software, call FP7), supported the PdP and Ijmuiden offshore measurement campaigns.
- Profs. Jakob Mann and Alfredo Peña (Denmark Technical University, DTU; Department of Wind and Energy Systems · Meteorology and Remote Sensing · Wind Energy Systems Division) are gratefully acknowledged for hosting A. Salcedo-Bosch during his Ph.D. secondments.
- UPC-LIM lead PdP and Ijmuiden offshore measurement campaigns in the framework of European project NEPTUNE (partners: Catalonia Energy Research Institute (IREC), Remote Sensing Lab. (RSLAB, today CommSensLab - UPC), Maritime Engineering Laboratory (LIM, UPC), Gas Natural Fenosa, CIEMAT, University of Stuttgart, Soluciones de Ingeniería Marítima Operacional, S.L. (SIMO)). EOLOS Floating Lidar Solutions is a sucessful spin-off from NEPTUNE.

# Abstract

Remote sensing of the atmosphere is widely used by the wind energy industry to both assess future wind farms deployment sites as well as to improve their operation. With the rising interest in offshore wind energy, remote sensing of the atmosphere has become essential in offshore deep-sea sites in order to reduce deployment and operation costs. Particularly, floating LiDARs have become the de-facto instrument for offshore wind resource assessment due to its flexibility and capabilities to measure the wind with equivalent accuracy as meteorological met-masts in a cost-effective manner.

The main goal of this Thesis is to study and exploit the potentialities of existing atmospheric remote sensing instruments, with special emphasis on floating Doppler wind LiDARs. Towards this purpose, different signal processing and machine learning solutions are proposed and analysed. First, the correction of the effect of vertical wind on micro-rain-radar measurements is tackled by means of inverse methods. Second, the capabilities of floating LiDARs to retrieve ocean-related parameters is studied. To that end, signal processing techniques based on spectral analysis of the buoy's motion are used to characterize the ocean waves period. Third, and core part of this Thesis, the motion-induced error of floating-LiDAR measurements of the wind is studied in terms of estimation and compensation. Regarding the former, a novel analytical formulation to estimate horizontal-wind-speed bias and turbulence-intensity-increment error products is presented. The latter topic is tackled using machine learning techniques, specifically, an Unscented Kalman filter for motion compensation of floating-Doppler-wind-LiDAR measurements is presented, and its performance is analyzed under different wave and atmospheric scenarios.

The presented methodologies are validated against reference fixed LiDARs and anemometers in the context of two measurement campaigns: "Pont del Petroli" and IJmuiden campaigns. Data clustering techniques are used to assess the quality of the retrieved data products under different scenarios of interest for the industry.

The results attained by the novel solutions presented here further demonstrate the capabilities of floating Doppler wind LiDARs for off-shore wind monitoring, which strengthens their position as key remote-sensing instruments for the off-shore wind energy industry.

# Resumen

La industria eólica utiliza la teledetección de la atmósfera como herramienta para identificar futuros emplazamientos de campos eólicos así como para optimizar su funcionamiento. En las últimas décadas, con el incremento de campos eólicos marinos, la teledetección se ha convertido en fundamental para reducir el coste de sus instalaciones. Especialmente, los LiDAR Doppler flotantes han ganado terreno en la industria eólica marina como instrumento estándar para la evaluació del recurso eólico gracias a su bajo coste, su flexibilidad y su precisión al mesurar el viento en comparación con otros métodos.

El objetivo principal de esta tesis es el estudio y explotación de las capacidades de instrumentos de teledetección ya existentes, con especial énfasis en el LiDAR Doppler flotante. Para hacerlo, se analizaron una serie de métodos de procesado de señal y "machine learning". En primer lugar se estudia la corrección del efecto del viento vertical en medidas del radar de lluvia "micro-rain-radar" empleando métodos inversos. En segundo lugar se abordaran las posibles aplicaciones del LiDAR flotante en la medida de parámetros oceanográficos. En este sentido, se presenta un nuevo método basado en estimación espectral para poder estimar el periodo de oleaje a partir de medidas de la inclinación del LiDAR flotante. En tercer lugar, la parte principal de la tesis aborda la estimación y la corrección del error causado por el oleaje en las medidas de los LiDAR Doppler flotantes. En cuanto a la estimación del error, se desarrolla una formulación analítica para estimar el sesgo de la velocidad horizontal del viento así como el incremento de la intensidad de turbulencia. En cuanto a la corrección del error, se presenta un "Unscented Kalman filter" capaz de corregir el error en las medidas del viento causado por el oleaje en LiDARs flotantes. Además, su rendimiento se estudia en diferentes escenarios atmosféricos y de oleaje de interés.

Los métodos desarrollados en esta tesis se han validado con medidas de LiDARs fijos y anemómetros como referencia. Los datos experimentales provienen principalmente de dos campañas de medidas: la campaña de "Pont del Petroli" y la campaña de "IJmuiden". Se han utilizado herramientas de clusterización de datos para estudiar la calidad de los productos de datos obtenidos en escenarios de interés para la industria eólica.

Los resultados logrados por los métodos presentados en esta tesis muestran las capacidades y posibles aplicaciones futuras de los LiDARs flotantes y refuerzan su posición como instrumento clave dentro de la industria eólica marina.

# Resum

La indústria eòlica utilitza la teledetecció de l'atmosfera com a eina per identificar futurs emplaçaments de camps eòlics així com per optimitzar el seu funcionament. En les últimes dècades, amb l'increment de camps eòlics marins, la teledetecció ha esdevingut fonamental per reduïr el cost de les seves instal·lacions. Especialment, els LiDAR Doppler flotants han guanyat terreny en la indústria eòlica marina com a instrument estandard per a la evaluació del recurs eòlic gràcies al seu baix cost, la seva flexibilitat i la seva precisió en mesurar el vent en comparació amb altres mètodes existents.

L'objectiu principal d'aquesta tesi és l'estudi i explotació de les capacitats d'instruments de teledetecció ja existents, amb especial èmfasi en el LiDAR Doppler flotant. Per a ferho, s'analitzaren una sèrie de mètodes de processat de senyal i "machine learning". En primer lloc s'estudia la correcció de l'efecte del vent vertical en mesures del radar de pluja "micro-rain-radar" emprant mètodes inversos. En segon lloc s'abordaren les possibles aplicacions del LiDAR flotant en la mesura de paràmetres oceanogràfics. En aquest sentit, es presenta un nou mètode basat en estimació espectral per poder estimar el període de les onades a partir de mesures de la inclinació del LiDAR flotant. En tercer lloc, la part principal de la tesi aborda l'estimació i la correcció de l'error causat per l'onatge en les mesures dels LiDAR Doppler flotants. Pel que fa a l'estimació de l'error, es desenvolupa una formulació analítica per estimar el biaix de la velocitat horitzontal del vent així com l'increment de la intensitat de turbulència. Pel que fa a la correcció de l'error, es presenta un "Unscented Kalman filter" capaç de corregir l'error en les mesures del vent causat per l'onatge en LiDARs flotants. A més a més, el seu rendiment s'estudia en diferents escenaris atmosfèrics i d'onatge d'interès.

Els mètodes desenvolupats en aquesta tesi s'han validat amb mesures de LiDARs fixes i anemòmetres com a referència. Les dades experimentals provenen principalment de dues campanyes de mesures: la campanya de Pont del Petroli i la campanya d'"IJmuiden". S'han utilitzat eines de clusterització de dades per tal d'estudiar la qualitat dels productes de dades obtinguts en escenaris d'interès per a la indústria eòlica.

Els resultats assolits pels mètodes presentats en aquesta tesi mostren les capacitats i possibles aplicacions futures dels LiDARs flotants i reforcen la seva posició com a instrument clau dins la indústria eòlica marina.

# Contents

# List of Figures

# List of Tables

# Acronyms

**AI** Artificial Intelligence. 5

**AR** Auto Regressive. xxi, 99–105, 108, 114, 115, 117, 119

**CW** Continuous Wave. 13, 14, 51–53, 58, 73, 74, 98

**DoF** Degrees of Freedom. xxi, 4, 24, 35, 36, 48, 52, 53, 59, 63, 64, 73, 76, 84, 88, 95, 98, 102, 103, 115

**DSD** Drop Size Distribution. xvii, xviii, 6, 27–34

**DWL** Doppler Wind LiDAR. 7, 8, 15, 16, 21, 22, 25, 35, 48–56, 58, 68, 69, 73, 74, 76, 98, 100, 111, 112, 114

**EKF** Extended Kalman Filter. 76, 131

**FDWL** floating Doppler Wind LiDAR. xvii, xix–xxiii, 6, 9, 17–19, 21, 22, 25, 35, 51–57, 59, 61–64, 66–71, 73–80, 83, 84, 88, 90–99, 102–112, 114–116

**FFT** Fast Fourier Transform. 36, 37, 43, 44

**FLS** Floating LiDAR Systems. xvii, 17, 21, 22, 25, 26

**FMCW** Frequency Modulated Continuous Wave. 6, 9, 27–29, 32, 34

**GPS** Global-Positioning-System. 37, 39

**HWS** Horizontal Wind Speed. xix–xxii, 3, 6, 8, 14, 16, 18, 52–56, 58, 59, 61–63, 66–69, 71–75, 77, 81, 82, 84, 87, 89–95, 98–101, 104–111, 115

**IMU** Inertial Measurement Unit. xxi, 9, 22, 23, 39, 44, 54, 56, 64, 65, 69, 78, 84, 88, 95, 98, 102, 103, 105, 114, 115

**IOP** Intensive Observational Period. 8, 9

**KF** Kalman Filter. 76, 78, 131

**KPI** Key Performance Indicators. xxiii, 5, 18, 19

**LAT** Lowest Astronomical Tide. 23

**LCoE** Levelized Cost of Energy. xvii, 2, 3

**LiDAR** Light Detection and Ranging. xvii, xx, xxi, xxiii, 3–5, 7–9, 11–15, 17, 18, 21, 22, 35, 36, 51, 74–77, 79–86, 88–95, 97, 98, 117

**LoS** Line of Sight. xvii, 8, 12–16, 21, 22, 57, 61, 62, 68, 73, 76, 78, 79, 81, 84, 85, 95, 97, 98, 113, 115

**LR** Linear Regression. 109, 112

**LSQ** Least Squares. 31, 58, 81

**MD** Mean Deviation. xviii, 45–47, 50, 92, 94, 95, 105, 109, 112, 115, 118, 119

**metmast** Meteorological Mast. xvii, xxiii, 2–5, 23–26, 37, 54, 68

**OWA** Offshore Wind Accelerator. 18

**PdP** Pont del Petroli. xvii, xx–xxii, 22, 24, 25, 56, 64, 68–74, 88, 89, 91, 92, 95, 98, 102, 107, 108, 110, 114, 115

**PSD** Power Spectral Density. xviii–xxi, 6, 36, 43–45, 47–50, 64, 65, 82, 90, 91, 98, 100, 101, 106–108, 125, 126

**PSLL** Primary-to-Secondary Lobe Level. 106, 107

**RAUKF** Robust Adaptive Unscented Kalman Filter. 76, 77, 86, 95, 134

**RMSE** Root-Mean-Squared Error. xviii, xx, 45–48, 50, 66, 67, 71–73, 90–92, 94, 95, 112, 116, 118, 119

**RR** Rain Rate. xviii, 6, 27, 29, 30, 32–34

**RVD** Random Variable Distribution. 131, 132

**RW** Random Walk. xx, xxi, 82, 83, 87, 90, 91, 93, 95, 97, 98, 100–102, 105, 114, 115, 117, 119

**SV** Spatial Variation. 68, 88, 89, 108

**TI** Turbulence Intensity. xix–xxiii, 6–8, 16, 17, 35, 52–56, 63, 64, 67, 69–75, 77, 88, 91, 93–95, 97, 98, 105–113, 115

**UCM** Uniform Circular Motion. xxi, 100–105, 115, 119

**UKF** Unscented Kalman Filter. xxi, 8, 9, 52, 76, 78, 85, 86, 91, 93, 95, 97, 98, 100, 102–106, 113, 115, 117, 119, 120, 131, 132, 134

**UT** Unscented Transform. 131–133

**UTC** Coordinated Universal Time. 33

**VAD** Velocity Azimuth Display. xvii, xx, 8, 14, 15, 21, 52–54, 58, 59, 61, 62, 68, 73, 78, 81, 82, 84, 85, 88, 95, 98, 114

**VAM** Vertical Air Motion. xviii, 6, 28–34

**VORTEX-SE** Verification of the ORigins Tornado EXperiment in South East US. 7, 9, 28, 29, 32, 34

**VWS** Vertical Wind Speed. 54, 58, 59, 77, 84, 87, 99, 100, 104, 115

**WD** Wind Direction. xix, xx, xxii, 3, 16, 18, 21, 52, 54, 58, 62, 63, 66, 73, 75, 77, 81, 82, 84, 87, 89–91, 93–95, 99, 104, 105, 108–112, 115

**WTG** Wind Turbine Generator. 1, 2, 16, 17

# Chapter 1

# Introduction

## 1.1 Wind Energy Market Outlook

In the path towards the achievement of 1.5ºC global warming by 2100, huge efforts are made globally to switch towards renewable energy sources. Recently, renewable energy sources (excluding hydropower) share in power generation reached 13% globally, exceeding nuclear energy generation (9.8% share) [BP 2022]. Among the different renewable sources, wind energy has reached a relevant position in the global energy market (6.65% share) due to its advantages in terms of environmental impact and technology improvements [Joyce Lee and Feng Zhao 2019]. In the recent years, a tendency towards offshore wind energy has been observed due to the more homogeneous winds that can be found over the ocean. In 2021, a record was set in newly installed offshore wind energy capacity (21.1 GW), reaching a global offshore wind capacity of 57.2 GW. Led by China and Europe, with a newly installed capacity of 17 GW and 3.3 GW in 2021, respectively, offshore wind energy has reached a share of approximately 30% of new wind energy installations [Lee & Zhao 2022].

Particularly in Europe, the wind energy industry shows a rising interest in deploying offshore wind farms further offshore, where there are more stable atmospheric conditions and power plants interfere less with economic activity [Ramírez et al. 2021]. When installed further from shore and in deeper waters, turbines face harsher meteorological conditions, requiring new turbine designs together with improved operating practices [Agency 2021]. The less accessible locations and the advanced technology requirements caused a peak in offshore wind farms installation costs in the 2010 decade. In order to reduce the costs, the industry focused on the economy of scale by standardizing the turbine manufacturing process and increasing the turbines capacity. As it can be observed in Figure 1.1, there has been a tendency towards the increment of the average rotor diameter and hub height of the installed wind turbine generators (WTG) in the last decade. Larger rotor diameter and higher hub-heights permit a higher power output, which enables an important reduction of

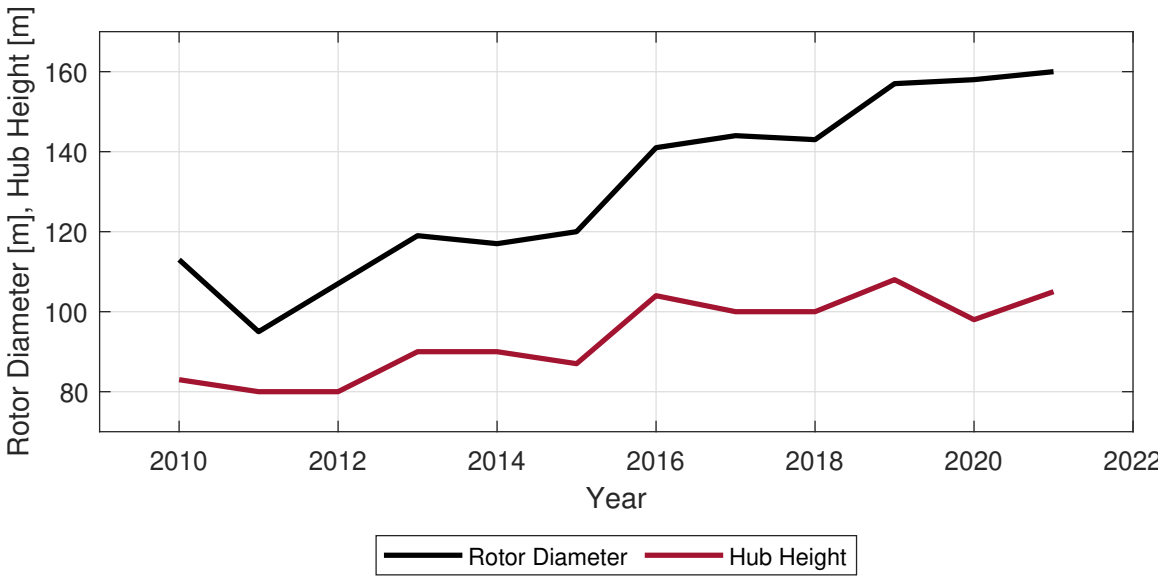


Figure 1.1: Evolution of the average rotor diameter and hub height of the offshore installed wind turbines per year. Adapted from [Taylor et al. 2022].

the installation costs and an amortization of wind farm projects, achieving in 2021 a reduction of the Levelized Cost of Energy (LCoE) by a 60% from its peak in 2011 [Taylor et al. 2022].

Nevertheless, offshore wind energy LCoE (0.075 USD/kWh) is significantly higher in comparison to onshore wind (0.033 USD/kWh) and is the second highest just after concentrating solar power (0.114 USD/kWh) (see Figure 1.2). One of the main differential factors are the higher operation and maintenance costs of offshore plants, which are more difficult to access. Offshore wind farms are complex and expensive facilities, with a budget that can easily reach thousand million Euros and several years of planning to the final deployment of the plant. Therefore, an optimal planning and operation of the wind farms is of main importance for the industry, which requires an accurate measurement of the offshore wind resource and other atmospheric parameters.

## 1.2 Remote Sensing of the Wind Resource

The most accepted sensors for wind measurements are the cup anemometers, which due to their limitations (measurement heights and point-like measurements), require them to be deployed on meteorological masts (metmast). However, in the case of offshore wind farms, as they are installed at more remote locations and into deeper waters, the deployment of metmasts planted on the seabed may be too expensive. Besides, due to the increase in WTGs hub height in the last decade, metmasts may not be a feasible solution for measuring the wind at those heights. This motivates the use of alternative remote sensing sensors such as satellites [Barthelmie & Pryor 2003, Chang et al. 2014], radars [Hirth et al. 2012], sodars [Vogt & Thomas 1995, Lang & McKeogh 2011], and combined methods [International Energy Association 2007, Sempreviva et al. 2008]. Nevertheless,

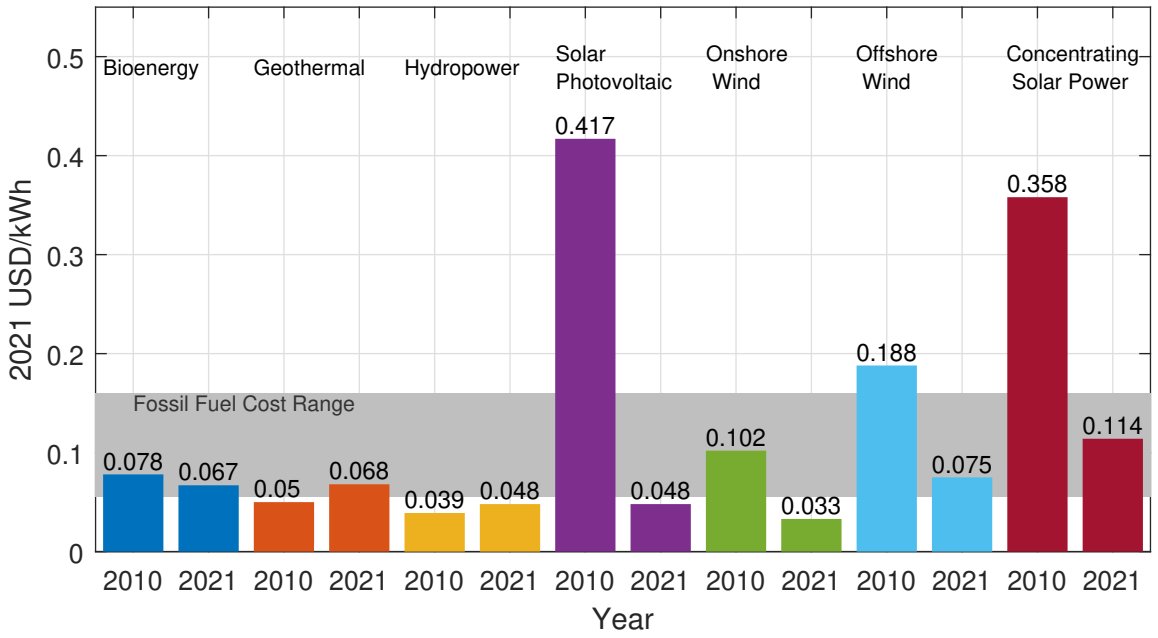


Figure 1.2: Comparison of the average LCoE of different renewable energy sources between 2010 and 2021. Adapted from [Taylor et al. 2022].

due to the high requirements of the industry in terms of measurement accuracy, temporal and spatial resolution, and data availability, LiDARs have become the most trustable device for wind remote sensing.

In the context of offshore wind energy, LiDARs placed atop floating platforms or buoys have arisen as the de-facto instrument for offshore wind vector measurements [Carbon Trust 2018]. When placed over a floating platform, LiDARs provide a series of advantages:

- They permit wind remote sensing in a cost-effective manner without relying on expensive facilities. For instance, the cost of a floating LiDAR deployment is of about hundred-of-thousand Euro whereas metmast installation can easily reach up to millions of Euros in installation and deployment costs.
- They are able to be easily re-deployed and thus cover large areas offering high versatility [Pichugina et al. 2012].
- They are capable of sensing the wind at hub-height altitudes without the need for an external structure.
- They provide reliable measurements of the 10-minute mean Horizontal Wind Speed (HWS) and Wind Direction (WD) vertical profiles with very high accuracy ($\rho^2 > 0.98$ using a metmast as a reference).

However, floating LiDARs suffer 6-Degrees of Freedom (DoF) motion due to the ocean waves, which induces errors on instantaneous wind vector measurements and adds variance to LiDAR measurements in comparison to fixed LiDARs [Gutiérrez et al. 2015]. Therefore, the correction of the motion-induced errors on floating LiDARs is a hot topic in the state of the art [Gottschall et al. 2012a, Gutiérrez-Antuñano et al. 2017, Gutiérrez-Antuñano et al. 2018, Kelberlau et al. 2020, Salcedo-Bosch et al. 2021c].

## 1.3 Off-shore Wind Energy in CommSensLab

NEPTUNE (Offshore Metocean Data Measuring Equipment and Wind, Wave and Current Analysis and Forecasting Software, 9/1/2011-10/31/2014) was a European project of the European Institute of Innovation and Technology (EIT). NEPTUNE was the starting point of CommSensLab (UPC) activity on the application of floating Doppler lidars for off-shore wind resource assessment and optimised location of off-shore wind-energy generators. The project involved several research and industrial partners: Instituto de Investigación de Energía de Cataluña (IREC), CommSensLab (formerly Remote Sensing LAb., UPC), Lab. de Ingeniería Marítima (LIM-UPC), Gas Natural Fenosa, Centro de Investigaciones Energéticas Medioambientales y Tecnológicas (CIEMAT), University of Stuttgart, and Soluciones de Ingeniería Marítima Operacional S.L. (SIMO).

NEPTUNE gave rise to a new technology of off-shore wind-lidar systems for wind farms as well as a wealth of wind, wave and current simulation and forecasting tools. Specifically, KIC (Knowledge Innovation Community)-InnoEnergy European project NEPTUNE [KIC InnoEnnergy 2015] aimed at developing cost-effective solutions for offshore wind energy. Towards this purpose, the project developed:

- (i) a floating Doppler wind Lidar (FDWL) buoy for offshore wind resource assessment, which gave rise to spin-off EOLOS$^{TM}$ [EOLOS 2023] and
- (ii) wind, wave and current measurement numerical models (hindcast/forecast).

The NEPTUNE$^{TM}$ FDWL buoy was capable of measuring the wind at heights up to 200 m from the sea surface by a fraction of the cost of a metmast with an equivalent accuracy. Along with the wind measurements, the buoy was designed to sense different ocean-related parameters such as waves and currents.

Spin-off company EOLOS (on floating Doppler lidar buoy systems for wind profiling) created after NEPTUNE received in 2015 the EIT Innovators Award to recognize KIC innovation teams that have developed in an exemplary manner an innovative product, service or process with a high potential for societal and economic impact [KIC InnoEnnergy 2015].

Project NEPTUNE also started to address the motion-compensation issue in FDWLs and conducted first test with the FDWL to measure the wind resource with the accuracy required by the industry standards in different maritime scenarios. The project went through three stages of development and testing of the lidar buoy:

- Test Campaign I. Two identical LiDARs were compared in lab conditions, one fixed on the ground and one co-located next to the fixed one on a moving platform.
- Test Campaign II. A proof-of-concept buoy was tested during a 38-days long campaign at "Pont del Petroli" pier (Barcelona coast), using a fixed LiDAR located 50 m apart as a reference. The results obtained during the campaign were revisited in [Gutiérrez-Antuñano et al. 2017] from a signal-processing and statistical perspective.
- Test Campaign III. The EOLOS$^{TM}$ floating LiDAR, the pre-commercial prototype of the NEPTUNE project, was tested during a 3-month period at IJmuiden test site (85 km offshore of the Netherlands). The IJmuiden campaign aimed to validate the EOLOS$^{TM}$ buoy against the IJmuiden metmast in order to demonstrate the measurement capabilities of the off-shore wind LiDAR and place it into the market. An internationally recognised consultancy (ECN) assessed the EOLOS$^{TM}$ buoy against a series of Key Performance Indicators (KPI).

The techniques and methods proposed in this Ph.D. will be evaluated over experimental data gathered during Test Campaign II and Test Campaign III, at "Pont del Petroli" and IJmuiden, respectively.

Departing from the background acquired with project NEPTUNE, CommSensLab (UPC) fostered the research line on off-shore wind-energy started with NEPTUNE as part of María-de-Maeztu Excellence project MDM-2016-060 (7/1/2017 - 6/30/2021) and National projects ARS (PGC-2018-094132-B-I00) and GENESIS (PID2021-126436OB-C21). Thus, as part of the latter project, the synergy among GNSS-R satellites, FDWLs and in-situ coastal sensors for wind observations is explored.

## 1.4 Main Objectives

This Ph.D. thesis focuses on ***floating LiDAR systems combined with advanced signal processing techniques (as inherited from the AI) for off-shore wind-speed measurement.*** Specific objectives are:

- **Objective 1. Methods for co-operative atmospheric observation over land and remote sensing quality assurance: Essentials** (obj. in collaboration with Purdue University, University of Massachusetts (UMASS), NOAA-NSSL, and Denmark Technical University (DTU)).- This

objective, used as an introductory complementary step in the Ph.D. project, aims at exploiting previous knowledge of the Unit (CommSensLab-UPC) in the field of co-operative atmospheric remote sensing and advanced signal processing. It focuses on the improvement of rain radar data products in cooperation with ground-based disdrometers.

- **Objective 2. Methods for co-operative atmospheric observation over sea: off-shore wind-energy applications** This is the core part of the Ph.D. and tackles the off-shore wind-lidar motion compensation problem from different points of view: First, characterization of the wave motional behaviour is tackled through Power Spectral Density (PSD) estimation techniques. Second, the motion-induced error on FDWL wind measurements is studied from numerical and analytical perspectives. And third, the motion compensation problem is approached by means of combining signal processing and machine learning techniques.

- **Objective 3. Advanced data processing methods for off-shore wind-energy remote sensing big-data analysis.** This objective is transversal to the entire thesis. It comprises the study and identification of unknown patterns (apparent HWS and TI vs. buoy motional variables) in "Pont del Petroli" and IJmuiden campaigns by using Big Data techniques and the knowledge acquired in objective 2.

### 1.4.1 Objective 1. Methods for co-operative atmospheric observation over land and remote sensing quality assurance: Essentials

WTGs are deteriorated when operating under precipitation. Therefore, in order to increase their lifetime, they need to be stopped in scenarios of heavy rain, snow or hail. An accurate measurement of the precipitation vertical profile is of main importance for the wind energy industry to preview heavy precipitation events close to the surface and stop the wind farms. Operationally, profiles of precipitation are derived from scanning weather radars using VVP-like (volume velocity processing) processing of a series of PPI scans at multiple elevations (e.g. 0.1, 0.3, 0.5, 1, 1.5, 3, 5, 10 degrees from the horizontal). On the other hand, local precipitation vertical profiles can be measured by means of vertically-pointed radars.

Vertically-pointed Frequency-Modulated Continuous-Wave (FMCW) radar measurements of rain are greatly influenced by strong vertical winds (vertical air motion, VAM) in convective rain scenarios. Particularly, 2nd order products such as rain rate (RR) and drop size distribution (DSD) experience high estimation errors due to VAM. This objective is aimed at estimating the VAM from vertically-pointed FCMW radar measurements in order to correct VAM-corrupted rain 2nd order products.

Towards this purpose, a forward methods to estimate VAM velocity at a particular height from vertically-pointing S-band FMCW radar measurements in convective rain scenarios is to be explored. The forward method relies on the parameterization of the DSD as a gamma distribution. It

estimates the VAM along with the constitutive parameters of the gamma distribution by means of a parametric solver.

The method is tested over radar measurements and taking a ground-based disdrometer as a reference during the Verification of the ORigins Tornado EXperiment in South East US (VORTEX-SE) project.

### 1.4.2 Objective 2. Methods for co-operative atmospheric observation over sea: off-shore wind-energy applications.

This objective, which is the core part of the Ph.D. project, tackles the study of the effect of floating LiDAR motion on wind measurements. This is a two-fold objective: (i) estimation of the characteristic motional-period of the floating DWL, (ii), estimation of the motion-induced error on the floating DWL, and (iii) motion-correction at floating DWL measurements. For this objective, data gathered during "Pont del Petroli" and IJmuiden campaigns will be used.

#### 1.4.2.1 Estimation of the DWL characteristic motional period

Floating DWL buoys are subject to angular motion around the three coordinate axes. Yaw motion is characterised by low variations with time whereas roll and pitch motion show much faster oscillatory behaviour. Therefore, roll and pitch motions are the most informative parameters of wave motion. Thus, wave information can be obtained from roll and pitch tilt measurements. This objective is aimed at estimating the ocean waves period from roll and pitch measurements of a FDWL buoy.

A new method to estimate the wave period from solely measurements of roll and pitch will be explored.

#### 1.4.2.2 Estimation of motion-induced error of FDWL measurements

FDWL motion induces errors on the retrieved wind vector, namely, a bias on the retrieved mean wind vector and an apparent turbulence additive to the wind TI. Standard temporal resolutions in wind energy are 10 min (typical) and 30 min. Here, it is aimed at study and quantify the motion-induced error on FDWLs.

We aim at studying and quantifying both the motion-induced bias and apparent TI on FDWLs. The motion-induced error on the retrieved wind products (HWS and TI) will be assessed by means of a thorough formulation of the FDWL buoy geometry and of the specific DWL retrieval algorithm employed. Methods to quantitatively estimate the FDWL error will also be explored from two perspectives: (i) at 1-s level (corresponding to the LiDAR-scan temporal resolution), and (ii) at a 10-min level.

Additionally, aligned with Objective 3, the motion-induced error will be revisited as a function of different motional and wind scenarios.

#### 1.4.2.3 Motion correction of FDWL measurements

In order to reduce the impact of DWL buoy motion on the HWS and TI measurements it is necessary to compensate the motion-induced error, which otherwise leads to an apparent HWS and apparent (increased) TI. This will be carried out by an Unscented Kalman Filter (UKF) departing from the motion compensation method proposed in [Kelberlau et al. 2020].

The DWL scanning cone becomes distorted due to the buoy movement and so is the lidar pointing direction. When having LoS information available, Kelberlau et al. (2020) depicts the algebraic transformations relating roll, pitch and yaw andlges to the real azimuth and zenith angles of the lidar pointing direction and it proposes a mathematical method to correct the wind measurements at a VAD level. In contrast to this method, the ZephIR$^{TM}$300 DWL used in the "Pont del Petroli" and the IJmuiden campaigns does not allow access to LoSs intormation.

To solve this "blind estimation" problem an UKF is proposed. We take advantage of the LoS geometrical transformations given in [Kelberlau et al. 2020] and of our knowledge of the lidar VAD retrieval model. The state vector to be estimated is formed by the "clean" (i.e., motion-free) wind vector and is extended with the LiDAR initial scan phase, an undisclosed parameter by the ZephIR$^{TM}$300. The observation vector is formed by the wind components measured in the moving buoy coordinate system ($u^{FDWL}$, $v^{FDWL}$, $w^{FDWL}$). This vector proposal attempts to make the filter able to estimate the reference wind vector from the motion-corrupted wind vector.

The unknown nature of the stochastic wind process to be included as the UKF state-transition function motivates the study of different wind process models. The impact of the wind modelling as a random walk or as an auto-regressive process will be discussed. Moreover, in alignment with objective 3, the performance of the motion-correction UKF will be discussed as a function of wind and motional scenarios.

### 1.4.3 Objective 3. Advanced data processing methods for off-shore wind-energy remote sensing big-data analysis.

Data-processing techniques are to be applied to analyse the experimental data gathered during the off-shore intensive observational periods (IOP) in "Pont del Petroli" and IJmuiden campaigns. They are expected to disclose multi-variable correlations and hidden patterns and features. Towards this end, obj. 3 is aimed at: (i) the development of a relational database encompassing IJmuiden experimental data and querying tools, and (ii) development of basic *data mining* tools relying on big-data techniques.

IJmuiden and "Pont del Petroli" IOP comprise large amounts of data from multiple instruments and sensors at different sampling rates, including 10-min sampled data (the standard resolution in wind energy) and 1-to-10 Hz data. Due to the hugenumber of data files, large sizes and different formats involved, integration into a single database with transparent characteristics to the user is

proposed: First, file formats are to be standarized to a unique one. Second, two goals are defined for database transparency: Concerning 10-min data, single files are to be created for the complete IOP. Concerning high-resolution data (1 s): (i) statistical parameters (wave period and amplitude for instance) are to be recomputed at a 10-min basis, hence creating analogous files as for 10-min data and, (ii) querying tools are to be created for data inspection.

As transversal tool, Data Mining will be carried out to discover hidden patterns among atmospheric and wave parameters in the FDWL records. Data clustering will be carried out over the measurement records to identify how different wave motion and atmospheric scenarios can affect performance of the FDWL.

## 1.5 Organization of the Ph.D. Thesis

This Ph.D. Thesis is organized as follows:

- **Chapter 1** motivates this Ph.D. thesis and presents its main goals contextualized in the offshore wind energy state of the art.
- **Chapter 2** introduces the foundations of LiDAR wind remote sensing and reviews its functioning principles.
- **Chapter 3** presents the instrumentation and "Pont del Petroli" and IJmuiden measurement campaigns used in the Ph.D. thesis.
- **Chapter 4** presents a forward method to estimate the VAM from stand-alone FMCW radar measurements in the context of VORTEX-SE campaign.
- **Chapter 5** presents the L-dB method to estimate the zero-crossing ocean-waves period from roll and pitch measurements by the FDWL IMU. The results are validated in the context of IJmuiden campaign using a wave buoy as a reference.
- **Chapter 6** presents a unified analytical formulation for the computation of motion-induced errors in FDWL measurement of the wind resource. The analytical model estimation performance is discussed as a function of the FDWL motion and wind scenario in the context of "Pont del Petroli" and IJmuiden campaigns.
- **Chapter 7** describes the UKF for FDWL motion compensation and discusses its performance as a function of different motion and wind scenarios. The filter behaviour is discussed under different LiDAR operation configurations as well.
- **Chapter 8** studies the impact of different wind and initial scan phase model combinations on the capabilities of the motion-correction filter as well as the impact of different sea and atmospheric scenarios on the filter performance.

- **Chapter 9** gives conclusion remarks and outlook.

# Chapter 2

# LiDAR in Off-shore Wind Energy

## 2.1 LiDAR Foundations

LiDARs are remote sensing devices that aim to measure a certain parameter of interest at a target location by sending a light beam and receiving a backscattered signal which is received by a photoreceiver with both high temporal and spatial resolution [Slinger & Harris 2012]. LiDAR stands for *Light Detection and Ranging*, and its acronym is an analogy to radars, which instead of using light beams, use electromagnetic waves at radio frequencies.

LiDARs were invented just after the development of the first lasers in the 1960's. One of the first applications of LiDARs was measuring the clouds and atmospheric pollution [Goyer & Watson 1963], and the measurement of the distance to the Moon from the Earth [Smullin & Fiocco 1962]. LiDARs became known to the general public by its usage in the Apolo 15 mission (1972), in which a LiDAR was used to map the surface of the moon. For the measurement of target distances, LiDARs measure the time of flight of an emitted laser beam to the target and its way back. This was possible thanks to the electronics technology available in the 60's.

LiDARs applications in wind remote sensing were demonstrated in the 1970s in aviation and meteorology fields [Jelalian 1992]. Their applications in wind energy were firstly explored in the 1980s [Hardesty & Weber 1987, Vaughan & Forrester 1989], but they were too large and expensive, and thus, were not accepted commercially in the wind energy industry. With the improvement of optical fiber technology in the 1990s, thanks to communications engineering, a new generation of all-fibre LiDARs emerged. They proved themselves able to reliably measure the wind resource with high sensitivity and low cost, being more and more accepted in the industry.

## 2.2 LiDAR Functioning Principle and Types

LiDAR functioning principle is based on the scattering process, in which atoms or molecules that are exposed to electromagnetic radiation with a wavelength similar to their size emit waves of the same frequency (and lower energy) in various directions. LiDARs take advantage of this physical

process by sending laser beams to the target to be sounded and then measuring the backscattered light re-emitted by the target. Therefore, depending on the target size, LiDARs use different wavelengths: from ultraviolet (250 $nm$) to infrared (10 $\mu m$).

As mentioned before, LiDARs are able to measure a target distance by measuring the time-of-flight of the backscattered light. Moreover, the frequency shift between emitted and received light beams due to the Doppler effect can be used to determine the target velocity.

Depending on the remote sensing technique used LiDARs can be classified into *coherent* or *incoherent*. Incoherent (or direct detection) LiDARs are based on amplitude changes of the backscattered signal whereas coherent LiDARs measure the frequency or phase shifts of the backscattered beam in comparison to the emitted one.

*Incoherent LiDARs* such as backscatter or Raman lidars are mainly used in atmospheric science to determine the atmospheric composition and distribution. Some of its applications are the determination of aerosol concentration, pollution detection, cloud height and classification, and determination of airborne particle properties, among others. They can be used to measure the wind speed and direction as well. The backscattered signal intensity pattern describes an aerosol density at the illuminated target location which shows variations with time, yielding recognisable aerosol patterns that pass over the measured LoS. When this already recognised signature passes over an additional LoS, knowing the distance and time of flight, the wind speed and direction can be measured (see Figure 2.1).

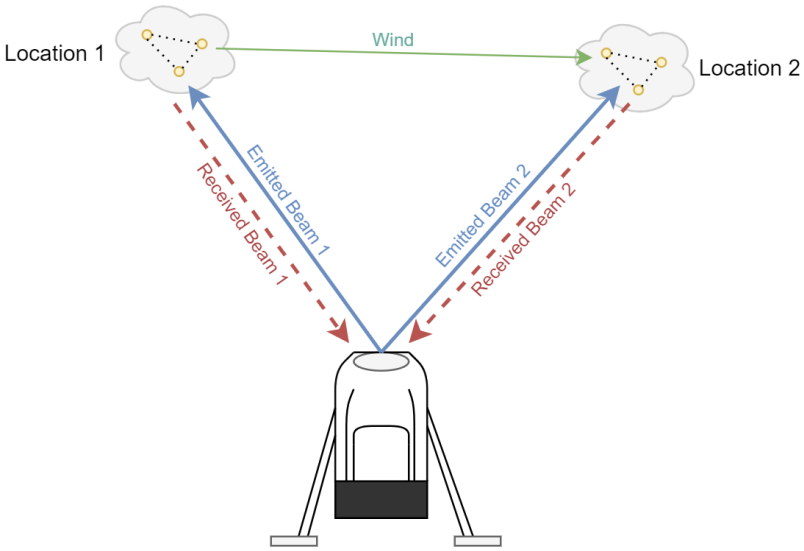


Figure 2.1: Incoherent LiDAR functioning principle. The aerosol pattern is first shown in Location 1 and then at Location 2. The correlated aerosol signatures acrossm multiple locations permit the wind speed and direction measurement.

*Coherent LiDARs* (or Doppler LiDARs) are mainly used to measure the wind speed by measuring the Doppler shift between the emitted and received light beams in a LoS. When the illumi-

nated airborne particles are in motion, the back-scattered beam suffers a frequency shift due to the Doppler effect. Coherent LiDARs make use of the Doppler relation to obtain the wind speed. It is formulated as

$$f_d = -\frac{2v_r}{\lambda}, \tag{2.1}$$

where $f_d$ is the Doppler frequency shift, $v_r$ is the velocity along the LiDAR LoS direction (positive away from the lidar), and $\lambda$ is the sounding wavelength. Therefore, as indicated by Equation 2.1, a target moving towards the LiDAR increases the frequency of the backscattered light (shift towards blue), and a target moving away from the LiDAR reduces the frequency of the returning light (shift towards red).

Coherent LiDARs make use of a local oscillator to retrieve the Doppler shift. This is, the backscattered beam is optically mixed with the the local oscillator (reference beam) resulting in a "beat" signal that is measured by a photodetector. When mixing two harmonic signals that oscillate at similar frequencies, the resulting wave shows intensity beats. The amplitude of the resulting signal can be described as

$$i(t) \propto [A_{LO}cos(\omega_{LO}t) + A_S cos(\omega_s t)]^2, \tag{2.2}$$

where $A_{LO}$ and $A_S$ are the amplitudes of the local oscillator and backscattered signals, respectively, and $\omega_{LO}$ and $\omega_S$ are the frequencies of the local oscillator and backscattered signals, respectively. This expression can be separated into a constant term and a cross term oscillating at the frequency difference between the local oscillator and the backscattered signal: the "beat signal". It can be formulated as

$$i(t) \propto [A_{LO}^2 + A_S^2] + 2A_{LO}A_S cos(|\omega_s - \omega_{LO}|t). \tag{2.3}$$

Coherent LiDARs are able to retrieve the frequency difference by measuring the "beat" frequency. There are two main coherent LiDAR configurations to measure the Doppler frequency shift: *homodyne* and *heterodyne* detection schemes. The homodyne detection scheme directly mixes the backscattered signal with the local oscillator, being only able to measure the magnitude of the frequency difference but not its sign. When using a heterodyne configuration, the backscattered signal is mixed with a frequency-shifted local oscillator, being able to measure both positive and negative Doppler shifts. A single LiDAR Line of Sight (LoS) measurement can only measure the radial component of the target velocity along the LiDAR pointing direction.

Depending on the emitted signal, LiDARs can be classified into *Continuous wave (CW)* or *pulsed*. *Pulsed* LiDARs use the time of flight to discern between the backscatter of different target ranges and *CW* LiDARs achieve the same by focusing the emitted beam to a particular height by changing its optics. *CW* LiDARs measurement range is very short being able to virtually measure at zero range, whereas *pulsed* LiDARs have a minum range of tenths of meters, typically at 40-50 m.

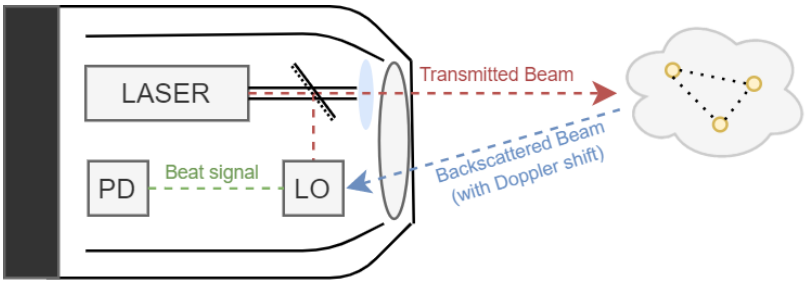


Figure 2.2: Coherent LiDAR functioning principle. The backscattered beam reflected by the airbourne particles is compared against a fraction of the emitted beam in the local oscillator (LO). The Doppler shift due to wind is measured at the photodetector (PD) as the frequency of the beat signal.

*Pulsed* LiDARs can assess atmospheric information at different heights with a single optical pulse. Range information is retrieved as the half of the time of flight between the emitted pulse and the time bin of interest ("range gate").

*CW* LiDARs continuously emit a light beam which is focused at a particular height. Therefore, in order to measure a vertical profile, *CW* LiDARs need to re-focus from one height to the next sequentially. Typically, they take multiple LoS measurements following a conical scan scheme from which the wind vector can be retrieved.

*This thesis uses the ZephIR$^{TM}$300 LiDAR, an all-fiber monostatic homodyne CW lidar.*

### 2.2.1 Velocity Azimuth Display algorithm

As mentioned, coherent LiDARs measure the radial component of the wind velocity at each LoS measurement. In order to retrieve the three components of the wind vector $\vec{U} = [u, v, w]$, they take multiple LoS measurements following a conically-shaped scan. The minimum number of LoS measurements required to obtain the 3-D vector is 3 since a system of 3 unknowns is faced. However, in the case of the ZephIR$^{TM}$300 LiDAR, 50 LoS measurements are taken per scan. The rapid sampling rate permits 1-s long scans, being able to measure a "snapshot" of the wind vector across the scan disk. The scanning cone is of an aperture $\theta_0$ of 30 deg from zenith. Figure 2.3 depicts a geometrical representation of the connical scanning configuration. The redundancy of the number of measured LoSs permits the velocity-azimuth-display (VAD).

The VAD algorithm is widely used for the retrieval of the wind speed vector since the 90s. Each LoS measurement of the radial velocity $v_r$ can be expressed as the dot product between the LiDAR pointing direction unitary vector $\hat{r}$ and the wind vector $\vec{U} = [u, v, w]$:

$$v_r(\phi(t)) = \hat{r}(t) \cdot \vec{U} = v_h \, sin(\theta_0) \, cos\,[\phi(t) - \phi_0] + w \, cos(\theta_0), \tag{2.4}$$

where $\theta_0$ is the LiDAR 30 deg aperture angle from zenith, $v_h$ is the HWS, $\phi(t)$ is the azimuth angle as a function of time, and $\phi_0$ is the azimuth angle of the wind vector ($\vec{U} = v_h \cos(\phi_0)\hat{x} + v_h \sin(\phi_0)\hat{y} +$

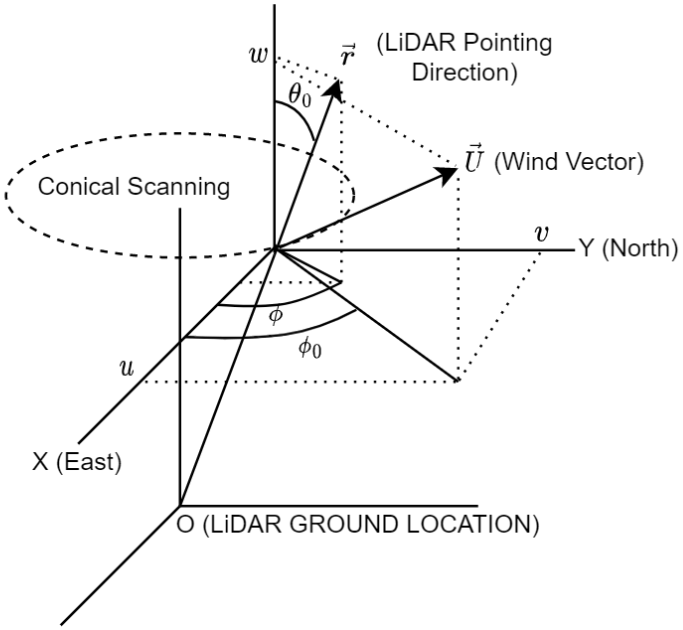


Figure 2.3: Geometrical scheme of the coherent LiDAR VAD scanning.

$w\hat{z}$. From Equation 2.4, the three components of the wind vector can be obtained as

$$u = A\,cos(\phi_0)\,csc(\theta_0), \tag{2.5}$$

$$v = A\,sin(\phi_0)\,csc(\theta_0), \tag{2.6}$$

$$w = A_{OS}\,sec(\theta_0), \tag{2.7}$$

where $v_h = \sqrt{u^2 + v^2}$, $A = v_h\,sin(\theta_0)$, and $A_{OS} = w\,cos(\theta_0)$. Thus, by knowing $A$, $A_{OS}$ and $\phi_0$, the wind vector can be retrieved.

The VAD algorithm uses the least-squares algorithm to fit the model function (Equation 2.4) to the measured LoSs ($v_r^{meas.}$) in order to retrieve the sought-after parameters $A$, $A_{OS}$, and $\phi_0$:

$$[A, A_{OS}, \phi_0] = \underset{A, A_{OS}, \phi_0}{\arg\max} ||v_r(\phi(t)) - v_r^{meas.}(\phi(t))||^2. \tag{2.8}$$

Figure 2.4 graphically depicts a VAD functioning example. The measured LoSs (black dots) follow the shape described by the model in Equation 2.4, and the best fit encountered by the VAD algorithm (Equation 2.8) is depicted in blue. $A$, $A_{OS}$ and $\phi_0$ parameters of interest are the amplitude, offset and phase of the fitted curve, respectively.

## 2.3 Doppler LiDAR in Wind Energy

DWL systems are widely used by the wind energy industry due to their reliability and robustness in sounding the wind [Slinger & Harris 2012]. They have been deployed around the globe in many different operations. Some of the applications of DWLs in wind energy are:

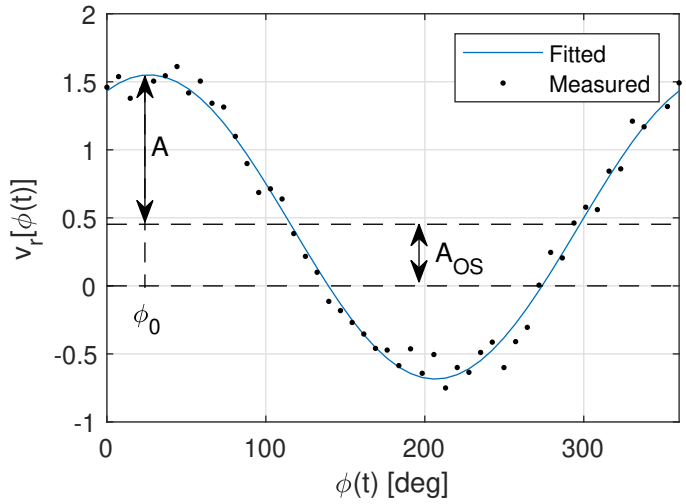


Figure 2.4: VAD result for the measured LoS velocities as a function of the $\phi$ azimuth scanning angle. Black dots represent the measured LoS velocities and the blue line represents the sinusoudal fitting. $A$ is the amplitude of the sinusoud, $A_{OS}$ is the sinusoid offset with respect to 0, and $\phi_0$ represents its phase.

- *On-site operations.* Unfavorable wind conditions may reduce WTGs power output and even challenge their integrity. For instance, an angular offset between the WD and the turbine nacelle orientation (*yaw missalignment*) causes an output power reduction. Moreover, sudden wind gusts may compromise the WTGs operation performance. DWLs deployed on WTGs nacelle may be used to warn for yaw missalignment or incoming gusts by measuring the wind up to 200 m in front of the blades.

- *Wind resource assessment.* Wind resource assessment is critical in investment decisions in wind farm projects [Carbon Trust 2018]. HWS, WD and TI parameters are of main importance when studying the adequacy of a future wind farm site. The standard instrument used towards this purpose are cup and sonic anemometers deployed on meteorological masts. However, in the last years, DWLs have been more and more employed for wind resource assessment, achieving a measurement accuracy comparable to the one of a meteorological mast with lower costs.

### 2.3.1 Doppler Wind LiDAR in Offshore Atmospheric Remote Sensing

Since the first offshore wind farm deployment at Vindeby, Denmark, in 1991, offshore wind industry has experienced a rapid growth (see Chapter 1) [Gottschall et al. 2017a]. In an offshore wind farm project, a broad knowledge of the prevailing wind conditions at a candidate wind farm location is needed to assess the return on the investment. High quality HWS, WD, and TI measurements of the future deployment site that are representative of a significant time period (e.g., seasonal and interannual variability) are required. This was traditionally achieved by means of

meteorological masts planted on the sea-bed. The increase in average water depths and WTGs heights increased the deployment costs of offshore meteorological masts, which motivated the industry to find an alternative solution. With the increasing popularity of LiDARs in the industry in the 2000's, deployment of LiDARs on offshore platforms arouse as a suitable alternative. This was due to the high flexibility of LiDARs combined to their capacity to measure at hub heights of the increasing size of WTGs. Between 2009 and 2013, a large ensemble of LiDARs were installed on offshore platforms (such as oil rigs and transformer stations) to obtain a comprehensive wind dataset within the EC-funded NORSEWIND project [Hasager et al. 2013]. The obtained results highlighted LiDARs potentialities in offshore operation in comparison to meteorological mast measurements. Besides, it permitted the development of a series of acceptance criteria on the LiDAR measurement performance [Kindler et al. 2009].

However, the installation of offshore platforms limits the flexibility of LiDARs, relying on fixed construction facilities. A more suitable and less expensive solution is to deploy LiDARs atop floating platforms or buoys, the so-called floating LiDAR systems (FLS) or FDWLs. FDWLs are formed by two key components: the LiDAR device and the floating platform. Two types of platforms are usually employed: standard wave buoys or spar buoys. The former is more subject to wave motion, and FDWLs of this type require active motion compensation. The latter may not require compensation due to their better stability and position keeping, however, they are only suitable for deep waters ($> 40$ m). In this thesis only FDWLs using wave buoys are considered. Moreover, FDWLs are required to host: (i) energy generation and storage systems, (ii) a data logging system, (iii) a communication system, (iv) a sea-bed mooring system, and (v) buoy's attitude measurement systems.

One of the main challenges to overcome by FDWLs is the wave-induced motion on the LiDAR, which compromises the accuracy of wind vector measurements. The commercial LiDARs used in FDWLs are conceived for a fixed operation, meaning that an accurate alignment of the instrument is required by the manufacturer. Thus, the 6-DoF motion induced by waves violates this assumption. The effect of motion on FDWL instantaneous measurements of the wind vector is reported in multiple studies in the literature [Gottschall et al. 2014a, Tiana-Alsina et al. 2015, Bischoff et al. 2018, Salcedo-Bosch et al. 2021a, Kelberlau & Mann 2022]. In wind enegy standard averaging periods, typically 10 or 30 min, the motion-induced error on the retrieved mean wind vector is found in terms of a bias of 1-2% in most cases [Gutiérrez-Antuñano et al. 2017, Gutiérrez-Antuñano et al. 2018, Kelberlau et al. 2020, Araújo da Silva et al. 2022a]. The error on instantaneous wind measurements is encountered as an "apparent variance addition" at higher wind statistical moments, such as the TI [Gutiérrez-Antuñano et al. 2018, Salcedo-Bosch et al. 2020a]. In the state of the art, study of the motion-induced error on FDWLs is two-fold: error estimation and error compensation. Error estimation is tackled separately at scan-time level [Tiana-Alsina et al. 2015, Bischoff

et al. 2018, Salcedo-Bosch et al. 2021a] and at 10-min level [Bischoff et al. 2018, Gutiérrez-Antuñano et al. 2018, Kelberlau & Mann 2022]. The motion compensation has been tackled by means of mechanical [Gutiérrez-Antuñano et al. 2017] or software approaches [Gutiérrez-Antuñano et al. 2018, Kelberlau et al. 2020, Salcedo-Bosch et al. 2021c; 2022b].

### 2.3.2 OWA Roadmap

The offshore wind accelerator (OWA) program aims at reducing the deployment and operating costs of offshore wind farms. Besides, it provides a series of recommendations and best practices for health and safety requirements. The program is aimed at reducing the costs through technology improvement and innovation, motivated by international competitors, and the most innovative and promising ideas are developed for commercialisation [Carbon Trust 2018].

Since the first commercially available FDWL in 2009, the technology was developed in alignment with the offshore wind industry interests as a support for financial decisions. In the context of OWA program, a working group coordinated by UK Carbon Trust set up a first framework for FDWL acceptance by the industry with their "roadmap for the commercial acceptance of floating LiDAR technology" [Carbon Trust 2013]. This roadmap defines the required steps for floating LiDAR technology to become commercially available. Additionally, it defines three stages of technology readiness for a FDWL system: *baseline*, *pre-commercial* and *commercial*. Since the first roadmap publication in 2013, FDWLs have been seen as a maturing technology with multiple developed systems achieving a pre-commercial stage as a part of commercial offshore wind farm developments. An updated roadmap published in 2018 [Carbon Trust 2018] reflects the latest status of FDWLs based on the expertise gathered accross the industry in the last years.

The OWA roadmap defines a series of KPIs which provide quantitative criteria for FDLW system acceptancy. Considering these requirements, the variety of the commercially available FDWLs has not been limited but has made sure that each system is evaluated against the same requirements. The KPIs define thresholds for beast practice of certain magnitudes measured on a 10-min basis. The quantitatively defined parameters of main importance are HWS and WD which are summarised in Table 2.1.

| KPI | Acceptance Criteria |
|---|---|
| mean HWS slope | 0.98 - 1.02 |
| mean HWS $R^2$ | >0.98 |
| mean WD slope | 0.97 - 1.03 |
| mean WD offset | <5 deg |
| mean WD $R^2$ | >0.97 |

Table 2.1: Best Practice Acceptance Criteria for KPIs of main importance. Adapted from [Carbon Trust 2018]

Additionally, KPIs of secondary importance are recommended to be measured but without quantitative Acceptance Criteria: *wind shear* and *TI*. Due to the limitations of FDWLs to measure theses parameters, a comparison of measurements against reference values measured by anemometry is recommended until there is sufficient knowledge in the sector on this subject.

# Chapter 3

# Experimental Data and Instrumentation Set-Up

One of the main objectives of the NEPTUNE project was to design and implement a FDWL able to be deployed commercially. At the end of the project, a first operational FDWL buoy prototype was the EOLOS$^{TM}$ FLS200 FDWL buoy. Towards this purpose, two buoy prototypes were tested in real offshore campaigns: a first buoy prototype (NEPTUNE$^{TM}$) in the "Pont del Petroli" campaign, and a second one (EOLOS$^{TM}$ FLS200), in IJmuiden campaign as part of the commisioning phase.

## 3.1 Instrumentation

*ZephIR 300 DWL.-* The ZephIR 300 is a continuous-wave focusable Doppler lidar specially conceived for offshore operation [Scientific 2016]. It is able to measure the wind at user-defined heights from 10 m up to 200 m in steps of 1 m [M. Pitter et al. 2014]. In order to retrieve the wind vector for a particular measurement height, the ZephIR 300 measures the Doppler radial speed along 50 LoSs every second over a scanning cone of 30 deg aperture from zenith. A wedge prism rotating with a uniform circular motion of one revolution per second is used to steer the laser beam in the directions of the 50 LoSs. In uniform wind, the projection of the wind vector along the 50 LoSs as a function of the azimuth scanning angle (i.e., the so called *VAD function*) takes the shape of a cosine. The lidar uses the VAD algorithm to retrieve the wind vector from the LoSs by fitting a cosine function to the LoS measurements [Slinger & Harris 2012]. The ZephIR 300 is a homodyne detection lidar, which means that it cannot discern the sign of the Doppler shift. As a result, the VAD function takes the form of a rectified cosine wave, creating an ambiguity of $\pm$180 deg for the WD measurement [Knoop et al. 2021]. The ZephIR 300 is equipped with a wind vane to disambiguate the WD. Table 3.1 summarises the main ZephIR$^{TM}$ 300 characteristics.

*NEPTUNE$^{TM}$ FDWL buoy.-* The proof-of-concept NEPTUNE$^{TM}$ FDWL buoy was a 3 m diameter buoy designed as a prototype for offshore LiDAR operations [Gutiérrez-Antuñano et al. 2017]. It had a modular four-floater structure designed to satisfy wind-energy measurement requirements

| Variable | Value |
|---|---|
| Measurement Height Range | 10 m to 200 m |
| Number of Measurement heights | up to 10 |
| LoS Sampling Rate | 50Hz |
| Wind Speed Accuracy | <0.5% |
| Wind Speed Range | <1 m/s to 70 m/s |
| Wind Direction Accuracy | <0.5 deg |

Table 3.1: ZephIR™300 specifications [Scientific 2016].

with a ZephIR$^{TM}$ 300 DWL as well as for tracking wave-induced motion on the device. The LiDAR was placed on a cardanic frame, aimed to keep the instrument still and to reduce the impact of buoy motion. The buoy was equipped with additional sensors to measure different wind and sea parameters. Specifically, it hosted two MicroStrain 3DM-GX2-45 inertial measurement units (IMU), which combined a high-precision GPS antenna, an accelerometer and a gyro. The 3DM-GX3-45 is able to measure the buoy's velocity and tilt with an accuracy of $\pm 0.1$ m/s and $\pm 0.35$ deg, respectively. The first IMU (i.e., the LiDAR IMU) was located under the LiDAR bottom, and the second IMU (i.e., the buoy IMU) was located on the buoy structure bottom (see Figure 3.1), being able to measure the buoy and LiDAR attitude.

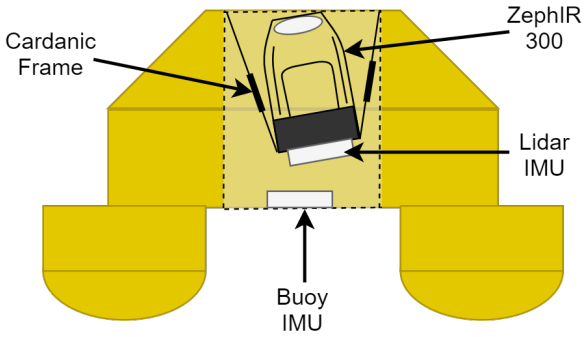


Figure 3.1: Instrumentation scheme of the FDWL proof-of-concept buoy used in PdP campaign.

*EOLOS$^{TM}$ FLS200.-* The EOLOS$^{TM}$ FLS200 buoy was an enhanced design of the NEPTUNE$^{TM}$ model, prepared for harsher scenarios and higher endurance during longer measurement campaigns [Tiana-Alsina et al. 2017]. It was also optimized to host a ZephIR$^{TM}$ 300 LiDAR. It had 3.77 m width, weighed 3 tons, and had a similar modular four-floater structure design. It hosted three wind generators and multiple solar panels generating a maximum of 2200 W to ensure energy autonomy for long measurement periods. The buoy's cover was constructed with aluminum reinforced fiberglass to safeguard the internal electronic equipment from external harshness. It hosted data acquisition and communication systems able to store and send the measurements from its different sensors. The data could be acquired through Iridium satellite and through WiFi communications in a 100-m range. In the EOLOS$^{TM}$ FLS200 design, the LiDAR was integrated in the buoy structure without a cardanic frame, being the whole structure a rigid body. Therefore, a single

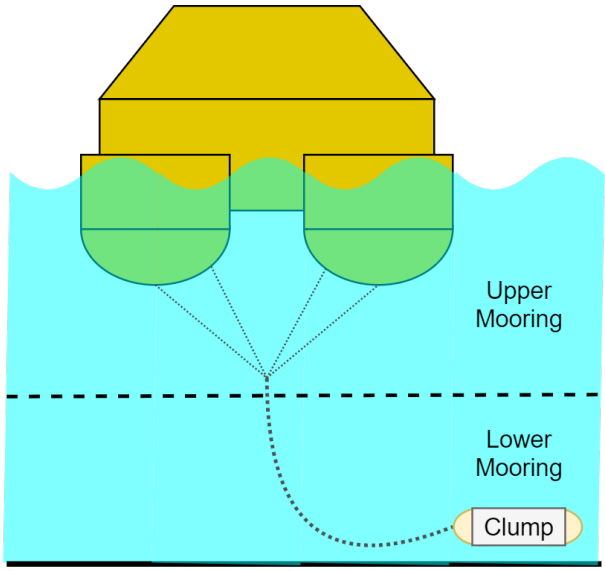


Figure 3.2: Mooring system scheme of EOLOS$^{TM}$ test lidar buoy used in IJmuiden campaign.

3DM-GX2-45 IMU was needed to track the buoy's motion. From one of the 4 corners of the buoy, a mounted tail acts as a "stern" for the buoy, so that the opposite corner faces wind direction. The buoy was moored to the seabed by a mooring system consisting of two main parts: (i) upper mooring consisting of four lines connected to each of the buoy's floaters united in its bottom to a single line, and (ii) lower mooring consisting of a clump weight (see Figure 3.2).

*IJmuiden metmast.-* The IJmuiden metmast is an offshore facility operated by the Energy research Centre of the Netherlands. It is located in the North Sea, 85 km offshore of the IJmuiden port (Netherlands, see Figure 3.4 b)). IJmuiden is a coastal city that hosts the sea lock at the entrance of the North Sea Canal providing access to the Amsterdam (Netherlands) port region. The IJmuiden 92-m tall metmast structure was formed by a platform at 20.88 m a.s.l. and three booms pointing at 46.5º, 166.5º, and 286.5º clockwise from the North cardinal direction. It was equipped with multiple cup and sonic anemometers measuring the wind speed and direction at 27, 58.5, 85, and 92 m height above the Lowest Astronomical Tide (LAT). A Zephir$^{TM}$ 300 was mounted at the metmast platform sensing the wind above the metmast top from 90 m up to 300 m height every 25 m. Pressure, temperature and humidity sensors were mounted on the metmast to monitor additional atmospheric parameters. IJmuiden sensors and their direct data products are summarised in Table 3.2.

*Triaxys$^{TM}$ wave buoy.-* The Triaxys$^{TM}$ wave buoy is a wave sensor designed for accurate measurement of directional waves and currents at a sampling period of 1 h. It is equipped with 3 accelerometers, 3 gyroscopes, and a compass in order to measure the most relevant directional and nondirectional wave parameters. Some of the parameters yielded by the wave sensor were wave-height definitions, wave-period definitions, mean direction, and mean spread. These parameters

| Variable | Sensor | Sampling Rate | height [m] | Units |
|---|---|---|---|---|
| Wind Speed | 2 x Thies First Class Advanced Anemometer | 4 Hz | 92 | m/s |
| | 6 x Thies First Class Advanced Anemometer | | 27, 58.5 | m/s |
| Air Pressure | 2 x Vaisala PTB210 | | 21, 90 | hPa |
| Temperature | 2 x Vaisala HMP155D | | 21, 90 | ºC |
| R. Humidity | | | | % |
| Wind Speed | 3 x Metek USA-1 Sonic Anemometer | | 85 | m/s |
| Wind Direction | 9 x First Class Wind Vane | | 26, 58, 87 | deg |
| Precipitation | 2 x Thies Disdrometer Laser 785 nm max 0.5 mW | | 21 | % |
| Synopt | | | | - |
| Amount | | | | mm |
| Intensity | | | | mm/ min |
| OK | | | | % |
| Qual | | | | % |
| Visibity | | | | m |
| Measuring points | ZephIR™300 | 1Hz | 90 to 315 | - |
| Missed points | | | | - |
| Packets in fit | | | | - |
| Wind direction | | | | deg |
| HWS | | | | m/s |
| VWS | | | | m/s |
| Spatial variation | | | | - |
| CS | | | | - |
| Backscatter | | | | - |
| Horizontal confidence | | | | - |

Table 3.2: Sensors summary of IJmuiden metmast facilities. [Werkhoven & Verhoef 2012].

are computed by Triaxys$^{TM}$ from heave, pitch, and roll measurements estimated from the 6 DoF measurements. The main Triaxys$^{TM}$ data products and resolution is summarised in Table 3.3.

| Variable | Range | Resolution | Accuracy |
|---|---|---|---|
| Heave | ±20 m | 0.01 m | Better than 1% |
| Period | 1.5 to 33 s | 0.1 s | Better than 1% |
| Direction | 0 to 360 deg | 1 deg | 3 deg |
| Currents | 0-10 m/s | 1 cm/s | ±10 cm/s |
| Water temp. | -5 to +50 ºC | 0.1 ºC | ±0.5 ºC |

Table 3.3: Triaxys™ Wave & Current Buoy specifications. [AXYS Technologies 2015].

## 3.2 Measurement Campaigns

*Pont del Petroli campaign.-* The Pont del Petroli (PdP) campaign took place between May 24th and June 31st of 2013 at "Pont del Petroli" pier (Badalona, Barcelona, Spain) [Sospedra et al. 2015]. It

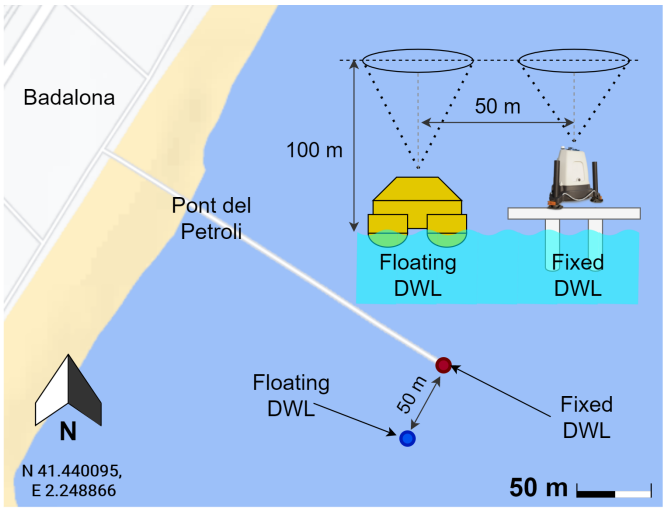


Figure 3.3: "Pont del Petroli" campaign location and scheme of the instrumental set-up.

aimed to assess the wind measurement capabilities of the proof-of-concept NEPTUNE$^{TM}$ FDWL buoy in the context of the NEPTUNE project by comparing its performance against a fixed lidar [Gutiérrez-Antuñano et al. 2017]. Both the fixed and the FDWL were ZephIR$^{TM}$ 300 focusable continuous-wave DWLs. The fixed DWL was situated at the PdP pier in a stand-still configuration, as the reference device. The FDWL was deployed offshore 50 m away from the fixed DWL (see Figure 3.3). Both ZephIR$^{TM}$ 300 were identical instruments and were calibrated onshore one beside the other 1 m apart during a period of 3 h. They were configured to measure the wind at a height 100 m above sea level (a.s.l.). The calibration ensured identical measurements at 1 s and 10 min intervals. "Pont del Petroli" is located on the coastline of Badalona (Barcelona, Spain), in the Barcelona metropolitan area. The experiment location surroundings are defined by an urban topology of low-height buildings (up to 20 m), which follow the coastline in the west and north cardinal directions, while the rest is defined by a sea-type topology.

*IJmuiden campaign*.- The IJmuiden campaign took place between March and October of 2015 at IJmuiden test site. The experimental campaign aimed at assessing the wind measurement accuracy of the EOLOS$^{TM}$ FLS200 FDWL pre-commercial buoy using the IJmuiden metmast as a reference. The FDWL ZephIR$^{TM}$ 300 was configured to sense the wind at four measurement heights (25, 38, 56, and 83 m) matching the metmast cup anemometers (see Figure 3.4 a)). The EOLOS parts were tested and assembled at LIM-UPC facilities in Barcelona. Once the preliminary performance was validated, the FDWL was moved to IJmuiden where the instrument was tested and calibrated in near-real conditions for a period of 1 month. Finally, the EOLOS FDWL buoy was moored next to its final deployment position 300-m apart from IJmuiden metmast (see Figure 3.4). Next to the metmast, a Triaxys$^{TM}$ wave buoy measured the main wave and current parameters.

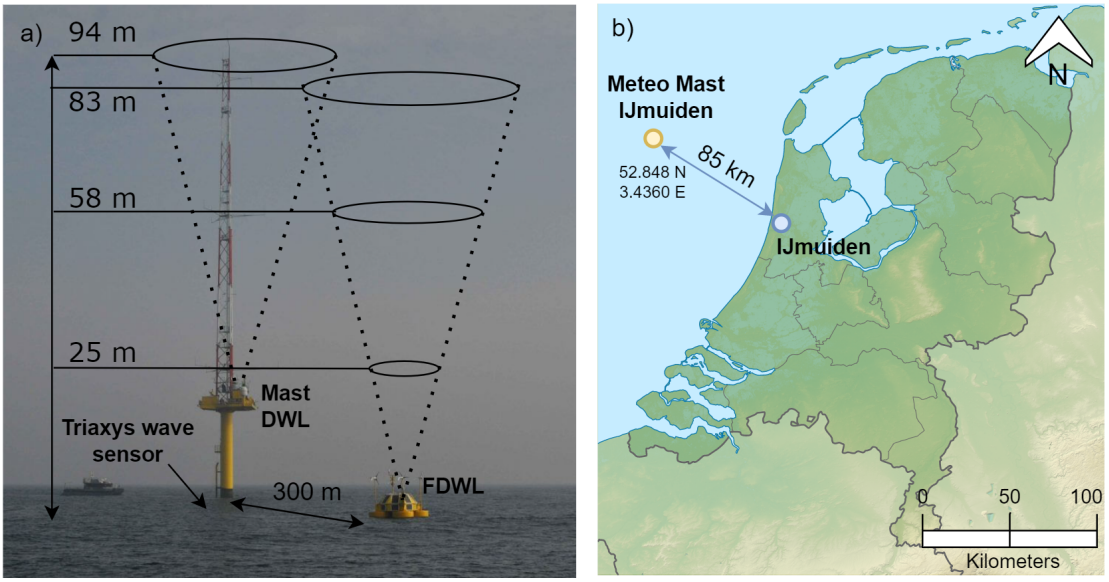


Figure 3.4: IJmuiden test campaign: (**a**) experimental setup at IJmuiden's test showing the EOLOS$^{TM}$ FLS200 and reference metmast, and (**b**) location map adapted from [Lencer 2008].

# Chapter 4

# Methods for Vertical-Air-Motion Estimation from Frequency-Modulated-Continuous-Wave Radar Rain Measurements

*The contents of this Chapter are aligned with the introductory Objective 1 and are part of the full paper [Salcedo et al. 2022]:* ***Salcedo-Bosch, A.****; Rocadenbosch, F.; Frasier, S.; Domínguez-Pla, P. "Forward method for vertical air motion estimation from frequency modulated continuous wave radar rain measurements," 11th European Conference on Radar in Meteorology and Hydrology (29$^{th}$ Aug. to 2$^{nd}$ Sept. 2022, Locarno, Switzerland), ERAD 2022. Proc. ERAD 2022, p. 104-111.". Systematic or multiple reproduction or distribution to multiple locations via electronic or other means is prohibited and is subject to penalties under law*

## 4.1 Introduction

Radars and disdrometers have been widely used to measure precipitation processes in the atmospheric boundary layer [Rogers 1984]. Ground-based S-band Frequency Modulated Continuous Wave (FMCW) radars have been used to assess the atmospheric boundary layer precipitation microphysical processes for more than 40 years [İnce et al. 2003], as they are unaffected by rain attenuation [Tanamachi et al. 2019, Rocadenbosch et al. 2020]. Vertically-pointed FMCW radars permit the derivation of key rain 2nd order integral parameters such as DSD and RR, among others [Doviak & Zrnic 1984]. The radar high spatial and temporal resolution permit an accurate monitoring of precipitation vertical profiles. Disdrometers record raindrop counts (at ground level) for different diameters during a measurement interval, and precisely derive rain DSDs from which 2nd order parameters such as RR can be obtained.

However, each of these devices has its limitations. On one hand, the disdrometer is not able to

give information of the vertical variations of precipitation. Moreover, large errors are common in scenarios with small diameter raindrops and low rain. On the other hand, radars have difficulty precisely measuring precipitation at low heights due to interference from ground clutter, near-field effects, and parallax influence (for FMCW radars employing dual antennas). Additionally, radars estimate the DSD from radar Doppler spectrum by assuming that rain drops are Rayleigh scatterers that fall at their terminal velocities, which are determined by the drop diameter. In practice, the droplets falling velocity are influenced by the Vertical Air Motion (VAM) [Tridon et al. 2011], which arises as a radar-measured spectrum shift in the velocity axis. In the presence of large VAM, such as in convective rain scenarios, radar-derived DSD and 2nd order parameters may be corrupted [Rocadenbosch et al. 2020, Tridon et al. 2011].

The VAM estimation and correction from stand-alone Doppler radar measurements has been of interest since the beggining of radar usage in precipitation measurement [Hauser & Amayenc 1981]. Lhermitte (1988) proposed a method to differentiate VAM and raindrops terminal velocity in W-band ($\lambda = 3.2$ mm) radars by exploiting Mie scattering. The VAM is determined by comparing the observed spectrum to a predicted spectrum assuming no VAM. However, this is only feasible for very-short wavelengths. Hauser & Amayenc (1981) proposed a fitting method in which the DSD was assumed to be with an exponential form characterised by two parameters (Marshall-Palmer distribution). This methodology optimised the best fit between the theoretical spectrum retrieved from the DSD model (shifted by VAM) with respect to the experimental spectrum observations. However, it required exponentially distributed size distributions and it is not suited for convective rain scenarios. More recently, Tridon et al. (2011) proposed a VAM-correction method by shifting the radar-measured spectrum to maximise the correlation with a no-VAM scenario. Rocadenbosch et al. (2020) proposed a VAM estimation method based on the correspondence between Z-RR measurements with three different Z-RR models. It consisted on a trial-and-error procedure in which the radar-measured spectrum was shifted until Z-RR relationship matched theoretical models. A similar approach was proposed by Kim & Lee (2016), which resorted to radar reflectivity empirical relationships as well to estimate the VAM and then unshift the spectrum. However, they require user expertise in rain radar observations for an accurate correction. In contrast, here, departing from the proposal by Hauser & Amayenc (1981), a forward method to estimate the VAM from stand-alone radar measurements is presented. The foundations of the forward method are to parameterise the DSD as a Gamma distribution and to project this parametric DSD through the radar processing chain up to the retrieved radar-measured reflectivity. The methodology is tested over experimental data measured by a vertically-pointed FMCW radar and validated by a disdrometer as a reference during a convective rain event in VORTEX-SE campaign in 2017.

This chapter is structured as follows: Section 4.2 describes the VORTEX-SE campaign and presents the OTT Parsivel2 disdrometer and the UMASS S-band radar; Section 4.3 revisits the dis-

drometer and rain radar operation procedure as well as the VAM correction method; Section 4.4 shows a case study of the VAM correction method; and Section 4.5 gives concluding remarks.

## 4.2 Instruments

The Verification of the ORigins of Rotation in Tornadoes Experiment-Southeast (VORTEX-SE) measurement campaign aimed at studying how different environmental scenarios affected the formation, characteristics, and evolution of tornadoes in the Southeast United States. The second measurement campaign of VORTEX-SE took place between 8 March and 8 May 2017 in northern Alabama. It involved multiple fixed and mobile instruments assessing the spatial and temporal evolution of storm events. During the experiment, the UMass S-band FMCW radar was deployed at the Scottsboro, Alabama airport along with an OTT Parsivel2 disdrometer, part of the Portable In-situ Precipitation Sensor (PIPS) package deployed by Purdue University.

The S-band FMCW radar was developed by the Microwave Remote Sensing Laboratory from the University of Massachusetts (UMASS). It is a transportable radar which uses two parabolic dish antennas of 2.4 m diameter with 34 dB gain, with a transmitter of 250 W [Waldinger et al. 2017]. It is able to vertically profile the volume reflectivity spectral density as a function of velocity ($\eta(v)$) with temporal and spatial resolutions of 16 s and 5 m, respectively. The radar bandwidth permits to measure drop falling velocities up to 14 m/s. Thanks to the radar signal wavelength, the atmospheric boundary layer can be studied both in clear-air and precipitation scenarios.

The OTT Parsivel2 is a laser-based disdrometer able to measure the ground-level rain droplets distribution as a function of diameter and falling velocity [Tokay et al. 2014]. Its operation is based on the shadowing effect that drops generate when passing through a light band. From the hydrometeors distribution, 2nd order parameters such as RR and DSD can be derived. It has been widely used in measurement campaigns, and here, it will be used as a reference.

## 4.3 Method

### 4.3.1 Radar Data Products

Following [Rocadenbosch et al. 2020], the DSD is obtained as the ratio of the volume reflectivity density with respect to the drop diameter, $\eta(D)$ [$m^{-1}/mm$], to the single-particle backscattering cross section of a drop of diameter D, $\sigma(D)$ [$m^2$/drop]. It can be formulated as

$$N(D) = \frac{\eta(D)}{\sigma(D)}. \tag{4.1}$$

FMCW radars are able to measure the *volume spectral reflectivity*, $\eta(v)$, which is the volume reflectivity (or radar cross section per unit volume) per unit Doppler velocity. In order to retrieve the DSD from radar measurements (see Equation 4.1 above), we need to express the spectral reflectivity as

a function of drop diameter. To do so, the relationship $\eta(D)\partial D = \eta(v)\partial v$ is used. This relationship was found empirically by Gunn & Kintzer (1949), and was put expressed analytically by Atlas et al. (1973) as

$$v_n(D)[\mathrm{m/s}] = (9.65 - 10.3e^{-0.6 \cdot D[\mathrm{mm}]})\delta v(h), \tag{4.2}$$

where $\delta v(h)$ is the height-dependent density correction for the terminal fall velocity, which is formulated as

$$\delta v(h) = 1 + 3.68 \cdot 10^{-5} h + 1.71 \cdot 10^{-9} h^2, \tag{4.3}$$

where $h$ is the measurement height.

From the DSD, second order products such as the *reflectivity factor* $Z$ and the $RR$ can be derived. The radar reflectivity factor can be obtained as the sixth power of the DSD as

$$Z = \int_0^\infty N(D) D^6 dD, \tag{4.4}$$

and the $RR$ can be estimated from the DSD third moment as a function of drop terminal fall velocity

$$RR = \frac{\pi}{6} \int_0^\infty N(D) D^3 v(D) dD. \tag{4.5}$$

### 4.3.2 VAM influence

Without VAM, the radar-measured Doppler velocities match the raindrops terminal falling velocities ($v_{Doppler} = v(D)$). In presence of VAM, the hydrometeors falling velocities are determined by both the drop terminal velocity as a function of diameter ($v(D)$ Equation 4.2) and the VAM velocity ($v_{VAM}$). Then, the radar-measured Doppler velocity is given by

$$v_{Doppler} = v(D) + v_{VAM}. \tag{4.6}$$

Therefore, drop diameter retrieval from velocity measurements and subsequent derivation of $\eta(D)$, DSD, and RR need to include the correction $v(D) = v_{Doppler} - v_{VAM}$. As $v_{VAM}$ could not be measured with the available instrumentation, we face a non-linear inverse problem in which we need to find the best $v_{VAM}$ estimation given radar volume reflectivity density $\eta(v)$ measurement [Rodgers 2004].

### 4.3.3 Methods: Forward model for VAM estimation

We propose a forward model approach to solve the inverse problem of radar RR retrieval as a function of the VAM correction by constraining the DSD as a gamma distribution:

$$N(D) = N_0 D^\mu e^{-\Lambda D}, \tag{4.7}$$

in which $N_0$ , $\mu$, and $\Lambda$ are the intercept, shape, and slope constitutive parameters of the distribution, respectively [Tokay & Short 1996].

In an inverse problem, the parameters to be estimated are represented by the state vector $\boldsymbol{x}$, and the measurements actually made to estimate $\boldsymbol{x}$ can be represented by the measurement vector $\boldsymbol{z}$ [Rodgers 2004].

In our inverse problem, the state vector $\boldsymbol{x}$ to be estimated is formed by the DSD gamma distribution parameters and the VAM. It can be formulated as

$$\boldsymbol{x} = [N_0, \mu, \Lambda, v_{VAM}]^T. \tag{4.8}$$

The measurement vector $\boldsymbol{z}$ is defined as the radar-measured volume reflectivity density $\eta(v)$. It is formulated as

$$\boldsymbol{z} = \eta(v). \tag{4.9}$$

$\boldsymbol{z}$ is a $N \times 1$ dimension vector, being $N$ the number of velocity bins measured by the radar.

We depart from Equation 4.1 in order to obtain the volume reflectivity density as a function of diameter from the DSD as

$$\eta(D) = N(D)\sigma(D). \tag{4.10}$$

Then, we make use of the relationship $\eta(v)\partial v = \eta(D)\partial D$ to obtain the volume reflectivity density as a function of velocity as

$$\eta(v) = N(D)\sigma(D)\frac{\partial D}{\partial v}. \tag{4.11}$$

For each state vector $\boldsymbol{x}$ there is an ideal measurement vector $\boldsymbol{z}$ related by a forward function $f(\cdot)$. The radar DSD-to-reflectivity forward function is defined as the expanded form of Equation 4.11 above as

$$f(\boldsymbol{x}) = N_0 D(v_{VAM})^{\mu} e^{-\Lambda D(v_{VAM})} \sigma(D(v_{VAM}))\frac{\partial D(v_{VAM})}{\partial v}, \tag{4.12}$$

where $D(v_{VAM})$ is the velocity-to-diameter relationship (see Equation 4.2) and $v_{VAM}$ is VAM velocity correction (see Equation 4.6).

Then, the forward model can be defined as

$$\boldsymbol{z} = f(\boldsymbol{x}) + \epsilon, \tag{4.13}$$

where $\epsilon$ is a residual error term. In order to solve the inverse problem, and thus, to estimate the state vector $\boldsymbol{x}$, we resort to a constrained non-linear Least Squares (LSQ) method, finding the optimal $\boldsymbol{x}$ that minimizes the squared error $\epsilon^2$ between the model observation $f(\boldsymbol{x})$ and the actual observation $\boldsymbol{z}$. It can be formulated as an optimization problem as

$$\boldsymbol{x} = \arg\min_{\boldsymbol{x}} ||\eta(v) - \hat{\eta}(v, \boldsymbol{x})||^2 \tag{4.14}$$

where $\hat{\eta}(v, \boldsymbol{x})$ is the estimated radar volume reflectivity, output of the radar DSD-to-reflectivity forward function $f(\boldsymbol{x})$. The block diagram in Figure 4.1 represents the optimization problem.

The optimization problem in Equation 4.14 is solved by means of the trust-region-reflective algorithm [Moré & Sorensen 1983].

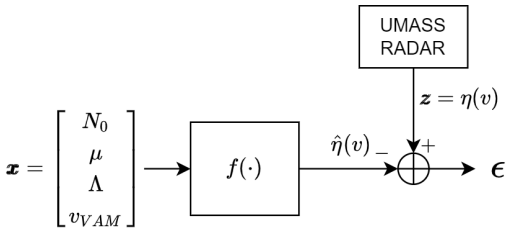


Figure 4.1: Block diagram of the forward model algorithm. $f(.)$ is the radar DSD-to-reflectivity forward function. The substractor is used to compute the residual error, $\epsilon$, between the measured and the estimated radar volume reflectivity density.

## 4.4 Results and Discussion

The algorithm was tested over experimental data measured by the UMASS S-band FMCW radar and the OTT Parsivel$^2$ during VORTEX-SE 2017 campaign (see Section 4.2). The VAM was estimated by means of the forward model method from radar volume reflectivity density measurements at 500 m. Reflectivity density measurements were 1-min averaged in order to reduce their uncertainty [Hauser & Amayenc 1981]. Then, radar measurements were corrected considering VAM estimations, and RR and DSD radar products at 500 m were recomputed. The VAM-corrected RR estimations were compared against the disdrometer RR as a reference, assuming vertical correlation between 500 m and 0 m measurement heights considering 10-min average ensembles. Although collision and coalescence processes are present in the precipitation process, correlation coefficients of $\rho \simeq 0.75$ were found for the RRs between the radar measurements at 500 m and the disdrometer in the VORTEX-SE campaign [Rocadenbosch et al. 2020].

Figure 4.2 shows the VAM estimation and correction results in terms of RR during a 20-minute observation period. By comparing the radar-retrieved RR without correction (dashed gray) to the disdrometer (dashed red), it can be observed how from 04:46 to 04:55 they largely disagree, being the first up to 3 $mm \cdot h^{-1}$ lower than the latter. The VAM estimated by the inverse method presented in Section 4.3.3 (dashed-dot green) shows constant -1 m/s values from 04:40 to 04:44, then it rises with a constant slope up to values around 1 m/s, and finally, at 04:55, it shows negative values down to -3 m/s. These VAM values seem to be in accordance with the RR, as a positive VAM implies a reduction of the radar-retrieved RR [Salcedo-Bosch et al. 2022a], corresponding to the 04:46-04:55 period in which the radar measures a lower RR as compared to the reference. After VAM correction, the radar-retrieved RR (dashed black) shows values of the same order of magnitude as the ones for the disdrometer, proving the validity of the VAM estimations. These results are further corroborated when comparing the 5-min window-averaged versions of the RR measurements (solid traces). The radar-measured RR (solid gray) shows significantly lower values in the 04:46-04:55 period with respect to the disdrometer (solid red). After correction, the radar-measured

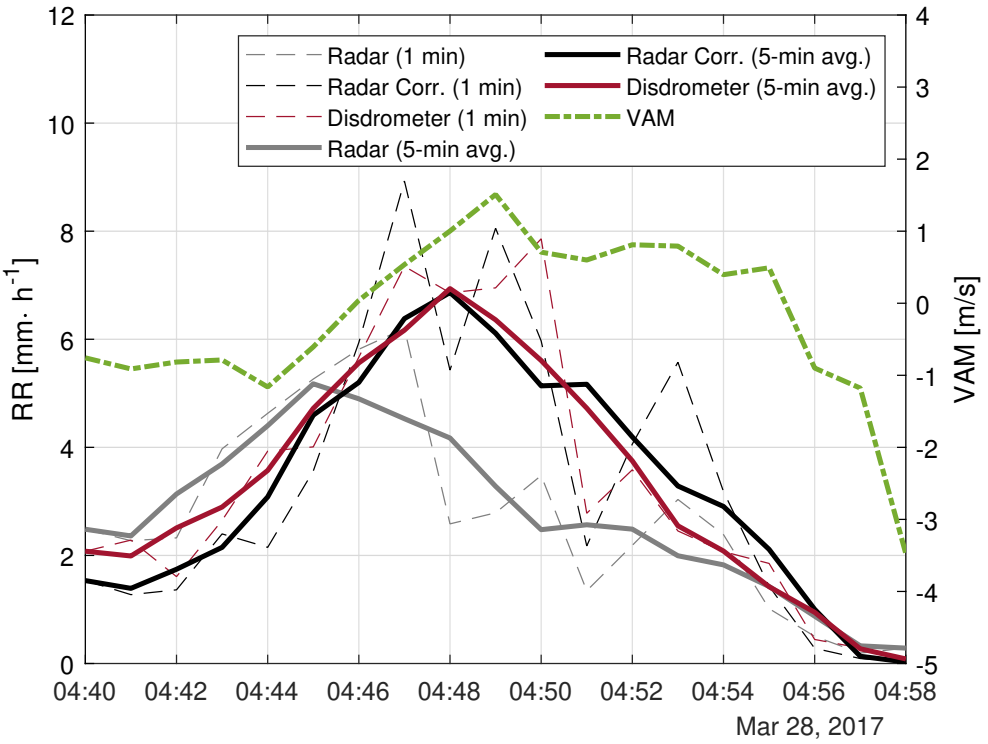


Figure 4.2: Time series representing the radar-measured RR (1 min), with (dashed black) and without (dashed gray) VAM correction, the disdrometer-measured RR (1 min, dashed red) and the VAM estimated by the forward method (green). Solid traces are the 5-min averaged versions of the respective dashed plots.

RR (solid black) matches almost ideally the reference. Note that when RR is very low, e.g., at 04:56-04:58 period, the VAM correction does not have a noticeable effect on the radar measurements, as reflectivity density values are too low. During the 04:40-04:44 period, it can be observed that the VAM-corrected radar RR shows lower values than the disdrometer reference. This may be due to an overestimation of negative VAMs. As a result, the algorithm estimates biased DSD parameters in order to match the measurements, i.e., to minimize the squared error between the measurement vector and the output of the forward function (see Equation 4.14).

Figure 4.3 compares two DSDs measured by the radar, with and without VAM correction, against the reference DSDs measured by the disdrometer. Figure 4.3 a) plots the radar and the disdrometer DSD measurements at 04:43 UTC. Surprisingly, the VAM-corrected radar RR becomes underestimated (see Figure 4.2). As it can be observed, the raw DSD radar measurement (gray) virtually overlaps the reference (red). Therefore, the estimated VAM should be close to 0 m/s and no correction should be required. However, the forward method presented overestimates the VAM (VAM$\simeq -0.8$ m/s), compensating the poorer functioning of the forward method with a miss-estimation of the DSD constitutive parameters ($N_0$, $\mu$, and $\Lambda$), which leads to wrong DSD retrievals

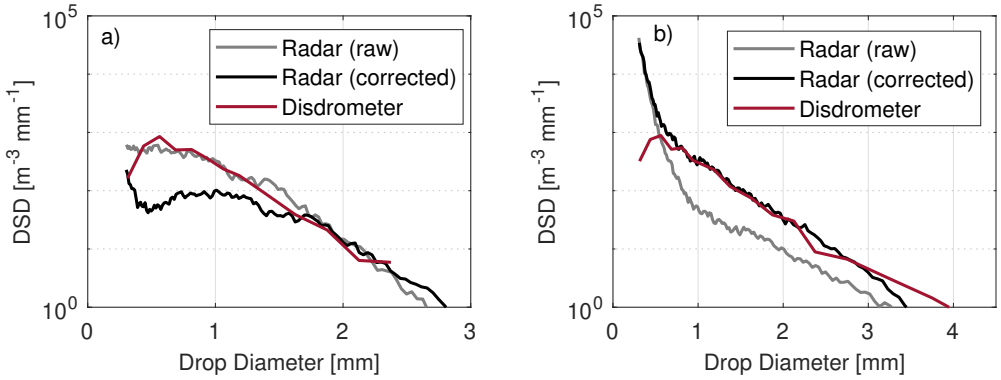


Figure 4.3: Comparison between DSDs measured by the radar, with (black) and without (gray) VAM correction, and the disdrometer (red). Two case examples are shown: (a)) biased VAM estimation; (b)) good VAM estimation.

(black). On the other hand, Figure 4.3 b) depicts the comparison of DSD measurements at 04:49, where a VAM of 1.5 m/s is estimated. Here, a factor 10 difference can be observed between the radar-measured and reference DSDs. After VAM correction, the radar-measured DSD matches almost perfectly the reference. However, as previously reported in the literature [Jash et al. 2019], optical disdrometers underestimate DSDs at low diameters (see $D < 0.5mm$ at Figure 4.3 b)).

## 4.5 Conclusions

An inverse method to estimate VAM velocity from stand-alone radar measurements was presented. The method consists on fitting a modelled volume reflectivity density, as a function of the VAM and DSD gamma distribution constitutive parameters, to the radar-measured reflectivity.

The method was tested over experimental data captured during a 20-minute period by an S-band FMCW radar and validated with an OTT Parsivel2 disdrometer in the context of VORTEX-SE 2017 measurement campaign. The estimation results found VAM values mainly ranging from -1 m/s up to 1.5 m/s during the period under analysis. After VAM correction, the radar-measured RRs were found to match almost ideally the disdrometer-measured RR for positive VAM values. However, overestimation of VAM negative values was found in no-VAM scenarios, leading to miss-estimation of the DSD constitutive parameters. These results were corroborated by comparing radar-retrieved DSD (with and without VAM correction) to disdrometer measurements.

Although promising, the algorithm still needs to be further tested over different stratiform and convective rain scenarios in order to see if overestimation of negative VAM is also found, and how to improve these estimations. The VAM estimations could also be further validated by direct measurements of vertical wind by wind profilers.

# Chapter 5

# Estimation of Wave Period from Pitch and Roll of a Lidar Buoy

*The contents of this Chapter are aligned with Obj. 2 of this Ph.D. and are part of the full paper [Salcedo-Bosch et al. 2021b]: A. Salcedo-Bosch, F. Rocadenbosch, M. A. Gutiérrez-Antuñano, and J. Tiana-Alsina. "Estimation of wave period from pitch and roll of a lidar buoy", Sensors, 21(4), 2021b. doi: https://doi.org/10.3390/s21041310. Systematic or multiple reproduction or distribution to multiple locations via electronic or other means is prohibited and is subject to penalties under law*

## 5.1 Introduction

As it has been explained in Chapter 2, FDWLs suffer wave-induced errors on wind measurements [Gottschall et al. 2014b]. Sea waves induce translational (sway, surge, and heave for x, y and z axes, respectively) and rotational (roll, pitch, and yaw for x, y, and z axes, respectively) motion to the floating DWL, which accounts for 6 Degrees of Freedom (DoF), creating a Doppler effect over the wind vector retrieval and TI [Tiana-Alsina et al. 2017, Kelberlau et al. 2020, Gutiérrez-Antuñano et al. 2018, Mangat et al. 2014, M. Pitter et al. 2014, Bischoff et al. 2014, Gottschall et al. 2012b].

LiDAR buoys are usually wave buoys moored to the seabed by means of a clump. The buoy's design is a trade-off between accurate LiDAR wind measurements and attitude measurements for wave-induced motion compensation [Schuon et al. 2012]. Of the 6 DoF of a wave buoy (sway, surge, heave, roll, pitch, and yaw), sway, surge, and yaw are mainly determined by wind and current forces, whereas heave, roll, and pitch are mainly determined by sea state [Kelberlau et al. 2020] and are used to study sea waves [Center 1996]. Sea waves are a subject of interest in various fields such as marine engineering [Faltinsen 1993], oceanography [Center 1996, Suh et al. 2010, Ardhuin et al. 2019, C. & S. 2018] and wind engineering [Gottschall et al. 2018, He et al. 2019]. Waves can be studied from directional and nondirectional perspectives by means of the directional and nondirectional spectra, which are estimated from a measuring wave buoy's heave, roll, and

pitch records [Center 1996, Kuik et al. 1988]. From spectrum estimations, wave period and height variables are derived and studied.

In this chapter, we present a spectral-analysis methodology to estimate the wave period from roll and pitch records (2 DoF) measured by a LiDAR buoy, and reconcile our methodology to classical oceanographic wave-period estimation methods in the state of the art, which usually rely on average and zero-crossing period computation. We assumed quasistatic yaw rotation and neglected translational motion on account of the buoy's mooring topology.

Incipient studies addressed the topic as follows: in [Gutiérrez-Antuñano et al. 2017], the wave-induced buoy's tilt period was computed from the smoothed Fast Fourier Transform (FFT) of pitch and roll time series. The most prominent peak of these 2 FFTs was chosen as the most relevant spectral component, and the period was estimated as the inverse of the frequency corresponding to it. In [Gutiérrez-Antuñano et al. 2018], roll and pitch tilt periods were virtually correlated ($\rho \simeq 0.5$); thus, 1-DoF was considered informative enough of the buoy's motional wave period. In [Salcedo-Bosch et al. 2020b], two estimation methods to assess the wave period from pitch and roll measurements based on Blackman–Tukey power-spectral-density (PSD) estimation method were presented. Because the correlation between pitch and roll periods showed up experimentally, estimations using 1-DoF (either roll or pitch) became meaningful enough for the study. The first, the peak method, estimated the period as the inverse of the frequency of the maximum of the PSD. The second, the 3 dB method, defined the 3 dB threshold as the frequency region containing PSD values higher than half of the PSD maximum. In this method, the period was estimated as the inverse of the average of the start and stop cut-off frequencies of the 3 dB region. The 3 dB method yielded much higher correlation coefficients ($\rho$ = 0.62) than those of the peak method ($\rho$ = 0.37) when compared to the measured wave periods from reference buoys. However, a formulation was missing explaining the 3 dB PSD approach in relation to the different oceanographic definitions existing in the state of the art for the wave period or the underlying foundations.

Here, we present the sought-after formulation of the 3 dB method in relation to well-established wave-period oceanographic definitions. We also extend our pitch and roll spectral analysis (2 DoF) to the derivation of the tilt-angle PSD (so-called buoy eigenangle) representing the combined rotation effects of pitch and roll angles on buoy rotation geometry.

## 5.2 Materials and Methods

### 5.2.1 Review of remote sensing instruments

For this study, we use data from IJmuiden campaign, the validation campaign of the EOLOS$^{TM}$ FLS200 test floating LiDAR buoy at the IJmuiden test site (see Chapter 3). The main instruments used in this study were: (i) the 3DM-GX3-45 inertial measurement unit (IMU) on the LiDAR buoy

measuring the buoy's tilt (roll, pitch, and yaw), accelerations in X, Y and Z axes, and Global-Positioning-System (GPS) position at a sampling rate of approximately 8 Hz; and (ii) the Triaxys™ wave buoy next to the metmast measuring the reference wave parameters at a sampling period of 1 hour [Werkhoven & Verhoef 2012]. Figure 3.4 shows the instrumentation setup of the campaign and the location of IJmuiden's test facilities. For this study, 1920 wave-buoy data records from 29 March to 17 June (80 days) were used.

*Triaxys reference parameters computation review.* Some of the parameters yielded by the wave sensor were: wave-height definitions ($H_{max}$, $H_{10}$, $H_{sig}$ and $H_{avg}$), wave-period definitions ($T_{max}$, $T_{10}$, $T_{sig}$, $T_z$, $T_{avg}$, $T_p$, and $T_{p5}$), $MeanDirection$, and $MeanSpread$. Subindices max, 10, sig, avg, z, p, and p5 refer to the maximal wave height and its corresponding period ($H_{max}$ and $T_{max}$ respectively), the highest tenth of the waves' average height and period ($H_{10}$ and $T_{10}$ respectively), the highest third of the waves' average height and period ($H_{sig}$ and $T_{sig}$ respectively), the average wave height and period ($H_{avg}$ and $T_{avg}$ respectively), the average zero upcrossing period ($T_z$), the period corresponding to the highest spectral component of the wave energy spectrum ($T_p$), and the peak wave period computed by the READ method ($T_{p5}$), respectively [MacIsaac & Naeth 2013]. Wave period parameters $T_z$, $T_{avg}$ and $T_p$ are formulated in Section 5.2.2.

Triaxys™ computes these parameters from heave, pitch, and roll measurements estimated from the 6-DoF measurements by 3 accelerometers and 3 gyros by solving the nonlinear differential equations relating the buoy motion to accelerations and angular rates. It follows a similar procedure to that in [Øyvind F. Auestad et al. 2013] to obtain heave, surge, and sway translational motions and roll, pitch, and yaw rotational motions. Wave analysis is then carried out on the buoy by performing zero-crossing analysis of wave elevation in the time domain, nondirectional analysis by means of FFT methods, and lastly directional wave analysis [MacIsaac & Naeth 2013].

### 5.2.2 Method (I): Estimation of Sea-Wave Period

Waves can be analysed from directional and nondirectional perspectives depending on the purpose of the study and the available data. Directional wave analysis studies the contribution of ocean waves propagating in different directions with different amplitudes and periods by means of the directional spectrum ($DS(f,\theta)$) of the wave heave by means of the two slope components of the buoy, computed from roll and pitch records [Barstow et al. 2005, Tannuri et al. 2003], with techniques such as the Fourier expansion method and the maximum entropy Method [Massel 2017]. Nondirectional wave analysis studies surface ocean waves from the nondirectional energy spectrum ($S(f)$, computed from wave elevation) [Center 1996, C. & S. 2018]. $S(f)$ is defined as [Sweitzer et al. 2004]

$$S(f) = FT(H(t)) = \int_0^T H(t)e^{-i2\pi ft}dt, \tag{5.1}$$

where $H(t)$ is the wave elevation as a function of time, t, f is frequency, and T is the study period.

Directional and nondirectional wave spectra are related in the following way:

$$DS(f,\theta) = S(f)D(f,\theta), \tag{5.2}$$

where $D(f,\theta)$ is the directional spreading function and $\theta$ is the wave angular direction. $S(f)$ in Equation 5.1 above can also be re-encountered by integrating $DS(f,\theta)$ over all angular directions ($\theta$ from 0 to $2\pi$), $S(f) = \int_0^{2\pi} D(f,\theta)d\theta$.

Spectral moments $m_n$ are defined as

$$m_n = \int_0^{\infty} f^n S(f)df, \tag{5.3}$$

where n stands for an n-th order moment.

Different wave amplitude and period characterization parameters can be derived from spectrum $S(f)$ and its spectral moments $m_n$. Some of the most relevant wave-period definitions are [Barstow et al. 2005]:

- mean zero-crossing period, which is defined as

$$T_z = \sqrt{\frac{m_0}{m_2}}; \tag{5.4}$$

- average period

$$T_{avg} = \frac{m_0}{m_1}; \tag{5.5}$$

- and peak period

$$T_p = \frac{1}{f_p}, \tag{5.6}$$

  where $f_p$ is the peak frequency of $S(f)$.

### 5.2.3 Method (II): Buoy-Motion Model

We define the buoy's *moving body* Cartesian right-handed XYZ coordinate system and the *global* Cartesian right-handed north–east–down (NED) frame of reference (Figure 5.1). Without external forces, the X, Y, and Z axes of the buoy's *moving body* XYZ coordinate system would be aligned with the north, east, and vertically down axes of the *global* NED frame of reference.

In practice, such external forces can cause translational motion in the N, E, and D directions (surge, sway, and heave, respectively), and rotational motion along the N, E, and D axes (roll, pitch and yaw, respectively) to the buoy [Tiana-Alsina et al. 2017, Bischoff et al. 2014]. The buoy's mooring limits surge and sway motion, while heave (Figure 5.2a) follows the wave altitude. Note at Figure 5.2a that there are no heave measurements below 0 m in IJmuiden campaign. Regarding rotational motion, *roll* and *pitch* are mainly characterised by wave-motion behaviour, whereas *yaw* motion is mainly determined by the wind and currents due to the buoy's tail acting as the stern. Therefore, heave (translational), and roll and pitch (rotational) motions are the most informative

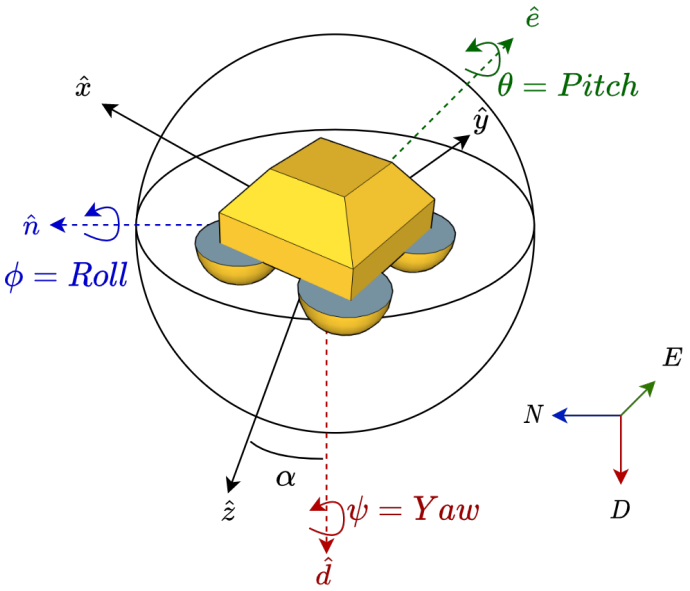


Figure 5.1: Fixed and moving-body (buoy's) coordinate systems used. The fixed coordinate system is the right-handed north–east–down (NED) system (dashed arrows with unitary vectors $\hat{n}$, $\hat{e}$, and $\hat{d}$ plotted in blue, green, and red, respectively). Buoy's coordinate system denoted as XYZ (solid arrows with unitary vectors $\hat{x}$, $\hat{y}$, $\hat{z}$). $\alpha$ is the buoy's eigenangle defined as the angle between unitary vectors, $\hat{d}$ and $\hat{z}$.

parameters of wave motion. Yaw motion showed slow variations with time (typically greater than 1 min; quasistatic approximation) due to wind and current influence, whereas roll and pitch motion exhibited comparatively much faster oscillatory behaviour due to wave influence (see Figure 5.2b) on time scales of the order of seconds.

The IMU was set up to measure the buoy's rotation angles on the basis of the fixed global right-handed NED coordinate system (see Figure 5.1). We defined $\hat{n}$, $\hat{e}$, and $\hat{d}$ as the unitary vectors aligned with the N, E, and D axes, respectively. On the other hand, we defined the $\hat{x}$, $\hat{y}$ and $\hat{z}$ unitary vectors along the rotated moving-body coordinate system (XYZ).

*Large-angle case*. In order to express our rotation problem with a single angle (so-called eigenvector-axis-associated angle or eigenangle for short in what follows denoted $\alpha$ in Figure 5.1) we resorted to Euler's rotation theorem, which states that every rotation in three dimensions is defined by its axis (a vector along this axis is unchanged by the rotation), and its angle—the amount of rotation about that axis. Euler's theorem also states that any 3D body rotation can be described by three angles. Therefore, the eigenangle can be expressed from roll, pitch, and yaw rotation angles. There are many different mathematical conventions for these three angles depending on the axes where the rotations are carried out and its order. We used the D-E-N convention defining the specific sequences of axes rotation (D-E-N axes are the global-coordinate (GPS) axes or fixed counterparts of Z-Y-X axes attached to the moving body, i.e., the buoy). In the D-E-N convention,

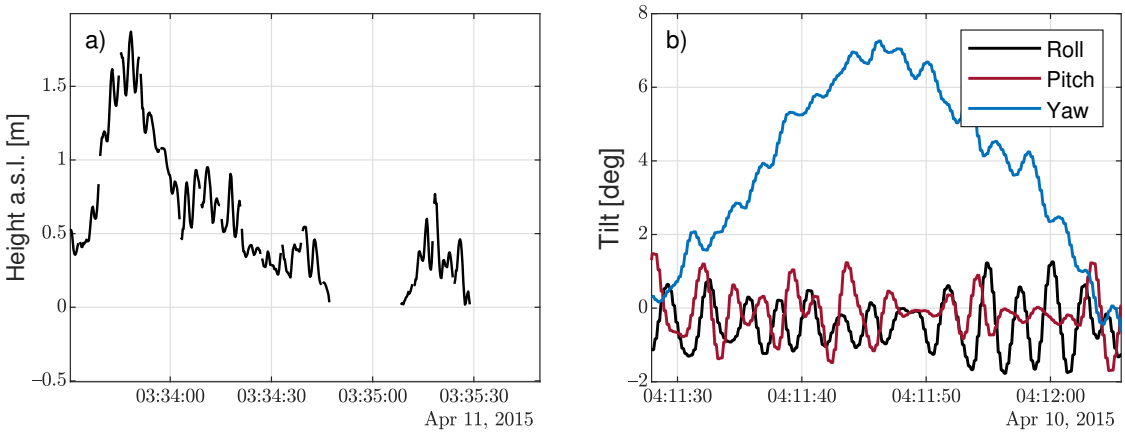


Figure 5.2: Motional temporal series (Ijmuiden campaign): (**a)**) Heave signal above sea level (a.s.l.) on April 11, 2015; (**b)**) Roll, pitch, and yaw signals on April 10, 2015).

we have three composed elemental rotations carried out sequentially in the global fixed coordinate axes: first, around the D axis (yaw motion, denoted by $\psi$); second, around the E axis (pitch, $\theta$); and third, around the N axis (roll, $\phi$), see Figure 5.1. Angles were positive counterclockwise. Considering these definitions, Euler's rotation matrix can be formatted as [Roithmayr & Hodges 2016]:

$$R = R_\psi R_\theta R_\phi, \tag{5.7}$$

where $R_\phi$, $R_\theta$, and $R_\psi$ are the counterclockwise extrinsic rotation matrices around the N axis (roll), E axis (pitch), and D axis (yaw), respectively.

$$\begin{aligned} R_\phi &= \begin{pmatrix} 1 & 0 & 0 \\ 0 & \cos\phi & \sin\phi \\ 0 & -\sin\phi & \cos\phi \end{pmatrix}, \\ R_\theta &= \begin{pmatrix} \cos\theta & 0 & -\sin\theta \\ 0 & 1 & 0 \\ \sin\theta & 0 & \cos\theta \end{pmatrix}, \\ R_\psi &= \begin{pmatrix} \cos\psi & \sin\psi & 0 \\ -\sin\psi & \cos\psi & 0 \\ 0 & 0 & 1 \end{pmatrix}. \end{aligned} \tag{5.8}$$

Then, any vector rotation can be described by right multiplying it by the rotation matrix,

$$\vec{r_{rot}} = R \cdot \vec{r}, \tag{5.9}$$

where $\vec{r}$ and $\vec{r_{rot}}$ are vectors (before and after rotation, respectively) with coordinates expressed in the fixed-coordinate system. We define $\alpha$ as the eigenvector-axis-associated angle of the buoy's combined motion in roll, pitch, and yaw angles. Conceptually, $\alpha$ is the angle between the down axis of the global coordinate system (NED) and the Z axis of the buoy (moving body, XYZ) (see Figure 5.1). As previously mentioned, the D and Z axes are described by unitary vectors $\hat{d} = [0, 0, 1]$

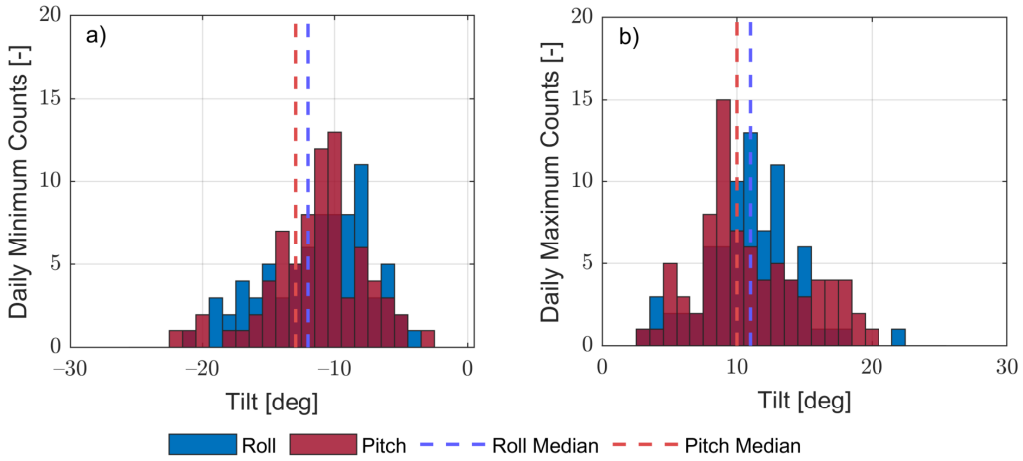


Figure 5.3: Histograms of daily minimal and maximal roll and pitch inertial-measurement-unit (IMU) records (57,520,000 records between 29 Match and 17 June): (**a**) Daily minimal tilt-record histogram; and (**b**) Daily maximal tilt-record histogram. Dashed lines represent roll (blue) and pitch (red) medians in both panels.

and $\hat{z}$, respectively. Given $\hat{d}$ (fixed coordinate system), vector $\hat{z}$ (moving coordinate system) can be expressed in the fixed coordinate system using Equation 5.9 as

$$\hat{z} = R \cdot \hat{d} = R_\phi R_\theta R_\psi \cdot \hat{d} = \begin{bmatrix} -\sin\theta \\ \sin\phi\cos\theta \\ \cos\phi\cos\theta \end{bmatrix}. \tag{5.10}$$

This can be seen graphically in Figure 5.4a, where $\hat{z}$ is the result of rotating $\hat{d}$ by $\theta$ deg around E (pitch) and $\phi$ deg around N (roll). Because of the D-E-N convention to describe chained rotations, $\alpha$ was invariant to the yaw rotation around D axis. Similarly, $\alpha$ is invariant to heave, which is translational motion along the D axis.

Then, $\alpha$ can be computed from the dot product between $\hat{d}$ and $\hat{z}$ as follows:

$$\alpha = \arccos(\hat{d} \cdot \hat{z}). \tag{5.11}$$

Inserting $\hat{d} = [0, 0, 1]$ and $\hat{z}$ (Equation 5.10) into Equation 5.11 yields

$$\alpha = \arccos(\cos\phi\cos\theta). \tag{5.12}$$

Because the cosine is an even function, $\alpha$ in Equation 5.12 above is always positively defined.

*Small-angle case*. Figure 5.3 plots 80 day histograms describing maximal and minimal, and pitch and roll daily buoy records. Both angles were below $\pm$22 deg (*maximum*). The median of the minima and the median of the maxima yielded [-13, +10] deg in pitch and [-12, +11] deg in roll,

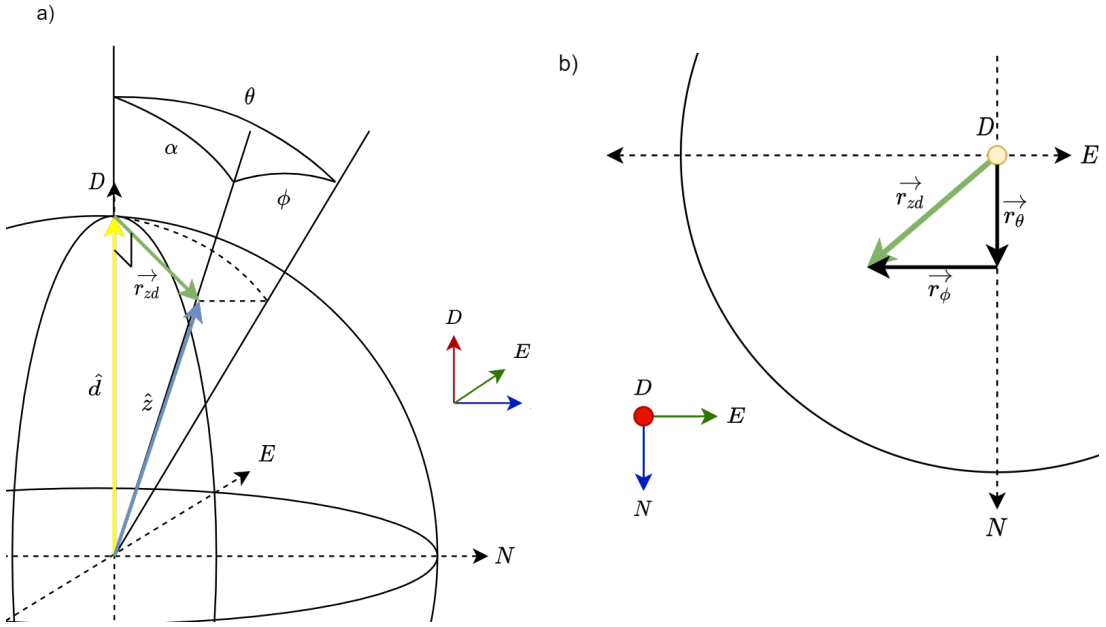


Figure 5.4: Geometrical representation of buoy's rotation in roll and pitch dimensions of movement and vector approximation for small angles: **(a)** Three-dimensional geometry sketch showing eigenangle $\alpha$, roll ($\phi$), and pitch ($\theta$) angles, and vectors $\hat{d}$ and $\hat{z}$ in NED coordinate system. $\hat{d}$ transforms into $\hat{z}$ after roll ($\phi$) and pitch ($\theta$) rotations about N and E axes, respectively (Equation 5.12). **(b)** Representation of roll and pitch rotations $\vec{r_\phi}$ and $\vec{r_\theta}$, respectively, on NE plane (Equation 5.10) along with resultant vector $\vec{r_{zd}}$, Equation 5.14).

which is representative of roughly $\pm$ 13 deg ($\pm$ 0.23-rad) angular excursion. Considering first-order Taylor's approximation, $\cos(x) \simeq 1$ and $\sin(x) \simeq x$, $x = \theta, \phi$ in Equation 5.10, this angular excursion yields $\cos(0.17) = 0.97 \simeq 1$ and $\sin(0.23) \simeq 0.22$, which are 2.5% and 0.8% errors, respectively. This enables us to propose the small-angles approximation, applied to Equation 5.10, which leads to

$$\hat{z} \simeq \begin{bmatrix} -\theta \\ \phi \\ 1 \end{bmatrix}. \tag{5.13}$$

We then define $\vec{r_{zd}}$ as the vector difference between $\hat{d}$ and $\hat{z}$ (see Figure 5.4),

$$\vec{r_{zd}} = \hat{d} - \hat{z} \simeq \begin{bmatrix} \theta \\ -\phi \\ 0 \end{bmatrix} = \theta \begin{bmatrix} 1 \\ 0 \\ 0 \end{bmatrix} + \phi \begin{bmatrix} 0 \\ -1 \\ 0 \end{bmatrix} = \vec{r_\theta} + \vec{r_\phi}. \tag{5.14}$$

Therefore, $\vec{r_{zd}}$ can be expressed as the sum of the two linearly independent vectors $\vec{r_\theta} = \theta[1, 0, 0]$ and $\vec{r_\phi} = \phi[0, -1, 0]$ with modules

$$|\vec{r_\theta}| = \theta, \; |\vec{r_\phi}| = \phi. \tag{5.15}$$

This is shown on N-E plane in Figure 5.4b.

Moreover, if $\alpha \to 0$, $\sin\alpha \simeq \alpha$ and

$$\alpha \simeq \sin(\alpha) = sin\left(\frac{|\vec{r_{dz}}|}{|\hat{z}|}\right) = \sin(|\vec{r_{dz}}|) \simeq |\vec{r_{dz}}|\,. \tag{5.16}$$

Because we use unitary vector $\hat{z}$, Equation 5.15 means that sought-after eigenangle $\alpha$ is directly modulus of difference vector $r_{zd}$. Combining Equation 5.15 and Equation 5.16, we obtain

$$\alpha \simeq \sqrt{\phi^2 + \theta^2}. \tag{5.17}$$

Equation 5.17 states that the eigenangle angle can be interpreted as the 1-DoF equivalent formulation for the real 2-DoF problem posed by motion in pitch and roll angles. This equivalent formulation is in accordance with previous published work [Salcedo-Bosch et al. 2020b], in which pitch and roll angular periods were shown experimentally to be correlated ($\rho = 0.54$ in that case).

The PSD of the eigenangle random process, $\boldsymbol{\alpha}$, is given by a linear combination of pitch and roll PSDs and pitch-to-roll cross-PSD (see Appendix B for details),

$$S_{\boldsymbol{\alpha},\boldsymbol{\alpha}}(f) = S_{\theta,\theta}(f) + S_{\phi,\phi}(f) - 2Im[S_{\theta,\phi}(f)]. \tag{5.18}$$

Because $roll(t)$ and $pitch(t)$ were real-valued time series, $R_{\phi,\theta}$ is also real-valued, and the associated cross-spectral density $S_{\theta,\phi}$ is Hermitian, i.e., its complex conjugate is equal to the original function with the variable $f$ changed in sign, $S_{\theta,\phi}(-f) = S^*_{\theta,\phi}(f)$ or, equivalently, the real part of $S_{\theta,\phi}(f)$ is an even function and the imaginary part is an odd function. The latter is important to understand which PSD terms contribute "power" to the random process $\boldsymbol{\alpha}$ (power is computed in units of $[rad^2]$, which is not actual physical power but the squared value of signal $\boldsymbol{\alpha}$).

If we integrate both terms of Equation 5.18 from $f$=$-\infty$ to $\infty$, $\int_{-\infty}^{\infty} S_{\boldsymbol{\alpha},\boldsymbol{\alpha}} df$ average power (in units of $[rad^2]$) is given by

$$\sigma^2_{\boldsymbol{\alpha}} = \sigma^2_{\theta} + \sigma^2_{\phi}. \tag{5.19}$$

Because $Im(S_{\theta,\phi}(f))$ is an odd function, integral $\int_{-\infty}^{\infty} Im(S_{\theta,\phi}) df$ vanishes out, and it emerges that the cross-spectral density does not contribute power to eigenangle random process $\boldsymbol{\alpha}$; only roll and pitch PSDs do.

### 5.2.4 PSD Estimation

In order to estimate the PSD of random process $\boldsymbol{\alpha}$, the Blackman–Tukey method was chosen on account of its computation simplicity and best trade-off between noise rejection and spectral-resolution characteristics [Proakis & Manolakis 2006]. The Blackman–Tukey method $S^{BT}_{xx}(f)$ consists of smoothing periodogram $P_{xx}(f)$, here computed through the FFT algorithm, by its convolution with a smoothing window $W(f)$ (rectangular window in this study). It can be formulated as

$$S^{BT}_{\boldsymbol{\alpha},\boldsymbol{\alpha}}(f) = \int_{-1/2}^{1/2} P_{\boldsymbol{\alpha},\boldsymbol{\alpha}}(\beta) W(f-\beta) d\beta, \tag{5.20}$$

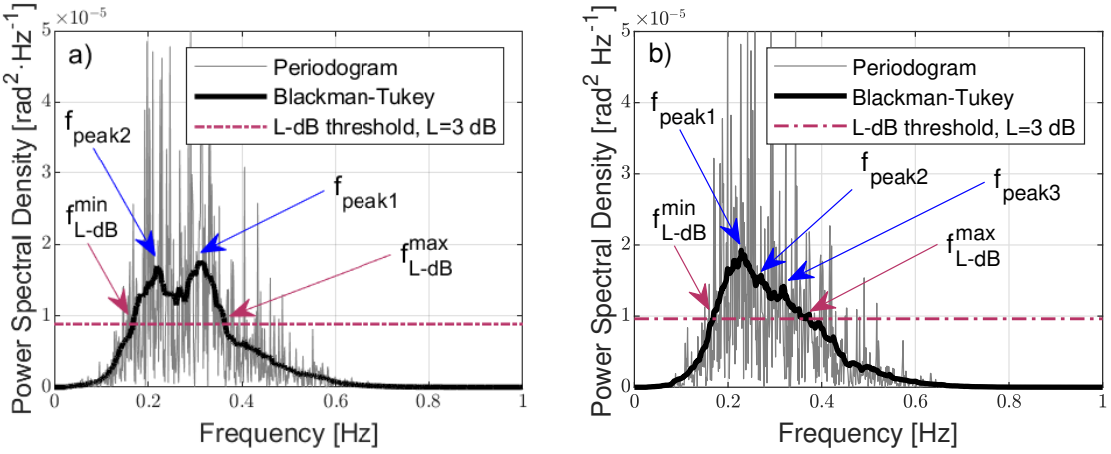


Figure 5.5: Two examples of PSD estimation by periodogram and Blackman–Tukey method of measured tilt data: (**a**) Bimodal case; and (**b**) Multimodal case. L-dB threshold and cut-off frequencies, $f^{min}_{L-dB}$, and $f^{max}_{L-dB}$, are also indicated by magenta dashed lines and arrows. L = 3 dB.

with

$$P_{\boldsymbol{\alpha},\boldsymbol{\alpha}}(f) = \frac{1}{L}\left|\sum_{n=0}^{L-1} \boldsymbol{\alpha}(n)e^{-j2\pi fn}\right|^2 = \frac{1}{L}|FFT(\boldsymbol{\alpha}(n))|^2, \tag{5.21}$$

where $L$ is the number of FFT samples, and "$n$" is shorthand notation for $nT$ with $T$ the sampling period ($T \simeq 0.125$ s).

From Equation 5.18, Blackman–Tukey estimation of the PSD is written as

$$S^{BT}_{\boldsymbol{\alpha},\boldsymbol{\alpha}} = S^{BT}_{\phi,\phi} + S^{BT}_{\theta,\theta} - 2Im[S^{BT}_{\theta,\phi}]. \tag{5.22}$$

Figure 5.5 shows PSD estimations of two 10 min tilt temporal series of eigenangle $\boldsymbol{\alpha}$ computed by using periodogram ($P_{\alpha\alpha}(f)$, grey) and the Blackman–Tukey method ($S^{BT}_{\boldsymbol{\alpha},\boldsymbol{\alpha}}(f)$, black).

IMU sampling frequency was 8 Hz, although some jitter showed up. Roll ($\phi$) and pitch ($\theta$) were resampled at a fixed sampling frequency of 10 Hz to ensure a uniform sampling rate and a sampling period that were a submultiple of 1 s for convenience. Then, the PSD of $\boldsymbol{\alpha}$ was computed following the Blackman–Tukey estimation method (Equation 5.20 and Equation 5.22).

Figure 5.5a shows bimodal behaviour for the PSD of $\boldsymbol{\alpha}$, with two dominant or modal frequencies at 0.22 Hz ($f_{peak2}$) and 0.31 Hz ($f_{peak1}$), equivalently, $T_2 = 1/0.22 = 4.5$ s and $T_1 = 1/0.30 = 3.2$ s, respectively, while Figure 5.5b shows nearly unimodal behaviour with a PSD peak at 0.22 Hz ($f_{peak1}$). The L-dB threshold is also plotted, which was computed as the relative level L-dB below the maximal peak level given by $f_{peak1}$. $f^{min}_{L-dB}$ and $f^{max}_{L-dB}$ denote the minimal and maximal frequency components of the PSD content that were higher than the L-dB threshold (see Section 5.2.5 for details).

### 5.2.5 PSD Significant-Wave-Period Estimation

We define the PSD significant wave period as the period associated to the buoy's eigenangle (Equation 5.17) and estimated it by imposing a threshold level on its PSD (Section 5.2.4). This threshold is found in Section 5.3 in relation to different well-accepted wave-period oceanographic definitions. Next, we formulate the PSD significant wave-period concept.

Figure 5.5 shows the buoy's eigenangle PSD for two different motional cases. In both, it emerged that there was not a single relevant spectral component, but multiple ones (labelled $f_{peak,i}$, blue arrows). In order to consider all relevant spectral components contributing power to the significant wave period, we defined an L-dB threshold (quantity "L" to be found) as the relative level L-dB below the maximal peak level of the PSD. This L-dB threshold (L = 3 dB in Figure 5.5) defines a frequency span, $[f_{L-dB}^{min}, f_{L-dB}^{max}]$ in which the PSD content is higher than a power factor of $10^{-L/10}$ compared to the peak level. The L-dB method computes the wave period as the average wavelength in the L-dB region. We defined the average wavelength as the arithmetic mean between maximal and minimal wavelengths:

$$\lambda_{L-dB} = \frac{\lambda_{L-dB}^{max} + \lambda_{L-dB}^{min}}{2}. \tag{5.23}$$

Introducing the concept of the phase velocity of a wave ($v_p$), which is the rate at which the wave propagates in the medium, and that any given phase of the wave (for example, the crest) appears to travel at the phase velocity [Brillouin & Massey 2013], we can write $\lambda = v_p T$, where $T$ is the wave period. By inserting this relation into Equation 5.23 and by using $T = 1/f$, Equation 5.23 can be rewritten as

$$T_{L-dB} = \frac{\frac{1}{f_{L-dB}^{min}} + \frac{1}{f_{L-dB}^{max}}}{2}, \tag{5.24}$$

which gives the sought-after significant wave-period estimated from the $f_{min}$ and $f_{max}$, L-dB cut-off frequencies of the PSD. Equation 5.24 can also be interpreted as the harmonic mean of the maximal and minimal cut-off frequencies, $f_{L-dB}^{max}$ and $f_{L-dB}^{min}$, respectively, of the L-dB region (Figure 5.5).

## 5.3 Results and Discussion

In order to validate the proposed methodology, $T_{L-dB}$ estimations (Equation 5.24) were carried out over tilt (eigenangle) experimental data measured during the whole IJmuiden campaign (80 days) and then compared against reference wave periods measured by the Triaxys™ buoy. Because the Triaxys™ buoy yielded multiple estimations of the wave period according to the different oceanographic definitions (Section 5.2), we first needed to assess which of these best matched the PSD wave period estimated by using the L-dB method ($T_{L-dB}$, Equation 5.24).

To carry out this comparison, three statistical indicators were used: (i) correlation coefficient ($\rho$), (ii) Root-Mean-Squared Error (RMSE), and (iii) Mean Deviation (MD). In the context of wind

energy, a typical sampling period is 10 min; thus, $T_{L-dB}$ was estimated every 10 minutes. When comparing the significant wave period estimated via the L-dB method and Triaxys™, $T_{L-dB}$ was resampled to the temporal resolution of Triaxys™ (1 h). Root-mean-square error is defined as

$$RMSE = \sqrt{\frac{\sum_i (T_{L-dB} - T_z)^2}{N}} \tag{5.25}$$

and the mean deviation is defined as

$$MD = \frac{\sum_i (T_{L-dB} - T_z)}{N}. \tag{5.26}$$

$T_{L-dB}$ was estimated at $L - dB$ values ranging from 3 to 11 dB and compared against oceanographic wave-period definitions $T_z$, $T_{avg}$, $T_p$, $T10$, $Te$, $Tp5$, and $T_{sig}$ defined in Section 5.2 and measured by Triaxys™, which were used as references. Figure 5.6 shows statistical indicators when comparing $T_{L-dB}$ as a function of L with each of these Triaxys™ reference periods. Figure 5.6 shows the results of these comparisons in terms of $\rho$ (Figure 5.6a), RMSE (Figure 5.6b), and MD (Figure 5.6c). The zero-crossing and the average-period methods ($T_z$ and $T_{avg}$, respectively) yielded by experiment identical statistical indicators, which is evidenced by the overlapping blue and dashed black lines in the three subfigures (Figure 5.6 a)–c)). When comparing $T_z$ and $T_{avg}$ to $T_{L-dB}$, maximal $\rho$, minimal RMSE, and MD closest to 0 were evidenced. The largest differences occurred for the wave energy spectrum peak methods ($T_{p5}$ and $T_p$). A possible explanation for that is that wave energy spectrum peak methods measured the period corresponding to the peak spectral component and did not consider wave multimodality. Lastly, $T_{10}$ and $T_{sig}$, which consider the highest tenth and third of the wave energy spectrum as the relevant wave spectral components, respectively, showed better agreement than the latter set did ($T_{p5}$ and $T_p$), with $T_{sig}$ showing better indicators. $T_{sig}$ showed higher $\rho$, lower RMSE, and MD closer to 0 than $T_{10}$ due to the broader frequency span. It emerged that the L-dB method best matched $T_z$ and $T_{avg}$ (with virtually identical indicators). In the following, the L-dB method is compared with reference to $T_z$.

Optimal threshold L was found heuristically using a parametric approach: $T_{L-dB}$ estimations were computed as a function of threshold L spanning from L = 3 to 10 dB for the whole measurement campaign, and then compared statistically against $T_z$. Statistically, indicators relating both methods for each threshold value L were computed for each week and each month of the 80 day campaign, and lastly for the whole campaign. Then, weekly and monthly sets were averaged over all weeks and months, respectively, to yield monthly and weekly ensemble averages (in what follows, the word "ensemble" is skipped). The chosen statistically indicators were the ones above ($\rho$, RMSE, and MD) along with the slope and intercept point of the linear regression (LR, y=mx+n) between $y = T_{L-dB}$ and $x = T_z$.

Figure 5.7 shows statistical indicators computed for the 80 day campaign as weekly and monthly averages, and for the whole campaign as a function of threshold L. $\rho$, RMSE, and LR slope showed

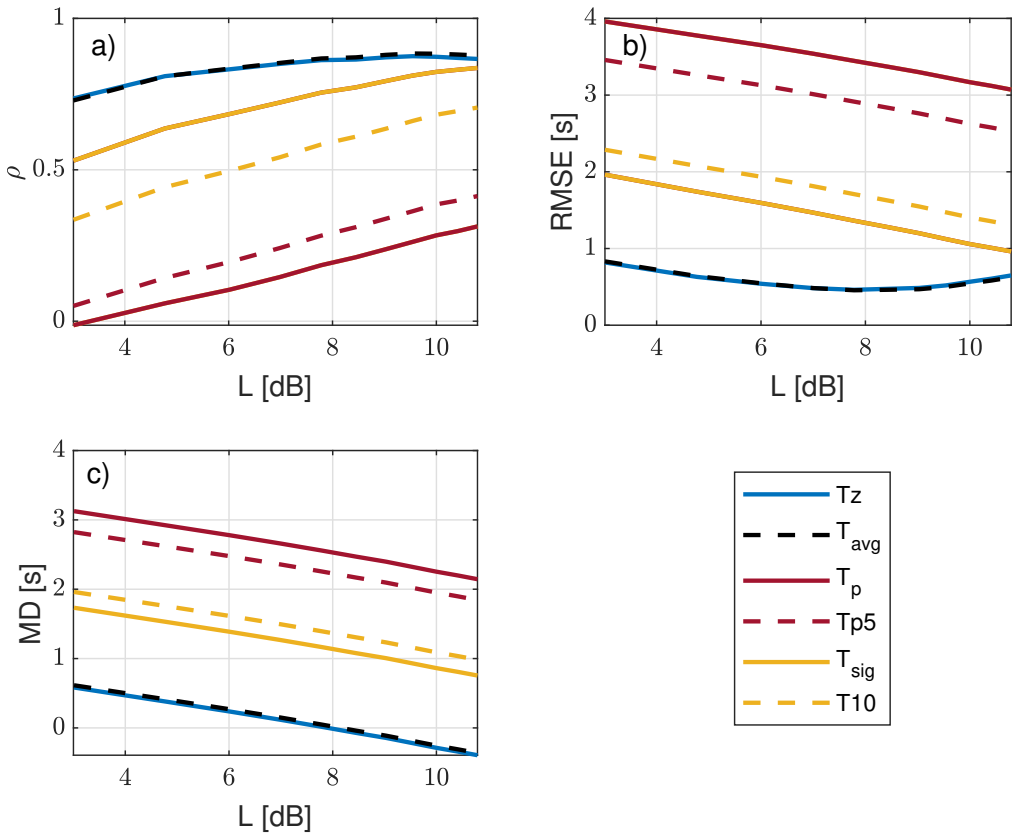


Figure 5.6: Comparison by 3 statistical indicators of agreement between estimated $T_{L-dB}$ and reference wave periods from IJmuiden campaign's experimental data at different $L$ values: **(a)** Correlation coefficient, $\rho$, as a function of threshold level, L; **(b)** Same as **(a)** for RMSE (Equation 5.25); and **(c)** MD (Equation 5.26).

similar values for the two time averages considered and for the whole campaign. $\rho$ grew from 0.7 at L = 3 dB to a maximum of 0.86 at 8 dB and onwards. On the other hand, RMSE showed parabolic behaviour with minimal RMSE = 0.46 s around L = 7.75 dB. The LR slope showed a linearly increasing trend, with the ideal value of 1 reached at L = 8.5 dB. The LR intercept reached 0 (ideality value) at L = 8.5 dB (weekly averages) and L = 9.5 dB (campaign), although the LR intercept became less relevant because slope deviations from unity (ideal value) are always associated to nonzero intercepts in the regression procedure. Lastly, the MD showed decreasing linear trend and cut the 0 dB baseline at L = 8 dB. Therefore, by choosing threshold L = 8 dB, virtually all ideal indicators' values were achieved, $\rho$ = 0.86, RMSE = 0.47 s, LR slope = 0.97, and MD $\simeq$ 0.02.

Figure 5.8 shows the scatter plot between the PSD L-dB method with L = 8 dB, 8-dB method $T_{8-dB}$, and zero-crossing method $T_z$. With the chosen 8 dB threshold, both methods reconciled, as evidenced by the indicator values above. Overall, narrowly scattered points represent $T_{8-dB}$ points that did not fall out of the ideal 1:1 line by more than the RMSE value. The straight-line fit

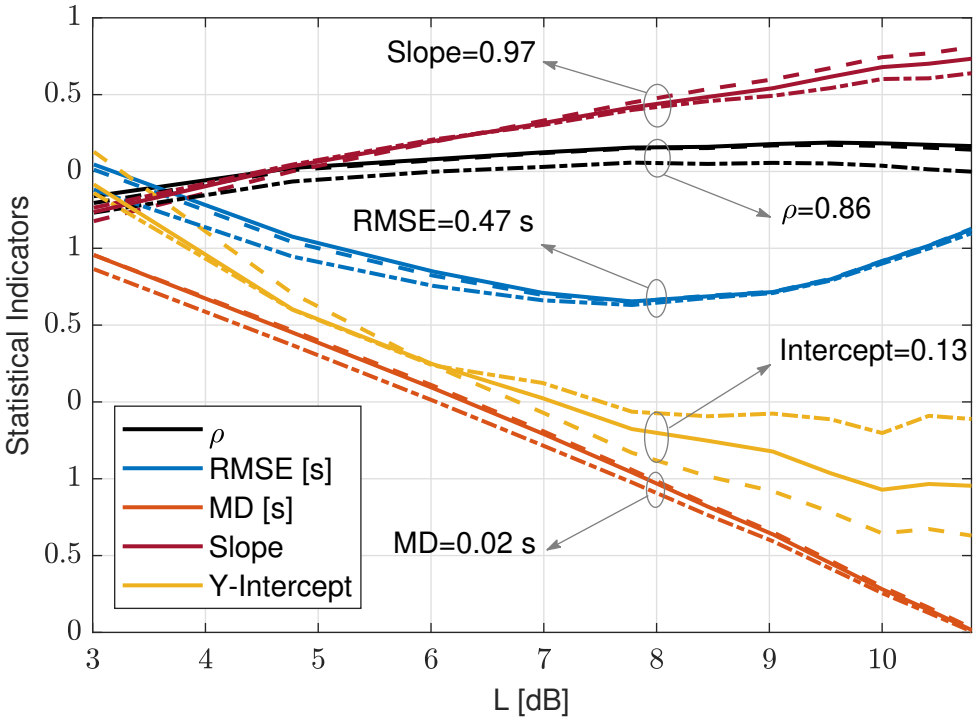


Figure 5.7: Statistical indicators comparing L-dB method $T_{L-dB}$ and zero-crossing method $T_z$, as a function of threshold value L (dB), parameterised by averaging time (IJmuiden campaign, 29 March–17 June 1920 records). (Dashed dot) Weekly averaged indicators. (Dashed) Monthly average. (Solid trace) Indicators computed for whole 80 day campaign.

had a slope equal to 0.97 and intercept equal to 0.13, all of which yielded virtual coincidence with the ideal 1:1 line.

Despite the good agreement between both methods, which reconciled PSD 8 dB method $T_{8-dB}$ to oceanographic zero-crossing method $T_z$, scatter-plot outliers accounting for an RMSE approximately equal to 10% of the mean wave period warrant some comments. First, Triaxys™ computation of reference period $T_z$ was affected by the buoy's translational and rotational movements; in our modelling, (Section 5.2.3 and Section 5.2.5) only roll and pitch were considered (2 DoF). Second, our methodology was experimentally tested under the assumption of small angles, the median of maximal tilt excursion was $\pm$13 deg (Figure 5.3), which incurred 2.5% and 0.8% errors when using first-order cosine and sine approximation, respectively. Lastly, the DWL and Triaxys™ reference buoys were 200 m apart during the campaign, which may also have accounted for small wind, current, and wave differences.

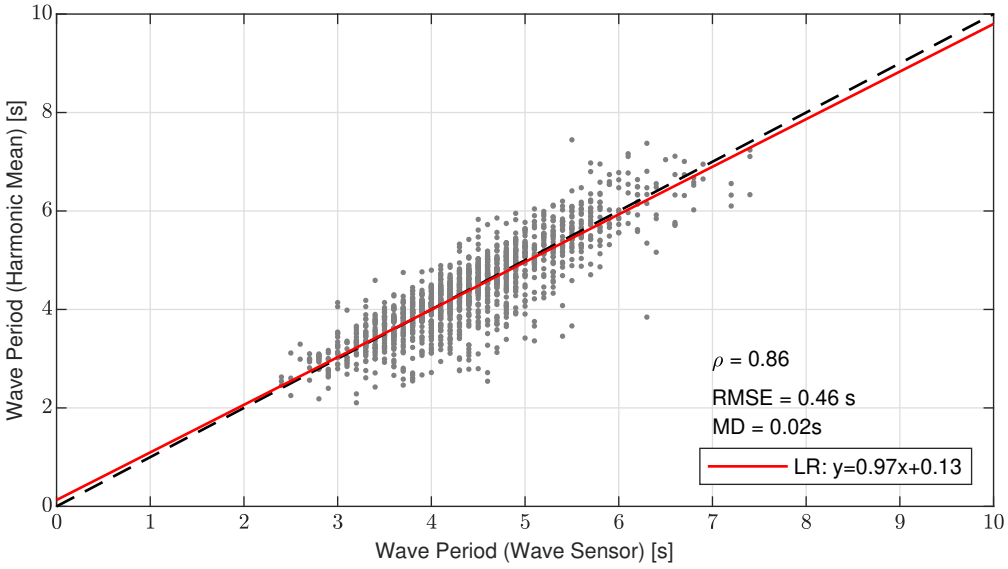


Figure 5.8: Scatter plot comparing wave period estimated by 8 dB method $T_{8-dB}$ in reference to zero-crossing method $T_z$. (Red trace) Linear regression modelling relationship between both methods; (dashed black) 1:1 ideal line.

## 5.4 Summary and Conclusions

A new method (L-dB) to estimate the wave period by the spectral analysis of pitch and roll time records measured on a DWL buoy was shown in the context of IJmuiden's campaign and in comparison to classical oceanographic wave-period estimation methods. This 2-DoF approach assumes quasistatic yaw rotation as compared to the wave period and negligible translational motion (see, e.g., Figure 3.2 mooring scheme).

The 2-DoF buoy motion model enabled the formulation of the so-called eigenangle, which is the buoy tilt angle around the eigenaxis of rotation of the lidar buoy (Euler's rotation theorem). Specifically, the eigenangle is the angle between the down (D) component of the north–east–down fixed coordinate system (IMU frame of reference) and the Z component (downwards) of the buoy's XYZ moving coordinate system.

Under the practical approximation of small angles, the eigenangle can be computed as the quadratic sum of pitch and roll angles (Equation 5.17), and it can be modelled as a complex-number random process, hence assimilating into its real and imaginary components both pitch and roll time series. Histograms records of daily maximal and daily minimal pitch and roll angles (160 records) yielded angular excursions of [-22, +22] deg (min/max values) and [-13, +11] deg (median values), these values showing quantitative description of the small-angle approximation used in our study.

Under these conditions, PSD of the eigenangle $S_{\boldsymbol{\alpha},\boldsymbol{\alpha}}$, was derived (see Appendix B) as the linear combination of pitch and roll PSDs ($S_{\theta,\theta}$ and $S_{\phi,\phi}$, respectively) and the pitch-to-roll cross-PSD

($S_{\theta,\phi}$). PSD was computed by applying the Blackman–Tukey method over 10 min data segments, and wave period $T_{L-dB}$ was computed from the $f_{min}$ and $f_{max}$ cut-off frequencies of the PSD (Equation 5.24) at which the spectral components dropped off L decibels from the peak level.

The proposed L-dB method, which is rooted in the spectral context, was compared to different wave-period definitions from the oceanographic context, namely, the mean zero-crossing, average, and peak periods, among others. The study was carried out by using threshold L as parameterization, and correlation coefficient, $\rho$, RMSE, MD, and LR slope and intercept as statistical indicators. The L-dB method was indistinctly in close agreement with the zero-crossing and average wave-period definitions, and a threshold value L = 8 dB exhibited the best indicators when comparing the L-dB and zero-crossing methods over daily, weekly, and whole-campaign averages, hence reconciling the spectral approach to the oceanographic one.

Lastly, when comparing our 8 dB method ($T_{8-dB}$) with the zero-crossing one ($T_z$), LR slope was 0.97 and intercept was 0.13, which virtually matched the ideal 1:1 line (Figure 5.8). Regarding the statistical indicators above, the 8 dB method yielded fairly good results with $\rho$ = 0.86, RMSE = 0.46 s (as compared to a mean wave-period over the campaign of 4.39 s), and MD = 0.02 s. In spite of this low RMSE value, a few outliers departed up to 2 s from the ideal line. We speculate that his misestimation was due to the assumption of 2-DoF (pitch and roll) in our methodology in comparison to the 3-DoF (heave, roll, and pitch) used by Triaxys (and in the literature) to compute the wave period, the small-angle approximation, and the 200 m distance between the DWL and Triaxys buoy references. All in all, the proposed L-dB method allows floating wind lidars themselves to provide increased knowledge on the sea state (i.e., sea period), which can enhance wind measurements and reduce offshore wind farms deployment cost. Such knowledge could be assimilated into offshore wind measurements and used to complement mesoscale wind prediction models, which could help improve ship safety under strong wind conditions. Particularly, the IJmuiden sea lock has recently been object of a study in order to explore techniques to improve the safety of ships mooring and navigating nearby [Ricci & Blocken 2020], which could benefit from these offshore wind lidar measurements.

# Chapter 6

# A Unified Formulation for Computation of Six-Degrees-of-Freedom-Motion-Induced Errors in Floating Doppler Wind Lidars

*The contents of this Chapter are aligned with Obj. 2 of this Ph.D. and are part of the full paper [Salcedo-Bosch et al. 2023]:* ***Salcedo-Bosch, A.****; Farré-Guarné, J.; Araújo da Silva, M.P.; Rocadenbosch, F. "A Unified Formulation for the Computation of the Six-Degrees-of-Freedom-Motion-Induced Errors in Floating Doppler Wind LiDARs", Remote Sens. 2023, 15, 1478.* `https://doi.org/10.3390/rs15061478`. *Systematic or multiple reproduction or distribution to multiple locations via electronic or other means is prohibited and is subject to penalties under law*

## 6.1 Introduction

As presented in Section 2.2, mainly two types of DWLs are used for wind remote sensing: *pulsed* and *focusable continuous-wave* (CW) DWLs [Slinger & Harris 2012]. Pulsed DWLs use the time of flight to discern between measurements at different altitudes whereas focusable CW DWLs achieve the same by focusing the emitted beam to a particular height by changing its optics.

When placed over floating platforms or buoys, DWLs are able to measure the wind profile in a cost-effective way [Carbon Trust 2013, Schuon et al. 2012, Silva et al. 2022]. On the other hand, FDWLs suffer 6-DoF motion, induced by the waves [Gottschall et al. 2014b, Salcedo-Bosch et al. 2021b; 2020b], which increases the variance on the reconstructed wind vector by the lidar [Gutiérrez-Antuñano et al. 2018, Salcedo-Bosch et al. 2020a]. However, in wind energy standard averaging periods, typically 10 or 30 min, the motion-induced error on the retrieved mean wind vector can be neglected, as it is averaged out [Gutiérrez-Antuñano et al. 2017, Gutiérrez-Antuñano et al. 2018, Kelberlau et al. 2020, Gottschall et al. 2017a].

The motion-induced variance on FDWL measurements is encountered at higher wind statistical moments, such as the TI [Kelberlau et al. 2020]. In the presence of wave motion, FDWLs measure an apparent turbulence addition due to the motion-induced variance, which corrupts the TI measurements [Salcedo-Bosch et al. 2020a, Gutiérrez-Antuñano et al. 2018]. TI is one of the parameters of main importance for wind farm design and operation, as wrong estimates of TI could lead to turbine overdesign or malfunctioning [Mücke et al. 2011] and, thus, higher costs.

In the state of the art, study of the motion-induced error on FDWLs is two-fold: error estimation and error compensation. This paper addresses the former topic, specifically, error estimation in focusable CW FDWLs, which is carried out using a thorough analytical formulation of the system mechanics and wind vector retrieval algorithm. Error estimation in pulsed FDWLs is tackled elsewhere [Désert et al. 2021, Gottschall et al. 2014a]. The latter topic, i.e., error compensation, be it using either mechanical [Gutiérrez-Antuñano et al. 2017] or signal processing techniques [Kelberlau et al. 2020, Salcedo-Bosch et al. 2021c; 2022b, Gutiérrez-Antuñano et al. 2018] is out of the scope of the present work.

So far, Multiple studies have addressed the study of the motion-induced *error* on focusable CW FDWLs at both scan-time and 10 min levels:

*At scan-time level,* Tiana-Alsina et al. (2015) proposed a basic CW FDWL-motion simulator in which roll and pitch motions were simulated by means of Euler's rotation matrices. This simulator provided insights on the HWS error in relation to the WD and the buoy tilt but was unable to simulate the effects of translational motion on the HWS error. Bischoff et al. (2018) presented a simulation environment to estimate uncertainties in measurements by CW FDWLs using a simplified buoy model. However, the error estimates could not match the measurements for high-resolution (1 Hz) data. Kelberlau et al. (2020) provided a thorough geometrical description of the FDWL dynamics taking into account the 6-DoF motion of the FDWL buoy and provided a method for compensating the apparent TI measured by the SEAWATCH CW FDWL buoy by Fugro$^{TM}$. This geometrical description permitted a preliminary study of the 6-DoF-motion-induced error in a lidar scan but was limited by the oversimplification of assuming a constant value for the initial scan phase. Departing from this geometrical description, Salcedo-Bosch et al. (2021c) numerically simulated the 6-DoF CW DWL measurement error [Salcedo-Bosch et al. 2021a] and provided a first 6-DoF-motion correction algorithm using an UKF. The simulator [Salcedo-Bosch et al. 2021a] modeled each of the six DoF as a sinusoidal signal with a given amplitude, frequency, and phase and enabled full understanding of the motion-induced error in a lidar scan through the principle of error superposition. Most of the CW FDWL-motion-related error studies in the literature resort to numerical simulations due to the inherent complexity of the VAD algorithm, because it involves a least-squares fit as a nonlinear operation. These simulations are computationally expensive and

difficult to implement [Tiana-Alsina et al. 2015, Salcedo-Bosch et al. 2021a, Bischoff et al. 2018, Kelberlau & Mann 2022].

*At 10 min level*, Kelberlau & Mann (2022) recently presented a study on the motion-induced error in the measurement of the mean HWS using a motion simulator. The study theoretically proved the reduced sensitivity of the mean HWS error to lidar motion and its relation to the buoy motion frequency. However, the study was limited to the mean HWS and provided error values up to one order of magnitude smaller than typical measured values. The study by Bischoff et al. (2018) was also limited to studying the bias in the HWS mean, and difficulties in validating the estimated values with experimental data were encountered. Gutiérrez-Antuñano et al. (2018) presented a method to estimate the TI measurement error based on a 2-DoF (roll and pitch) motion simulator as a way to compensate for this error. Overall, it showed good estimation of the motion-induced error, but the performance of the method largely depended on the motion scenario because only two DoF were taken into account. In addition, the simulation was computationally demanding.

The above considerations motivate the study of a unified 6-DoF (rotational and translational) method to quantify the motion-induced error in focusable CW FDWLs: In this work, we provide, for the first time, a complete *analytical formulation* and calculus of the 6-DoF-motion-induced error on the HWS retrieved by the focusable CW FDWL in a scan. The formulation relies on the VAD lidar wind retrieval algorithm and motion parameterization using the characteristic amplitude, frequency, and phase of each of the six DoF (i.e., three rotational and three translational components). Methods to statistically quantify the 10 min HWS bias and TI increment in response to floating lidar motion are also derived. The framework is the focusable continuous-wave $ZephIR^{TM}$ 300 lidar tested using experimental data gathered during "Pont del Petroli" and IJmuiden measurement campaigns.

This chapter is structured as follows: Section 6.2 presents "Pont del Petroli" and IJmuiden measurement campaigns and describes the instrumentation used; Section 6.3 describes the analytical motion model of the FDWL and presents the motion estimation method; Section 6.4 validates the analytical model by means of the simulator [Salcedo-Bosch et al. 2021a] and experimental measurements from "Pont del Petroli" and IJmuiden campaigns; Section 6.5 gives concluding remarks.

## 6.2 Materials

For this study, data from "Pont del Petroli" and IJmuiden campaigns (see Chapter 3) was used.

*The Pont del Petroli campaign.*- From "Pont del Petroli" campaign, we considered:

i. wind measurements from the reference fixed DWL sited at "Pont del Petroli" pier,

ii. wind measurements from the FDWL,

iii. fixed DWL and FDWL buoy internal parameters for data-quality control and

iv. 6-DoF motion measurements obtained by the "lidar IMU" and the "buoy IMU".

*The IJmuiden campaign.-* From IJmuiden campaign, we considered:

i. wind measurements at 92 m height from the reference fixed DWL installed on the metmast platform (21 m),

ii. wind measurements at 83 m height from the EOLOS$^{TM}$ FLS200 FDWL,

iii. fixed DWL and FDWL buoy internal parameters for data-quality control and

iv. 6-DoF motion measurements obtained by the 3DM-GX2-45 IMU installed inside the EOLOS$^{TM}$ FLS200 buoy.

## 6.3 Methods

### 6.3.1 Basic Definitions

The instantaneous wind vector $\vec{u}$ ($\vec{u} = \vec{U} + \vec{u'}$, where $\vec{U}$ denotes the mean wind and $\vec{u'}$ the turbulent component) is defined as the three-dimensional vector $(u_1, u_2, u_3)$ computed here from the HWS, WD, and Vertical Wind Speed (VWS) as

$$\vec{u} = [HWS \cdot \cos(WD), HWS \cdot \sin(WD), VWS]. \tag{6.1}$$

In wind energy, the 10 min mean wind vector is the usual standard and, hereafter, HWS, WD, and VWS refer to the *10 min mean values* unless otherwise indicated.

The TI is indicative of the HWS variations with respect to the mean HWS, and it is computed as

$$TI = \frac{\sigma_{HWS}}{HWS}, \tag{6.2}$$

where $\sigma_{HWS}$ is the 10 min HWS standard deviation.

*Instantaneous error.* With a view to study the motion-induced FDWL measurement error in the retrieved HWS at the *i-th lidar scan*, we define the "instantaneous" error (in practice, the 1 s error considering a scan rate of 1 scan/s) as

$$\epsilon_{HWS,i} = \hat{HWS}_i - HWS_i, \tag{6.3}$$

where $\hat{HWS}$ denotes the HWS "estimated" by the VAD algorithm and $HWS_i$ denotes the "true" HWS at the *i-th* scan.

*10 min error.* The wind energy industry is interested in quantifying both the HWS measurement bias and TI increment due to wave-induced motion on FDWLs at a 10 min level.

The *bias* during a sequence of $N$ measurement scans (i.e., the sample statistical interval; usually $N = 600$ for 10 min measurements when measuring at a single height) is defined as the difference between the mean HWS measured by the FDWL and the mean HWS measured by the reference fixed lidar. Formally,

$$bias_{meas} = \frac{1}{N}\sum_{i=1}^{N} H\hat{W}S_i - \frac{1}{N}\sum_{i=1}^{N} HWS_i = \frac{1}{N}\sum_{i=1}^{N} \epsilon_{HWS,i}. \tag{6.4}$$

Statistically, it can be expressed as

$$bias_{est} = E[H\hat{W}S] - HWS = E[\epsilon_{HWS,i}], \tag{6.5}$$

where $E[\cdot]$ denotes the expectation operator, $H\hat{W}S$ is the 10 min horizontal wind speed estimated by the FDWL, and $HWS$ is the "true" 10 min horizontal wind speed.

The TI increment, $\Delta TI_{meas}$, is defined as the TI measured by the FDWL minus the TI measured by the reference fixed lidar. Formally,

$$\Delta TI_{meas} = \left.\frac{\sigma_{HWS_{FDWL}}}{\overline{HWS}_{FDWL}}\right|_{bin} - \left.\frac{\sigma_{HWS_{fixed}}}{\overline{HWS}_{fixed}}\right|_{bin}, \tag{6.6}$$

where the *overbar* denotes "mean" over the 10 min HWS samples in the calculus bin.

On the other hand, the TI increment can be estimated as

$$\Delta TI_{est} = \frac{\sigma_{\epsilon_{HWS,i}}}{HWS}, \tag{6.7}$$

where $\sigma_{\epsilon_{HWS,i}}$ is the standard deviation of the instantaneous error (Equation 6.3).

### 6.3.2 Reconciling the estimated and the measured TI

Next, we relate Equation 6.7 to Equation 6.6 from the statistics and probability theory viewpoint. Towards this goal and in order to aid mathematical notation, we introduce *short-hand notation* F-R-W as follows: we change mnemonics "FDWL" into "F" and "fixed" into "R" (as a reminder of "reference" fixed lidar). We also introduce subscript "W" as a reminder of "wind" to denote the wind that a *nonmoving DWL* would measure *at the same place* as the moving FDWL. In other words, subscript "W" denotes the "true" wind measurement but including the 1 s average and spatial smoothing inherent to the DWL scanning procedure. To simplify notation, the "true" wind HWS, $HWS_W$, is simply denoted as $HWS$.

#### 6.3.2.1 On the estimated TI

According to probability theory, the variance of the difference of two random variables (i.e., $\epsilon_{F,W} = HWS_F - HWS_W$, which reproduces Equation 6.3) is equal to the sum of each of their variances minus twice their covariance [Barlow 1989],

$$\sigma^2_{\epsilon_{F,W}} = \sigma^2_F + \sigma^2_W - 2\rho\sigma_F\sigma_W, \tag{6.8}$$

where $\rho$ is the correlation coefficient between "F" and "W" variables, and $cov(F,W) = \rho_{F,W}\sigma_F\sigma_W$.

At this point, we introduce the assumption that the FDWL-measured and the "true" HWS (subscripts "F" and "W", respectively) are linearly correlated so that $\rho_{F,W} \approx 1$. By experiment, Tiana-Alsina et al. (2015) reported correlation coefficients of $\rho_{F,R} = 0.9$, $\rho_{F,R} = 0.86$, and $\rho_{F,R} = 0.66$ between co-located moving and reference DWLs in a controlled-motion experiment for tilt motion amplitudes of 10, 16, and 25 deg, respectively. In past experimental campaigns involving different FDWL buoy topologies [Kelberlau & Mann 2022, Salcedo-Bosch et al. 2021b, Gutiérrez-Antuñano et al. 2018, Kelberlau et al. 2020], the most frequent buoy tilts were reported to range from 0 up to 10 deg. These low tilts are also supportive of high F-to-W correlation coefficients, $\rho_{F,W} \approx 1$, at the FDWL location. Inserting $\rho_{F,W} = 1$ in Equation 6.8 above and re-arranging terms,

$$\sigma^2_{\epsilon_{F,W}} \simeq (\sigma_F - \sigma_W)^2. \tag{6.9}$$

By taking the square root of Equation 6.9 above and substituting it into Equation 6.7, the estimated turbulence intensity can be written as

$$\Delta TI_{est} \simeq \frac{\sigma_F - \sigma_W}{HWS}. \tag{6.10}$$

#### 6.3.2.2 On the measured TI

As in the preceding subsection, one can assume that the 10 min FDWL- and reference-lidar-measured HWS are virtually identical so that $HWS_{FDWL} \approx HWS_{fixed} \approx HWS$ [Gottschall et al. 2017b, Araújo da Silva et al. 2022a]. Introducing this approximation into Equation 6.6 and using the shorthand notation F-R-W-M introduced above, it can be rewritten as

$$\Delta TI_{meas} = \frac{\sigma_F - \sigma_R}{HWS}. \tag{6.11}$$

If the FDWL and the fixed lidar carried out exactly co-located measurements, the estimated TI (Equation 6.10) and the measured TI (Equation 6.11) *would be* identical (i.e., $\sigma_R = \sigma_W$). In practice, the fixed and the FDWL were located 50 m apart in PdP campaign and 300 m apart in IJmuiden campaign (see Section 6.2) and, therefore, small differences up to 1% [Salcedo-Bosch et al. 2021c] are expected to arise between the estimated and the measured TI increment when different wind flows are measured by the reference and floating lidars.

### 6.3.3 FDWL geometrical model

We define the right-handed Cartesian XYZ "moving body" coordinate system of the lidar buoy (hereafter, the "moving" coordinate system) and the right-handed Cartesian north–east–down (NED) "fixed" inertial frame of reference (hereafter, the "fixed" system, Figure 6.1). The IMU (see Section 6.2) measures the rotation and translation of the "moving" coordinate system with respect to the "fixed" system. Vectors $\hat{n}$, $\hat{e}$, and $\hat{d}$ are unitary vectors aligned with the N, E, and D axes of the

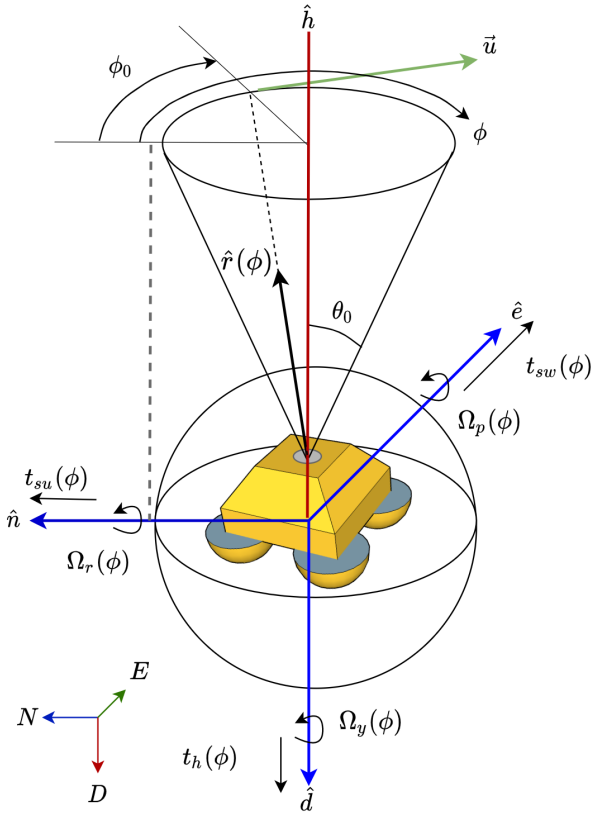


Figure 6.1: Motion geometry of the FDWL buoy.

fixed coordinate system, respectively. $\hat{x}$, $\hat{y}$, and $\hat{z}$ are unitary vectors aligned with the X, Y, and Z axes, respectively, of the moving coordinate system. $\hat{h}$ is a unit vector in the outbound direction of the lidar scanning cone axis and is defined as the opposite of $\hat{z}$. The half-angle cone aperture is $\theta_0$ = 30 deg.

Unitary vector $\hat{r}$ defines the lidar beam pointing direction in each LoS measurement during the lidar scan. In what follows, $\hat{r}$ is given in spherical coordinates relative to moving coordinate system. Specifically, $\hat{r}$ is given by the zenith angle relative to $\hat{h}$, which is denoted $\theta_0$ (i.e., the cone aperture), and by the azimuth angle relative to $\hat{x}$, which is denoted $\phi$ (Figure 6.1). As mentioned, $\theta_0$ is the constant value of 30 deg corresponding to the scanning-cone aperture. $\phi$ is a time-variable angle representing the lidar scanning phase (positive towards $\hat{y}$).

During the lidar scan, the vector $\hat{r}$ rotates about $\hat{h}$ with uniform circular motion at a rate of 1 revolution per second, i.e., $\phi(t) = 2\pi \times t$ [rad]. In what follows, for simplicity, we stick to variable $\phi$ instead of the usual time variable $t$. Variable $\phi$ ranges from 0 to $2\pi$ [rad] during a lidar scan. Therefore, $\hat{r}$ can be formulated in the moving coordinate system as follows:

$$\hat{r}(\phi) = \sin(\theta_0) \cdot \cos(\phi - \phi_0)\hat{x} + \sin(\theta_0) \cdot \sin(\phi - \phi_0)\hat{y} - \cos(\theta_0)\hat{z}, \tag{6.12}$$

where $\phi_0$ is the lidar initial scan phase or, from now on, the "initial phase".

### 6.3.4 The VAD algorithm as a first-order Fourier series

Focusable CW DWLs use the VAD algorithm to retrieve the wind vector from the *measured*, along-LoS-projected wind velocity during the lidar scan, which is computed as the so-called *VAD function*,

$$f(\phi) = \vec{u} \cdot \hat{r}(\phi). \tag{6.13}$$

In a motionless uniform nonturbulent wind scenario, the wind vector can be decomposed as $\vec{u} = HWS\hat{\rho} + w\hat{h}$, where $\hat{\rho} = cos(WD)\hat{x} + sin(WD)\hat{y}$, WD positive counterclockwise. Then, the ideal VAD function $f(\phi)$ takes the shape of the *model* cosine function [Peña et al. 2015, Slinger & Harris 2012],

$$f_{model}(\phi) = A \cdot cos(\phi - B) + C, \tag{6.14}$$

where $A$ is the amplitude, $B$ is the phase, and $C$ is the offset term. From Equation 6.14 above, the HWS, WD, and VWS components of the wind vector are obtained as [Kelberlau et al. 2020]

$$\begin{aligned} HWS &= \frac{A}{sin(\theta_0)}, \\ WD &= B, \\ VWS &= \frac{C}{cos(\theta_0)}. \end{aligned} \tag{6.15}$$

In Equation 6.15 above HWS, WD, and VWS refer to the values retrieved at the *i-th* scan.

The VAD algorithm uses the Least Squares (LSQ) algorithm to fit the model cosine function $f_{model}$ (Equation 6.14) to the measured function $f(\phi)$ in order to obtain the sought-after parameters $A$, $B$, and $C$:

$$min\Big|_{A,B,C} \left\{ \left|\left| f(\phi) - [A \cdot cos(\phi - B) + C] \right|\right|^2 \right\}. \tag{6.16}$$

The LSQ fit is usually carried out by means of numerical methods. Yet, they do not allow explicit analytical formulation of solving coefficients $A$, $B$, and $C$ with a view to understand propagation of the motion-induced error. A way out of this problem is to treat the error-norm minimization of Equation 6.16 in the Hilbert space of the square integrable functions $L^2[0, 2\pi]$, in which $\{1, \cos(m \cdot \phi), \sin(n \cdot \phi)\}$, $m, n = 1...\infty$ form an orthogonal basis. Equivalently, the Fourier series is the LSQ projection of a target function to an orthogonal space defined by a sum of sine and cosine functions Tolstov (1976). Therefore, the solution of Equation 6.16 is the first-order Fourier series of $f(\phi)$ in the basis function $\{1, \cos(\phi), \sin(\phi)\}$. The first-order Fourier series can be rewritten in the form of Equation 6.14, in which $A$, $B$, and $C$ parameters can be expressed as a function of the

Fourier coefficients as Stearns & Hush (2011)

$$\begin{aligned} A &= \sqrt{a_1^2 + b_1^2}, \\ B &= arctan\left(-\frac{b_1}{a_1}\right), \\ C &= \frac{a_0}{2}, \end{aligned} \tag{6.17}$$

where $a_0$, $a_1$, and $b_1$ are first-order Fourier coefficients of $f(\phi)$, obtained as Stade (2015)

$$\begin{aligned} a_0 &= \frac{2}{P}\int_0^P f(\phi)d\phi, \\ a_1 &= \frac{2}{P}\int_0^P f(\phi)\cos(\phi)d\phi, \\ b_1 &= \frac{2}{P}\int_0^P f(\phi)\sin(\phi)d\phi, \end{aligned} \tag{6.18}$$

where $P = 2\pi$.

From Equation 6.15 and Equation 6.17 above, it emerges that Fourier coefficients $a_1$ and $b_1$ propagate errors to the $HWS$ and $WD$ (i.e., to the wind horizontal components), while coefficient $a_0$ propagates errors only to the retrieved $VWS$.

As mentioned, homodyne-detection lidars, as in the case of the ZephIR$^{TM}$ 300, are only able to measure the magnitude of the along-LoS radial velocities but not the sign. This is equivalent to saying that $f(\phi)$ takes the shape of a rectified cosine, i.e., the absolute value of $f(\phi)$ [Kelberlau et al. 2020]. When applying the VAD algorithm to $|f(\phi)|$, parameters $A$ and $C$ retain the same value as for the heterodyne case (VAD applied to $f(\phi)$) but $B$ has a $\pm\pi$ rad ambiguity. The latter can be disambiguated by a wind vane co-located with the lidar buoy.

### 6.3.5 Estimation error methodology

In the absence of buoy motion, the X, Y, and Z axes of the moving coordinate system would coincide with the N, E, and D axes of the fixed system [Salcedo-Bosch et al. 2021b]. In the presence of waves, the FDWL experiences angular and translational motion about the three NED axes. In this section, we formulate analytical expressions for the motion influence on the VAD-retrieved wind vector.

In order to simplify the obtained analytical expressions, the following assumptions are considered: (i) motion in each of the six DoF is considered to be a zero-mean simple harmonic motion; (ii) rotational and translational motions are considered to be independent error sources; and (iii) under motion, the VWS contribution to the HWS error is considered to be null as compared to the HWS contribution [Kogaki et al. 2020].

#### 6.3.5.1 Rotational Motion Model

The FDWL buoy undergoes roll, pitch, and yaw motion around the three fixed coordinate axes, i.e., N, E, and D, respectively. As observed experimentally [Salcedo-Bosch et al. 2021b], roll and pitch

motions can be modeled using first-order small-angle approximation as simple harmonic motions. *Yaw motion*, which shows larger and more constant values with time, can be modeled by *constant tilt*.

We define roll and pitch tilts (in units of radians) as sinusoidal signals of the form

$$\Omega_x(\phi) = A_x \cdot \sin(f_x\phi - \alpha_x), \tag{6.19}$$

where $A_x$, $f_x$, and $\alpha_x$ denote the amplitude, frequency, and motional phase, respectively. Subindex $x = roll, pitch$ denotes $roll$ and $pitch$ motion, respectively. Note that, for convenience, Equation 6.19 is expressed as a function of lidar scan phase variable $\phi$ ($\phi = 2\pi t$) instead of time variable $t$.

As mentioned, the yaw tilt is considered a constant value $\Omega_{yaw}(\phi) = A_{yaw}$. This is conducted without limiting the general formulation of the problem. Thus, the reader can extend formulation of the yaw angle to the harmonic case by defining the yaw motion as a sinusoidal signal (Equation 6.19) plus an offset term equal to its mean value during the interval under study, and by following the formulas in Section 6.3.5.1 and Appendix C.1.

First, in order to compute the rotated lidar pointing direction, $\hat{r}_{rot}$, in the fixed NED coordinate system given roll, pitch, and yaw rotations, we use the Euler rotation matrix. Euler's rotation theorem states that any rigid-body rotation can be defined by three rotation angles [Palais et al. 2009]. There are many different conventions regarding the rotation angles and its order of application. Here, we consider the NED convention, i.e., three elemental rotations are carried out sequentially: first, a rotation around the N axis (roll motion); second, a rotation around the E axis (pitch motion); and finally, a rotation around the D axis (yaw motion). Rotations are positive counterclockwise. Therefore, the Euler rotation matrix can be written as [Roithmayr & Hodges 2016]

$$\boldsymbol{R} = \boldsymbol{R_D} \cdot \boldsymbol{R_E} \cdot \boldsymbol{R_N}, \tag{6.20}$$

where $\boldsymbol{R_N}$, $\boldsymbol{R_E}$, and $\boldsymbol{R_D}$ are the elemental rotation matrices about the N, E, and D axes, respectively. They can be formulated as follows:

$$\begin{aligned}
\boldsymbol{R_D} &= \begin{bmatrix} \cos(\Omega_y) & -\sin(\Omega_y) & 0 \\ \sin(\Omega_y) & \cos(\Omega_y) & 0 \\ 0 & 0 & 1 \end{bmatrix}, \\
\boldsymbol{R_E} &= \begin{bmatrix} \cos(\Omega_p(\phi)) & 0 & \sin(\Omega_p(\phi)) \\ 0 & 1 & 0 \\ -\sin(\Omega_p(\phi)) & 0 & \cos(\Omega_p(\phi)) \end{bmatrix}, \\
\boldsymbol{R_N} &= \begin{bmatrix} 1 & 0 & 0 \\ 0 & \cos(\Omega_r(\phi)) & -\sin(\Omega_r(\phi)) \\ 0 & \sin(\Omega_r(\phi)) & \cos(\Omega_r(\phi)) \end{bmatrix},
\end{aligned} \tag{6.21}$$

where subindexes $y$, $p$, and $r$ stand for "yaw", "pitch", and "roll", respectively.

The small-angle approximation for roll and pitch angles [Salcedo-Bosch et al. 2021b, Kelberlau et al. 2020] translates into first-order Taylor approximation for the sine and cosine functions (i.e.,

$sin(x) \simeq x$ and $cos(x) \simeq 1$). These first-order approximations have already been incorporated into Equation C.1, Appendix C.1, in order to simplify rotation matrix $\boldsymbol{R}$.

The second step is to compute the rotated version of the lidar pointing vector, $\hat{r}_{rot}(\phi)$, in the NED fixed coordinate system:

$$\hat{r}_{rot}(\phi) = \boldsymbol{R} \cdot \hat{r}(\phi). \tag{6.22}$$

Third, the FDWL-measured wind under rotational motion is computed by projecting the wind vector over the rotated lidar pointing vector for each LoS. This can be expressed by means of the dot product as follows:

$$f_{rot}(\phi) = \vec{u} \cdot \hat{r}_{rot}(\phi). \tag{6.23}$$

Eventually, the motion-corrupted FDWL wind vector is derived by applying the VAD algorithm to function $f_{rot}(\phi)$ above. With this aim, the first-order Fourier coefficients of $f_{rot}(\phi)$ (i.e., $a_0^{rot}$, $a_1^{rot}$, and $b_1^{rot}$) are computed through Equation 6.18 by substituting $f_{rot}(\phi)$ in place of $f(\phi)$. The HWS retrieval error is computed as the difference between the "true" HWS (i.e., without motion influence) and the FDWL-retrieved HWS under rotational motion:

$$\epsilon_{HWS,i}^{rot} = HWS, i - \frac{1}{\sin(\theta_0)} \sqrt{(a_1^{rot})^2 + (b_1^{rot})^2}, \tag{6.24}$$

where $a_1^{rot}$ and $b_1^{rot}$ are the Fourier coefficients of $f_{rot}(\phi)$. See Section C.3 for the mathematical results in expanded form.

#### 6.3.5.2 Translational-Motion Model

Waves also induce translational motion to the FDWL in the N, E, and D directions, i.e., surge, sway, and heave motions, respectively. Similar to the derivation of the rotational motion components in Equation 6.19, sinusoidal variation is assumed for each translational-motion component. They are formulated as follows:

$$t_x(\phi) = A_x \cdot \sin(f_x \phi - \alpha_x), \tag{6.25}$$

where $A_x$, $f_x$, and $\alpha_x$, are the amplitude, frequency, and phase of translational motion $x$, where $x$ denotes the surge, sway, or heave components. We also define translational-velocity vector $\vec{t}(\phi)$ in the NED fixed coordinate system as the three-component vector,

$$\vec{t}(\phi) = [t_{su}(\phi), t_{sw}(\phi), t_{he}(\phi)], \tag{6.26}$$

where subscripts $su$, $sw$, and $he$ refer to *surge*, *sway*, and *heave*, respectively.

First, with a view to compute the FDWL-measured wind under translational motion, we compute the apparent wind vector. The apparent wind vector measured by the FDWL is the difference between the wind vector and the translational-velocity vector:

$$\vec{u}^{trans}(\phi) = \vec{u} - \vec{t}(\phi). \tag{6.27}$$

Second, the translational-velocity contribution to the lidar-measured LoS, $f_{trans}(\phi)$, can be obtained by projecting the apparent wind vector, $\vec{u}^{trans}$, on the lidar pointing direction $\hat{r}(\phi)$ as follows:

$$f_{trans}(\phi) = \vec{u}^{trans}(\phi) \cdot \hat{r}(\phi). \tag{6.28}$$

The lidar-retrieved wind vector is the result of applying the VAD algorithm over the motion-corrupted LoS, $f_{trans}(\phi)$. The Fourier coefficients $a_0^{trans}$, $a_1^{trans}$, and $b_1^{trans}$ are obtained through Equation 6.18 by substituting $f(\phi)$ by $f_{trans}(\phi)$. The Fourier coefficients are given in expanded form in Section C.4 of the Appendix.

Finally, the HWS measurement error due to FDWL's translational motion $\epsilon_{HWS,i}^{trans}$ becomes

$$\epsilon_{HWS,i}^{trans} = HWS_i - \frac{1}{\sin(\theta_0)}\sqrt{(a_1^{trans})^2 + (b_1^{trans})^2}. \tag{6.29}$$

#### 6.3.5.3 Total Error Model

In order to estimate the total error, we depart from the assumption that rotational and translational motion are independent error sources (see Section 6.3.5). Therefore, the total error in the retrieved HWS in a lidar scan is the superposition of errors:

$$\epsilon_{HWS,i}(\vec{u}, \phi_0) = \epsilon_{HWS,i}^{rot}(\vec{u}, \phi_0) + \epsilon_{HWS,i}^{trans}(\vec{u}, \phi_0). \tag{6.30}$$

In Equation 6.30 above, the total error, $\epsilon_{HWS,i}(\vec{u}, \phi_0)$, is parameterized by the instantaneous wind vector $\vec{u}$ and initial phase $\phi_0$.

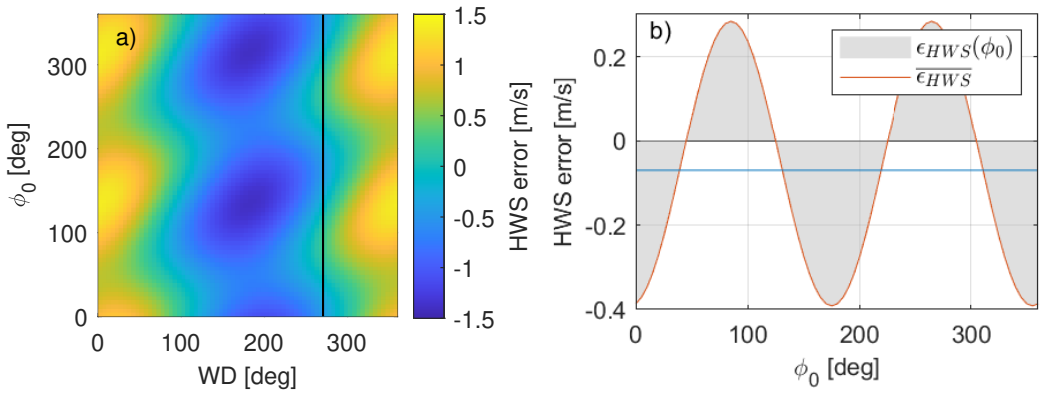


Figure 6.2: Example of estimation of the HWS total error in a lidar scan ($HWS = 10$ m/s, $VWS = 0$ m/s, WD ranging from 0 to 360 deg, roll-only motion). **(a)** Colorplot of the HWS error as a function of the wind direction, $WD$, and initial phase, $\phi_0$. **(b)** HWS error for $WD = 275$ deg (vertical black line in panel (a)) as a function of the initial phase. Blue horizontal line indicates the mean HWS error.

Figure 6.2a illustrates the estimated HWS total error in a lidar scan parameterized as a function of the wind direction (WD ranging from 0 to 360 deg) and initial phase $\phi_0$ in a roll-only motion

scenario ($HWS = 10\,\mathrm{m/s}$, $VWS = 0\,\mathrm{m/s}$). As can be observed, the HWS error is highly dependent on both input parameters (WD and initial phase), ranging from -1.5 up to 1.5 m/s (HWS errors for other input HWSs are scalable through simple direct proportionality). If the WD is known, the HWS error in a lidar scan is dependent only on the initial phase. This is represented in Figure 6.2b, where the HWS error in a lidar scan of Figure 6.2a is represented as a function of the initial phase $\phi_0$ for the constraint settings $HWS = 10\,\mathrm{m/s}$, $WD = 275$ deg, and $VWS = 0\,\mathrm{m/s}$.

However, the initial phase is a manufacturer's undisclosed parameter for the ZephIR 300 lidar. As the instantaneous value of the initial phase at each lidar scan cannot be known nor, consequently, the total error, we assume the initial phase to be a random variable with uniform distribution between 0 and $2\pi$ rad [Gutiérrez-Antuñano et al. 2018]. As a result, HWS error moments rather than instantaneous values must be derived:

The 10 min HWS *bias* (Equation 6.5) is computed as the expectation (first raw moment) of the HWS total error function (Equation 6.30), $\epsilon_{HWS,i}(\vec{u}, \phi_0)$, with respect to the initial phase, $\phi_0$, constrained to the mean wind vector $\vec{U}$ as follows:

$$bias_{est} = E_{\phi_0}[\epsilon_{HWS,i}(\vec{U}, \phi_0)]. \tag{6.31}$$

In practice, $bias_{est}$ is simply the mean value of $\epsilon_{HWS,i}(\vec{U}, \phi_0)$ computed as

$$bias_{est} = \frac{1}{N}\sum_{i=1}^{N} \epsilon_{HWS,i}(\vec{U}, \phi_{0,i}), \tag{6.32}$$

where discrete random variable $\phi_0$ is defined by a finite list $\{\phi_{0,1}, ..., \phi_{0,N}\}$ of equally likely outcomes (vertical line in Figure 6.2a).

Analogously, the 10 min *TI increment* of Equation 6.7 is estimated as follows:

$$\Delta TI_{est} = \frac{STD_{\phi_0}[\epsilon_{HWS,i}(\vec{U}, \phi_0)]}{\hat{HWS}}, \tag{6.33}$$

where $STD$ stands for standard deviation which is the square root of the variance of the total error ($\sigma_{\epsilon_{HWS,i}}$), and $\hat{HWS}$ is the 10 min mean HWS measured by the FDWL.

### 6.3.6 Bias and TI-increment estimation procedure

Figure 6.3 summarizes the procedure described in Section 6.3.5 to compute the estimated 10 min bias and TI increment. The 10 min mean wind vector ($\vec{U}$) as well as the characteristic amplitude, frequency, and phase of each of the 6 DoF are the inputs. In practice, the yaw frequency and phase are set to zero. Fourier coefficients $a_1^{rot}$ and $b_1^{rot}$ are obtained through Equation C.3 and Equation C.4, respectively, which estimate the HWS measurement error due to *rotational* motion ($\epsilon_{HWS,i}^{rot}$, Equation 6.24). Similarly, Fourier coefficients $a_1^{trans}$ and $b_1^{trans}$ are obtained through Equation C.5 and Equation C.6, respectively, which estimate the HWS measurement error due to *translational* motion

($\epsilon^{trans}_{HWS,i}$, Equation 6.29). The following step is to sum the rotational- and translational-error expressions to yield the total error as a function of the wind vector and initial scan phase (Equation 6.30). Then, it is constrained to the 10 min mean wind vector, $\vec{U}$, by substituting $\vec{u}$ in Equation 6.30 with $\vec{U}$. Finally, the bias and TI increment are estimated by means of Equation 6.31 and Equation 6.33, respectively.

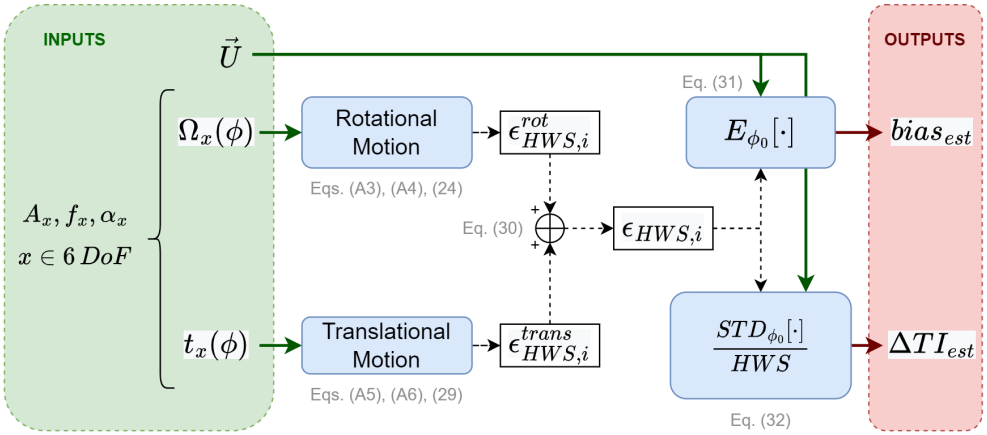


Figure 6.3: Block diagram depicting Section 6.3.5 estimation procedure for the bias and TI increment.

Alternatively, for specific 1 s error model validation (refer to Section 6.4.1), the total error (Equation 6.30) can be obtained as a function of the instantaneous wind vector and lidar initial scan phase.

### 6.3.7 Sinusoidal characterization of measured motion time series

In order to estimate the FDWL-motion-induced error with the presented methodology based on Equation 6.19 and Equation 6.25, there is a requirement that the motion time series in each of the DoF to be modeled as a sinusoidal signal with a characteristic amplitude, frequency, and phase ($A$, $f$, and $\alpha$, respectively). The estimation procedure for these parameters is described next through a case example.

Figure 6.4a shows a record of the IMU-measured roll time series during the PdP campaign. As can be noticed, the signal is composed of multiple frequency components. To analyze the signal spectrum, the Power Spectral Density (PSD) was computed in batches of 10 min segments using the Blackman–Tukey method [Proakis & Manolakis 2006]. In Figure 6.4b, it emerges that the signal has a broad spectrum with relevant frequency components from approximately 0.25 up to 0.5 Hz. The characteristic frequency $f$ was computed as the frequency corresponding to the peak PSD maximum ($\simeq 0.3$ Hz).

In order to estimate the characteristic amplitude $A$, we make use of the fact that the amplitude of a sinusoidal signal is related to its power, $P$, through the relationship $P = A^2/2$ [Proakis &

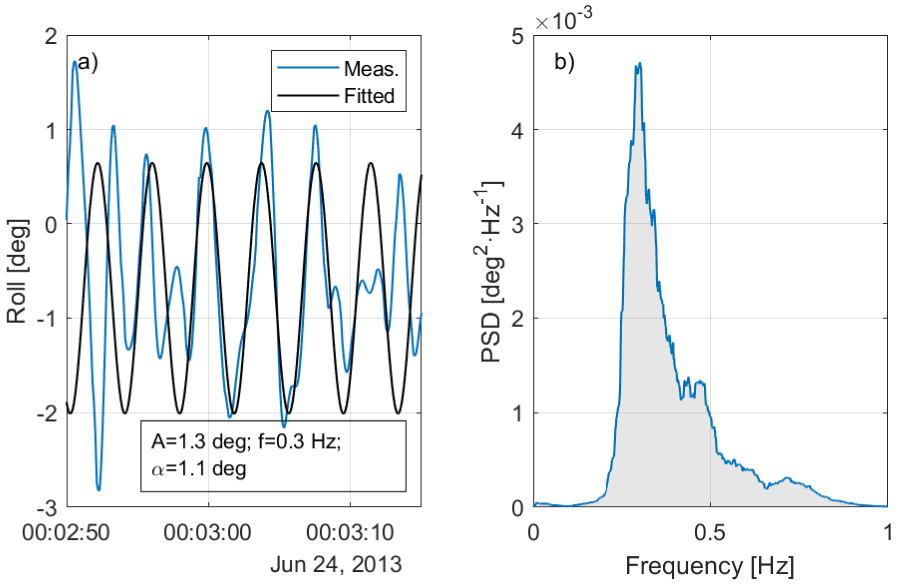


Figure 6.4: FDWL-motion characterization as a sinusoidal signal: roll motion example (PdP, 24 of June 2013, 00:00 LT). **(a)** 10 min roll time series (blue trace) and fitted sinusoidal signal (black trace). **(b)** PSD of panel (a) time series.

Manolakis 2006]. Moreover, the mean power $\overline{P}$ of a stochastic signal $s(t)$ (i.e., the IMU-measured motion) with duration $T$ is computed as [Proakis & Manolakis 2006]

$$\overline{P} = \int_0^T |s(t)|^2 dt. \tag{6.34}$$

The mean power, $\overline{P}$, takes into account all frequency components of the signal spectrum [Plancherel & Leffler 1910]. Therefore, the characteristic amplitude can be estimated from the mean signal power as $A = \sqrt{2\overline{P}}$. Finally, the characteristic phase $\alpha$ is obtained from first-order Fourier decomposition of $s(t)$ in similar fashion as calculation of phase term $B$ in Equation 6.17 given first-order coefficients $a_1$ and $b_1$ in Equation 6.18 (see Section 6.3.4).

Figure 6.4a shows the IMU-measured roll time series against the "fitted" sinusoidal signal with characteristic amplitude, frequency, and phase of $A = 1.3$ deg, $f = 0.3$ Hz, and $\alpha = 1.1$ deg, respectively. It can be observed that the fitted sinusoidal signal reproduces the measured time series under first-harmonic approximation with reasonable accuracy.

### 6.3.8 A note on Appendix A and Supplementary Materials maths formulation

Provided in Appendix C is a formulation compendium to compute the 6-DoF-motion-induced error (Section 6.3.5.3). A MATLAB$^{TM}$ R2020a code to compute the total error (Section 6.3.5.3) is also included as part of the Supplementary Materials of this manuscript.

The mathematical derivations of this Appendix C have been checked both algebraically and numerically. Algebraically, manually derived maths expressions have been validated using MATLAB$^{TM}$

R2020a symbolic toolbox. Numerically, these expressions have been coded in MATLAB and compared with the outputs of the FDWL simulator [Tiana-Alsina et al. 2015] (Figure 6.5, 6.6, and 6.7) for quality assurance.

## 6.4 Results and Discussion

### 6.4.1 Error model validation

In order to validate the presented *analytical-error* formulation (Section 6.3.5 and Appendix C; in what follows, "the unified-error formulation"), the estimated total error in the FDWL-retrieved HWS (Equation 6.30) was compared with the lidar motion simulator as a reference [Salcedo-Bosch et al. 2021a]. The study was carried out by inputting the same reference wind vector ($HWS = 10$ m/s and $VWS = 0$ m/s) into both the unified formulation and the simulator under three different motion scenarios: (i) rotational motion only, (ii) translational motion only, and (iii) 6-DoF motion. In all cases, $f_x = 0.3$ Hz and $\alpha_x = 0$ deg, $x = roll, pitch$, were used. In each scenario, performance of the analytically estimated error was evaluated as a function of the WD and initial scan phase $\phi_0$.

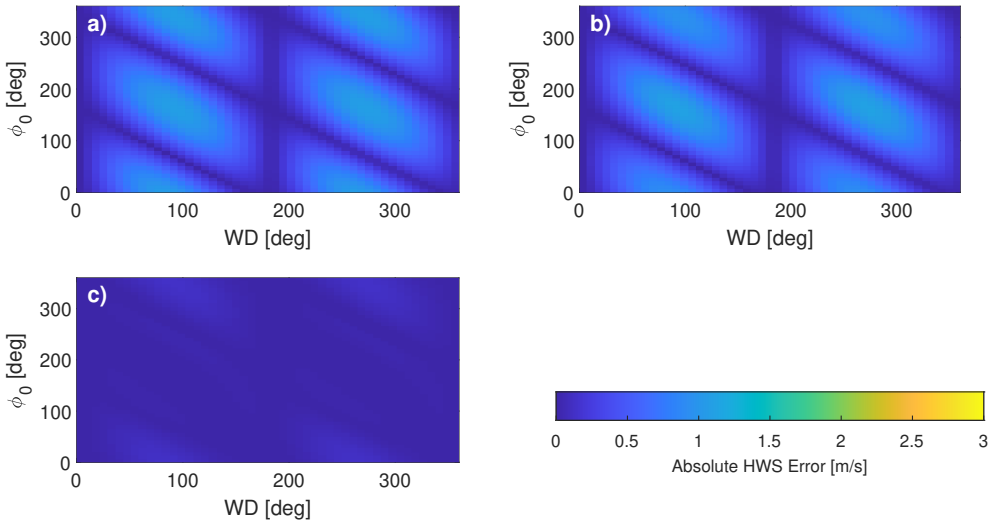


Figure 6.5: Validation of the analytical-error formulation in roll-only scenario #1: *HWS error* (parameters: $A_{roll} = 10$ deg, $f_{roll} = 0.3$ Hz and $\alpha_r oll = 0$ deg. Input wind: $HWS = 10$ m/s, $VWS = 0$ m/s). (a) Analytically estimated HWS error as function of wind direction (WD) and initial scan phase ($\phi_0$). (b) Simulator-estimated HWS error. (c) Difference (a) minus (b) (in absolute value).

In *roll-only scenario #1* (Figure 6.5), the analytically estimated error (Figure 6.5a, Equation 6.24) was virtually identical to the simulator-estimated error (Figure 6.5b) over the whole span of WDs and initial-phase values. From Figure 6.5c, all error differences between panels (a) and (b) were lower than 0.3 m/s, which is evidence of the satisfactory accuracy attained using first-order approximation in the formulation. The RMSE between the error estimates of Figure 6.5a and Figure 6.5b

(equivalently, the square root of the mean of the squares of the error values shown in Figure 6.5c) was 0.04 m/s.

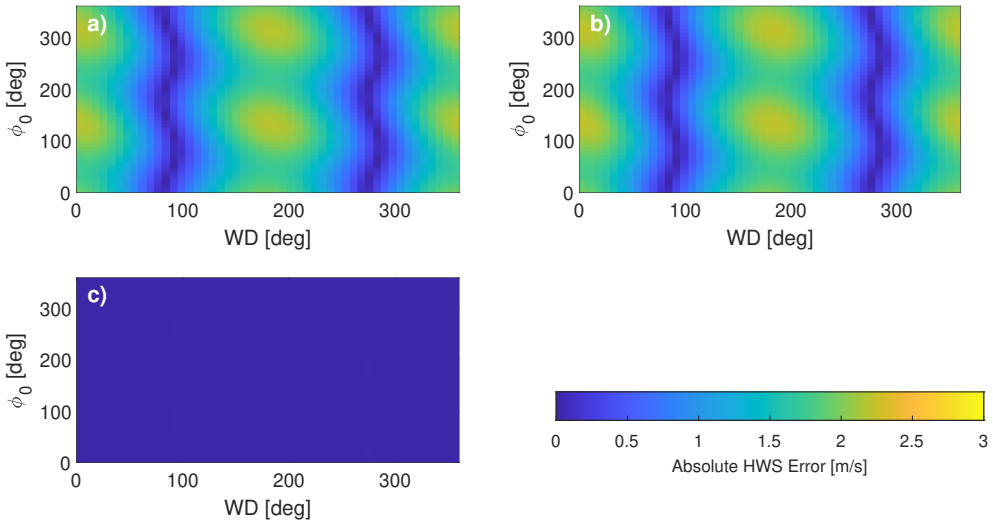


Figure 6.6: Validation of the analytical-error formulation in translational-only scenario #2: *HWS error* (parameters: $A_{surge} = 10$ deg, remaining parameters and panel labels same as in Figure 6.5).

When addressing *translational-only scenario* #2 (Figure 6.6), null differences (0 m/s) were found in Figure 6.6c between the analytically and the simulator-estimated error. The exact 0 m/s error difference is explained by the fact that no approximations were used when deriving the analytical expressions for the translational-motion component.

Opposite to other floating remote-sensing devices such as high-frequency surface-wave radars, which measure the horizontal propagation of waves and thus are not sensitive to heave-induced Doppler effect [Yao et al. 2021, Wan et al. 2022], the ZephIR$^{TM}$ 300 FDWL is sensitive to all three translational motion components due to its inherent conical scanning pattern [Slinger & Harris 2012].

Finally, successful performance of the unified formulation presented for the analytically estimated error is re-encountered in Figure 6.7, where both translational and rotational motion were combined into 6-DoF motion *scenario #3.* Despite the greater complexity of this scenario, error differences (Figure 6.7c) remained below 0.7 m/s. The RMSE was 0.22 m/s.

### 6.4.2 Experimental results

The unified-error formulation (Section 6.3.5 and Appendix C) was also validated by comparing the analytically estimated HWS mean bias and TI increment (Equation 6.31 and Equation 6.33, respectively) against their experimental values (Equation 6.4 and Equation 6.6, respectively). Experimental values were computed from the 10 min errors between the FDWL and the reference fixed lidar used in both the nearshore ("Pont del Petroli") and open-sea (IJmuiden) scenarios. For

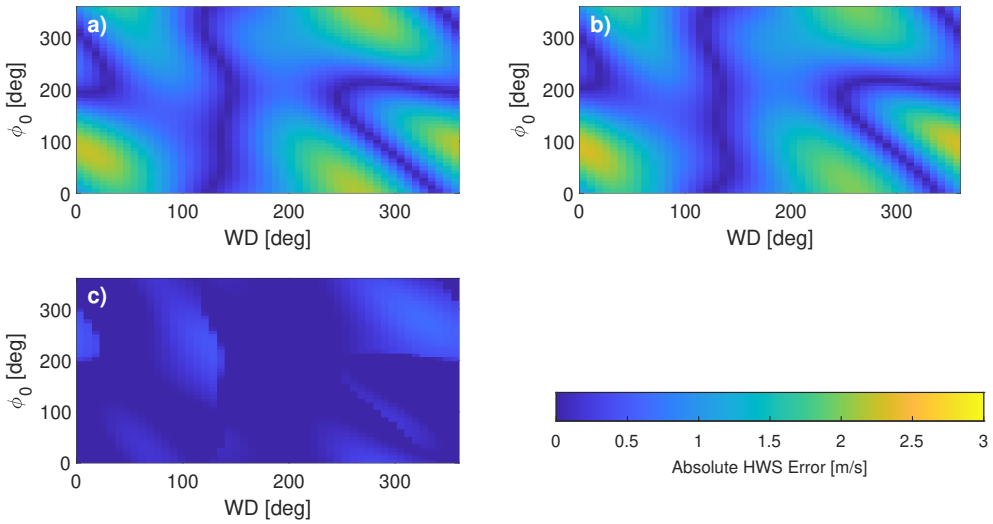


Figure 6.7: Validation of the analytical-error formulation in 6-DoF scenario #3: *HWS error* (parameters: $A_{roll} = A_{pitch} = 10$ deg, and $A_{surge} = A_{sway} = A_{heave} = 2$ m/s, remaining parameters and panel labels same as in Figure 6.5).

the IJmuiden campaign, measurements of the FDWL at 83 m and measurements of the metmast DWL at 92 m were considered. Towards this purpose, 848 data records (6 to 30 June 2013) from PdP campaign and 3893 data records (1 April to 7 May 2015) from IJmuiden campaign were used (see Section 6.2). Data were filtered for quality assurance following the outlier-rejection criteria presented by Salcedo-Bosch et al. (2021c): measured HWS values outside the 1-80 m/s range, rain-flagged data, Spatial Variation (SV) values higher than 0.2, and backscatter coefficients lower than 0.02 were removed. The SV is an indicator of the goodness of the VAD fitting of the measured LoS in a lidar scan [Wagner et al. 2009]. The backscatter coefficient is indicative of the power of the received lidar echo.

#### 6.4.2.1 Performance according to estimation of the HWS bias

In PdP campaign, using statistical analysis (figure not shown), the measured 10 min HWS bias (Equation 6.4) showed virtually nil values in accordance with previous results in nearshore locations in the state of the art [Kelberlau et al. 2020, Gutiérrez-Antuñano et al. 2017]. The median of the measured 10 min HWS bias was -0.02% with 25th and 75th percentiles of -0.89% and 0.76%, respectively. On the other hand, the analytically estimated 10 min HWS bias (Equation 6.5) showed values of the same order of magnitude as the measured one, thus validating the method. Thus, the median of the estimated bias was 0.06%, and the 25th and 75th percentiles were -0.66%, and 0.64%, respectively. The median bias is in accordance with the results obtained in other state-of-the-art studies [Kelberlau & Mann 2022].

In Ijmuiden campaign, the measured 10 min HWS showed higher values than the observed ones in "Pont del Petroli" campaign: the median of the measured 10 min HWS bias was -0.53% with 25th

and 75th percentiles of -2.30% and 1.08%, respectively (and notice the asymmetrical distribution of these percentiles around 0%). These values are in accordance with previous open-sea measurement campaigns [Gottschall et al. 2012a; 2014a]. This is due to the fact that in an open-sea scenario there is stronger wave motion, which induces higher error on FDWL measurements. The above-mentioned asymmetry on the measured biases accounts for the wind shear between the fixed DWL and FDWL measurement heights (92 and 83 m, respectively). The analytical model estimated biases of the same order of magnitude as the measured ones with a median of 0.05%, and 25th and 75th percentiles of -1.48% and 1.47%, respectively, which further validates the analytical model.

#### 6.4.2.2 Performance according to estimation of the TI increment (I): case example

As part of the validation study, in the next case example, the *analytically estimated* 10 min TI increment, $\Delta TI_{est}$ (Equation 6.33), is compared with the *measured* one, $\Delta TI_{meas}$ (Equation 6.7). The different motion conditions studied are described as a function of the *mean tilt amplitude* and *mean translational-velocity amplitude* of the lidar buoy:

The *mean tilt amplitude* is computed as the 10 min mean of the quadratic sum of roll and pitch tilts (simple harmonic motion, Equation 6.19) [Kelberlau et al. 2020]. It can be formulated as follows:

$$\overline{A_{tilt}} = \frac{\sum_{k=1}^{N} \sqrt{\Omega_{roll}(k)^2 + \Omega_{pitch}(k)^2}}{N}, \tag{6.35}$$

where $\Omega_x$, $x = rollpitch$ is the IMU-measured roll/pitch tilt, $N = 6000$ is the number of samples in a 10 min interval at 10 Hz IMU-sampling frequency, and $k$ is a reminder of discrete time $t_k$.

The *mean translational-velocity amplitude* is computed as the 10 min mean norm of the FDWL translational-velocity vector,

$$\overline{A_{v_{trans}}} = \frac{\sum_{k=1}^{N} ||\vec{t}(k)||}{N}, \tag{6.36}$$

where $\vec{t}(k)$ is the translational-velocity vector defined by Equation 6.26.

Figure 6.8a compares the estimated TI-increment time series ($\Delta TI_{est}$) with the measured one ($\Delta TI_{meas}$) in the context of PdP campaign. The motion-induced error on the FDWL-measured TI manifested as TI increments between 0.5 and 5%. The highest TI increments occurred during the daytime (from 10 a.m. to 4 p.m., approximately), corresponding to time periods with high HWSs. These periods were also related to high wave motion [Gutiérrez-Antuñano et al. 2017, Jeffreys & Taylor 1925]. This is corroborated in Figure 6.8b, where the mean tilt amplitude and mean translational-velocity amplitude of the floating lidar are depicted as time series. It can be observed that high TI-increment values in Figure 6.8a were linked to high-motion scenarios, i.e., to time periods with high tilt and velocity amplitudes in Figure 6.8b.

In Figure 6.8a, the estimated TI increment exhibited similar values as the measured one over the period under study. The 1-hour-averaged time series further shows the goodness of the TI-increment estimates. However, small underestimation of the peak values occurred. Thus, while

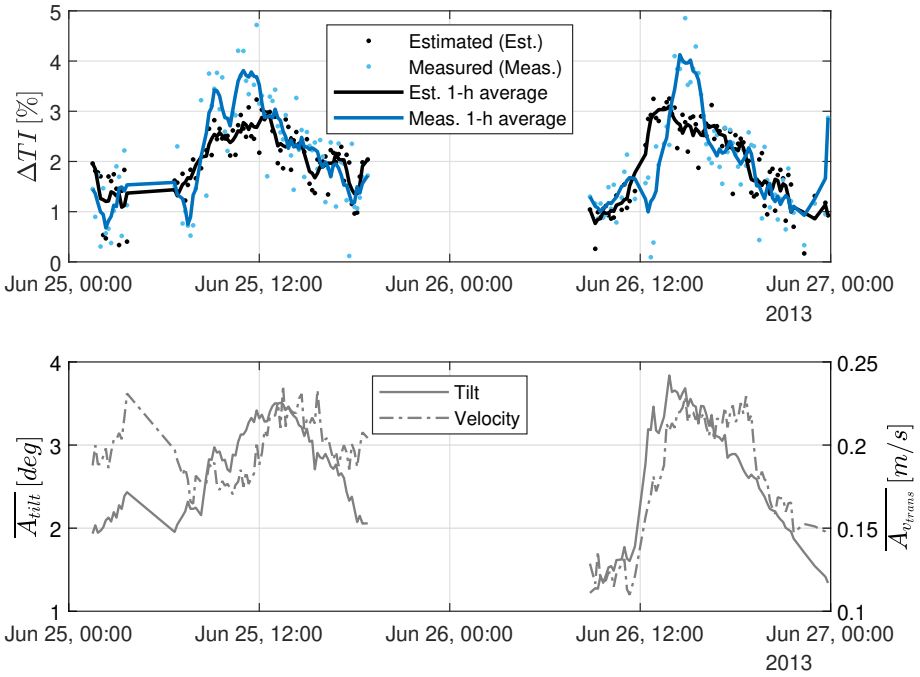


Figure 6.8: Validation of the analytical-error formulation in a real case scenario (PdP campaign, 25 June 2013, 00:00 UTC to 27 June 2013, 00:00 UTC): *TI increment. (a)* Analytically estimated vs. measured TI-increment time series. Black dots are 10 min analytically estimated TI increment, $\Delta TI_{est}$ (Equation 6.7). Blue dots are 10 min measured TI increment, $\Delta TI_{meas}$ (Equation 6.6). *(b)* Mean tilt amplitude (Equation 6.35) and mean translational-velocity amplitude (Equation 6.36) time series. In both panels, the solid trace represent 1 h averaged time series.

the measured TI increment peaked at 5% close to noon time, the estimated one only reached 3.5%. Larger differences were observed in one-to-one comparisons of the 10 min estimates with the 10 min measurements. A suitable explanation for this is that in the unified formulation presented in Section 6.3.5.3, wind flow during 10 min periods is assumed to be uniform, and only the motion influence is considered. As the lidars were located 50 m apart, wind scenarios with high spatial variability (e.g., turbulent winds coming from the urban area, Section 6.2) usually led to different instantaneous measurements between the floating and the reference lidar. Therefore, correlation coefficients $\rho_{F,R} < 1$ ( Section 6.3.2.1), which may limit the validity of the estimates, $\Delta TI_{est}$. This effect may also occur in low-motion scenarios [Salcedo-Bosch et al. 2021c].

### 6.4.3 Performance on the estimation of the TI increment (II): statistical analysis

Performance of the analytical-error formulation when estimating the 10 min TI increment was also assessed with reference to the FDWL-measured TI increment under near-shore and open-sea motional scenarios (PdP and IJmuiden campaigns, respectivley). The statistical sample consisted of 848 data records (from 6 to 30 June 2013) for PdP campaign and 3893 data records (from 1 April to 7

May of 2015) for IJmuiden campaign. The estimated and the measured TI increments ($\Delta TI_{est}$ and $\Delta TI_{meas}$, respectively) for the whole campaign were clustered as a function of the wind intensity, using the *HWS* as the binning variable, and as a function of the type of motion (i.e., rotational or translational) using the *mean tilt amplitude* and *mean translational-velocity amplitude* as the respective binning variables.

The estimation accuracy was quantitatively assessed according to the RMSE, which is formulated as follows:

$$RMSE = \sqrt{\frac{\sum_{p=1}^{N}[\Delta TI_{est}(p) - \Delta TI_{meas}(p)]^2}{N}}, \tag{6.37}$$

where $N$ is the number of samples in the bin under study, $\Delta TI_{est}(p)$ is the *p-th* TI-increment estimate in the bin, and $\Delta TI_{meas}(p)$ is the corresponding *p-th* measurement.

Figure 6.9 depicts the statistical results for PdP (left panels) and IJmuiden (right panels) campaigns. In all panels, it can be observed that the TI increment, $\Delta TI$, was always positive, evidencing the motion-induced additive turbulence [Salcedo-Bosch et al. 2020a, Kelberlau et al. 2020]. Moreover, it increased with increasing wave motion, i.e., with increasing mean tilt amplitude (panels (a), (b)) and mean translational-velocity amplitude (panels (c), (d)). $\Delta TI$ ranged from median values of $\Delta TI \simeq 1\%$ in low-motion scenarios to $\Delta TI \simeq 2\%$ in high-motion ones. The green bars illustrating statistically significant bins (i.e., bins containing greater or equal than 5% of the population of PdP campaign, i.e., $\simeq 50$ samples) showed mean tilt amplitudes between 1 and 3.5 deg for PdP campaign and between 1 and 5.5 deg for IJmuiden campaign (notice the different X-axis ranges used). The observed mean translational-velocity amplitudes ranged between 0.1 and 0.2 m/s for PdP campaign, and between 0.1 and 0.65 m/s for IJmuiden campaign (notice the different X-axis ranges used). The HWS ranged between 2 and 8 m/s in PdP campaign, and between 2 and 22 m/s in IJmuiden campaign (notice the different X-axis ranges used). The higher motion and wind magnitudes evidence the harsher scenario experienced by the FDWL during IJmuiden campaign.

On one hand, Figure 6.9a)-b) plot the TI increment as a function of the mean tilt amplitude in 0.5 deg bins, which is representative of the *rotational-motion* component. The median of the estimated $\Delta TI$ values virtually matched that of the measurements, thus validating the overall analytical-error formulation. In PdP campaign (Figure 6.9a)), error bars showed larger dispersion for the measured values ($\Delta TI_{meas}$) than for the estimated ones ($\Delta TI_{est}$). This is attributable to the urban topology surrounding the experimental area, which creates high spatial variation of the wind field. In contrast, this was not found in IJmuiden. Thus, Figure 6.9b)-d)-f) shows estimated error bars virtually coincidental with the measured ones on account of the more homogeneous wind fields found over the ocean.

On the other hand, Figure 6.9c)-d) represent the TI increment as a function of the FDWL mean *translational* velocity in 0.025 m/s bins for PdP campaign and 0.05 m/s bins for IJmuiden campaign, respectively. Similar to Figure 6.9a)-b), the median of the estimated $\Delta TI$ values almost ideally

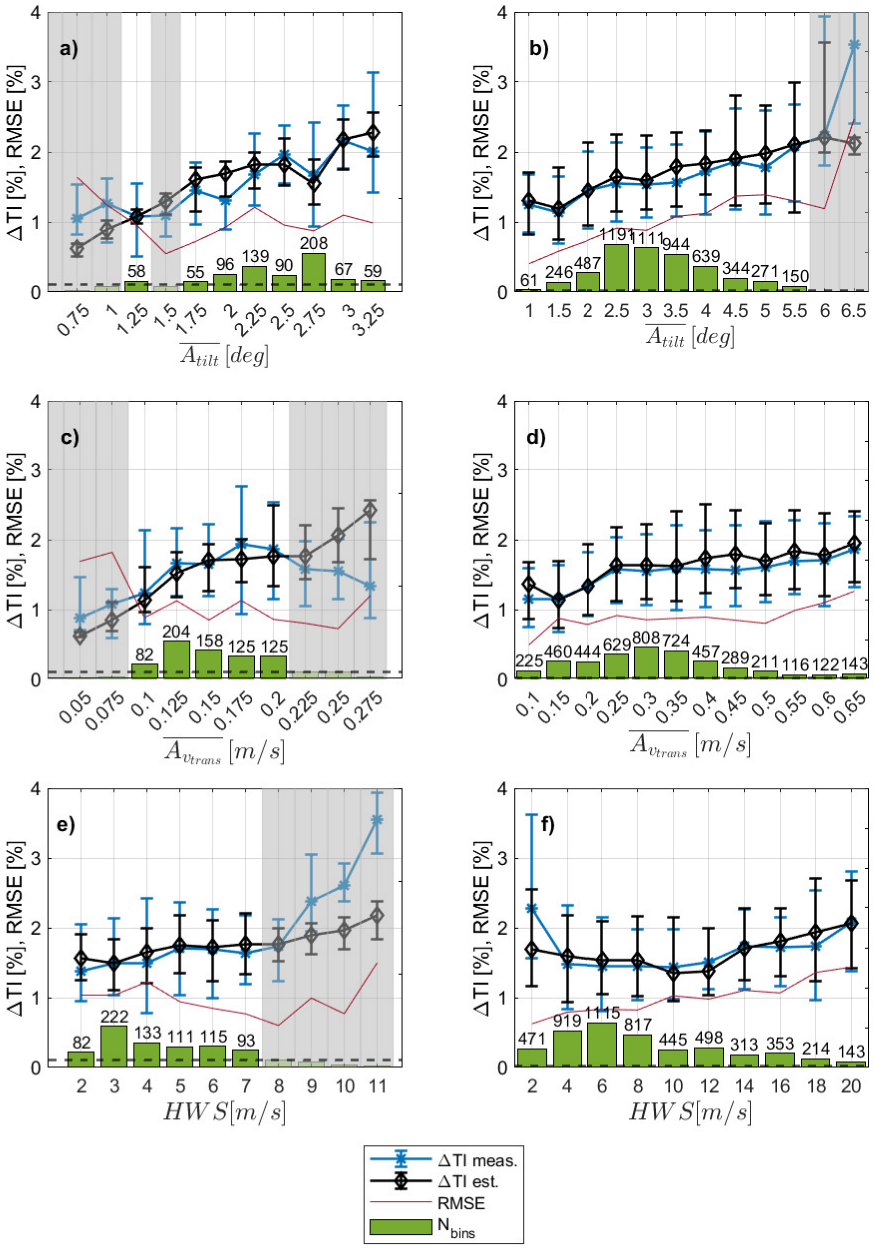


Figure 6.9: Validation of the analytical-error formulation: *Global statistics for the PdP campaign (6 to 30 June 2013) and IJmuiden campaign (1 April to 1 June 2015).* Left panels show the results obtained for the PdP campaign, and right panels show the results obtained for IJmuiden campaign. Comparison between the measured and the estimated TI increment as a function of different motion conditions clustered by (panels **a, b**) *mean tilt amplitude* (rotational motion), (panels **c, d**) *mean translational-velocity amplitude*, and (panels **e,f**) *mean HWS*. Error bars indicate the 25th and 75th percentiles. Bar graphs represent the number of occurrences in the data for each category bin. Solid red lines represent the RMSE between $\Delta TI_{est}$ and $\Delta TI_{meas}$ for each category bin. Bins containing less than 5% of the PdP population are gray shaded.

matched the measurements in all the significant bins (dark green, Figure 6.9c)-d)). The largest difference was $\Delta TI_{meas} - \Delta TI_{est} = 0.26\%$ for the 0.175 m/s bin. Similar comments apply to those for Figure 6.9a)-b) regarding the measurement error bars.

Finally, Figure 6.9e)-f) depict the TI increment as a function of the mean HWS in 1 m/s bins for PdP campaign and 2 m/s for IJmuiden campaign, respectively. Similar concurrent results are observed, with the estimated $\Delta TI$ median values matching the measurements for all HWS bins except for the 2 m/s one. This is due to the fact that ZephIR$^{TM}$ 300 HWS measurements below 3 m/s are tagged as "unreliable" according to the manufacturer's specs for the lidar [Scientific 2016]. Similar discussion comments apply for the error bars shown in Figure 6.9 e)-f).

The RMSE between the estimated with the measured $\Delta TI$ (Equation 6.37) is depicted in red for each of the tilt, velocity, and HWS bins. Similar values were obtained in all statistically significant bins, ranging from $RMSE = 0.004$ (0.4%) up to $RMSE = 0.013$ (1.3%), which is comparable to (and, therefore, consistent with) the size of the measurement error bars obtained for $\Delta TI_{meas}$. As can be observed, the RMSE is slightly correlated with the tilt so that the larger the buoy tilt, the larger the RMSE in rough approximation, which in turn accounts for the 1st-order approximation used in Equation C.1 (refer to Appendix C.1).

## 6.5 Summary and Conclusions

A *unified analytical formulation* for the computation of the 6-DoF-motion-induced error in focusable CW FDWLs was presented (Figure 6.3). The total error in the retrieved HWS was computed as the superposition of rotational- and translational-motion errors. The formulation proved to be capable of estimating the HWS bias (Section 6.4.2.1) and TI increment (Figure 6.8, and Figure 6.9).

The analytical model departed from a thorough formulation of the FDWL buoy geometry and dynamics in order to derive the rotational- and translational-motion influence on the lidar-measured LoS measurements in a CW DWL scan. The well-known VAD algorithm was computed as a first-order Fourier series, which allowed derivation of the sought-after analytical expressions describing the FDWL-measured wind-vector error as a function of the buoy attitude and the "true" wind vector. First-order approximation was retained when computing the buoy rotational matrix. The assumption of a uniformly distributed random initial scan phase permitted the estimation of the HWS measurement bias and RMSE over 10 min time intervals.

The wave-induced motion in each of the six DoF was modeled as a simple harmonic motion with a characteristic amplitude, frequency, and phase recomputed every 10 minutes for each DoF. A method to estimate these variables based on spectral analysis of the lidar-buoy motional time series was presented in Section 6.3.7.

The proposed formulation was numerically validated by comparing the HWS error figures obtained as a function of WD and initial scan phase with those output by the FDWL-motion simulator

[Salcedo-Bosch et al. 2021a]. A virtually perfect match between both methods was found except for the second-order approximation errors.

The methodology was further validated using experimental data from "Pont del Petroli" (Badalona, Barcelona) and IJmuiden (North sea, 85 km offshore the Netherlands) campaigns, in which an FDWL and a reference fixed lidar were used. The estimated 10 min bias using the analytical formulation presented here yielded similar results to the measured one. Thus, for the PdP campaign, the median values obtained for the estimated and the experimental HWS bias were -0.02% and 0.06%, respectively, and the 25th and 75th percentiles were -0.66% (estimated) and -0.89% (measured); and 0.76% (measured) and 0.64% (estimated), respectively. For the IJmuiden campaign, median values of -0.53% (measured) and 0.05% (estimated) were found, and the 25th and 75th percentiles were -2.30% (measured) and -1.48% (estimated); and 1.08% (measured) and 1.47% (estimated), respectively. The inherent asymmetry between positive and negative biases accounts for wind shear between the fixed DWL and FDWL measurement heights. The slight differences between the measured and estimated values are inconsequential and account for the harsher sea conditions at the IJmuiden site. With regard to estimation of the TI increment, the analytical estimates matched the measured values in statistical terms under all motion and wind scenarios for both PdP and IJmuiden campaigns (Figure 6.9). Thus, the root mean square differences between the medians of $\Delta TI_{est}$ and $\Delta TI_{meas}$ were 0.16% (PdP) and 0.11% (IJmuiden) for the rotational motion (Figure 6.9a), b)), 0.13% and 0.16% for the translational motion (Figure 6.9c), d)), and 0.14% and 0.21% for the HWS (Figure 6.9e), f)), given mean values of about 0.015 (1.5%). Experimental validation was limited by the fact that the intercompared lidars were a minimum of 50 m apart and subject to wind flows that were not always uniform. This caused moderate dispersion in the turbulence values measured by the two lidars, which deteriorated in one-to-one comparison of the 10 min TI.

All in all, the unified formulation presented here proves to be a straightforward and accurate tool for evaluating the motion-induced error in focusable CW FDWLs in terms of both HWS-bias and TI-increment estimation, which is additive to the real one. Although the proposed method enables to correct the FDWL-measured TI (i.e., the apparent TI) via subraction of the estimated TI increment to the lidar-measured one, the accuracy of this methodology on a 10-min basis will be studied in future work. $Matlab^{TM}$ R2020a codes are also provided to the reader as part of the *Supplementary Materials* of this manuscript. Further steps could include the study of multi-modal motion as well as the wind flow variability in a lidar scan. Finally, experimental validation would benefit from tests at different LiDAR sounding heights.

# Chapter 7

# A Robust Adaptive Unscented Kalman Filter for Floating Doppler Wind Lidar Motion Correction

*The contents of this Chapter are aligned with Obj. 2 of this Ph.D. and are part of the full paper [Salcedo-Bosch et al. 2021c]:* ***Salcedo-Bosch, A.****; Rocadenbosch, F.; Sospedra, J. "A Robust Adaptive Unscented Kalman Filter for Floating Doppler Wind-LiDAR Motion Correction", Remote Sens. 2021, 13, 4167.* `https://doi.org/10.3390/rs13204167`. *Systematic or multiple reproduction or distribution to multiple locations via electronic or other means is prohibited and is subject to penalties under law*

## 7.1 Introduction

As it has been exposed in Chapter 2, multiple validation campaigns have shown the robustness and reliability of HWS and WD FDWL measurements at the ten-minute level [Gutiérrez et al. 2015, Gutierrez-Antunano et al. 2017, Schuon et al. 2012, Mathisen 2013, Gutiérrez-Antuñano et al. 2018]. However, FDWLs measure an increased TI, in contrast to fixed LiDARs, due to wave-induced motion [Salcedo-Bosch et al. 2020a, Courtney & Hasager 2016].

TI is a relevant parameter in wind farm design and operation [Mücke et al. 2011]. For instance, erroneous TI could lead to over-design of the wind turbines, causing extra costs. Therefore, there is a need to compensate for the effect of wave-induced motion on FDWL measurements [Gottschall et al. 2017a; 2014b]. Both the rotational motion (roll, pitch, and yaw) and translational motion (surge, sway, and heave) of the LiDAR induce errors in the retrieved HWS and WD [Tiana-Alsina et al. 2017, Kelberlau et al. 2020]. The latter is of lesser concern because WD errors can easily be corrected by means of a reference compass installed on the buoy [Gutiérrez-Antuñano et al. 2017].

Multiple approaches have been presented for reduction of the motion-induced error in FDWL measurements [Wolken-Möhlmann et al. 2010, M. Pitter et al. 2014, Tiana-Alsina et al. 2015, Gutiérrez-Antuñano et al. 2017, Kelberlau et al. 2020, Salcedo-Bosch et al. 2021c, Gutiérrez-Antuñano et al.

2018, Bischoff et al. 2015, Gottschall et al. 2014a; 2012b, Schlipf et al. 2012]. Thus, the works of Wolken-Möhlmann et al. (2010) and Gottschall et al. (2014a) are representative of the first studies on the simulation and offshore tests of lidars on floating platforms. Schlipf et al. (2012) demonstrated the potentialities of theoretically modeling a lidar system in order to reconstruct the wind field from corrupted lidar measurements. Regarding the ZephIR lidar, M. Pitter et al. (2014) studied its performance when mounted on buoys or wind turbines and proved that the 10-min averaged wind speed recorded by ZephIRs is very resilient to motion. It was also found that angular motion is the main error source. The study of Bischoff et al. (2015) addressed the motion compensation of FDWLs by means of a wind field reconstruction method and demonstrated that the quality of horizontal wind measurements can be improved if the lidar attitude is known. Tiana-Alsina et al. (2015) presented a mechanical approach by deploying the ZephIR-300 lidar on a cardanic frame. This method was able to compensate for most of the rotational motion but not for the translational one. However, mechanical resonance was a risk to be minimized and the cardarnic method increased the hardware costs of the instrument.

More recently, Gutiérrez-Antuñano et al. (2017) presented an adaptive averaging window technique to filter out the motion-induced errors on $HWS$ measurements. The window length has to be comparable to the tilting period of the lidar (roll and pitch motion only). Unfortunately, this method requires the lidar wind-vector sampling frequency to be higher (approximately by a factor 2) than the wave motion frequency, which is not always the case. In 2020, Kelberlau et al. (2020) proposed a signal processing approach, in which the 6-DoF motion of the FDWL were taken into account to correct for the motion-induced error at a Line of Sight (LoS) level. The algorithm demonstrated itself able to take the motion out in multiple wind and sea scenarios in a coastal environment but it requires access to the high-frequency internal LoS measurements of the lidar. The latter is usually undisclosed information for most commercial continuous-wave lidars.

In this study, we aim to correct the motion-induced error on wind measurements by a floating continuous-wave conical-scanning DWL without accessing LoS information. We rely on the fact that successively measured wind observations tend to be correlated and that past measurements provide a priori information on the wind vector at the current estimation time [Mann 1998, Brown et al. 1984]. Moreover, the LiDAR measurement process and the wave-induced 6-DoF LiDAR motion can be accurately modelled. In this scenario, the Kalman Filter (KF) is considered to be a promising candidate for tackling this problem. The KF is used to estimate discrete time-series, which are governed by linear differential operators [Rodgers 2004]. It can estimate the hidden variables of a dynamic system from observations over time.

In non-linear systems, as in our case, the plain KF is not adequate to solve the problem. Instead, upgrades of the KF, such as the Extended Kalman Filter (EKF) or the Unscented Kalman Filter (UKF) [Robert Grover & Y.C. Hwang 2012], are used. In this study, we present a Robust Adaptive

Unscented Kalman Filter (RAUKF) based on the FDWL model proposed by Kelberlau et al. [Kelberlau et al. 2020], to estimate the LiDAR-retrieved wind vector without motion influence. We rely on the FDWL geometrical model and the Velocity–Azimuth Display (VAD) LiDAR wind-retrieval algorithm [Slinger & Harris 2012].

Filter performance is assessed using experimental data from the "El Pont del Petroli" (PdP) campaign (see Chapter 3), in which a proof-of-concept FDWL buoy was compared, with reference to a fixed LiDAR [Gutiérrez-Antuñano et al. 2017]. This allowed us to compare the motion-corrected FDWL TI to the fixed-LiDAR reference TI.

## 7.2 Materials and Methods

### 7.2.1 Instrumental Setup Review

For this study, data from "Pont del Petroli" campaign (see Chapter 3) was used. The main parameters used were: (i) wind measurements from the reference ZephIR$^{TM}$ 300 DWL deployed at "Pont del Petroli" pier, (ii) wind measurements from the NEPTUNE$^{TM}$ floating LiDAR buoy, (iii) ZephIR$^{TM}$ 300 internal parameters for data-quality control and (iv) 6-DoF motion measurements captured by the "LiDAR IMU" and the "buoy IMU".

### 7.2.2 Basic Theoretical Definitions

In this chapter, the wind vector, $\boldsymbol{U}$, is defined as a three-component vector formed by the HWS, WD (clockwise from north), and vertical wind speed (VWS), as

$$\boldsymbol{U} = \begin{bmatrix} HWS \\ WD \\ VWS \end{bmatrix}. \tag{7.1}$$

In wind energy, a standard sampling period of 10 min was used. The mean wind conditions at this resolution were obtained by simply averaging the high-resolution (1 s) wind-vector components into a 10 min period. Thus, the mean *HWS* was computed as

$$\overline{HWS} = \frac{1}{N}\sum_{n=1}^{N} HWS_n, \tag{7.2}$$

where $HWS_n$ is the high-resolution *HWS* measurement and $N = 600$ is the number of 1 s measurements in one minute.

We are also interested in the *HWS* variations, with respect to the mean *HWS*. This variability was measured by means of the *TI*, which is defined as

$$TI = \frac{\sigma_{HWS}}{\overline{HWS}}, \tag{7.3}$$

where $\sigma_{HWS}$ is the 10 min *HWS* standard deviation. The standard deviation is defined as

$$\sigma_{HWS} = \sqrt{\frac{1}{N-1}\sum_{n=1}^{N}(HWS_n - \overline{HWS})}. \tag{7.4}$$

### 7.2.3 The Estimation Viewpoint

The KF relies on two steps to estimate the hidden state-vector of the physical system under study: The prediction step and the innovation step [Rodgers 2004].

The *prediction step* is defined by two equations, which are formulated in state-space notation as

$$\boldsymbol{x}_{k|k-1} = f(\boldsymbol{x}_{k-1|k-1}) + \boldsymbol{v}_k, \tag{7.5}$$

$$\boldsymbol{z}_{k|k-1} = h(\boldsymbol{x}_{k|k-1}) + \boldsymbol{n}_k. \tag{7.6}$$

The first equation is the *prediction equation*, in which $\boldsymbol{x}_{k|k-1}$ is the hidden state-vector to be estimated, based on the previous state-vector estimate, $\boldsymbol{x}_{k-1|k-1}$. Sub-indices $n|m$ denote estimation at the discrete time instant $n$, conditioned to all available information up to time $m$. Here, $\boldsymbol{x}_{k|k-1}$ is the motion-free wind vector to be estimated, based on previous wind-vector estimations. $f(\cdot)$ is the state-transition function predicting the state-vector at discrete time $k$, $\boldsymbol{x}_{k|k-1}$, given previous knowledge of the state-vector, $\boldsymbol{x}_{k-1|k-1}$; that is, $f(\cdot)$ describes the stochastic wind model (to be found) that predicts the measured wind vector at the next time step from the wind vector at the previous one. $\boldsymbol{v}_k$ is the process noise. The temporal resolution is the scan period (1 s approximately, see Section 7.2.4).

The second equation is the *measurement equation*, which estimates the present-time measurement, $\boldsymbol{z}_{k|k-1}$, given the *a priori* state-vector, $\boldsymbol{x}_{k|k-1}$, and motion information (to be further developed in Section 7.2.6), through the measurement function $h(\cdot)$. In other words, the measurement function models the FDWL motion dynamics and estimates the expected motion-corrupted wind measurements, based on the *a priori* state-vector and IMU motion information vector $\boldsymbol{M}$ (to be defined in Section 7.2.6). $\boldsymbol{n}_k$ is the measurement noise.

On the other hand, the *innovation step* allows for the assimilation of the present-time measurement information into the a priori state-vector estimate through a projection gain (the so-called Kalman gain). Formally,

$$\hat{\boldsymbol{x}}_{k|k} = \boldsymbol{x}_{k|k-1} + \boldsymbol{K}_k(\boldsymbol{z}_k - \boldsymbol{z}_{k|k-1}), \tag{7.7}$$

where $\boldsymbol{z}_k$ is the wind-vector measurement and $\boldsymbol{K}_k$ is the Kalman gain matrix. The latter relates the measurement estimation error, $\Delta\boldsymbol{z} = \boldsymbol{z}_{k|k} - \boldsymbol{z}_{k|k-1}$, to the a priori state-vector estimation error, $\Delta\boldsymbol{x} = \boldsymbol{x}_{k|k} - \boldsymbol{x}_{k|k-1}$.

To implement the UKF, both the state-transition wind model $f(.)$ and FDWL motion-dynamics measurement function $h(.)$ must be found. This is tackled in the following section.

### 7.2.4 The Measurement Model: FDWL Motion

The wind vector is retrieved from the Doppler wind projection along the LoSs in the conical scan pattern by means of the VAD algorithm (see Section 7.2.4.3). In real operating conditions of the

FDWL, sea-induced motion disturbs the conical scan, such that the pointing direction and measured radial velocities become affected by rotational and translational motion. In the motion-correction study by Kelberlau et al. (2020), a complete geometrical description of the problem is thoroughly given. Next, we summarize and adapt information from this reference which are relevant to derive the measurement function $h(.)$ shown in Equation (6) above.

To describe the FDWL system, we first define the right-handed Cartesian XYZ "moving-body" coordinate system of the buoy and the north–east–down right-handed Cartesian NED "fixed" global frame of reference (see Figure 7.1). The latter is the inertial frame of reference in which the wind vector and FDWL motion are defined. Without external influence, the X, Y, and Z axes of the moving-body coordinate system are aligned with the north, east, and vertically down vectors of the fixed NED frame of reference. Wind, waves, and external forces cause translational motion in the N, E, and D directions (surge, sway, and heave, respectively), and rotational motion along the N, E, and D axes (roll, pitch, and yaw, respectively). We define $\hat{x}$, $\hat{y}$, and $\hat{z}$ as unit vectors aligned with the X, Y, and Z axes of the moving-body coordinate system. On the other hand, $\hat{n}$, $\hat{e}$, and $\hat{d}$ are defined as the unit vectors aligned with the north, east, and vertically down axes of the global NED frame of reference. $\hat{h}$ is defined as the LiDAR beam direction before the prism deflection. The vector $\hat{h}$ is defined as the opposite vector to $\hat{z}$. The LoSs are measured in a cone of $\phi_0$-deg width from $\hat{h}$. Finally, we define $\theta_0$ as the LiDAR initial scan phase (i.e., the azimuth angle of the LiDAR pointing direction at the first LoS; denoted $\hat{r}_1$), with respect to $\hat{x}$ in the XY plane. During a scan, the LiDAR pointing direction $\hat{r}$ ranges from $\theta = -\theta_0$ to $\theta = -\theta_0 + 360 \times 1s$, with a fixed step $\Delta\theta$ between consecutive LoSs in a scan, which are denoted by $\hat{r}_n$ and $\hat{r}_{n+1}$, where $n$ is the LoS number.

#### 7.2.4.1 Rotational Motion

The rotational model (to be formulated as function $h_{rot}(\cdot)$ in Section 7.2.6) computes the "true" LiDAR pointing direction vectors by means of a series of geometrical operations. Rotational motion affects the LiDAR pointing direction in each LoS, $\hat{r}_n, n = 1, \ldots, 50$. A series of chained vector rotations (refer to Kelberlau et al. (2020), Equations (5)–(12)) are needed to *re-encounter $\hat{r}$ in the NED reference frame* (in the following, $\hat{r}$ will be used as shorthand notation for the vector set $\hat{r}_n, n = 1, \ldots, 50$). This is derived next:

The Euler rotation matrix is used to express $\hat{x}$, $\hat{y}$, and $\hat{z}$ in the NED frame of reference given roll, pitch, and yaw values (Kelberlau et al. (2020), Equations (5)–(7)). The unitary vector $\hat{h}$ in the direction of the laser beam, before it is deflected by the LiDAR prism, is computed as (Kelberlau et al. (2020), Equation (8)):

$$\hat{h} = -\hat{z}. \tag{7.8}$$

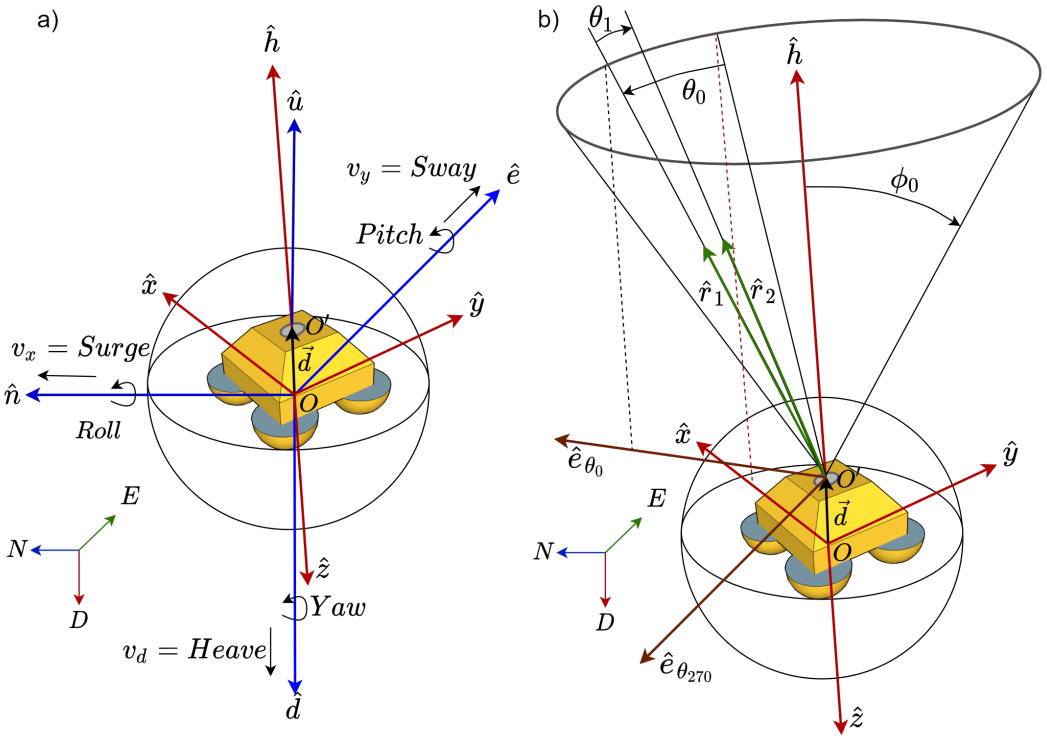


Figure 7.1: Schematic of the motion geometry of the FDWL buoy. (**a**) The moving-body coordinate system (red arrows) and the fixed coordinate system (blue arrows). (**b**) The LiDAR scanning cone and LiDAR pointing direction (green arrows) in relation to the XYZ coordinate system.

$\hat{e}_{\theta_0}$, which denotes the vector in the direction of LiDAR heading in the N-E plane (i.e., the azimuth angle of $\hat{r}_1$), is obtained by rotating $\hat{x}$ along $\hat{h}$ by $\theta$ deg, as:

$$\hat{e}_{\theta_1} = R(\hat{h}, \theta) \cdot \hat{x}, \tag{7.9}$$

where $R(\hat{h}, \theta)$ is the rotation matrix about $\hat{h}$ $\theta$ degrees (Kelberlau et al. (2020), Equation (9)). Then, auxiliary vector $\hat{e}_{\theta_{270}}$, defined as the unit vector perpendicular to $\hat{e}_{\theta_0}$ in the N-E plane, is encountered as (Kelberlau et al. (2020), Equation (10)):

$$\hat{e}_{\theta_{270}} = \hat{h} \times \hat{e}_{\theta_0}. \tag{7.10}$$

Finally, the first LiDAR pointing direction $\hat{r_1}$ can be expressed in the NED frame of reference by rotating $\hat{h}$ by $\phi_0$ deg along $\hat{e}_{\theta_{270}}$, as:

$$\hat{r}_1 = R(\hat{e}_{\theta_{270}}, \phi_0) \cdot \hat{h}. \tag{7.11}$$

The remaining LiDAR pointing directions in a scan, $\hat{r}_n, n = 2, \ldots, 50$ are obtained by changing the scan angle $\theta_0$ into $\theta_{n-1}$, with $n$ as above.

#### 7.2.4.2 Translational Motion

The translational model (formulated as function $h_{trans}(\cdot)$ in Section 7.2.6) computes the set of 50 LiDAR-measured, LoS radial velocities during a scan, $\boldsymbol{v}_{LoS}$. Translational motion also influences the measured LoS velocities. To study its effects, we need to account for all the velocity components at the position of the LiDAR scanning prism (origin of the scanning cone, $O'$ in Figure 7.1). First, we define $\vec{d}$ as the distance vector between the origin of the NED coordinate system ($O$ in Figure 7.1) and that of the scanning cone in the NED frame of reference ($O'$ in Figure 7.1). The velocity experienced at measurement location $O'$, $v_{\vec{lidar}}$, becomes influenced by both the translational velocities experienced by the LiDAR and rigid-body motion caused by the angular velocities. This composite effect can be expressed as (Kelberlau et al. (2020), Equation (14))

$$v_{\vec{lidar}} = \hat{n}v_n + \hat{e}v_e + \hat{d}v_d + (\hat{n}\omega_n) \times \vec{d} + (\hat{e}\omega_e) \times \vec{d} + (\hat{d}\omega_d) \times \vec{d}, \tag{7.12}$$

where $v_n$, $v_e$, and $v_d$ are surge, sway, and heave motions, respectively, and $\omega_n$, $\omega_e$ and $\omega_d$ are roll, pitch, and yaw angular velocities, respectively.

Finally, the translational velocity contribution into a LoS (Kelberlau et al. (2020), Equation (15)) is the projection of $v_{\vec{lidar}}$ onto $\hat{r}$ (Kelberlau et al. (2020), Equation (15)):

$$v_{LoS} = \hat{r} \cdot v_{\vec{lidar}}. \tag{7.13}$$

The radial velocity measured by the LiDAR along a LoS is encountered as the difference between the wind-vector projection over $\hat{r}$ and $v_{LoS}$, as:

$$v_r = \vec{U} \cdot \hat{r} - v_{LoS}. \tag{7.14}$$

#### 7.2.4.3 VAD Algorithm

The VAD model (formulated as $h_{VAD}(\cdot)$ in Section 7.2.6) retrieves the wind vector $\boldsymbol{U}$ from the measured LoS velocities, $\boldsymbol{v}_{LoS}$. Assuming a uniform wind field, the measured radial wind, as a function of the azimuth LiDAR scan angle, takes the form of a cosine wave [Slinger & Harris 2012] (see Chapter 2). The VAD algorithm uses the Least Squares (LSQ) method to fit a sinusoidal function to the measured radial velocities in the conical scan, $v_r$, at LoS azimuth angles $\phi$. Formally,

$$v_r(\phi) = |A\cos(\phi - B) + C|, \tag{7.15}$$

where $A$, $B$, and $C$ are the LSQ solving variables, which yield the wind-vector information as:

$$\begin{aligned} HWS &= A/\sin(\phi), \\ WD &= B \pm 180\, deg, \\ VWS &= C/\cos(\phi). \end{aligned} \tag{7.16}$$

The sign ambiguity in the WD is due to the ZephIR 300 homodyne LiDAR detection, i.e., the LiDAR can only measure unsigned Doppler frequency shifts, which leads to 180-deg ambiguity in the WD retrieved by the VAD algorithm [Slinger & Harris 2012]. This ambiguity is resolved by means of the wind vane installed on the buoy.

### 7.2.5 State-Transition Model

#### 7.2.5.1 Wind Model

The LiDAR-retrieved wind vector is a non-stationary stochastic process dependent on the atmospheric conditions [Smith & Mehta 1993]. For instance, the wind field gusty nature causes high wind speed increments during short time periods [Mücke et al. 2011]. Although physically rooted, advanced turbulent models describing the spectral tensor for atmospheric surface-layer turbulence [Mann 1998] provide a refined solution, their application is hampered by their complexity and demand for computational resources. Instead, we propose a straightforward and oversimplified approach, in which the wind process is modelled as a Random Walk (RW) stochastic process, in a similar fashion as what was used for the initial scan-phase model. It is formulated as:

$$\boldsymbol{U}_k = \boldsymbol{U}_{k-1} + \boldsymbol{\epsilon}_k, \tag{7.17}$$

where $\boldsymbol{\epsilon}_k$ is a random variable with zero-mean Gaussian distribution, $N(0, \sigma)$.

Figure 7.2 compares the HWS time-series estimated from the RW model (Equation (7.17)) to that measured by the fixed LiDAR. Figure 7.2a) demonstrates a similar dynamic range and process variability between both time-series, during most of the time. This is corroborated in Figure 7.2b), in terms of their associated Power Spectral Densities (PSD). Both PSDs were virtually coincident in the first spectral lobe (10 Hz cut off, $-15$ dB), indicating that RW modelling is a promising candidate for our estimation purposes. Discrepancies above 10 Hz were responsible for partial time-series tracking around sample nos. 150–200 in Figure 7.2a).

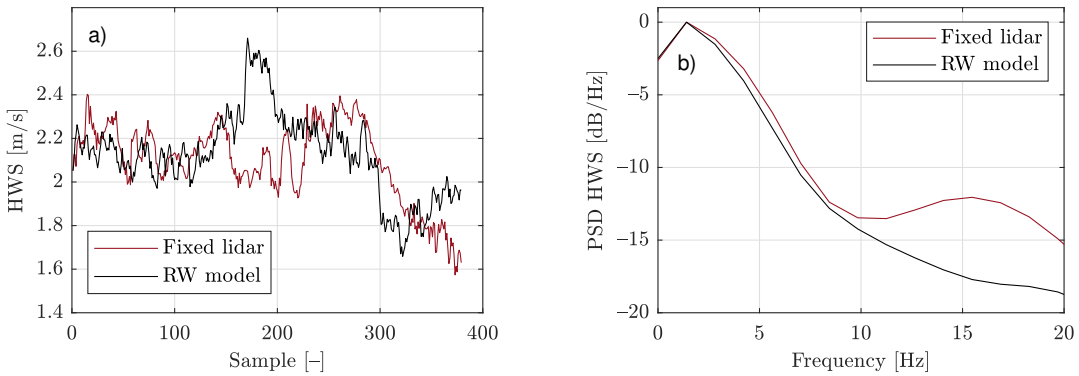


Figure 7.2: Comparison between the HWS RW model presented in Section 7.2.5.1 and experimental data: (**a**) Temporal series; and (**b**) PSD.

#### 7.2.5.2 Initial Scan-Phase Model

The LiDAR initial scan phase, $\theta_0$, has great influence on the measurement error and, therefore, is of key importance for LiDAR motion correction [Gutiérrez-Antuñano et al. 2018]. However, $\theta_0$ is an *undisclosed* parameter from the manufacturer's side, which needs to be estimated. In the motion-correction study by Gutiérrez-Antuñano et al. (2018), $\theta_0$ is considered a random variable with uniform probability density from 0 to 360 deg. Based on this assumption, the LiDAR initial scan-phase process is modelled as a RW process, as:

$$\theta_{0,k} = \theta_{0,k-1} + \epsilon_k, \tag{7.18}$$

where $\epsilon_k$ is a uniform random variable in $[0, 360)$ deg.

### 7.2.6 State-Space Formulation of the Problem

Once the measurement (Section 7.2.4) and state-transition *models* (Section 7.2.5) have been formulated, we aim to derive associated measurement and state-transition *functions* $h(.)$ and $f(.)$, respectively, in accordance with the state-space formulation presented in Section 7.2.3.

*State-transition function* $f(.)$.- To derive the state-transition function, first we considered the "clean" (i.e., motion-free) wind vector, $\boldsymbol{U}_k$, which is to be estimated from the motion-corrupted wind vector $\boldsymbol{U}_k^{FDWL}$ from the FDWL. The state-vector to be estimated, $\boldsymbol{x_k}$, is formed by the clean wind vector at time $k$, $\boldsymbol{U}_k$, and the LiDAR initial scan phase at that discrete time, $\theta_{0,k}$. This is formulated as

$$\boldsymbol{x}_k = \begin{bmatrix} \boldsymbol{U}_k^T & \theta_{0,k} \end{bmatrix}^T, \tag{7.19}$$

which using Equation (7.1), can be expanded to

$$\boldsymbol{x}_k = \begin{bmatrix} HWS_k & WD_k & VWS_k & \theta_{0,k} \end{bmatrix}^T. \tag{7.20}$$

By inserting the state-vector Equation (7.20) above, along with the RW models for the wind and initial scan-phase processes (Equations (7.17) and (7.18), respectively) into prediction Equation (7.5), we obtain

$$\boldsymbol{x}_{k|k-1} = \boldsymbol{I} \cdot \boldsymbol{x}_{k-1|k-1} + \boldsymbol{v}_k, \tag{7.21}$$

where $\boldsymbol{I}$ is the identity matrix. This enables us to identify state-transition function $f(\cdot)$, as:

$$f(\boldsymbol{x}_{k-1|k-1}) = \boldsymbol{I} \cdot \boldsymbol{x}_{k-1|k-1}. \tag{7.22}$$

In Equation (7.22) above, the state-vector is a 4-component vector, estimated at each successive LiDAR scan (i.e., with approximately 1 s temporal resolution). Recall that sub-indices $n|m$ refer to estimation at discrete time $n$, based on past information up to discrete time $m$.

*Measurement function* $h(.)$—The measurement equation (Equation (7.6)) predicts the *motion-corrupted* wind-vector $\boldsymbol{z}_{k|k-1}$ measured by the FDWL (i.e., the observation vector) from the estimated state-vector, $\boldsymbol{x}_{k|k-1}$. The observation vector is written as

$$\boldsymbol{z}_k = \boldsymbol{U}_k^{FDWL} = [HWS_{FDWL}, WD_{FDWL}, VWS_{FDWL}]^T, \tag{7.23}$$

where $HWS_{FDWL}$, $WD_{FDWL}$, and $VWS_{FDWL}$ are the FDWL measurements of HWS, WD, and VWS, respectively. $\boldsymbol{z}_k$ is a 3-component vector computed at each successive time scan.

As the measurement function $h(\cdot)$ is time variant depending on the attitude motion of the LiDAR, we define the motion block-vector $\boldsymbol{M}_k$ describing the 6-DoF motion of the FDWL during a scan as:

$$\boldsymbol{M}_k = [\boldsymbol{R}_k, \boldsymbol{P}_k, \boldsymbol{Y}_k, \boldsymbol{v}_{\boldsymbol{x}k}, \boldsymbol{v}_{\boldsymbol{y}k}, \boldsymbol{v}_{\boldsymbol{d}k}], \tag{7.24}$$

where $\boldsymbol{R}_k$, $\boldsymbol{P}_k$, $\boldsymbol{Y}_k$, $\boldsymbol{v}_{\boldsymbol{x}k}$, $\boldsymbol{v}_{\boldsymbol{y}k}$, and $\boldsymbol{v}_{\boldsymbol{d}k}$ are the roll, pitch, yaw, surge, sway, and heave time-series measured by the IMU at 10 Hz temporal resolution and interpolated at 50 Hz. Numerically, the block-vector $\boldsymbol{M}$ is a $50 \times 6$ matrix, where each row is a LoS attitude measurement, and each column is an attitude parameter.

Assuming uniform wind flow during the LiDAR scan at time $k$, the motion-corrupted FDWL observations in a scan can be described by a set of three successive operations (Section 7.2.4, and refer to Figure 7.3):

(i) retrieval of the motion-corrupted instantaneous LoS set, $\hat{\boldsymbol{r}}$;

(ii) estimation of the associated LoS velocities, $\boldsymbol{v}_{LoS}$; and

(iii) VAD retrieval of the motion-corrupted observation wind vector, $\boldsymbol{z}_{k|k-1}$;

where $\hat{\boldsymbol{r}}$ denotes the block-vector $[\hat{r}_1, \hat{r}_2, ..., \hat{r}_n]$, $n = 1, \cdots, 50$, and each component represents the $n$th LoS unit vector (Figure 7.1).

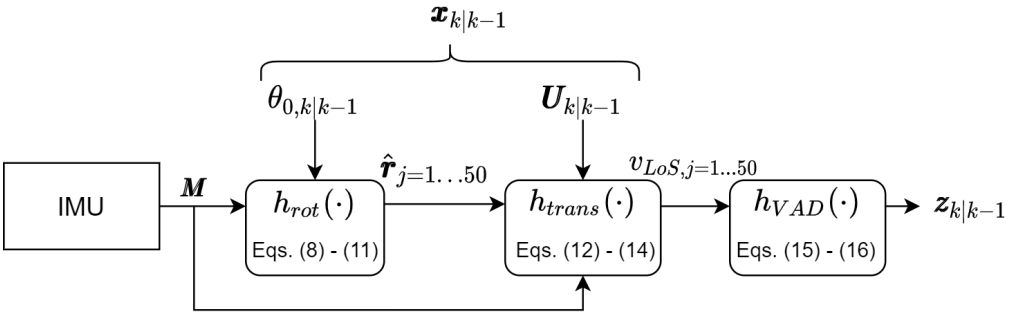


Figure 7.3: Block diagram depicting the measurement function $h(.)$, as a chain process in which rotation, translation, and VAD retrieval are modelled as elementary functions. Equation numbers inside each block refer to pertinent equations in the text.

Figure 7.3 block diagram depicts the filter measurement function $h(\cdot)$ as a chain calculus process:

First, at each discrete time $k$, the 50 motion-corrupted LoSs during the scan ($[\hat{r}_1, \hat{r}_2, ..., \hat{r}_n]$, $n = 1, \cdots, 50$) are computed by means of the geometrical operations presented in Section 7.2.4.1 (Equations (9)–(12)). This set of operations is denoted $h_{rot}(\cdot)$ in Figure 7.3. The function $h_{rot}(\cdot)$ computes the block-vector $\hat{\boldsymbol{r}} = [\hat{r}_1, \hat{r}_2, ..., \hat{r}_{50}]$ in the global NED frame of reference based on roll, pitch, and yaw instantaneous angles from attitude vector $\boldsymbol{M}_k$ and predicted initial phase $\theta_{0,k|k-1}$ from the state-vector, $\boldsymbol{x}_{k|k-1}$. Therefore, the block-vector $\hat{\boldsymbol{r}}$ can be written as

$$\hat{\boldsymbol{r}} = h_{rot}(\boldsymbol{x}_{k|k-1}, \boldsymbol{M}_k). \tag{7.25}$$

Second, the motion-corrupted LoS velocities at time $k$, $\boldsymbol{v}_{LoS,k}$, are calculated through the set of operations described in Section 7.2.4.2 (Equations (7.12) and (7.13)), and denoted $h_{trans}(\cdot)$ in Figure 7.3. Function $h_{trans}(\cdot)$ computes this set of velocities given the predicted wind vector, $\boldsymbol{U}_{k|k-1}$, the estimated LoS directions from the previous block, $\hat{\boldsymbol{r}}$, and by considering the influence of LiDAR translational and rigid-body motion information, through Equation (7.14) and Section 7.2.4.2, given $\boldsymbol{M}_k$. Then, $\boldsymbol{v}_{LoS,k}$ is obtained as

$$\boldsymbol{v}_{LoS,k} = h_{trans}(\boldsymbol{x}_{k|k-1}, \boldsymbol{M}, \hat{\boldsymbol{r}}). \tag{7.26}$$

Third, the motion-corrupted VAD-retrieved wind vector $\boldsymbol{z}_{k|k-1}$ is determined from the 50-LoS set of velocities, $\boldsymbol{v}_{LoS,k}$, by means of the least-squares VAD algorithm presented in Section 7.2.4.3 (Equations (7.15) and (7.16)). The VAD algorithm is denoted by $h_{VAD}(\cdot)$ in Figure 7.3. Hence,

$$\boldsymbol{z}_{k|k-1} = h_{VAD}(\boldsymbol{v}_{LoS,k}). \tag{7.27}$$

This chain calculus to compute measurement function $h(\cdot)$ can be formulated as the composition of $h_{rot}(\cdot)$, $h_{trans}(\cdot)$, and $h_{VAD}(\cdot)$ functions (through the so-called "chain rule"), as:

$$h(\cdot) = h_{VAD}(\cdot) \circ h_{trans}(\cdot) \circ h_{rot}(\cdot). \tag{7.28}$$

The time-variant observation model Equation (7.6) can be formulated as

$$\boldsymbol{z}_{k|k-1} = h(\boldsymbol{x}_{k|k-1}, \boldsymbol{M}) + \boldsymbol{n}_k. \tag{7.29}$$

### 7.2.7 Estimation of State- and Observation-Noise Covariance Matrices

To ensure convergent, unbiased estimates, the UKF must have *a priori* knowledge of both the process noise, $\boldsymbol{v}_k$, and measurement noise, $\boldsymbol{n}_k$. These are zero-mean, additive white Gaussian noise processes with covariances, $\boldsymbol{Q}_k$ and $\boldsymbol{R}_k$, respectively, which must be found.

The process-noise covariance matrix, $\boldsymbol{Q}_k$, is defined as

$$\boldsymbol{Q}_k = E[\boldsymbol{v}_k \boldsymbol{v}_k^T]. \tag{7.30}$$

Likewise, the measurement-noise covariance is defined as

$$\boldsymbol{R}_k = E[\boldsymbol{n}_k \boldsymbol{n}_k^T]. \tag{7.31}$$

As the measurement function $h(.)$ is time variant with the LiDAR motion vector $\boldsymbol{M}$, so is the measurement noise. Additionally, the wind statistical moments are not stationary, and the noise covariance matrices are difficult to accurately describe. Instead, we propose the adaptive estimation of these matrices based on statistical physical inference [Davari & Gholami 2017, Koivisto et al. 2016, Li et al. 2016]. In this study, the RAUKF [Zheng et al. 2018] is chosen, due to its low computational requirements, fast convergence, and overall good performance to adaptively estimate the noise covariances. Moreover, the RAUKF uses a fault-detection mechanism to detect filter failure due to inaccurate estimation of the noise covariance matrices. When a fault is detected, $\boldsymbol{Q}$ and $\boldsymbol{R}$ are adjusted (see Appendix D.3 for details).

In contrast to Equation (7.30), the RAUKF does not estimate $\boldsymbol{Q}$ as the ensemble average of $\boldsymbol{v}_k \boldsymbol{v}_k^T$ [WANG 1999, Hajiyev & Soken 2014]. A more straightforward approach is to estimate the matrix $\boldsymbol{Q}_k$ instantaneously (i.e., at each discrete time $k$), using the approximation $E[\boldsymbol{v}_k \boldsymbol{v}_k^T]$, and to balance it with previous estimates. As a further refinement, the RAUKF dynamically adjusts $\hat{\boldsymbol{Q}}_k$ by blending present and past estimates of the covariance matrix through a forgetting factor, $\lambda$, as:

$$\hat{\boldsymbol{Q}}_k = (1 - \lambda)\hat{\boldsymbol{Q}}_{k-1} + \lambda \boldsymbol{v}_k \boldsymbol{v}_k^T. \tag{7.32}$$

The RAUKF uses similar procedure as for $\hat{\boldsymbol{Q}}_k$, to compute the instantaneous estimations of $\boldsymbol{R}_k$ through a forgetting factor $\delta$, as:

$$\hat{\boldsymbol{R}}_k = (1 - \delta)\hat{\boldsymbol{R}}_{k-1} + \delta \boldsymbol{n}_k \boldsymbol{n}_k^T. \tag{7.33}$$

A similar memory-fading procedure has been used in the radar application of the filter for atmospheric boundary layer height estimation Lange et al. (2015). In practice, factors in the range 0.1–0.2 provided convergent, unbiased results, as shown in Section 7.3.

### 7.2.8 Filter Initialization

The UKF initial space vector takes the form

$$\hat{\boldsymbol{x}}_0 = [\boldsymbol{U}_0^{proxy}, \theta_{0,0}]^T, \tag{7.34}$$

where $\boldsymbol{U}_0^{proxy}$ is the "proxy" wind time-series and $\theta_{0,0}$ is initial scan phase, $\theta_0$, at time $k = 0$.

To initialize the filter, a 10 min length, moving-average time-series Gutiérrez-Antuñano et al. (2017) of the first 1 s-resolution wind measurements (the so-called "proxy" time-series, $\boldsymbol{U}_k^{proxy}$) is computed. The window length chosen is the wave period over the 10 min series, which is estimated

by means of the *L-dB* method [Salcedo-Bosch et al. 2021b] (see Chapter 5. Other wave-period estimation methods in the literature [Salcedo-Bosch et al. 2020b, Center 1996] yielded virtually identical results. The wind component of the state-vector is initialized by retaining the first-time sample of the proxy wind, $\boldsymbol{U}_k^{proxy}$. The initial scan-phase component of the state-vector is initialized with a random value between 0 and 360 deg, as dictated by the assumption of the *a priori* unknown uniform phase distribution.

The state-noise covariance matrix is linked to RW process noise $\boldsymbol{v}_k$ (Equation (7.5)). For simplicity, this matrix is assumed to be diagonal. At time $k = 0$, this matrix is written as

$$\boldsymbol{Q}_0 = diag(\begin{bmatrix}\sigma_{HWS}^2 & \sigma_{WD}^2 & \sigma_{VWS}^2 & \sigma_{\theta_0}^2,\end{bmatrix}), \tag{7.35}$$

where each component represents a variance.

As a RW process is characterized at each discrete time by incremental/detrimental random steps away from the previous value of the variable, $\sigma_{HWS}^2$, $\sigma_{WD}^2$, and $\sigma_{VWS}^2$ are estimated as the variance of difference between consecutive samples. For example, $\sigma_{HWS}^2$ is calculated from $\boldsymbol{U}^{proxy}$ as

$$\sigma_{HWS}^2 = E[(HWS_k^{proxy} - HWS_{k-1}^{proxy})^2], \tag{7.36}$$

where $E(.)$ is the expectancy operator (in practice, a 10 min window average). Process noise $\theta_0$ is initialized with the noise variance of a uniform distribution from 0 to 360 deg as

$$\sigma_{\theta_0}^2 = \frac{(b-a)^2}{12} = \frac{360^2}{12}, \tag{7.37}$$

where $a = 0$ and $b = 360$ deg are the lower and upper limits of the uniform distribution, respectively.

The measurement-noise covariance matrix at initial time, $k = 0$, is formulated as

$$\boldsymbol{R}_0 = diag(\begin{bmatrix}\sigma_{R,HWS}^2 & \sigma_{R,WD}^2 & \sigma_{R,VWS}^2\end{bmatrix}), \tag{7.38}$$

where the subscript $R$ is a remainder of covariance matrix $\boldsymbol{R}_k$ and $\sigma_{R,i}$, $i = HWS, WD, VWS$ is the estimated measurement-noise standard deviation for each of the variables. We used $\sigma_{R,HWS} = 0.05$ m/s, $\sigma_{R,WD} = 50$ deg, and $\sigma_{R,VWS} = 0.025$ m/s for the experimental data of Section 7.3. These measurement-noise standard deviations were roughly estimated from the 10 min proxy wind time-series, $\boldsymbol{U}_k^{proxy}$, used to initialize the filter. These values were deliberately low, to ensure the smooth start-up of the filter, hence preventing divergence.

Finally, the *a priori* error covariance matrix, $\hat{\boldsymbol{P}}_0^{xx}$, is initialized as

$$\boldsymbol{P}_0^- = \boldsymbol{Q}_0, \tag{7.39}$$

which indicates that the user's expected *a priori* error during initialization is comparable to the state-noise "nervousness" of the filter, $\boldsymbol{Q}_0$.

## 7.3 Results

The motion-compensation algorithm was tested on the PdP experimental campaign by comparing the FDWL with reference to the fixed LiDAR. This is discussed in the following:

### 7.3.1 Data Set

The data set used for validation of the motion-correction algorithm comprised data from 6 to 30 June of 2013, with both LiDARs measuring at a fixed height of 100 m; specifically, (i) wind-LiDAR data from the FDWL, (ii) FDWL internal status parameters, and (iii) 6-DoF motion measurements by two IMUs, one on the LiDAR instrument ("lidar IMU" in what follows) and another on the buoy ("buoy IMU"), were used.

Lidar internal status parameters were available, to assess the LiDAR status as well as to ensure the quality of the VAD-retrieved wind-vector measurements. These parameters include the Spatial Variation (SV), backscatter, and other system parameters. The SV parameter is a LiDAR internal parameter representing the turbulence intensity of the variation degree of the radial wind speeds (LoS) within the circle of scan of the LiDAR [Gutiérrez-Antuñano et al. 2017]. The SV can be understood as a goodness-of-fit parameter of the VAD algorithm which is used to retrieve the wind vector at a given height [Wagner et al. 2009, Slinger & Harris 2012]. By experiment, Gutiérrez-Antuñano et al. (2017) showed strong correlation between the wind TI and the SV values measured by a fixed ZephIR 300 LiDAR at 100 m in height (SV = 0.02 was approximately related to TI = 5% and SV = 0.1 to TI = 30% therein). The backscatter coefficient is an internal dimensionless parameter indicative of the intensity of the backscattered light return. By experiment, a backscatter threshold of 0.1 is reported in Gutiérrez Antuñano (2019) to distinguish between normal and low signal LiDAR returns.

Regarding the IMU data used for motion compensation, each of the IMUs was used for a different purpose: On one hand, the LiDAR IMU was used to measure rotational motion, as the LiDAR was mounted on the cardanic frame in such a way that its rotation center coincided with the LiDAR scan cone apex (location of the scanning prism; point $O$ in Figure 7.1). On the other hand, the buoy IMU was used to measure translational motion.

### 7.3.2 Data Filtering

Lidar-measured data from both the fixed and FDWLs required outlier removal, which encompassed 999X values (a label for system measurement error), too-high wind speed, and rain-flagged data.

The ZephIR 300 LiDAR has a wind measurement range of 1–80 m/s [Scientific 2016]. In high-motion scenarios, wind measurements by the FDWL exhibited high variances as compared to the

mean HWS. Ten-minute time-series with a HWS mean lower than 2.5 m/s were removed, to ensure reliable instantaneous HWS measurements [Gutiérrez-Antuñano et al. 2018]. Complex-terrain effects also cause non-negligible effects on the wind flow variability, which may well invalidate the assumption of uniform wind flow during the LiDAR scan [Bingöl et al. 2009]. Thus, metropolitan buildings along the coastline cause high spatial variability on the wind field [Al-Khalidy 2018], which demonstrates as a non-uniform wind vector along the LiDAR scanning cone. On the other hand, winds blowing from sea to land exhibit higher spatial homogeneity, which leads to more reliable LiDAR measurements. Following Section 7.3.1, 1-s data with SV greater than 0.2, which were indicative of spatially non-homogeneous winds, were filtered out. Similarly, data with associated backscatter coefficients smaller than a threshold of 0.02, which is indicative of LiDAR measurements with very low signal return, were rejected.

### 7.3.3 Campaign Overview

During the measurement period (6–30 June 2013), the surface layer was dominated by local thermal winds hardly rising above 15 m/s at 100 m in height [Gutiérrez-Antuñano et al. 2017]. The observed HWS in this period ranged from 1 m/s to 15 m/s, with three predominant WDs: North East (NE), North West (NW) and South (S); see Figure 7.4.

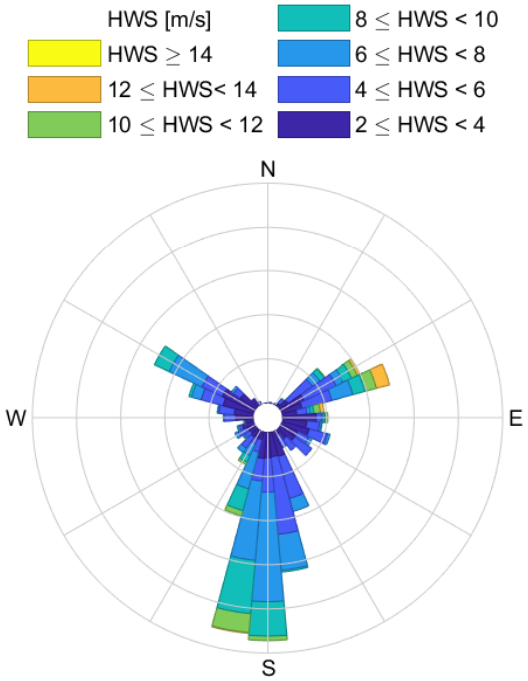


Figure 7.4: Wind rose representing the HWS and WD (after data filtering), measured during the PdP campaign, by the reference LiDAR (10 min) from June 6 to June 30 of 2013 (1875 records).

During the night, the wind was light, coming predominantly from the urban area (NW), showing low HWS values with high turbulence and spatial variability. During the day, the atmosphere was dominated by winds coming from the sea towards land (S and NE), with higher HWS and lower turbulence.

Both the fixed- and floating-lidar 10 min WD time-series showed unexpected high noise (roughly about ±5-deg uncertainty in Figure 7.5). This phenomenon is called "granularity" herein, and was caused by a LiDAR flaw. This issue was solved in a later manufacturing series of the instrument [Gutierrez-Antunano et al. 2017].

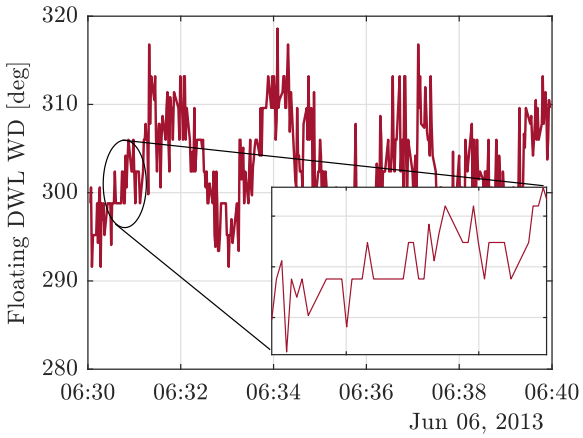


Figure 7.5: WD time-series measured by the FDWL at 100 m height, showing the so-called "granularity" effect.

### 7.3.4 UKF Results

*Low/High-turbulence scenario analysis.*—The filter was applied to the campaign data set described in Section 7.3.3. The filter converged in most cases, achieving successful motion correction when compared to the reference fixed LiDAR. Divergent cases (accounting for less than 0.5% of the statistical sample) were attributable to strong wind shears, which motivated retuning of the measurement-noise variance settings in Equation (7.38).

Figure 7.6 shows a low-turbulence case example, comparing a FDWL HWS measurement time-series with and without correction against the reference fixed-LiDAR time-series. Besides evident filter convergence, the motion-corrected HWS time-series matched almost ideally that of the reference LiDAR. The motion-induced error was greatly reduced from 0.14 m/s to 0.05 m/s RMSE, thus achieving good performance. When analyzing the PSD of these three time-series (see inset), it emerged that the RW model was able to emulate the wind process with high accuracy, up to some 21 dB roll-off at 7 Hz. However, the high-frequency components below −30 dB, which were not as relevant, were underestimated (data not shown).

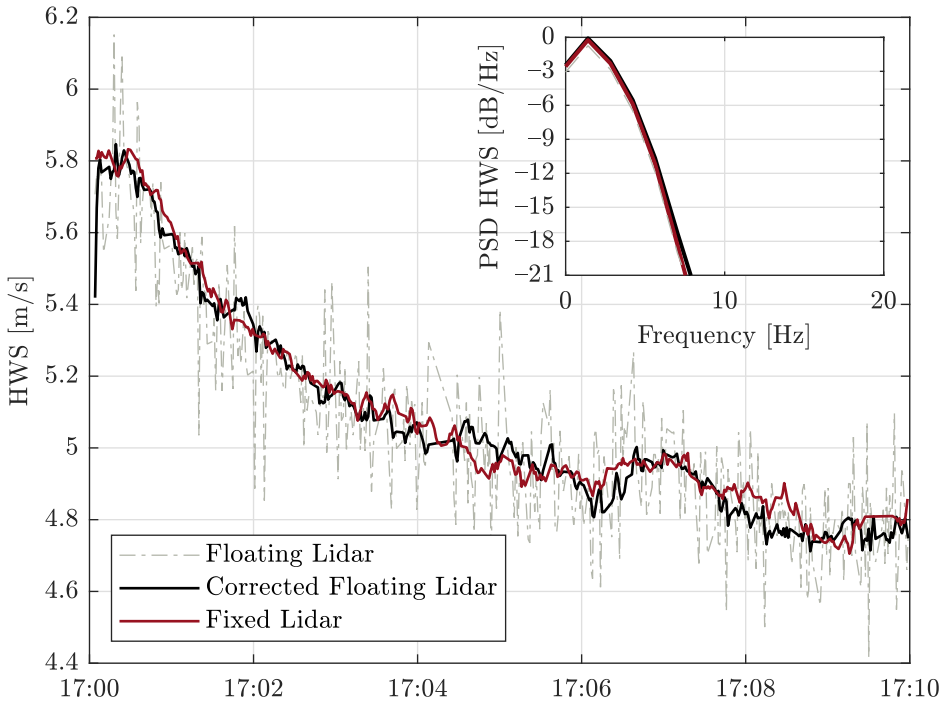


Figure 7.6: HWS time-series measured at 100 m height between the fixed LiDAR and the FDWL, with and without correction (see legend). Inset: PSD comparison. Low HWS-variance scenario (7 June 2013, PdP).

Underestimation of frequency components may lead to motion over-correction by the UKF in high variance scenarios, as illustrated in Figure 7.7. It can be observed that the motion-corrected FDWL and fixed-LiDAR temporal series only partially matched each other. Spectral analysis underlined differences between the HWS PSDs (red and black traces), being as high as 5 dB at low frequencies (0 to 5 Hz) and increasing to $\simeq$10 dB at high frequencies (5 to 20 Hz). This is a limitation of the used RW wind model, which was not able to emulate the high-frequency components of the wind spectrum. Consequently, the filter assimilated the wind model error as a measurement error, which led to biased estimations at specific times in Figure 7.7. Regarding 10-min WD estimation in either high-or low-variance scenarios (counterparts of Figures 7.6 and 7.7, respectively, data not shown), the filter was able to retrieve the yaw-error-free WD with a RMSE as low as roughly 5 deg for both the high- and low-variance cases. Regarding the so-called 1-s WD estimation, the "granularity" effect showed up in the retrieved time-series in similar fashion as for the retrieved HWS.

*Overall campaign analysis.-* With a view to assess the overall filter performance, the TIs measured by the FDWL during the PdP campaign (25 days, 1875 records) with and without correction ($TI_{float.,corr.}$ and $TI_{float.}$, respectively) were compared to the TI measured by the fixed LiDAR

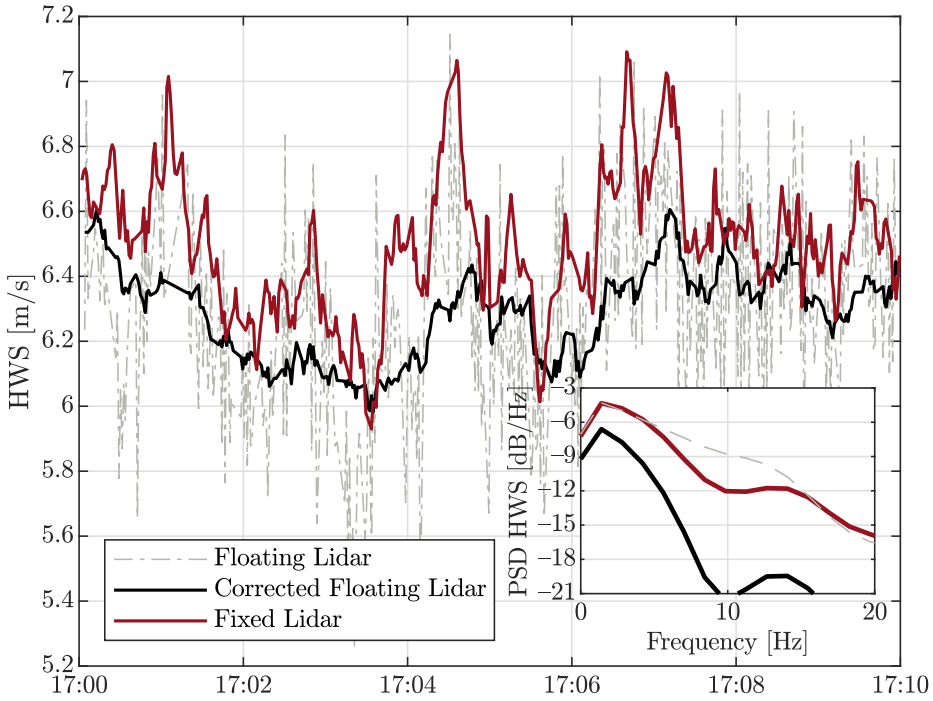


Figure 7.7: Same as Figure 7.6. High HWS-variance scenario (22 June 2013, PdP).

($TI_{fixed}$). In the context of WE, the typical temporal resolution of wind-related data products is 10 min; thus, the comparison was carried out at 10 min temporal resolution. To carry out this comparison, different statistical indicators were considered: (i) The determination coefficient ($R^2$), (ii) RMSE, and (iii) Mean Deviation (MD).

The RMSE for a sample of $N$ motion-corrected measurements is defined as

$$RMSE = \sqrt{\frac{\sum_n^N (TI_{float.,corr.} - TI_{fixed})^2}{N}}, \tag{7.40}$$

and the MD is defined as

$$MD = \frac{\sum_n^N TI_{float.,corr.} - TI_{fixed}}{N}. \tag{7.41}$$

The MD accounts for the systematic error in the LiDAR-measured *TI* (equivalently, HWS standard deviation) caused by wave-induced motion [Gutiérrez et al. 2015, Gottschall et al. 2014a]. The RMSE and MD definitional formulae to compare FDWL uncorrected measurements to fixed-LiDAR measurements are analogous to Equations (7.40) and (7.41) above, by changing $TI_{float.,corr}$ to $TI_{float.}$.

The scatter plot shown in Figure 7.8 compares the *TI* measured by the FDWL (with and without correction) against the *TI* measured by the fixed LiDAR. Without correction, most of the $TI_{floating}$ values fell below the ideal 1:1 line. This was because buoy motion added an apparent variance to

the HWS measurements, which increased the LiDAR-measured turbulence. The linear regression (LR, red dashed-dot line) offset of $-0.0185$ indicated the amount of added turbulence [Salcedo-Bosch et al. 2020a]. The LR slope of 1.0358, which is virtually identical to the ideal unity slope, indicates that the apparent turbulence equally affected all HWS measurements.

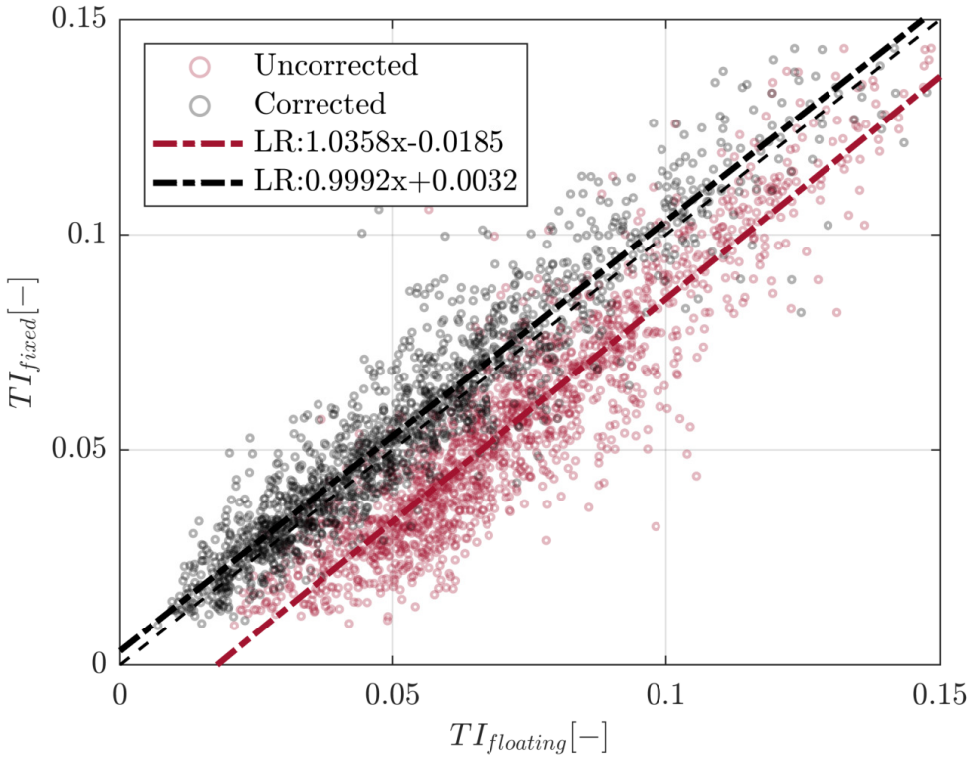


Figure 7.8: Scatter plot comparing the TI measured by the FDWL with reference to the fixed LiDAR, with and without correction (Red, without motion correction; Black, with motion correction). The dashed line indicates the ideal 1:1 line. Dot-dashed lines indicate corresponding color-coded linear regressions.

Regarding the motion-corrected TI measurements (black dots), the scatter points lay closer to the ideal 1:1 line, as demonstrated by an LR offset as low as 0.0032. This represented an 83% reduction factor, in comparison to the uncorrected measurements (offset term equal to 0.0185), and very small over-correction from the UKF side.

Scatter points away from the ideal 1:1 are a consequence of different filter model limitations: First, the LiDAR initial scan-phase model (Section 7.2.5.2) was unknown, the proposed RW models being only a reasonable rough approximation. Second, the retrieved WD by any of the two LiDAR instruments showed the so-called "granularity" issue, which accounted for uncertainties of some $\pm$ 5 degrees (see Section 7.3.3), and which could have well led to inaccurate correction by the UKF. Finally, in Figure 7.8, we did not include the start-up period of the filter, in which the noise covariance matrices are still not well-estimated. Third, a more homogeneous terrain ex-

Table 7.1: Statistical indicators evaluating the comparison between FDWL (with and without correction) and fixed LiDAR TI measurements at the 10 min level.

| | **Uncorrected** | **Motion-Corrected** | **WD Filtered Motion-Corrected** |
|---|---|---|---|
| $R^2$ | 0.85 | 0.90 | 0.93 |
| RMSE | 2.01% | 1.01% | 0.86% |
| MD | −1.70% | 0.29% | 0.36% |

perimental scenario should be used. FDWLs are conceived for open-sea environments, and the motion-correction should be tested in these scenarios.

The overall campaign results demonstrated the good performance of the filter in reducing the apparent TI caused by buoy motion. All statistical indicators (see Table 7.1) improved: (i) the coefficient of determination, $R^2$, rose from 0.85 (without compensation) to 0.90 (with compensation); (ii) the RMSE reduced from 2.01% (without) to 1.01% (with); and (iii) the MD increased from $-1.70\%$ to 0.29%, accounting for an 83% factor improvement.

However, closer inspection of the measurement setup warrants some comments, regarding the statistical indicators shown: First, the floating and the fixed LiDARs were located 50 m apart and, although they measured similar wind conditions, the instantaneous wind measurements were not the same. This would have required setting up two LiDARs co-located at the same place. Specifically, winds blowing from/to the urban area (WDs between 270 and 330 deg, and between 90 and 150 deg, respectively) experienced higher spatial and temporal variation, due to terrain roughness [Al-Khalidy 2018], which led to different HWS time-series being measured by the LiDARs (see Section 7.3.3).

According to Taylor's frozen-atmosphere theory [Taylor 1938], turbulent eddies transported by the mean wind hold their properties as if they were "frozen", such that two points aligned with the mean WD will observe the same wind stochastic realization, with a time delay. This delay is inversely proportional to the mean HWS. The floating and the fixed LiDARs were mainly aligned along the north-south direction and, therefore, only measurement records with WDs within $180\pm30$ deg will be considered for further, enhanced statistical analysis. The maximum delay measured between the two LiDARs was 25 s, which is a negligible value, compared to the measurement period of 10 min.

After the WD was filtered, as indicated, the statistical indicators improved, as shown in the third column of Table 7.1. The coefficient of determination increased to 0.93 and the RMSE decreased to 0.86%. The small increase in MD (0.36%) was not significant, on account of the approximate WD filtering procedure.

## 7.4 Summary and Conclusions

An adaptive method for 6-DoF motion compensation of ZephIR 300 FDWL wind measurements was presented in this chapter. The RAUKF algorithm proved to be capable of correcting the motion-induced error in the retrieved HWS (Figure 7.6) and TI (Figure 7.8), without accessing LiDAR LoS velocity measurements, which is undisclosed information from the manufacturer's side for most of the commercial continuous-wave wind LiDARs. To the best of our knowledge, this is a key state-of-the-art contribution of this work.

The proposed solution departed from the FDWL motion dynamics study by Kelberlau et al. (2020) and the well-known VAD wind-retrieval algorithm, to derive an ad-hoc state-space formulation of the problem from the point of view of control theory, using an UKF and stochastic modelling. The state-vector transition model relied on a RW model to describe the unknown motion-corrected wind vector (to be found) and blind LiDAR initial scan phase. The measurement model was time variant and combined the buoy's 6-DoF IMU information with the filter's estimated motion-corrected wind vector, to predict the FDWL motion-corrupted wind measurements. The recursive loop of the filter, combined with run-time estimation of the state-vector and measurement-noise covariance matrices, ensured successful and convergent results.

The methodology was validated using the experimental data collected during a PdP measurement campaign in Barcelona, using a fixed LiDAR on the PdP pier as the reference instrument. To quantitatively assess filter performance, the 10 min TI measured by the FDWL with and without correction was compared to the TI measured by the reference LiDAR. Wind measurements were also WD screened, to ensure the validity of Taylor's frozen-atmosphere assumption along the connecting line between the two LiDARs. All statistical indicators showed significant improvement Table 7.1: MD improved from $-1.60\%$ (without correction) to 0.36% (with correction), the RMSE improved from 1.9% to 0.86%, and the determination coefficient ($R^2$) increased from 0.86 to 0.93. Linear regression between floating- and fixed-TI measurements showed an offset equal to the apparent motion-induced TI added; which, upon correction by the filter, was virtually removed.

A limitation of the filter was its underestimation of the high-frequency components (i.e., fast transients) when comparing floating-lidar HWS temporal series with reference to fixed-LiDAR ones. This was due to the oversimplified RW wind model used. Notwithstanding the overall improvement in all the statistical indicators shown, a few outliers departed from the ideal 1:1 line between the motion-corrected and fixed-LiDAR TI observations. We hypothesize that this may be due to the filter start-up time (about 60 s before stable tracking condition is reached), as well as the so-called "granularity" effect in the LiDAR-retrieved WD.

All in all, the RAUKF was demonstrated to be an effective tool for 6-DoF motion correction of FDWL measurements and accurate TI measurements. Furthermore, the recursive operation of the

filter allows room for stand-alone, nearly real-time correction of FDWL measurements.

# Chapter 8

# Enhanced Dual Filter for Floating Wind Lidar Motion Correction: The Impact of Wind and Initial Scan Phase Models

*The contents of this Chapter are aligned with Obj. 2 of this Ph.D. and part of the full paper [Salcedo-Bosch et al. 2022b]:* ***Salcedo-Bosch, A.****; Rocadenbosch, F.; Sospedra, J. "Enhanced Dual Filter for Floating Wind Lidar Motion Correction: The Impact of Wind and Initial Scan Phase Models", Remote Sens. 2022, 14, 4704.* `https://doi.org/10.3390/rs14194704`. *Systematic or multiple reproduction or distribution to multiple locations via electronic or other means is prohibited and is subject to penalties under law*

## 8.1 Introduction

In Chapter 7, the FDWL motion-correction method for a focusable continuous-wave lidar based on the Unscented Kalman Filter (UKF) is presented. The method demonstrated to be able to correct FDWL measurements for motion-induced additive $TI$ on the run without having access to the LiDAR internal LoS measurements. Thus, when comparing the FDWL to a reference fixed lidar, the apparent $TI$ was reduced from $-1.70\%$ (without correction) to $0.29\%$ (with correction). However, moderate $TI$ differences between the two lidars remained, which manifested with a coefficient of determination of 0.93. Moreover, this first UKF prototype overcompensates the $TI$, which we hypothesize is caused by the assumptions of oversimplified random process models of the Random Walk (RW) type for both the wind and initial scan phase. The flaws of these models demonstrate prominently in high wind turbulence or transitioning scenarios, which may often cause filter divergence Robert Grover & Y.C. Hwang (2012). Therefore, it is sensible to assume that refined wind and LiDAR initial scan phase models are to enhance filter tracking and reduce divergence.

In the present chapter, we study the impact of different wind and phase model combinations

on the motion-correction capabilities of the filter as well as the impact of different near-shore sea and atmospheric scenarios on the filter performance. The novelty of the enhanced filter lies in the expected superior wind-tracking capabilities of the filter, particularly in high-frequency turbulence regimes and in the operation of the filter without having access to the LiDAR internal LoS measurements.

## 8.2 Materials and Methods

### 8.2.1 Review of Materials

For this study, data from "Pont del Petroli" campaign (see Chapter 3) was used. Specifically, the dataset comprised (i) wind measurements from the reference fixed DWL sited at PdP pier, (ii) wind measurements from the FDWL, (iii) fixed DWL and FDWL buoy internal parameters for data-quality control and (iv) 6 DoF motion measurements obtained by the "lidar IMU" and the "buoy IMU". HWS values were measured by the fixed reference lidar and ranged from 1.2 to 14.4 m/s, whereas $TI$ values ranged from 0.90% to 24.89%. According to the manufacturer's specifications [M. Pitter et al. 2014], lidar $HWS$ measurement records lower than 2 m/s were considered unreliable; therefore, records with 10 min mean $HWS$ lower than 2 m/s were filtered out.

*ZephIR 300 LiDAR rotating prism and focusing.* As mentioned in Section 3.1, ZephIR 300 is a focusable CW DWL. The LiDAR uses a rotating prism to deflect the emitted laser beam (Figure 8.1) and create a scanning cone of 30-degree width from zenith. The prism rotates with uniform circular motion at a rate of one rotation per second (360 degs/s). The LiDAR uses the VAD algorithm to retrieve the wind vector from the 50 LoS velocity measurements in a scan. By refocusing, the LiDAR is able to sequentially measure at a set of user-defined heights. However, this is performed at the expense of reducing the sounding time resolution at a given height by a factor greater than the number of sounding heights, because dead times are needed to refocus from one height to another. When the LiDAR measures at a single height (no refocusing) the wind vector is retrieved with a nearly uniform resolution of 1 s (1 scan/s). This was the preferred option in this study, and a fixed height of 100 m, was used.

### 8.2.2 Methods

#### 8.2.2.1 Enhanced Wind Models: The Auto-Regressive Approach

In this section, we aim to revisit the basic RW wind model of Equation 7.17 for the improved estimation of the wind process spectrum by the UKF. To this end, different models are presented and compared in terms of their power spectral density (PSD) with reference to the fixed lidar. The PSD indicates the signal power distribution as a function of the frequency [Proakis & Manolakis 2006].

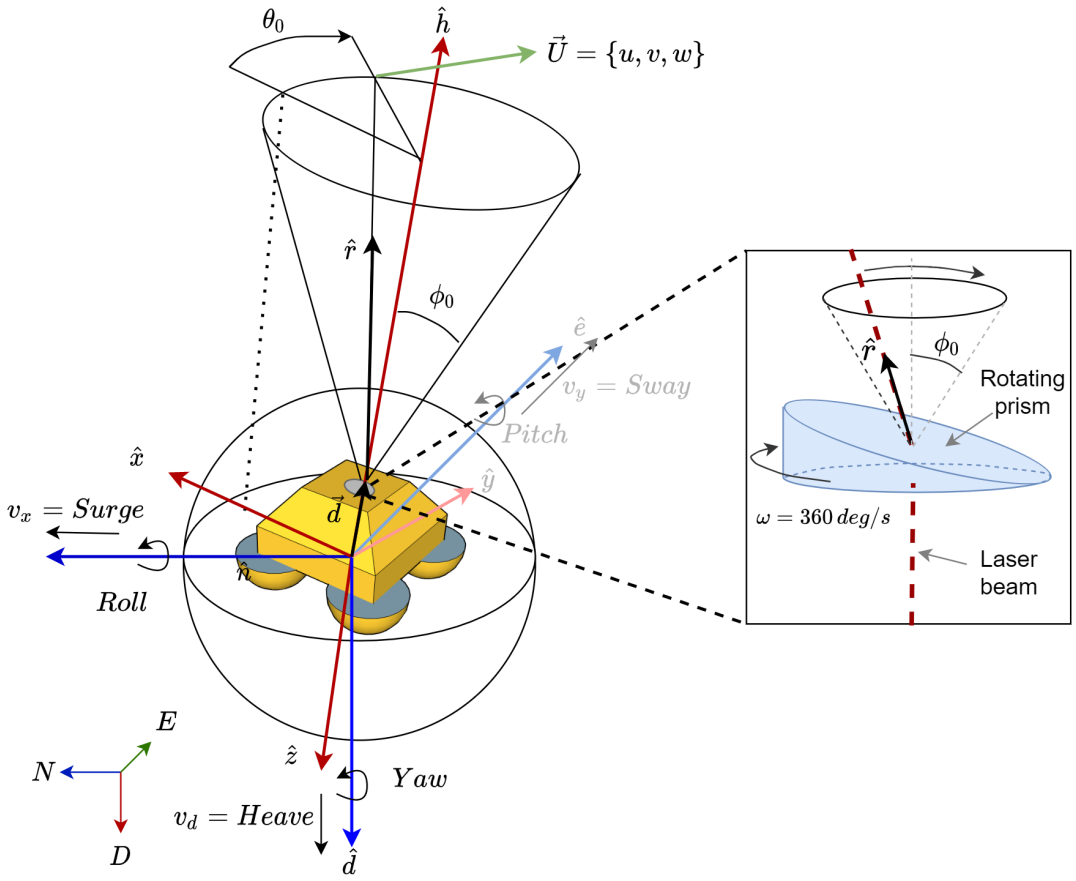


Figure 8.1: Geometry of the NEPTUNE FDWL proof-of-concept buoy. Inset shows the lidar rotating prism used for deflection of the laser beam.

Random walk (Equation (7.21)) models the state-vector wind component, $\boldsymbol{U}_k$ (Equation (7.20)), at discrete time $t_k$ as the superposition of the measured wind vector, $\boldsymbol{U}_{k-1}$, at previous time $t_{k-1}$ plus a stochastic term $\epsilon_k$:

$$\boldsymbol{U}_k = \boldsymbol{U}_{k-1} + \epsilon_k. \tag{8.1}$$

Alternatively, we propose a low computationally demanding, straightforward wind model based on an Auto Regressive (AR) process of order $P$, AR(P). In this model, the measured wind vector, $\boldsymbol{U}_k$, at each time $t_k$ is a linear combination of its $P$ previous values (i.e., at time instants $t_{k-1}, \ldots, t_{k-P}$) plus a stochastic term modeling an imperfectly predictable term. The AR(P) model is formulated as follows:

$$\boldsymbol{U}_k = \left[\boldsymbol{w}^{HWS^T} \cdot \boldsymbol{HWS}_k \quad \boldsymbol{w}^{WD^T} \cdot \boldsymbol{WD}_k \quad \boldsymbol{w}^{VWS^T} \cdot \boldsymbol{VWS}_k\right]^T + \epsilon_k, \tag{8.2}$$

where $\boldsymbol{U}_k$ is the $3 \times 1$-dimension wind vector at time $t_k$ (Equation (6.1)); $\boldsymbol{HWS}_k$, $\boldsymbol{WD}_k$ and $\boldsymbol{VWS}_k$ are the $P \times 1$-dimension vectors denoting the measured HWS, $WD$ and $VWS$ at previous times $t_{k-1}, \ldots, t_{k-P}$. $\epsilon_k$ is zero-mean white noise with constant variance $\sigma_\epsilon^2$. $\boldsymbol{w}^x$, $x = HWS, WD, VWS$ are the $P \times 1$-dimension vectors containing the AR(P) model coefficients for the $HWS$, $WD$ and

$VWS$ wind components, respectively:

$$\boldsymbol{w} = \left[\boldsymbol{w}^{HWS^T} \quad \boldsymbol{w}^{WD^T} \quad \boldsymbol{w}^{VWS^T}\right]^T. \tag{8.3}$$

The AR-process PSD is computed by means of the Yule–Walker equations [Proakis & Manolakis 2006].

The accuracy of the AR wind model depends on the process order as discussed next:

Thus, in Figure 8.2, we compared the PSD of four different 10 min $HWS$ time series measured by the fixed lidar with the estimated PSDs using different random process models. Two high- and two low-frequency wind scenarios (panels (a,b) and (c,d), respectively) characterized by low and high $HWS$s ((a,c) and (b,d), respectively) were chosen. It can be observed that the RW model was not able to follow all the spectral details of the measured PSD in high frequency scenarios. At low frequencies ($f \approx 0$ Hz), RW was biased up to 4 dBs. In addition, RW was not able to follow the second lobe of the lidar-measured PSDs at $f \approx 0.05$ Hz. On the other hand, the RW matched quite well the reference PSD in low frequency scenarios irrespective of the $HWS$ chosen. Regarding the AR models, they emulated more accurately the PSD in high frequency scenarios in comparison to the RW model. Moreover, it is evident that the higher the process order was, the better the model capability to equal the measured PSD was. The AR process order $P$ was determined on the basis of the lowest order, ensuring a difference lower than 3 dB between the secondary lobes of the measured and emulated PSDs in high-frequency scenarios (Figure 8.2a,b). By experiment, the AR process order $P = 10$ was found.

#### 8.2.2.2 Lidar-Scan Initial-Phase Model

The UKF lidar motion-correction algorithm by Salcedo-Bosch et al. [Salcedo-Bosch et al. 2021c] assumes the oversimplification that initial phase $\theta_0$ is a random variable with uniform distribution over 0-360 deg, and that there are *independent phases* from one conical scan to the next [Gutiérrez-Antuñano et al. 2018]. An RW model was considered for the initial phase:

$$\theta_{0,k} = \theta_{0,k-1} + \epsilon_k, \tag{8.4}$$

where $\theta_{0,k}$ and $\theta_{0,k-1}$ are the initial phases at discrete times $t_k$ and $t_{k-1}$, respectively, and $\epsilon_k$ is a random variable with uniform distribution over $[0, 360]$ deg.

Alternatively, here, we propose a phase model based on the kinematics of the DWL rotating prism used to implement the scanning mechanism (Section 8.2.1 and Figure 8.1, inset) that breaks this independence assumption. Because the prism has Uniform Circular Motion (UCM) at a rate of 360 deg/s, if the initial phase is known at a given time instant, it can be known elsewhere in time. The UCM initial-phase model can be formulated as follows:

$$\theta_{0,k} = \theta_{0,k-1} + 360 \times \Delta t_k, \tag{8.5}$$

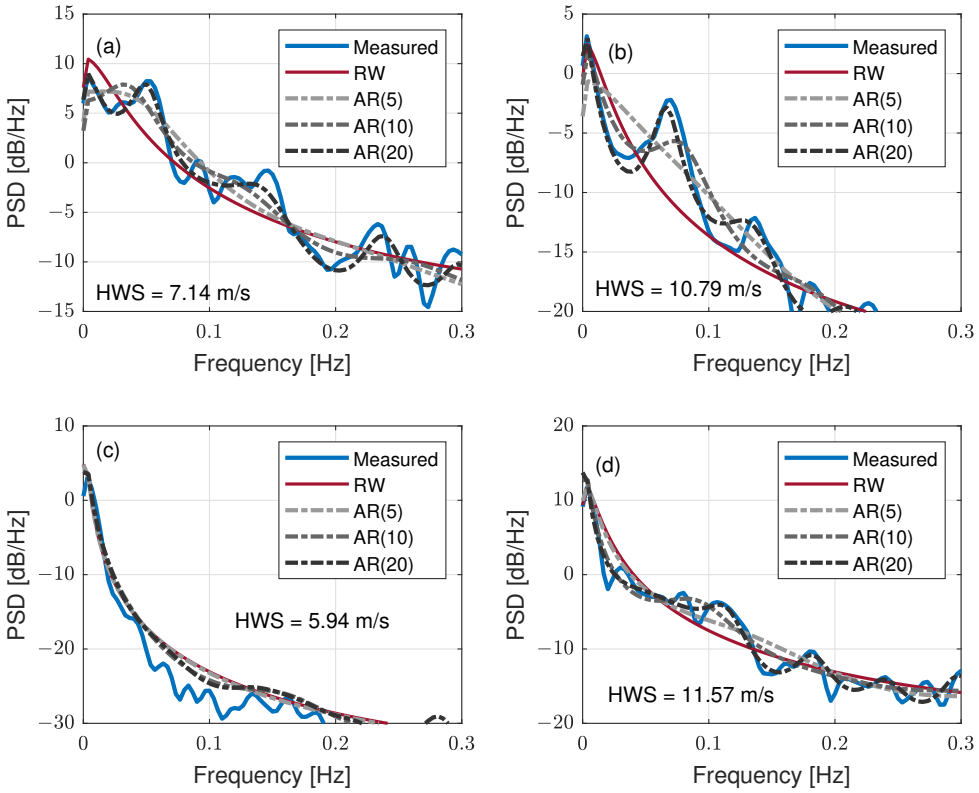


Figure 8.2: Comparison between the $HWS$ PSD measured by the fixed lidar (PdP campaign; Barcelona; 10 min $HWS$ time series) and the PSDs estimated from a set of different RW and AR random process models (see legend). Panels (**a**,**b**): *high-frequency* wind scenarios (19 June 2013, 17:10 LT; and 28 June 2013, 12:40 LT, respectively). Panels (**c**,**d**): *low-frequency* wind scenarios (24 June 2013, 12:30 LT, and 22 June 2013, 12:10 LT, respectively).

where $\theta_{0,k}$ and $\theta_{0,k-1}$ are the initial phases (in degrees) at discrete times $t_k$ and $t_{k-1}$, respectively, and $\Delta t_k$ is the time lag between $t_k$ and $t_{k-1}$. Experimentally, there is a small time lapse between consecutive lidar scans as well as a variability in this time lapse, which can be caused by CPU internal processes or the re-focusing of the lidar at different heights. This leads to observed initial phases, $\theta_0$, with apparent uniform distribution between 0 and 360 deg.

Figure 8.3 shows the initial-phase time series, $\theta_{0,k}$, for the UCM model in response to the time-lag series, $\Delta t_k$. The resulting initial-phase distribution is also shown. The time-lag series was generated from one hour of lidar-recorded timestamps. The initial phase at start time $t_0 = 0$ s was $\theta_{0,0}$ = 180 deg. In Figure 8.3b, it can be observed that the time lag, $\Delta t_k$, usually departed from the nominal $\simeq$1 s scan time (baseline), with noticeable lag dropouts approximately every 15 s being caused by the lidar internal CPU interruptions. The initial-phase time series shown in Figure 8.3a tentatively demonstrated uniform random behavior over [0, 360) degs. The uniform distribution was corroborated in the 30 deg bin histogram in Figure 8.3c.

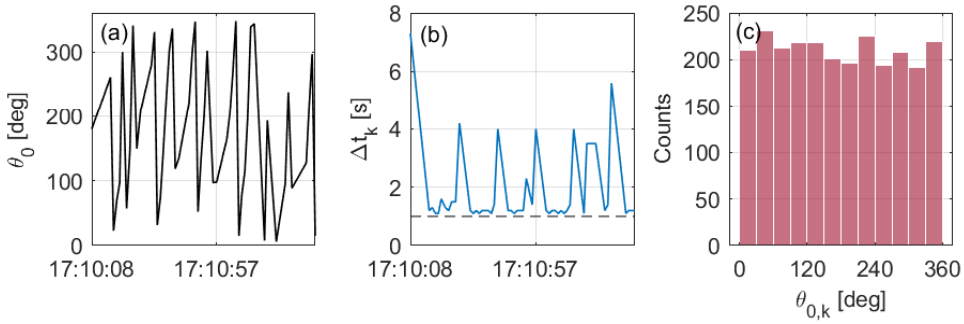


Figure 8.3: The UCM initial-phase model (19 June 2013; 17:10–17:20 LT; PdP campaign). (**a**) Initial-phase time series, $\theta_{0,k}$ (sub-segment 17:10:08–17:11:35 LT). (**b**) Time-lag time series, $\Delta t_k$. Baseline (dashed line) indicates the 1 s nominal lidar scan time. (**c**) Histogram plot of the initial phase (panel (**a**)).

#### 8.2.2.3 Dual UKF Estimation

We propose a dual UKF approach consisting of two unscented Kalman filters working cooperatively: the *main filter* (UKF1), which estimates the wind vector (Equation (8.2)) and initial phase, and the *auxiliary filter* (UKF2), which estimates the weight vector (Equation (8.3)). The motivation behind this is the non-stationarity of wind fields. Although, in theory, the wind process is usually considered stationary over short-term intervals ($\simeq$15 min [Smith & Mehta 1993]), in practice, it is non-stationary and is dependent on the atmospheric conditions. Therefore, weight vector $\boldsymbol{w}$, which describes the AR model coefficients, is an unknown set of random variables that needs to be continuously estimated at each discrete time $t_k$ along with state vector $\boldsymbol{x}_k$.

As illustrated in Figure 8.4, the weight vector estimated at time $t_{k-1}$ by UKF2, $\boldsymbol{w}_{k-1|k-1}$, is used by UKF1 to estimate the wind vector at the prediction step. Similarly, the wind-vector and initial-phase estimates at $t_{k-1}$, denoted as $\boldsymbol{U}_{k-1|k-1}$ and $\theta_{0,k-1|k-1}$, respectively, which are part of the state-vector $\boldsymbol{x}_{k-1|k-1}$ estimated by UKF1, are used to estimate the weight vector at the UKF2 innovation step. Both filters use the motion-corrupted wind vectors retrieved by the FDWL ($\boldsymbol{U}_k^{FDWL}$) at both the prediction and innovation steps, and the IMU-measured FDWL attitude (6 DoFs) at the prediction step. The formulation of the two filters is detailed in the subsections below.

#### 8.2.2.4 Main UKF

The *main filter*, UKF1, exhibits great similarities with the former motion-correction filter designed by Salcedo-Bosch et al. Salcedo-Bosch et al. (2021c) (refer to Section 7.2.6). Similar to such implementation, UKF1 aims to estimate the wind vector and initial phase from motion-corrupted wind data; however, this is achieved using enhanced models in the version here shown. Thus, UKF1 uses the AR(P) model instead of RW for the wind process and the UCM model instead of RW for the initial phase.

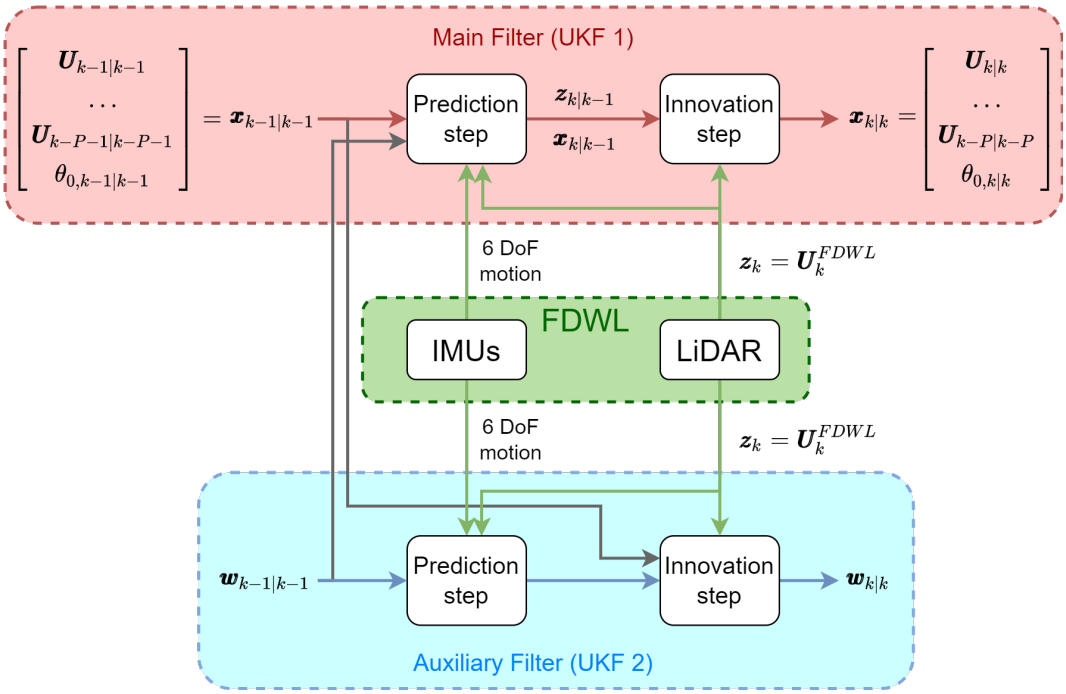


Figure 8.4: The dual UKF approach. (Red box) Main filter (UKF1) used to estimate the motion-free wind vector ($\boldsymbol{U}_k$, i.e., the "true" wind vector at time $t_k$) and initial phase $\theta_{0,k}$. (Blue box) Auxiliary filter (UKF2) used to estimate the weight vector defining the AR wind model. (Green Box) FDWL block. Green arrows depict that both filters assimilate FDWL 6 DoF motion information from the buoy IMUs as well as the motion-corrupted FDWL wind retrievals, $\boldsymbol{U}_k^{FDWL}$. The black arrows depict the exchange of information between filters UKF1 and UKF2.

In order to formulate UKF1, the previous equation for the state vector (Equation (7.20)) is reformulated by including the $P$ past wind-vector estimations relative to times from $t_{k-P}$ to $t_{k-1}$:

$$\boldsymbol{x}_k = \begin{bmatrix} \boldsymbol{U}_k^T & \boldsymbol{U}_{k-1}^T & \dots & \boldsymbol{U}_{k-P}^T & \theta_{0,k} \end{bmatrix}^T . \tag{8.6}$$

The state-transition function of the *main filter*, $f^{UKF1}(\cdot)$, is composed of AR wind-model state-transition function $f_{\boldsymbol{U}}^{AR}(\cdot)$ and UCM initial-phase state-transition function $f_{\theta_0}^{UCM}(\cdot)$:

$$f^{UKF1}(\boldsymbol{w}_{k-1|k-1}, \boldsymbol{x}_{k-1|k-1}) = \begin{bmatrix} f_{\boldsymbol{U}}^{AR}(\boldsymbol{w}_{k-1|k-1}, \boldsymbol{U}_{k-1|k-1} \dots \boldsymbol{U}_{k-P|k-P}) \\ f_{\theta_0}^{UCM}(\theta_{0,k-1|k-1}) \end{bmatrix}, \tag{8.7}$$

where $\boldsymbol{w}_{k-1|k-1}$ is the current "a posteriori" estimate of the weight vector by UKF2, and $f_{\boldsymbol{U}}^{AR}(\cdot)$ and $f_{\theta_0}^{UCM}(\cdot)$ are written in state-space formulation upon the models of Equation (8.3) and Equation (8.5), respectively. Explicitly:

$$f_{\boldsymbol{U}}^{AR}(\boldsymbol{w}, \boldsymbol{U}_{k-1|k-1}, \dots, \boldsymbol{U}_{k-P|k-P}) = \begin{bmatrix} \begin{bmatrix} {\boldsymbol{w}^{HWS}}^T \cdot \boldsymbol{HWS}_{k-1|k-1} \\ {\boldsymbol{w}^{WD}}^T \cdot \boldsymbol{WD}_{k-1|k-1} \\ {\boldsymbol{w}^{VWS}}^T \cdot \boldsymbol{VWS}_{k-1|k-1} \end{bmatrix} \\ \boldsymbol{I} \begin{bmatrix} \boldsymbol{U}_{k-1|k-1} \\ \boldsymbol{U}_{k-2|k-2} \\ \vdots \\ \boldsymbol{U}_{k-P+1|k-P+1} \end{bmatrix} \end{bmatrix}, \tag{8.8}$$

and:

$$f_{\theta_0}^{UCM}(\theta_{0,k-1|k-1}) = \left[\theta_{0,k-1|k-1} + 360 \times \Delta t_k\right]. \tag{8.9}$$

In Equations (8.8) and (8.9) above, the state-space formulation provides a convenient way to rewrite the simple random process description of Equations (8.3) and (8.5) into the vector forms of Equations (8.8) and (8.9), respectively. The advantage of this state-space representation is that it allows the AR wind model and UCM initial-phase model to be easily integrated into filter Equation (7.5) through state-transition function $f(\cdot) = f^{UKF1}$.

Measurement vector $\boldsymbol{z}_k^{UKF1}$ and measurement function $h^{UKF1}(\cdot)$ are identical to the UKF filter described in Section 7.2.6 with measurement function $h(\cdot)$ defined by Equation (7.28).

#### 8.2.2.5 Auxiliary UKF

The *auxiliary filter*, UKF2, aims to estimate AR wind-model weight vector $\boldsymbol{w}$. Therefore, the state-vector is vector $\boldsymbol{w}_k$ to be estimated, formed by the $HWS$, $WD$ and $VWS$ as AR process coefficients of $P$-th order:

$$\boldsymbol{w}_k = \left[\boldsymbol{w}_k^{HWS^T} \quad \boldsymbol{w}_k^{WD^T} \quad \boldsymbol{w}_k^{VWS^T}\right]^T. \tag{8.10}$$

Because it is assumed that random step changes in any of the weights occur with equal probability and are independent of each other, the state-transition model is considered as random walk [Wan & Van Der Merwe 2000]. It is formulated as follows:

$$f^{UKF2}(\boldsymbol{w}_{k-1|k-1}) = \boldsymbol{I} \cdot \boldsymbol{w}_{k-1|k-1}. \tag{8.11}$$

Similar to UKF1, the UKF2 observation vector is FDWL-measured wind vector $\boldsymbol{U}_k^{DWL}$. In expanded form:

$$\boldsymbol{z}_k^{UKF2} = \left[HWS^{FDWL} \quad WD^{FDWL} \quad VWS^{FDWL}\right]^T, \tag{8.12}$$

where $HWS^{FDWL}$, $WD^{FDWL}$ and $VWS^{FDWL}$ are the FDWL-measured (i.e., motion-corrupted) $HWS$, $WD$ and $VWS$, respectively.

The UKF2 measurement function, $h^{UKF2}(\cdot)$, relates the "a priori" estimation of weight vector $\boldsymbol{w}_{k|k-1}$ to the motion-corrupted measurement vector $\boldsymbol{z}_k^{UKF2}$. To perform the above, the $P$ previous motion-corrected wind vectors estimated by UKF1 ($\boldsymbol{U}_{k-1|k-1}, \ldots, \boldsymbol{U}_{k-P-1|k-P-1}$) must be propagated to the AR wind model via function $f_{\boldsymbol{U}}^{AR}(\cdot)$) and weights $\boldsymbol{w}_{k|k-1}$ in order to predict motion-corrected or "true" wind vector $\boldsymbol{U}_k$ at present time $t_k$. Then, the predicted wind vector is transformed by UKF1 lidar measurement function $h^{UKF1}(\cdot)$ to predict measured motion-corrupted wind vector $\boldsymbol{U}^{FDWL}$ in the recursive loop of the filter. These steps can be written as follows:

$$h^{UKF2}(\boldsymbol{w}_{k|k-1}, \boldsymbol{U}_{k-1|k-1}) = h^{UKF1}(f_{\boldsymbol{U}}^{AR}(\boldsymbol{w}_{k|k-1}, \boldsymbol{U}_{k-1|k-1})). \tag{8.13}$$

Note that, for short, $h^{UKF1}(\cdot) = h(\cdot)$ in Equation (7.28), Section 7.2.6.

Concerning filter *initialization*, both the main and auxiliary filters use a rough estimate of the motion-corrected wind-vector time series computed using the window averaging technique [Gutiérrez-Antuñano et al. 2017]. The initial weight vector, $\boldsymbol{w}_0$, is derived by fitting an AR model to the rough motion-corrected time series. The process-noise covariance initial matrices are derived as the mean squared error between the observations and the predictions by the fitted AR model. Measurement-noise covariance matrices are initialized from the rough motion-corrected time series as in [Salcedo-Bosch et al. 2021c].

#### 8.2.2.6 Model Intercomparison Methodology

In order to assess the motion-correction performance of the improved wind and initial-phase models presented in Sections 8.2.2.1 and 8.2.2.2, two model combinations were considered (Table 8.1):

- **(1) Basic model** Both the wind process and initial phase are modeled as RWs;
- **(2) Enhanced model**: The wind process is modeled as an AR process (order $P = 10$) and the initial phase as UCM (see Section 8.2.2.2).

Table 8.1: Basic and enhanced model combinations studied to assess the motion-correction filter performance.

| Model Combinations | Wind Model | Initial-Phase Model | Dual UKF |
|---|---|---|---|
| Basic | RW (Equation (7.17)) | RW (Equation (7.18)) | No |
| Enhanced | AR (Equation (8.8)) | UCM (Equation (8.9)) | Yes |

For each of the model combinations above, the motion-correction performance was analyzed in terms of $TI$ and its mean deviation with reference to the fixed lidar. The *statistical descriptors* below were considered.

*(a) Floating-lidar $TI$ measurements* with and without correction ($TI_{float.-corr.}$ and $TI_{float.}$, respectively) were compared against fixed-DWL $TI$ measurements ($TI_{fixed}$), which were used as reference. Model comparisons were carried out considering different motion scenarios clustered as a function of *(i) mean WD, (ii) mean HWS* and *(iii) FDWL mean tilt*. The mean tilt was computed from 10 min roll and pitch-tilt measurements [Salcedo-Bosch et al. 2021b]:

$$Tilt = \frac{\sum_{n=1}^{N} \sqrt{roll\,(t_n)^2 + pitch\,(t_n)^2}}{N}, \tag{8.14}$$

where $N = 6000$ is the number of samples in a 10 min interval, and $\Delta t_n = 100$ ms is the IMU sampling time increment (10 Hz sampling frequency).

*(b) The Mean Deviation (MD)* of the FDWL motion-corrected $TI$ with reference to the fixed lidar was computed as follows:

$$MD = \frac{1}{N}\sum_{n=1}^{N}(TI^n_{float.-corr.} - TI^n_{fixed}), \tag{8.15}$$

where $N$ is the number of measurements in each $HWS$ cluster.

## 8.3 Results and Discussion

In this section, the performance of the enhanced motion-correction UKF is studied. First, two case examples are presented under low- and high-frequency turbulent regimes. Second, the performance of the basic and enhanced filters in terms of $TI$ estimation is compared under different motion and wind scenarios. Third, the motion-correction accuracy achieved by both filters is examined through numerical analysis. Finally, the limitations of the enhanced filter are presented and discussed.

### 8.3.1 Case Examples

Two case examples are presented next to illustrate the comparative performance between the basic and enhanced models of Section 8.2.2.1 and Section 8.2.2.2, respectively, under two different turbulent regimes: (i) low-frequency turbulence (Figure 8.5) and (ii) high-frequency turbulence (Figure 8.6). These figures compare the 10 min motion-corrected $HWS$ time series and related spectra when using the basic and enhanced models with reference to the fixed lidar and the uncorrected FDWL. The error bars depicted are indicative of the uncertainty in the $HWS$ estimations. The $HWS$ uncertainty is computed as the square root of the main diagonal first element of the a posteriori error covariance matrix $\boldsymbol{P}_k^{xx}$ (Algorithm 1, step 3 in Appendix D). The $\boldsymbol{P}_k^{xx}$ main diagonal is the a posteriori state-noise error variance vector associated with the state vector (see Equation (7.20) and Equation (8.6)), so that its first element (Equation (6.1)) corresponds to the $HWS$ error [Rocadenbosch et al. 1999]. A similar approach was followed by Araújo et al. Araújo da Silva et al. (2022b) to assess the Kalman filter error on the estimation of the atmospheric boundary layer height.

The first case is shown in Figure 8.5. The weak turbulence of the wind in Figure 8.5a was evidenced by the fixed-lidar time series, showing an approximately constant $HWS$ ($HWS \approx 6$ m/s) along with slow speed variations (notice that the Y-axis scale only spans 1.5 m/s). In the PSD plot of Figure 8.5b, the prominent low-frequency behavior of the turbulence was associated with a primary-to-secondary lobe level (PSLL) as high as 29 dB. The primary lobe, which concentrates most of the wind energy, was close to 0 Hz and peaked at 4 dBs, while the secondary lobe, which assimilates rapid turbulent variations, lay at 0.08 Hz and peaked at $-25$ dBs.

In Figure 8.5a, both the basic and the enhanced model combinations enabled the filter to motion-correct the corrupted FDWL measurements and to acceptably track the fixed-lidar $HWS$ reference. This is re-encountered in Figure 8.5b, with similar spectra between the enhanced and the basic models, albeit with the remark that the enhanced models overestimated the high-frequency components above 0.1 Hz. Moreover, both model combinations were able to correctly estimate the true

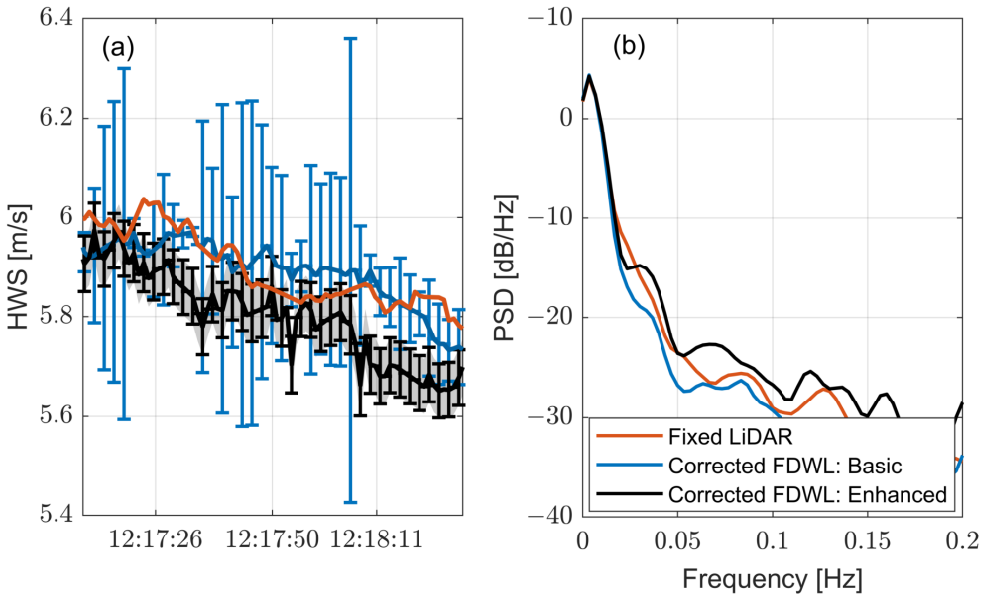


Figure 8.5: Case example #1: Low-frequency turbulence scenario (PdP campaign; 22 June 2013; 12:10 LT). $HWS$ time-series measured during PdP campaign by the fixed lidar and the FDWL with motion correction considering the basic and enhanced models combinations. (**a**) Time-series comparison between the basic and enhanced floating-lidar motion-correction models with reference to the fixed lidar. (**b**) Related PSDs.

wind $TI$ (figure not shown) as $TI_{float.-corr.}$ = 2.77% (basic) and 2.87% (enhanced), which were nearly identical to the reference $TI$, $TI_{fixed}$ = 2.76%.

However, the error bars evidence that $HWS$ estimates from the basic filter have very high uncertainties as compared to the enhanced filter. This is due to the improved wind and initial phase models used, providing more accurate a priori estimation of the wind vector.

The second case is shown in Figure 8.6. In Figure 8.6a, the reference $HWS$ time series measured by the fixed lidar demonstrated rapid and more intense variations, including sudden wind gusts lasting between 20 and 30 s. These fast $HWS$ variations manifested in the PSD of Figure 8.6b as a much lower PSLL than that in Figure 8.5b. The PSLL was only 7 dB (the main lobe around 0 Hz (low frequencies) was at $\simeq$4 dB, and the secondary lobe at $\simeq -3$ dB lay between 0.03 and 0.05 Hz (high frequencies)).

From the temporal series plots, it arises that the motion-correction filter was not able to follow the $HWS$ peaks when using the basic model combination. These peaks were treated by the filter as if they were noise; therefore, such turbulent situations led to biased estimations. In contrast, the enhanced combination permitted the filter to track the wind gusts. Based on the error bars shown in Figures 8.5 and 8.6, it emerges that in a fast-changing wind scenario, the enhanced-filter uncertainties in the $HWS$ estimates remain small and attain similar values to those attributable to low-frequency scenarios. The PSD demonstrated that the basic model combination (blue trace) un-

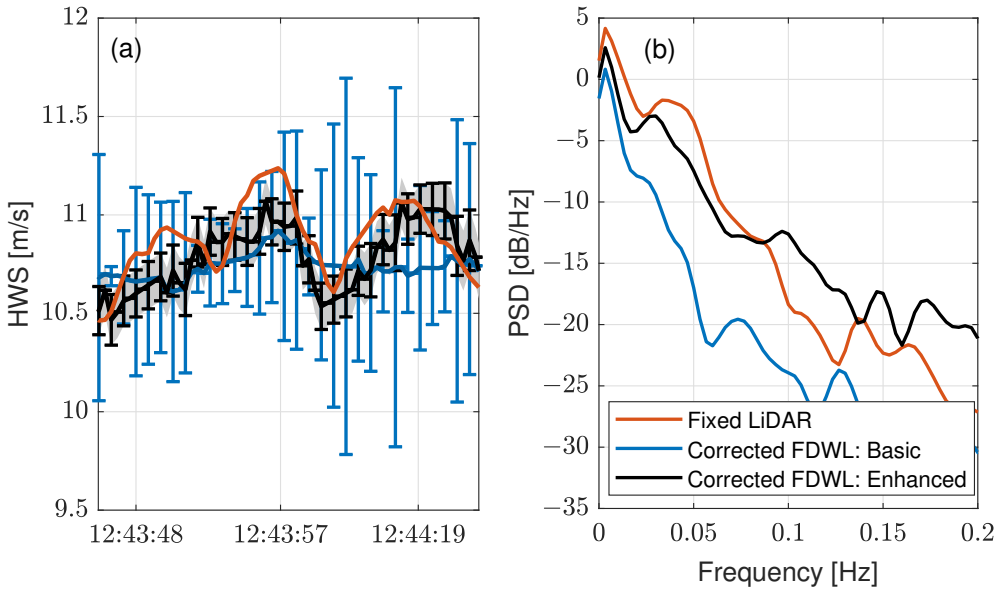


Figure 8.6: Case example #2: High-frequency turbulence scenario (PdP; 28 June 2013; 12:40 LT). Same legend as in Figure 8.5. Note the larger Y-axis limits in panel (**a**) to accommodate much higher $HWS$ variations.

derestimated all frequency components higher than approximately 0.02 Hz by about ≃8 dB (blue trace versus black trace). On the contrary, the enhanced combination permitted the filter to reasonably follow the high-frequency wind components up to 0.1 Hz. The numerical estimation yielded $TI_{float.-corr.}$ = 1.17% (basic), and 2.08% (enhanced) as compared with $TI_{fixed}$ = 2.07%. It is important to highlight that higher AR-model orders (for example, $P = 20$ and $P = 30$) yielded biased estimations of both the PSD and $TI$ due to the much longer convergence time required by the filter. Therefore, in a fast-changing wind scenario, such as the one in Figure 8.6, the filter may not be able to converge.

### 8.3.2 Global Statistics

To complete the analysis, the performance of the motion-correction model combinations mentioned above (Section 8.2.2.6) was studied by comparing the 10 min $TI$ measured by the FDWL (before and after motion correction) with reference to the fixed lidar under different wind and motion conditions. In total, 1786 data records (from 6 to 30 June 2013) from the PdP experimental campaign were used. The statistical database was filtered out for outliers according to the quality assurance criteria described in detail in Salcedo-Bosch et al. (2021c). In brief, the removed outliers encompassed rain-flagged data, $HWS$ measurement values outside the 1–80 m/s range, $SV$ values higher than 0.2 and backscattering coefficients smaller than 0.02.

The 10-min mean $HWS$ and $WD$ measured by the FDWL without motion compensation matched

almost ideally the measurements of the reference fixed lidar as expected from previous studies [Araújo da Silva et al. 2022a, Kelberlau et al. 2020, Gutiérrez-Antuñano et al. 2017, Gutierrez-Antunano et al. 2017]. Regarding the mean $HWS$, when regressing FDWL $HWS$ data onto fixed-lidar $HWS$ for the whole campaign, the coefficient of the determination ($R^2$) was 0.997, linear regression (LR) slope was 0.99 and LR offset was 0.06 m/s. Regarding the mean $WD$, the coefficient of determination was $0.990$, LR slope 0.98 and LR offset 0.41 deg. These values are compliant with the key performance indicators defined by the Carbon Trust Offshore Wind Accelerator [Carbon Trust 2018]. The same indicators were obtained after motion correction with both the basic and the enhanced filters.

Figure 8.7 shows the performance of the motion-correction model combinations mentioned above in Section 8.2.2.6, studied by comparing the $TI$ measured by the fixed lidar and by the FDWL (before and after motion correction) under different wind and motion conditions. The input statistical variables of the study or *clustering variables* were $WD$, $HWS$ and buoy tilt angle, and the output ones were mean $TI$, $MD$ and FDWL translational velocity.

In Figure 8.7a,c,d, it can be observed that the measured FDWL $TI$, $TI_{float}$, was higher than the fixed-lidar reference $TI$, $TI_{fixed}$, for all the clustering variables and range of values because of the additive turbulence caused by wave motion [Kelberlau et al. 2020, Salcedo-Bosch et al. 2020a, Gutiérrez-Antuñano et al. 2018]. In Figure 8.7c, the difference between $TI_{float}$ and $TI_{fixed}$ increased with the HWS, because higher wind speeds cause higher wave motion [Jeffreys & Taylor 1925]. In Figure 8.7d, the difference between $TI_{float.}$ and $TI_{fixed}$ increased in with the increase in tilt and FDWL translational velocity.

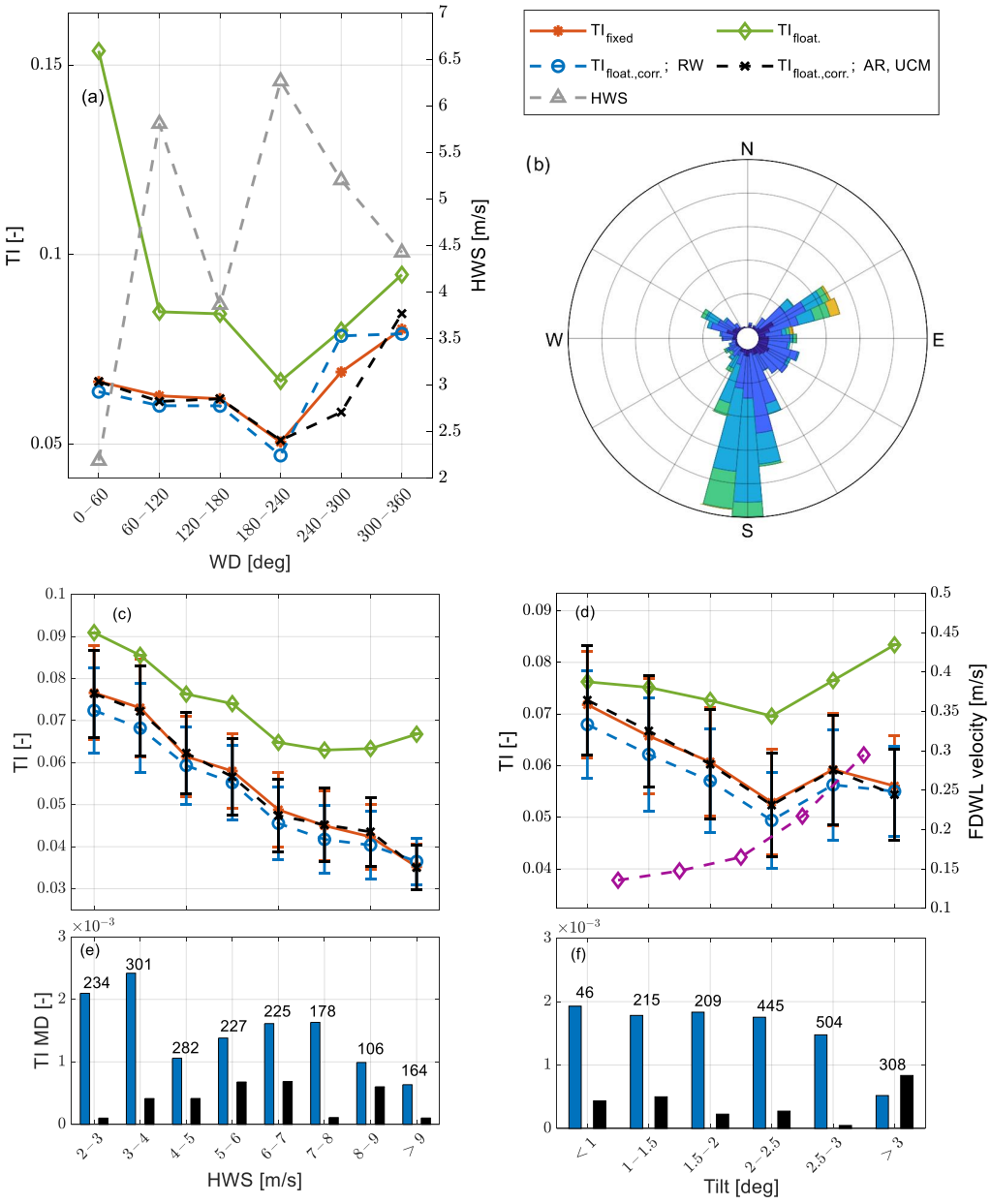


Figure 8.7: Motion correction performance as a function of different wind and wave-motion conditions clustered by (**a**) $WD$, (**c**) $HWS$ and (**d**) tilt. Panels (**a**,**c**,**d**): (Red trace with dots) Fixed-lidar mean $TI$. (Green trace with diamonds) FDWL mean $TI$ *before* motion correction. (Blue trace with circles) FDWL mean $TI$ *after* motion correction using the basic model combination. (Black trace with plus signs) Same as blue trace but for the enhanced model combination. Dispersion bars represent the 1-$\sigma$ dispersion of the data in each bin ($\simeq$68% percentile). Panel (**a**): (Gray trace with triangles, read on the right Y-axis) Fixed-lidar mean $HWS$. Panel (**d**): (Purple) trace with diamonds, read on the right Y-axis) FDWL mean translational velocity. (**e**,**f**) *Error bar analysis*: $TI$ Mean deviation bar charts (Equation (8.15), in absolute value) binned by $HWS$ and tilt angle, respectively. Blue and black bars stand for the basic and the enhanced model combinations, respectively. Values above the bars indicate the number of samples in each bin. Panel (**b**): PdP campaign wind rose.

Regarding Figure 8.7a (where $TI$ measurements were clustered in 60 deg wide bins), the $TI$ increased between 240 and 360 deg, which was due to winds coming from the urban area (see Figure 8.7b). The higher roughness of the urban terrain was also responsible for larger spatial and temporal variations in the wind field, which resulted in higher turbulence. The opposite was true for winds coming from the sea ($WD$s between 0 and 240 deg) because of the lower roughness of the sea surface [He et al. 2021]. It is known that lower roughness is directly related to higher wind speeds [Stull 1988]. Thus, the mean $HWS$ measured by the fixed DWL (gray trace) demonstrated peak values of 6.3 and 5.9 m/s for winds following the coast line ($WD$s between 60 and 120 deg and between 180 and 240 deg, respectively). In contrast, turbulent winds blowing from land ($WD$s between 240 and 360 deg) translated into lower $HWS$ values of 5.2 and 4.4 m/s.

Figure 8.7c depicts the $TI$ as a function of the mean $HWS$. $HWS$s were clustered into 2 m/s bins and speeds higher than 9 m/s were merged into a single bin (“>9” label) on account of the low number of samples available. When considering the reference $TI$ measured by the fixed lidar, $TI_{fixed}$, it decreased with the increase in the $HWS$. A suitable explanation for that is that at low $HWS$s, turbulence is mainly caused by thermal gradients (thermal turbulence) [Monin & Obukhov 1954], which smooth out with the increase in wind speeds [Kelberlau et al. 2020, Türk & Emeis 2010, MacEachern & İlhami Yıldız 2018]. In addition, it usually occurs that the $TI$ measured offshore tends to stabilize and even increment at high $HWS$ values due to the increased sea roughness induced by higher waves [Stull 1988, Türk & Emeis 2010, Lange et al. 2004]. However, this latter effect was not observed (Figure 8.7c) possibly because of the interfering effect caused by winds blowing from land (see Figure 8.7b).

In Figure 8.7d, the $TI$ is shown as a function of the FDWL tilt angle in 0.5 deg wide bins. Values higher than 3 deg were merged into a single bin (“>3” label). The reference $TI$, $TI_{fixed}$, exhibited high values at low tilt angles (<1 deg) and decreased with a virtually constant slope up to a 2.5 deg tilt. We hypothesize that this reduction in $TI$ was associated with higher $HWS$s that progressively smoothed out the thermal turbulence. In the last section of the curve, above 2.5 deg tilt, it is likely that higher $HWS$s made sea-surface roughness, rather than thermals, the dominant source of turbulence, and that this caused the small increase in $TI$ in the plot.

Overall, both the basic and the enhanced model combinations demonstrated a high level of motion correction, as shown in all Figure 8.7 panels, with $TI_{float.-corr.}$ matching almost ideally the reference $TI$, $TI_{fixed}$. On one hand, the basic model combination demonstrated a small over-correction of $TI_{float}$, which exhibited mean $TI_{float.-corr.}$ values below the reference $TI$, $TI_{fixed}$, in almost all ranges of values. This is in accordance with previous results [Salcedo-Bosch et al. 2021c]. On the other hand, the enhanced model combination demonstrated that the FDWL motion-corrected the $TI$, $TI_{float.-corr.}$, to be virtually identical to that of the fixed lidar, $TI_{fixed}$. In the bar charts of Figure 8.7e,f, it can be clearly observed that the enhanced model combination yielded

much lower $MD$s than the basic model for both binning variables and ranges of values. A limiting point arises in Figure 8.7a for winds coming from the urban area ($WD$s between 240 and 360 deg). For these $WD$s, the high spatial variability observed may invalidate the assumption of uniform wind during the DWL scan, which would not hold true for the motion-correction filter and would lead to filter divergence.

### 8.3.3 Numerical Analyses

Using numerical analyses, we compared the raw FDWL $TI$, $TI_{float.}$, and the corrected one by the different models, $TI_{float.-corr.}$, with the fixed-lidar reference $TI$, $TI_{fixed}$. The descriptive indicators used to quantitatively assess the statistical deviation between any two datasets were (i) the mean deviation ($MD$; defined in Equation (8.15)), (ii) the root-mean-squared error ($RMSE$), (iii) the coefficient of determination ($R^2$) and (iv) the slope and offset term of the Linear Regression (LR).

Table 8.2 shows the descriptive indicators obtained for the correlation variables and the model combinations indicated. The superior performance of the enhanced model with respect to the basic model and, in turn, that of the basic model with respect to the motion-uncorrected case are evident. Thus, without motion correction, the floating vs. fixed lidar $TI$ data attained an $R^2$ value of 0.90, an $RMSE$ of 1.87% and an MD of 1.62%. In addition, the LR was the poorest ($y = 0.96x + 0.02$). Using the basic model, the motion-correction filter improved the correlation to $R^2$ = 0.93, $RMSE$ = 0.81% and $MD$ = $-$0.32%. Still, the filter demonstrated its flaws in the form of an overcompensated $TI$. This was evidenced by a negative $MD$ ($MD$ = $-$0.32%), which was approximately one-fifth of the bias for the uncorrected case ($MD$ = 1.62%) in absolute value. Finally, the enhanced model attained almost ideal indicators: $R^2$ = 0.96, $RMSE$ = 0.58% and $MD$ = $-$0.07%. The latter indicator represents an $\simeq$80% reduction in $MD$ as compared with the basic model.

Table 8.2: Statistical indicators comparing the 10 min fixed-lidar to floating-lidar $TI$ (with and without motion compensation) using the "basic" and the "enhanced" models of Table 8.1.

| | **Uncorrected** | **Corrected (Basic)** | **Corrected (Enhanced)** |
|---|---|---|---|
| Correlated variables | $TI_{float.}$ vs. $TI_{fixed}$ | $TI_{float.-corr.}$ vs. $TI_{fixed}$ | $TI_{float.-corr.}$ vs. $TI_{fixed}$ |
| $R^2$ | 0.90 | 0.93 | 0.96 |
| $RMSE$ | 1.87% | 0.81% | 0.58% |
| $MD$ | 1.62% | $-$0.32% | $-$0.07% |
| Slope | 0.96 | 0.97 | 0.99 |
| Offset | $1.81 \times 10^{-2}$ | $1.70 \times 10^{-3}$ | $7.41 \times 10^{-4}$ |

The improved motion correction achieved by the enhanced model as compared with the basic model is shown in Figure 8.8 in terms of $TI$. Thus, the motion-corrected FDWL data points using the enhanced model (Figure 8.8b, blue points), $(TI_{fixed}, TI_{float.-corr.})$, became less scattered than the uncorrected ones (Figure 8.8a,b, black points), $(TI_{fixed}, TI_{float.})$, and less scattered than

the points corrected using the basic model (Figure 8.8a, red points). This reduction in scattering was best evidenced by the narrower minor axes in the associated standard-deviation ellipses. The major and minor axis directions of the ellipses are the eigenvectors of the data covariance matrix. The lengths of the semi-major and -minor axes are computed as the square root of the associated eigenvalues.

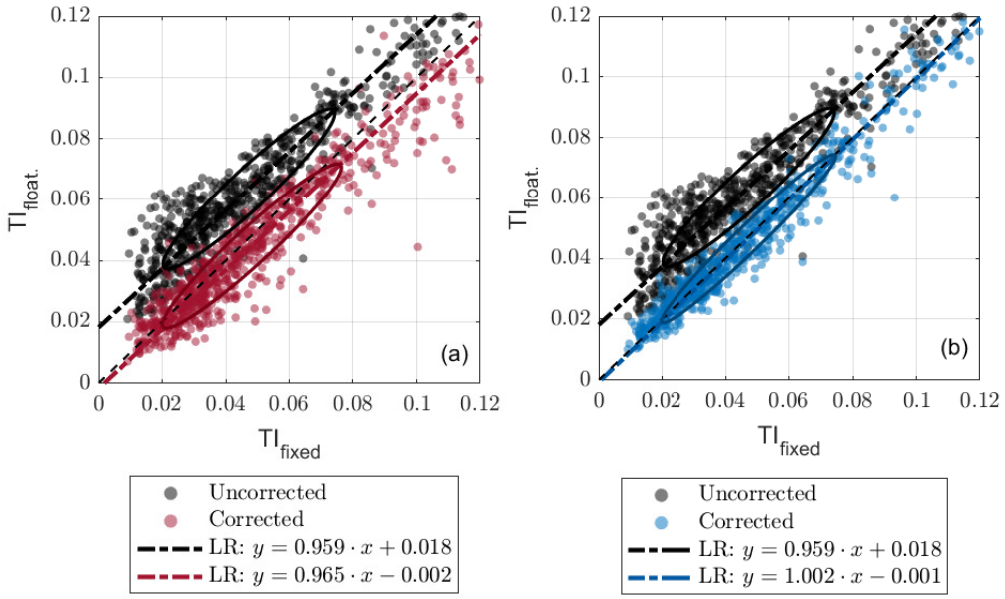


Figure 8.8: Comparison between the motion-corrected floating-lidar $TI$ (basic and enhanced models) and the fixed-lidar TI. (**a**) *Basic* model of Table 8.1 and (**b**) *enhanced* model. (Black dot-dashed line, *both panels*) Linear regression $TI_{float.}$ (uncorrected) on $TI_{fixed}$. (Red dot-dashed line, panel (**a**)) Linear regression $TI_{float.-corr.}$ on $TI_{fixed}$ for the basic model. (Blue dot-dashed line, panel (**b**)) Linear regression $TI_{float.-corr.}$ on $TI_{fixed}$ for the enhanced model. The minor axes of the ellipses delimit the population spread outside of the linear-regression line (see text).

When comparing the correction performance of the enhanced filter with previously published results in the state-of-the-art, the filter outperformed other methods [Gutiérrez-Antuñano et al. 2017, Gutiérrez-Antuñano et al. 2018] because of the demonstrated wind tracking capabilities under the different turbulent regimes (Figures 8.5a and 8.6b) and convergence in all motion scenarios. Without having access to the lidar internal LoS measurements, the enhanced filter attains similar correction accuracy as the motion compensation algorithm by Kelberlau et al. (2020) under similar wave ($tilt < 3$ deg) and wind conditions ($HWS < 10$ m/s). Yet, the outstanding feature of the UKF is that it is able to operate in a stand-alone run-time fashion, i.e., with no need to synchronize with the lidar measurement timestamps for data post-processing.

### 8.3.4 Method Limitations

First, the results demonstrated in this study are limited to the ZephIR-300 FDWL sounding at a *single height*. The single-height configuration was chosen in this study for its simplicity when assessing the comparative filter performance between the "basic" and the "enhanced" models. However, a typical configuration for this type of lidar is multiple-height sounding. Under this configuration, the filter has less information available from each individual measurement height because the observation time is divided into the number of sounding heights. The latter is due to the ZephIR lidar measuring the wind at multiple heights by following a sequential pattern. Therefore, filter performance (which was computed from the one-to-one correspondence between the motion-corrected measurements and the ones from the reference fixed lidar in Figure 8.8) is expected to degrade with an increasing number of sounding heights. See [Salcedo-Bosch et al. 2022c] for an in-depth discussion. A consequence of this poorer performance is that the enhanced filter will continue to be able to take the motion out "on average" over time but losing the fine detail of the wind time series.

Second, it is important to highlight that, in contrast to anemometers, continuous-wave focusable lidars measure a temporally- and spatially-averaged version of the wind vector. They assume a uniform wind flow during the lidar scan when retrieving the wind vector by means of the VAD algorithm. Therefore, in the turbulent conditions prevailing in the interference created by wind turbines (e.g., induction effect in the inflow and disturbance in the wake Micallef & Rezaeiha (2021)), DWLs cannot provide valid measurements of the wind field Gottschall (2020). Under these circumstances, the proposed AR and RW wind models are no longer valid for modeling such high turbulent flows, which may lead to filter divergence.

Finally, regarding filter convergence, the enhanced filter demonstrate itself able to successfully correct the corrupted wind measurements under all motional conditions in the mild near-shore scenario of the PdP campaign (FDWL mean translational velociy lower than 0.5 m/s, mean tilt amplitude lower than 3 deg and wave periods longer than 3 s). Provided correct measurement of the FDWL motion attitude by the IMUs (according to Nyquist criterion and sampling requirements [Shannon 1949]), which was always the case, the filter was at all times able to compensate for the motion-corrupted wind. Therefore, rougher conditions such as those occurring in open seas (higher tilt amplitudes about 5 deg and wave periods longer than 2 s [Salcedo-Bosch et al. 2021b]) or the hydrodynamics associated with floating offshore wind turbines [Gao et al. 2022] are not expected to affect the filter performance.

Although future research is to give further insight into harsher sea-wave and wind conditions, preliminary limits of filter convergence were analyzed via simulation. FDWL measurements were simulated from turbulent wind fields generated using the Mann model [Mann 1998]. The filter was found to be reliable under these extreme motional conditions: mean tilt $>$ 15 deg and mean translational velocity $>$ 2 m/s, provided that correct measurements of the FDWL attitude were

input from the IMUs. On the other hand, the filter was unable to track highly turbulent wind fields with TIs higher than $\simeq$30%.

## 8.4 Summary and Conclusions

Enhanced wind and lidar initial scan phase models for the FDWL motion-correction UKF filter by Salcedo-Bosch et al. (2021c) are presented. The novelty of the enhanced filter relies on the superior wind-tracking capabilities of the filter at a 10-min level under different turbulent regimes without having access to the lidar internal LoS measurements, nor to the lidar measurement timestamps for filter synchronization. The new UKF combines an AR wind model with a UCM initial-phase model, which supersedes the basic RW used for both the wind and initial-phase models in the previous filter. In addition, the state-space reformulation of the UKF along with an implementation based on a dual filter enables the fine removal of the motion-induced $TI$ as well as straightforward processing to be achieved.

Regarding the wind model, it is shown that while the former RW model can follow only up to the first lobe of the wind spectrum, an AR model of order 10 can reproduce high-frequency wind fluctuations up to 0.1 Hz. According to our experiments, the improvement was higher with the increase in the order of the AR process.

With respect to the lidar-scan model, the rotation of the wedge prism used for laser-beam steering is modeled assuming a uniform circular model. Our results demonstrate that this model clearly outperformed the RW model previously used, which inaccurately assumed a random uniform distribution of the initial phase.

As far as filter implementation is concerned, the dual UKF combines two filters working cooperatively (Figure 8.4): the main filter (UKF1), which is the motion-correction filter itself, and the auxiliary filter (UKF2), which estimates the AR wind-model coefficients. The main filter estimates the true wind-vector ($HWS$, $WD$ and $VWS$) and the initial scan phase given the AR coefficients estimated by the auxiliary filter, i.e., the IMU-measured 6 DoF motion of the floating lidar and the lidar-measured wind. The prediction step aims at estimating the true wind vector and initial phase prior to the assimilation of the present-time motion-corrupted wind. The innovation step aims at matching the present-time floating-lidar-measured wind vector to the filter-predicted motion-corrupted wind at each recursive cycle of the filter.

The dual-UKF motion-correction performance was validated over the 06 Jun–30 Jun 2013 intensive observation period during the PdP campaign in different wind and motional scenarios using big-data clustering. The enhanced model combination proved itself as the best candidate to address the FDWL motion compensation in all wind and motional scenarios and statistically demonstrated a virtually ideal correction. With reference to the 10 min fixed-lidar data, the $MD$ improved from 1.62% (floating lidar without motion correction) to $-0.07$% (with correction), while $R^2$ increased

from 0.90 to 0.96, and the $RMSE$ improved from 1.87% to 0.58%. Though the superior performance of the enhanced model as compared with the basic one is undeniable, the basic model also provided convergent results and acceptable indicators to correct the FDWL motion in most cases. At a finer level of detail, the enhanced model permitted the over-compensation issue of the basic model to be overcome thanks to its capability to track the high-frequency spectral fluctuations of wind turbulence (Figures 8.5 and 8.6). The latter proves the enhanced filter as a better candidate for the measurement of incoming wind disturbances in floating wind turbine control. Feasibility and convergence of the enhanced filter is discussed in Section 8.3.4.

All in all, this study demonstrates the importance of the accurate modeling of the wind turbulence spectrum, initial scan phase and motion dynamics for the successful removal of motion-induced turbulence in floating-lidar measurements. However, the filter was tested over experimental data measured under mild environmental conditions (Mediterranean shore). Future research is to extend this study to harsher scenarios. Furthermore, a better experimental set-up, having both the reference and the floating lidars beside each other, could help minimize wind-direction-induced errors when computing performance statistics. Finally, the filter needs to be tested with FDWLs configured to measure the wind at multiple heights.

# Chapter 9

# Conclusions and Outlook

## 9.1 Conclusions

The research conducted in this Ph.D. Thesis focused on the evaluation and improvement of FDWL capabilities in sensing atmospheric and ocean parameters with the aim to reduce the associated costs of offshore wind farms assessment phase. The work carried out was particularly centered on the effect of wave-induced motion on FDWL measurements of the wind. In this context, the scope of the main conclusions drawn from this work is two-fold: (i) motion-induced error estimation, and (ii) motion-induced error correction.

Regarding motion-induced error estimation:

1. **A unified analytical formulation of the 6-DoF-motion-induced-error on FDWLs was derived, being able to accurately estimate the 10-minute bias and TI increment observed in FDWLs.**

2. **The analytical model showed promising results in both near-shore and open-sea scenarios, proving its capabilities in a wide range of wind and motion scenarios.**

Regarding the motion-induced error correction:

1. **Motion compensation of FDWL wind measurements with an UKF showed promising results ($R^2 = 0.96$ in terms of TI), being able to correct the motion-induced error on-the-run without having access to the LiDAR LoS measurements (undisclosed by the manufacturer).**

2. **The motion-correction UKF was found to be able to compensate for the motion-induced error in all motional and wind scenarios studied.**

3. **The wind and initial scan phase models used by the motion-correction filters were found to have an important influence on the motion correction, being an AR model able to track the high frequencies of the wind process, opposite to a RW model.**

More detailed conclusions of this Ph.D. dissertation are given next:

### 9.1.1 On the Estimation of Ocean Waves Period from FDWL Measurements.

A new method (L-dB method) to estimate the wave period from roll and pitch records measured by a FDWL buoy was presented. By means of the spectral analysis of tilt measurements, the L-dB method showed itself able to estimate the wave period in the context of IJmuiden campaign with reference to classical oceanographic wave-period estimation methods by a wave buoy. For the estimation, the L-dB method considered only roll and pitch tilts and assumed negligible translational motion. The low-angle assumption enabled the formulation of the so-called eigenangle as a complex-number random process. Wave period was computed from the cut-off frequencies of the PSD of the eigenangle process.

By parameterizing the results as a function of L, it was found that the L-dB method was in close agreement with the zero-crossing and average wave-period definitions, and a threshold value L=8 dB exhibited the best statistical indicators when compared to the zero-crossing method. We reconciled the spectral approach to the oceanographic one, yielding the L-dB method fairly good results when compared against the Tryaxis$^{TM}$ wave buoy as a reference, with $\rho = 0.86$, $RMSE = 0.46$ s, and $MD = 0.02$ s.

All in all, the proposed L-dB method allowed FDWLs to increase the knowledge of sea state without relying on external equipment, which could enhance wind measurements and reduce offshore wind farms deployment cost.

### 9.1.2 On the Estimation of 6-Degrees-of-Freedom-Motion-Induced Errors in FDWLs.

A unified analytical formulation for the computation of the 6-DoF-motion-induced error in focusable CW FDWLs was presented. The formulation showed itself capable to estimate the HWS bias and TI increment at a 10-minute level. Rotational and translational motion effect on FDWL measurements were formulated separately and added assuming superposition. The VAD algorithm was computed as a first-order Fourier series, that allowed derivation of the sought-after analytical expressions that related attitude measurements to FDWL-measurement errors. The assumption of uniformly distributed random initial scan phase allowed the derivation of 10-min mean HWS bias and TI increment estimation expressions. The analytical model was numerically validated by means of a numerical simulator [Salcedo-Bosch et al. 2021a].

The analytical model was validated experimentally under two different scenarios, a near-shore scenario (PdP campaign) and an open-sea scenario (Ijmuiden campaign). The estimations of mean HWS bias yielded similar results to the measure ones. The TI increment estimates matched the measured values in statistical terms under all motion and wind scenarios.

The unified formulation proved to be a useful tool for evaluating the motion-induced error in focusable CW FDWLs in terms of both HWS-bias and TI-increment estimation.

### 9.1.3 On the Motion Compensation of FDWLs.

Two adaptive UKFs for motion compensation of ZephIR$^{TM}$ 300 FDWL wind measurements were presented and compared. Both filters proved to be capable of correcting the motion-induced error in the retrieved HWS and TI without accessing LiDAR LoS velocity measurements. The filters measurement models departed from the FDWL motion dynamics study by Kelberlau et al. (2020) and the VAD wind-retrieval algorithm to derive an ad-hoc state-space formulation of the problem from the point of view of control theory. The proposed filters differed in the state-vector transition models used: the so-called basic filter considered a RW model for the wind and initial scan phase processes, whereas the so-called enhanced filter considered an AR model for the wind process and an UCM model for the initial scan phase process. The latter combined two UKFs working cooperatively, i.e., the main and auxiliary filters, to recursively estimate the motion-free wind vector as well as the AR wind-model coefficients.

Both filters were validated over experimental data gathered during PdP campaign, by using the filters over FDWL-measured data and taking as a reference wind measurements from a fixed DWL 50-m appart. Their performance was analyzed and compared in terms of TI in different wind and motional scenarios using big-data clustering. The enhanced filter proved itself as the best candidate to address the FDWL motion compensation in all wind and motional scenarios and statistically demonstrated a virtually ideal correction. When comparing 10-minute TI measurements by the FDWL against the reference measured by the fixed DWL, all statistical indicators improved. With the enhanced filter, the coefficient of determination improved from $R^2 = 0.90$ (without correction) to $R^2 = 0.96$ (with correction), the RMSE from 1.87% to 0.58%, and the MD from 1.62% to -0.07%. Worse results were attained with the basic filter, with $R^2 = 0.93$, RMSE=0.81%, and MD=-0.32% after compensation. The latter was found to be attributable to the wind and initial phase models used, that were not able to track the high-frequency spectral fluctuations of the wind turbulence. Thus, the basic filter showed over-compensation of the motion-induced error on FDWL wind measurements.

All in all, the UKF demonstrated to be an effective tool for 6-DoF motion correction of FDWL measurements and accurate TI measurements. Furthermore, the recursive operation of the filter allowed room for stand-alone, nearly real-time correction of FDWL measurements.

## 9.2 Outlook

Future work should further validate the presented methods at additional locations and different LiDAR configurations.

The L-dB method for wave period estimation should be validated in other sites with different sea conditions such as near-shore scenarios where breaking waves can be found. In addition, its

reconciliation with other oceanographic wave period indicators, e.g., significant wave period, could be explored. Its applications in vessels and oceanographic buoys could also be of interest.

The unified analytical model for the estimation of motion-induced errors on FDWLs could be improved by considering motion spectral multi-modality and the wind flow variability within the LiDAR scanning cone. The study of the influence of the FDWL measurement height could also improve the accuracy of the method. Finally, it is worth exploring how the error estimation could be used for motion compensation and compare the obtained results with other methods in the state of the art.

The performance of the motion-correction UKFs for FDWL motion compensation should be studied in harsher scenarios such as open-sea scenarios where stronger wave motion and wind turbulence is observed. It is also worth studying how the FDWL measurement of the wind profile at different heights affects the filter performance. All in all, the study of FDWL motion compensation could benefit from a temptative implementation of the filter in a commercial FDWL during an assessment phase of a future offshore wind farm.

# Appendix A

# List of Publications

## A.1 Journals

1. **Salcedo-Bosch, A.**; Farré-Guarné, J.; Araújo da Silva, M.P.; Rocadenbosch, F. A Unified Formulation for the Computation of the Six-Degrees-of-Freedom-Motion-Induced Errors in Floating Doppler Wind LiDARs. Remote Sens. 2023, 15, 1478. https://doi.org/10.3390/rs15061478

2. **Salcedo-Bosch, A.**; Rocadenbosch, F.; Sospedra, J. Enhanced Dual Filter for Floating Wind Lidar Motion Correction: The Impact of Wind and Initial Scan Phase Models. Remote Sens. 2022, 14, 4704. https://doi.org/10.3390/rs14194704

3. Araújo da Silva, M.P.; Rocadenbosch, F.; Farré-Guarné, J.; **Salcedo-Bosch, A.**; González-Marco, D.; Peña, A. Assessing Obukhov Length and Friction Velocity from Floating Lidar Observations: A Data Screening and Sensitivity Computation Approach. Remote Sens. 2022, 14, 1394. https://doi.org/10.3390/rs14061394

4. **Salcedo-Bosch, A.**; Rocadenbosch, F.; Sospedra, J. A Robust Adaptive Unscented Kalman Filter for Floating Doppler Wind-LiDAR Motion Correction. Remote Sens. 2021, 13, 4167. https://doi.org/10.3390/rs13204167

5. **Salcedo-Bosch, A.**; Rocadenbosch, F.; Gutiérrez-Antuñano, M.A.; Tiana-Alsina, J. Estimation of Wave Period from Pitch and Roll of a Lidar Buoy. Sensors 2021, 21, 1310. https://doi.org/10.3390/s21041310

## A.2 International Conferences

(1) **Salcedo-Bosch, A.**; Rocadenbosch, F. On the performance of the unscented Kalman filter for floating Doppler wind LiDAR motion correction in an open-sea scenario. "IGARSS 2023 - 2023 IEEE International Geoscience and Remote Sensing Symposium: 16-21 July, 2023 Pasadena, U.S.". Institute of Electrical and Electronics Engineers (IEEE), 2023. Accepted.

(2) **Salcedo-Bosch, A.**; Rocadenbosch, F.; Araujo da Silva, M.P. Atmospheric stability classification from floating Doppler wind LiDAR measurements: a machine learning approach. "IGARSS 2023 - 2023 IEEE International Geoscience and Remote Sensing Symposium: 16-21 July, 2023 Pasadena, U.S.". Institute of Electrical and Electronics Engineers (IEEE), 2023. Accepted.

(3) Araujo da Silva, M.P.; Rocadenbosch, F.; **Salcedo-Bosch, A.**; Peña, A. Retrieving Monin-Obukhov dimensionless wind shear and stability from floating LiDAR observations. "IGARSS 2023 - 2023 IEEE International Geoscience and Remote Sensing Symposium: 16-21 July, 2023 Pasadena, U.S.". Institute of Electrical and Electronics Engineers (IEEE), 2023. Accepted.

(4) Araujo da Silva, M.P.; Rocadenbosch, F.; **Salcedo-Bosch, A.**; Peña, A. On the use of wind profiles to assess surface boundary-layer parameters. "IGARSS 2023 - 2023 IEEE International Geoscience and Remote Sensing Symposium: 16-21 July, 2023 Pasadena, U.S.". Institute of Electrical and Electronics Engineers (IEEE), 2023. Accepted.

5. **Salcedo-Bosch, A.**; Rocadenbosch, F.; Frasier, S.; Domínguez-Pla, P. Forward method for vertical air motion estimation from frequency modulated continuous wave radar rain measurements. A: European Conference on Radar in Meteorology and Hydrology. "ERAD 2022: book of extended abstracts: 11th European Conference on Radar in Meteorology and Hydrology: 29th August-02nd September 2022, Locarno, Switzerland". MeteoSwiss (Bundesamt für Meteorologie und Klimatologie MeteoSchweiz), 2022, p. 104-111.

6. **Salcedo-Bosch, A.**; Rocadenbosch, F.; Sospedra, J. On adaptive unscented Kalman filtering for floating Doppler wind-lidar motion correction: Effect of the number of lidar measurement heights. A: IEEE International Geoscience and Remote Sensing Symposium. "IGARSS 2022 - 2022 IEEE International Geoscience and Remote Sensing Symposium: 17-22 July, 2022 Kuala Lumpur, Malaysia: proceedings". Institute of Electrical and Electronics Engineers (IEEE), 2022, p. 6578-6581. ISBN 978-1-6654-2792-0. DOI 10.1109/IGARSS46834.2022.9884115.

7. **Salcedo-Bosch, A.**; Rocadenbosch, F.; Sospedra, J. "Influence of the number of lidar sounding heights on Adaptive Unscented Kalman Filtering for Floating Doppler wind-lidar motion correction", EGU General Assembly 2022, Vienna, Austria, 23–27 May 2022, EGU22-9818, https://doi.org/10.5194/egusphere-egu22-9818, 2022.

8. **Salcedo-Bosch, A.**; Domínguez-Pla, P.; Rocadenbosch, F.; Frasier, S. J. "Numerical Solver for Vertical Air Motion Estimation," IGARSS 2022 - 2022 IEEE International Geoscience and Remote Sensing Symposium, Kuala Lumpur, Malaysia, 2022, pp. 7193-7196, doi: 10.1109/IGARSS46834.2022.9884354.

9. **Salcedo-Bosch, A.**; Farré-Guarné, J.; Sala-Álvarez, J.; Villares-Piera, J.; Tanamachi, R. L.; Rocadenbosch, F. "Floating Doppler Wind Lidar Motion Simulator for Horizontal Wind Speed Measurement Error Assessment," 2021 IEEE International Geoscience and Remote Sensing Symposium IGARSS, Brussels, Belgium, 2021, pp. 7716-7719, doi: 10.1109/IGARSS47720.2021.9555023.

10. **Salcedo-Bosch, A.**; Farré-Guarné, J.; Sala-Álvarez, J.; Villares-Piera, J.; Tanamachi, R. L.; Rocadenbosch, F. "Horizontal wind speed motion-induced error assessment on a floating Doppler wind lidar," 2021 European Geosciences Union General Assembly, Online, 19–30 Apr 2021, EGU21-7656, https://doi.org/10.5194/egusphere-egu21-7656, 2021.

11. **Salcedo-Bosch, A.**; Gutierrez-Antunano, M. A.; Tiana-Alsina, J.; Rocadenbosch, F. "Floating Doppler Wind Lidar Measurement of Wind Turbulence: A Cluster Analysis," IGARSS 2020 - 2020 IEEE International Geoscience and Remote Sensing Symposium, Waikoloa, HI, USA, 2020, pp. 6077-6080, doi: 10.1109/IGARSS39084.2020.9323578.

12. **Salcedo-Bosch, A.**; Rocadenbosch, F.; Gutierrez-Antunano, M. A.; Tiana-Alsina, J. "Motional Behavior Estimation Using Simple Spectral Estimation: Application to The Off-Shore Wind Lidar," IGARSS 2020 - 2020 IEEE International Geoscience and Remote Sensing Symposium, Waikoloa, HI, USA, 2020, pp. 5682-5685, doi: 10.1109/IGARSS39084.2020.9323801.

13. Araujo da Silva, M. P.; **Salcedo-Bosch, A.**; Gutierrez-Antunano M. A.; Rocadenbosch, F. "Offshore Doppler Wind LiDAR Assessment of Atmospheric Stability," IGARSS 2020 - 2020 IEEE International Geoscience and Remote Sensing Symposium, Waikoloa, HI, USA, 2020, pp. 6081-6084, doi: 10.1109/IGARSS39084.2020.9324044.

## A.3 Co-Advised BSc and MSc Theses

1. Farré Guarné, Joan. 2022. "Floating Doppler Wind Lidar: Assessment of the Sea-Motion-Induced Error in the Retrieved Wind Vector." Projecte Final de Màster Oficial, UPC, Escola Tècnica Superior d'Enginyeria de Telecomunicació de Barcelona, Departament de Teoria del Senyal i Comunicacions. Advisors: A. Salcedo-Bosch and Prof. F. Rocadenbosch. http://hdl.handle.net/2117/377557.

2. Domínguez Pla, Paula. 2022. "Rainfall Radar Observations in the U.S. VORTEX-SE Campaign: VAM Correction of Doppler Spectra to Improve Data Quality." Treball Final de Grau, UPC, Escola Tècnica Superior d'Enginyeria de Telecomunicació de Barcelona, Departament de Teoria del Senyal i Comunicacions. Advisors: A. Salcedo-Bosch and Prof. F. Rocadenbosch. http://hdl.handle.net/2117/378106.

3. Farré Guarné, Joan. 2021. "Assessment of Sea-Motion Influence on Wind Vector Retrieval and Atmospheric Stability Estimation by Doppler Wind Lidar." Treball Final de Grau, UPC, Escola Tècnica Superior d'Enginyeria de Telecomunicació de Barcelona, Departament de Teoria del Senyal i Comunicacions. Advisors: A. Salcedo-Bosch and Prof. F. Rocadenbosch. http://hdl.handle.net/2117/355747.

# Appendix B

# Power-Spectral-Density Derivation

*Appendix related to Chapter 5.*

Next, we compute the PSD associated to the time variations of eigenangle $\alpha$, given by Equation 5.17. Using the superposition principle described by Equation 5.17 and illustrated in Figure 5.4a, where pitch and roll contributions add up in quadrature, $\alpha$ can be described in a straightforward form by means of time-varying complex function

$$\boldsymbol{\alpha(t)} = \theta(t) - j\phi(t), \tag{B.1}$$

where bold is used to denote a complex number.

The PSD of a complex random process, $\boldsymbol{\alpha(t)}$, is defined as the Fourier transform of the autocorrelation function. Formally,

$$S_{\boldsymbol{\alpha},\boldsymbol{\alpha}}(f) = \int_{-\infty}^{\infty} R_{\alpha,\alpha}(\tau) e^{-i2\pi f\tau} d\tau, \tag{B.2}$$

where $R_{\boldsymbol{\alpha},\boldsymbol{\alpha}}(\tau)$ is the autocorrelation of $\boldsymbol{\alpha}$ Proakis & Manolakis (2006), $\tau$ is the time lag, and $f$ is the frequency. The autocorrelation of a complex process is defined as Proakis & Manolakis (2006)

$$R_{x,x}(\tau) = E[x(t)x^*(t+\tau)], \tag{B.3}$$

where * denotes complex conjugate.

By inserting Equation B.1 into Equation B.3 above. the autocorrelation function of random complex process $\boldsymbol{\alpha(t)}$ yields

$$R_{\boldsymbol{\alpha},\boldsymbol{\alpha}}(\tau) = R_{\phi,\phi}(\tau) + R_{\theta,\theta}(\tau) + j[R_{\theta,\phi}(\tau) - R_{\phi,\theta}(\tau)]. \tag{B.4}$$

Using that $R_{\phi,\theta}(\tau) = R^*_{\theta,\phi}(-\tau)$ (using similar definition to Equation B.3 but for the cross-correlation between random processes $\theta(t)$ and $\phi(t)$, Bracewell (2000)) Equation B.4 above reduces to

$$R_{\boldsymbol{\alpha},\boldsymbol{\alpha}}(\tau) = R_{\phi,\phi}(\tau) + R_{\theta,\theta}(\tau) + j[R_{\theta,\phi}(\tau) - R^*_{\phi,\theta}(-\tau)]. \tag{B.5}$$

By inserting Equation B.5 into the PSD definition of Equation B.2 and using that:

(i) the cross-PSD (also called cross spectral density) between two processes $x(t)$ and $y(t)$ is the Fourier transform (***FT***) of the cross-correlation function, $S_{x,y} = \int_{-\infty}^{\infty} R_{x,y}(\tau)e^{-i2\pi f\tau}d\tau$, and that

(ii) $R^*_{\theta,\phi}(\tau) \rightarrow S^*_{\theta,\phi}(f)$ according to the $FT$ conjugation property, $x^*(t) \rightarrow X^*(-f)$, with $X$ the $FT$ of signal $x(t)$ and the arrow symbol denoting $FT$,

the PSD of $\boldsymbol{\alpha}$ is obtained as

$$S_{\boldsymbol{\alpha},\boldsymbol{\alpha}}(f) = S_{\theta,\theta}(f) + S_{\phi,\phi}(f) + j[S_{\theta,\phi}(f) - S^*_{\theta,\phi}(f)]. \tag{B.6}$$

The terms into square brackets on the right side of Equation B.6 can be recognized as the complex subtraction, $z - z^* = 2iIm(z)$, with $z = S_{\theta,\phi}(f)$ and $Im(\dot{})$ denoting the imaginary part. Therefore,

$$S_{\boldsymbol{\alpha},\boldsymbol{\alpha}}(f) = S_{\theta,\theta}(f) + S_{\phi,\phi}(f) - 2Im[S_{\theta,\phi}(f)], \tag{B.7}$$

with units of $[rad^2/Hz]$.

# Appendix C

# Formulation compendium

*Appendix related to Chapter 6.*

This Appendix provides exhaustive details for the formulation of the 6-DoF-motion-induced error. Specifically, Section C.1 addresses first-order approximation of the Euler rotation matrix, $\boldsymbol{R}$, in connection with Equation 6.20 and 6.21. Section C.2 tackles calculation of the LoS-projected wind vector under rotational motion to obtain VAD function $f_{rot}(\phi)$. The first-order Fourier coefficient under rotational and translational motion are formulated in Sections C.3 and C.4, respectively, by using the auxiliary integrals given in Section C.5.

Refer to Section 6.4.1 and Figures 6.5, 6.6, and 6.7 for quality assurance.

## C.1 First-order Approximation of the Rotation Matrix

The Euler rotation matrix, $\boldsymbol{R}$, is the result of elemental rotations about the N, E, and D axes, $\boldsymbol{R_N}$, $\boldsymbol{R_E}$, and $\boldsymbol{R_D}$, respectively, representing roll, pitch, and yaw rotations. Inserting Equation 6.21 into Equation 6.20 and retaining first-order terms yields:

$$\boldsymbol{R} \simeq \begin{bmatrix} \cos(\Omega_y) & -\sin(\Omega_y) & \sin(\Omega_y)\cdot\Omega_r(\phi) + \cos(\Omega_y)\cdot\Omega_p(\phi) \\ \sin(\Omega_y) & \cos(\Omega_y) & -\cos(\Omega_y)\cdot\Omega_r(\phi) + \sin(\Omega_y)\cdot\Omega_p(\phi) \\ -\Omega_p(\phi) & \Omega_r(\phi) & 1 \end{bmatrix}, \tag{C.1}$$

where $\Omega_x$, $x = r, p, y$ is the tilt angle already defined in Equation 6.19. $r, p, y$ is shorthand notation for "roll", "pitch", and "yaw".

## C.2 Wind-vector Projection Over the Rotated Lidar Pointing Vector

In rotational motion, the FDWL-measured wind as a function of the scan phase, $f_{rot}(\phi)$, is the projection of the wind vector $\vec{u}$ on the lidar pointing vector $\hat{r}_{rot}(\phi)$. Inserting Equation 6.12 and Equation C.1 into Equation 6.22 gives $\hat{r}_{rot}(\phi)$, and substituting this vector and definitional Equation 6.1 for the wind vector into Equation 6.23 gives the VAD function for the measured wind. The

result can be expressed as follows:

$$\begin{aligned} f_{rot}(\phi) = \vec{u} \cdot \hat{r}_{rot}(\phi) = HWS \cdot [\cos(WD) \cdot (\sin(\theta_0) \cdot [\cos(\phi - \phi_0) \cdot r_{11} + \sin(\phi - \phi_0) \cdot r_{12}] \\ - \cos(\theta_0) \cdot r_{13}) + \sin(WD) \cdot (\sin(\theta_0) \cdot [\cos(\phi - \phi_0) \cdot r_{21} + \sin(\phi - \phi_0) \cdot r_{22}] \\ - \cos(\theta_0) \cdot r_{23})] + VWS \cdot (\sin(\theta_0) \cdot [\cos(\phi - \phi_0) \cdot r_{31} + \sin(\phi - \phi_0) \cdot r_{32}] \\ - \cos(\theta_0) \cdot r_{33}), \end{aligned} \tag{C.2}$$

where coefficients $r_{ij}, i, j = 1..3$ are the entries in the $i$-th row and $j$-th column of the rotation matrix $\boldsymbol{R}$ (Equation C.1).

## C.3 Fourier Coefficients for the Rotational Motion Model

In rotational motion of the FDWL (Section 6.3.5.1), the first-order Fourier coefficients $a_1^{rot}$ and $b_1^{rot}$ of Equation 6.24 that give the HWS rotational error are obtained in analytical form by inserting Equation C.2 above into definitional Equation 6.18. They take the following form:

$$\begin{aligned} a_1^{rot} = \frac{1}{\pi} \int_0^{2\pi} f_{rot}(\phi) \cos(\phi) d\phi = \frac{1}{\pi} HWS \cdot [\cos(WD) \cdot (\sin(\theta_0) \cdot [\cos(y) I_{11} \\ - \sin(y) I_{12}] - \cos(\theta_0) \cdot [A_r \sin(y) I_{1,r} + A_p \cos(y) I_{1,p}]) \\ + \sin(WD) \cdot (\sin(\theta_0) \cdot [\sin(y) I_{11} + \cos(y) I_{12}] \\ - \cos(\theta_0) \cdot [-A_r \cos(y) I_{1,r} + A_p \sin(y) I_{1,p}])], \end{aligned} \tag{C.3}$$

and

$$\begin{aligned} b_1^{rot} = \frac{1}{\pi} \int_0^{2\pi} f_{rot}(\phi) \sin(\phi) d\phi = \frac{1}{\pi} HWS \cdot [\cos(WD) \cdot (\sin(\theta_0) \cdot [\cos(y) I_{21} \\ - \sin(y) I_{22}] - \cos(\theta_0) \cdot [A_r \sin(y) I_{2,r} + A_p \cos(y) I_{2,p}]) \\ + \sin(WD) \cdot (\sin(\theta_0) \cdot [\sin(y) I_{21} + \cos(y) I_{22}] \\ - \cos(\theta_0) \cdot [-A_r \cos(y) I_{2,r} + A_p \sin(y) I_{2,p}])], \end{aligned} \tag{C.4}$$

where coefficients $I_{mn}$ and $I_{m,x}$ with $m, n = 1, 2$ and $x = r, p$ are the auxiliary integrals of Table C.1. Mnemonic subscript $m = 1$ ($m = 2$) refers to Fourier coefficient $a_1$ ($b_1$), and as mentioned, subscripts $r$ and $p$ denote "roll" and "pitch", respectively.

## C.4 Fourier Coefficients for the Translational-Motion Model

In translational motion, the FDWL-measured wind as a function of the scan phase, $f_{trans}(\phi)$ (Equation 6.28), is the projection of the apparent wind vector (Equation 6.27) on the lidar pointing vector (Equation 6.12). The first step towards computing the Fourier coefficients is, therefore, computation of the apparent wind by substituting translational-velocity vector Equation 6.26 and definitional Equation 6.1 for the wind vector into Equation 6.27. The second step is substituting Equation 6.27

for the measured wind and Equation 6.12 for the lidar pointing vector into Equation 6.28 which gives the VAD function for the measured wind, $f_{trans}(\phi)$.

Finally, first-order Fourier coefficients $a_1^{trans}$ and $b_1^{trans}$ in Equation 6.29, giving the HWS translational error, are derived in analytical form by inserting Equation 6.28 into definitional Equation 6.18. This gives

$$\begin{aligned} a_1^{trans} = \frac{1}{\pi}\int_0^{2\pi} f_{trans}(\phi)\cos(\phi)d\phi = \frac{1}{\pi}\cdot(\sin(\theta_0)\cdot[HWS\cdot(\cos(WD)I_{11} \\ +\sin(WD)I_{12}) - A_{su}\cdot I_{11,su} - A_{sw}\cdot I_{12,sw}] \\ +A_h\cdot\cos(\theta_0)\cdot I_{1,h}), \end{aligned} \tag{C.5}$$

and

$$\begin{aligned} b_1^{trans} = \frac{1}{\pi}\int_0^{2\pi} f_{trans}(\phi)\sin(\phi)d\phi = \frac{1}{\pi}\cdot(\sin(\theta_0)\cdot[HWS\cdot(\cos(WD)I_{21} \\ +\sin(WD)I_{22}) - A_{su}\cdot I_{21,su} - A_{sw}\cdot I_{22,sw}] \\ +A_h\cdot\cos(\theta_0)\cdot I_{2,h}), \end{aligned} \tag{C.6}$$

where coefficients $I_{mn}$, $I_{m,x}$, and $I_{mn,x}$ with $m, n = 1, 2$ and $x = su, sw, h$ are the auxiliary integrals of Table C.1. As mentioned, mnemonic subscript $m = 1$ ($m = 2$) refers to Fourier coefficient $a_1$ ($b_1$). Subscripts $su$, $sw$, and $h$ denote "surge", "sway", and "heave", respectively.

## C.5 Auxiliary Integrals

| Coef. | $g(\phi)$ | $\int_0^{2\pi} g(\phi)\, d\phi$ |
|---|---|---|
| $I_{11}$ | $\cos(\phi)\cdot\cos(\phi-\phi_0)$ | $\pi\cdot\cos(\phi_0)$ |
| $I_{12}$ | $\cos(\phi)\cdot\sin(\phi-\phi_0)$ | $-\pi\cdot\sin(\phi_0)$ |
| $I_{21}$ | $\sin(\phi)\cdot\cos(\phi-\phi_0)$ | $\pi\cdot\sin(\phi_0)$ |
| $I_{22}$ | $\sin(\phi)\cdot\sin(\phi-\phi_0)$ | $\pi\cdot\cos(\phi_0)$ |
| $I_{1,x}$ | $\cos(\phi)\cdot\sin(f_x\phi-\alpha_x)$ | $-\frac{f_x}{f_x^2-1}\cdot[\cos(\alpha_x-2\pi f_x)-\cos(\alpha_x)]$<br>if $f_x=1\longrightarrow -\pi\sin(\alpha_x)$ |
| $I_{2,x}$ | $\sin(\phi)\cdot\sin(f_x\phi-\alpha_x)$ | $-\frac{1}{f_x^2-1}\cdot[\sin(\alpha_x-2\pi f_x)-\sin(\alpha_x)]$<br>if $f_x=1\longrightarrow \pi\cos(\alpha_x)$ |
| $I_{11,x}$ | $\cos(\phi)\cdot\cos(\phi-\phi_0)\cdot\sin(f_x\phi-\alpha_x)$ | $\frac{1}{f_x(f_x^2-4)}[f_x\sin(\phi_0)A_x-(f_x^2-2)\cos(\phi_0)B_x]$<br>if $f_x=2\longrightarrow \frac{\pi}{2}\sin(\alpha_x-\phi_0)$ |
| $I_{12,x}$ | $\cos(\phi)\cdot\sin(\phi-\phi_0)\cdot\sin(f_x\phi-\alpha_x)$ | $\frac{1}{f_x(f_x^2-4)}[f_x\cos(\phi_0)A_x+(f_x^2-2)\sin(\phi_0)B_x]$<br>if $f_x=2\longrightarrow \frac{\pi}{2}\cos(\alpha_x-\phi_0)$ |
| $I_{21,x}$ | $\sin(\phi)\cdot\cos(\phi-\phi_0)\cdot\sin(f_x\phi-\alpha_x)$ | $\frac{1}{f_x(f_x^2-4)}[f_x\cos(\phi_0)A_x+2\sin(\phi_0)B_x]$<br>if $f_x=2\longrightarrow \frac{\pi}{2}\cos(\alpha_x-\phi_0)$ |
| $I_{22,x}$ | $\sin(\phi)\cdot\sin(\phi-\phi_0)\cdot\sin(f_x\phi-\alpha_x)$ | $\frac{1}{f_x(f_x^2-4)}[-f_x\sin(\phi_0)A_x+2\cos(\phi_0)B_x]$<br>if $f_x=2\longrightarrow \frac{\pi}{2}\sin(\alpha_x-\phi_0)$ |
| | where:<br>$x\in[r=roll, p=pitch$<br>$su=surge, sw=sway, h=heave]$ | being:<br>$A_x=\sin(\alpha_x)(1-\cos(2\pi f_x))$<br>$+\cos(\alpha_x)\sin(2\pi f_x)$<br>$B_x=\sin(\alpha_x)\sin(2\pi f_x)$<br>$-\cos(\alpha_x)(1-\cos(2\pi f_x))$ |

Table C.1: Auxiliary integrals for computation of the rotational- and translational-motion Fourier coefficients given by Equation C.3–Equation C.4 and Equation C.5–Equation C.6, respectively. *Note* that not all possible subscript combinations are simultaneously used.

# Appendix D

# Kalman Filter Review

*Appendix related to Chapter 7.*

This Section summarizes the study on UKF by Wan & Van Der Merwe (2000), for self-completeness of the theoretical foundations given in Section 7.2.3. The reader is referred to this reference for further insight.

The Kalman Filter (KF) is a recursive filter that optimally estimates the internal (i.e., hidden) state-vector of a linear dynamic system from noisy observations, as described in Section 7.2.3. The KF is the optimal estimator for linear systems under a statistical minimum-variance criterion over time. In contrast, the Extended Kalman Filter (EKF) is one of the most widely used methods to estimate the state variables of non-linear systems, as is the case of moving FDWLs. The main limitation of the EKF is that it linearizes system non-linearities by first-order Taylor's series expansion. This implies propagation of the random variables distribution (RVD) through the system equations, which usually leads to large errors in the statistical moments of the transformed variables and, hence, to sub-optimal filter performance. The Unscented Kalman Filter (UKF) provides an elegant solution to solve these weaknesses [Wan & Van Der Merwe 2000].

## D.1 The Unscented Transform

The UKF addresses the RVD approximation errors of the EKF by means of the Unscented Transform (UT). In the UT, a set of samples representative of the mean and covariance of the RVD are chosen. These samples are propagated through the non-linear dynamics of the system, to accurately capture the system-propagated RVD mean and covariance. This is formulated in the following:

Consider an $N$-dimensional random variable $\boldsymbol{x}$ (e.g., the state-vector previously introduced in Section 7.2.3) with mean $\overline{\boldsymbol{x}}$ and covariance $\boldsymbol{P_x}$ propagating through a non-linear function $f(\cdot)$ (e.g., the state-transition function of Section 7.2.3), $\boldsymbol{y} = f(\boldsymbol{x})$. The UT chooses a set of $2N + 1$ auxiliary vectors (the so-called *sigma vectors*), $\boldsymbol{\chi_i}$, to estimate the RVD [Julier & Uhlmann 1997]. Their sample

mean and sample covariance are $\overline{\boldsymbol{x}}$ and $\boldsymbol{P}_x$, respectively. The *sigma vectors* are chosen as

$$\boldsymbol{\chi}_0 = \overline{\boldsymbol{x}} \tag{D.1}$$

$$\boldsymbol{\chi}_i = \overline{\boldsymbol{x}} + (\sqrt{(L+\lambda)\boldsymbol{P}^{xx}})_i \qquad i = 1, \ldots, L \tag{D.2}$$

$$\boldsymbol{\chi}_i = \overline{\boldsymbol{x}} - (\sqrt{(L+\lambda)\boldsymbol{P}^{xx}})_i \qquad i = L+1, \ldots, 2L, \tag{D.3}$$

where $(\sqrt{(L+\lambda)\boldsymbol{P}^{xx}})_i$ denotes the $i^{\text{th}}$ row of the square-root matrix, and $\lambda$ is a scaling parameter (typically, $\lambda = 3 - N$ for Gaussian distributions). When *sigma* vectors $\boldsymbol{\chi}$ propagate through the non-linear function $f(\boldsymbol{x})$, a transformed variable set, $\boldsymbol{v_i}$, is obtained,

$$\boldsymbol{v}_i = f(\boldsymbol{\chi}^i). \tag{D.4}$$

The sought-after mean and covariance of system output variable $\boldsymbol{y}$ are approximated as a weighted mean of the propagated sigma points,

$$\overline{\boldsymbol{y}} \simeq \sum_{i=0}^{2N} W_i^m \boldsymbol{v}^i, \tag{D.5}$$

$$\boldsymbol{P}^{yy} \simeq \sum_{i=0}^{2N} W_i^m (\boldsymbol{v}^i - \overline{\boldsymbol{y}})(\boldsymbol{v}^i - \overline{\boldsymbol{y}})^T, \tag{D.6}$$

where the weights are defined as

$$W_0^m = W_0^c = \lambda/(N+\lambda), \tag{D.7}$$

$$W_i^m = W_i^c = 1/(2(N+\lambda)). \tag{D.8}$$

## D.2 The Unscented Kalman Filter

The UKF uses the UT to estimate the RVDs of both the state-vector and the observation vector. The recursive algorithm of the filter can be summarized by the following ten-step procedure:

*Step 1.* Initialize the filter with the initial-guess state-vector and state-vector covariance, as:

$$\hat{\boldsymbol{x}}_0 = E[\boldsymbol{x}_k^T] \tag{D.9}$$

$$\hat{\boldsymbol{P}}_0^{xx} = E\left[(\boldsymbol{x}_0 - \hat{\boldsymbol{x}}_0)(\boldsymbol{x}_0 - \hat{\boldsymbol{x}}_0)^T\right]. \tag{D.10}$$

*Step 2.* Calculate the sigma points at discrete time $k-1$, used as a proxy of the state-vector RVD (see Appendix D.1), as:

$$\boldsymbol{\chi}_{k-1} = \left[\hat{\boldsymbol{x}}_{k-1} \quad \boldsymbol{x}_{k-1} \pm \sqrt{(L + \hat{\boldsymbol{P}}_{k-1|k-1}^{xx})}\right]. \tag{D.11}$$

*Step 3.* Compute the sigma-points output at time $k$, in response to the sigma points input at time $k-1$, by the system state-transition function, $f(\cdot)$, as:

$$\boldsymbol{\chi}_{k|k-1} = f(\boldsymbol{\chi}_{k-1}). \tag{D.12}$$

*Step 4.* Obtain the predicted *a priori* state-vector mean and covariance matrix at time $k$, as:

$$\overline{\boldsymbol{x}}_{k|k-1} = \sum_{i=0}^{2N} W_i^m \boldsymbol{\chi}_{k|k-1}^i \tag{D.13}$$

$$\boldsymbol{P}_{k|k-1}^{xx} = \sum_{i=0}^{2N} W_i^c [\boldsymbol{\chi}_{k|k-1}^i - \overline{\boldsymbol{x}}_{k|k-1}][\boldsymbol{\chi}_{k|k-1}^i - \overline{\boldsymbol{x}}_{k|k-1}]^T + \boldsymbol{Q}_k, \tag{D.14}$$

where $\boldsymbol{Q}_k$ is the state-noise covariance matrix defined in Section 7.2.7.

*Step 5.* Propagate the sigma-points set computed in Step 3 above, through the non-linear measurement function $h(\cdot)$, to obtain the so-called *sigma-Z* points, as:

$$\boldsymbol{Z}_{k|k-1} = h(\boldsymbol{\chi}_{k|k-1}). \tag{D.15}$$

*Step 6.* Estimate the mean and covariance of the *innovation* set at time $k$ from the obtained sigma-Z points and observation-noise covariance matrix, $\boldsymbol{R}_k$ (refer to Section 7.2.7),

$$\overline{\boldsymbol{z}}_{k|k-1} = \sum_{i=0}^{2N} W_i^m \boldsymbol{Z}_{k|k-1}^i. \tag{D.16}$$

$$\boldsymbol{P}_{k|k-1}^{zz} = \sum_{i=0}^{2N} W_i^c [\boldsymbol{Z}_{k|k-1}^i - \overline{\boldsymbol{z}}_{k|k-1}][\boldsymbol{Z}_{k|k-1}^i - \overline{\boldsymbol{z}}_{k|k-1}]^T + \boldsymbol{R}_k. \tag{D.17}$$

In Equation (D.17) above, $\boldsymbol{Z}$ denotes the sigma-Z points in the UT domain, whereas $\boldsymbol{z}$ denotes the observation vector in the "non-transformed" measurement domain (e.g., the LiDAR wind-vector measurements). An overbar is used to indicate the approximated mean, by means of the UT as computed in Appendix D.1.

*Step 7.* Compute the *a priori* state-vector covariance matrix at time $k$, as the cross covariance between $\overline{\boldsymbol{x}}_{k|k-1}$ and $\overline{\boldsymbol{z}}_{k|k-1}$:

$$\boldsymbol{P}_{k|k-1}^{xz} = \sum_{i=0}^{2N} W_i^c [\boldsymbol{\chi}_{k|k-1}^i - \overline{\boldsymbol{x}}_{k|k-1}][\boldsymbol{Z}_{k|k-1}^i - \overline{\boldsymbol{z}}_{k|k-1}]^T. \tag{D.18}$$

*Step 8.* Derive the Kalman gain as

$$\boldsymbol{K}_k = \boldsymbol{P}_{k|k-1}^{xz} (\boldsymbol{P}_{k|k-1}^{zz})^{-1}. \tag{D.19}$$

*Step 9.* Compute the *a posteriori* state-vector and *a posteriori* covariance as:

$$\hat{\boldsymbol{x}}_k = \overline{\boldsymbol{x}}_{k|k-1} + K_k(\boldsymbol{z}_k - \overline{\boldsymbol{z}}_{k|k-1}) \tag{D.20}$$

$$\hat{\boldsymbol{P}}_{k|k}^{xx} = \boldsymbol{P}_{k|k-1}^{xx} - \boldsymbol{P}_{k|k-1}^{zz} - \boldsymbol{K}_k \boldsymbol{P}_{k|k-1}^{zz} \boldsymbol{K}^T. \tag{D.21}$$

*Step 10.* (Recursive step) Time update and go to Step 2:

$$\hat{\boldsymbol{x}}_{k-1} = \hat{\boldsymbol{x}}_k \tag{D.22}$$

$$\hat{\boldsymbol{P}}_{k-1|k-1}^{xx} = \hat{\boldsymbol{P}}_{k|k}^{xx}. \tag{D.23}$$

**Algorithm 1:** UKF algorithm [Julier & Uhlmann 1997].

1: **Initialize:**
$\hat{\boldsymbol{x}}_0 = E[\boldsymbol{x}_0]$
$\hat{\boldsymbol{P}}_0^{xx} = E[(\boldsymbol{x}_0 - \hat{\boldsymbol{x}}_0)(\boldsymbol{x}_0 - \hat{\boldsymbol{x}}_0)^T]$
2: **Calculate Sigma-points:**
$\boldsymbol{\chi}_{k-1} = \left[\hat{\boldsymbol{x}}_{k-1} \quad \hat{\boldsymbol{x}}_{k-1} \pm \sqrt{L + \hat{\boldsymbol{P}}_{k-1}^{xx}}\right]$
3: **Prediction step (estimate $\boldsymbol{x}_k$ based on prior information):**
Propagate $\boldsymbol{\chi}_{k-1}$ through state-transition function:
$\boldsymbol{\chi}_{k|k-1} = f(\boldsymbol{\chi}_{k-1})$
Obtain $\boldsymbol{x}_k$ $\boldsymbol{\chi}_{k|k-1}$ mean and covariance:
$\overline{\boldsymbol{x}}_{k|k-1} = \sum_{i=0}^{2N} W_i^m \boldsymbol{\chi}_{k|k-1}^i$
$\boldsymbol{P}_{k|k-1}^{xx} = \sum_{i=0}^{2N} W_i^c [\boldsymbol{\chi}_{k|k-1}^i - \overline{\boldsymbol{x}}_{k|k-1}][\boldsymbol{\chi}_{k|k-1}^i - \overline{\boldsymbol{x}}_{k|k-1}]^T + \boldsymbol{Q}_k$
Propagate $\boldsymbol{\chi}_{k|k-1}$ through measurement function:
$\boldsymbol{Z}_{k|k-1} = h(\boldsymbol{\chi}_{k|k-1})$
Obtain $\boldsymbol{Z}_{k|k-1}$ mean and covariance:
$\overline{\boldsymbol{z}}_{k|k-1} = \sum_{i=0}^{2N} W_i^m \boldsymbol{Z}_{k|k-1}^i$
$\boldsymbol{P}_{k|k-1}^{zz} = \sum_{i=0}^{2N} W_i^c [\boldsymbol{Z}_{k|k-1}^i - \overline{\boldsymbol{z}}_{k|k-1}][\boldsymbol{Z}_{k|k-1}^i - \overline{\boldsymbol{z}}_{k|k-1}]^T + \boldsymbol{R}_k$
4: **Innovation step (improve $\boldsymbol{x}_k$ estimate with measurement $\boldsymbol{z}_k$ information):**
Obtain Kalman gain:
$\boldsymbol{P}_{k|k-1}^{xz} = \sum_{i=0}^{2N} W_i^c [\boldsymbol{\chi}_{k|k-1}^i - \overline{\boldsymbol{x}}_{k|k-1}][\boldsymbol{Z}_{k|k-1}^i - \overline{\boldsymbol{z}}_{k|k-1}]^T$
$\boldsymbol{K}_k = \boldsymbol{P}_{k|k-1}^{xz} (\boldsymbol{P}_{k|k-1}^{zz})^{-1}$
Use measurement $\boldsymbol{z}_k$ to improve estimates $\hat{\boldsymbol{x}}_k$ and $\hat{\boldsymbol{P}}_k^{xx}$:
$\hat{\boldsymbol{x}}_k = \overline{\boldsymbol{x}}_{k|k-1} + \boldsymbol{K}_k(\boldsymbol{z}_k - \overline{\boldsymbol{z}}_{k|k-1})$
$\hat{\boldsymbol{P}}_k^{xx} = \boldsymbol{P}_{k|k-1}^{xx} - \boldsymbol{K}_k \boldsymbol{P}_{k|k-1}^{zz} (\boldsymbol{K}_k)^T$
5: **Recursion step:**
$\hat{\boldsymbol{x}}_{k-1} = \hat{\boldsymbol{x}}_k$
$\hat{\boldsymbol{P}}_{k-1}^{xx} = \hat{\boldsymbol{P}}_k^{xx}$
Return back to step 2.

## D.3 RAUKF Fault-Detection Mechanism

The RAUKF algorithm uses the fault-detection mechanism described in the study by Zheng et al. (2018). In short, this method computes a test variable $\phi_k$, which signals the need to re-adjust the covariance matrices $\boldsymbol{R}_k$ and $\boldsymbol{Q}_k$. The test variable at time $k$ is defined as

$$\phi_k = [\boldsymbol{z}_k - h(\overline{x}_{k|k-1})]^T [\boldsymbol{P}_{k|k-1}^{zz}]^{-1} [\boldsymbol{z}_k - h(\overline{x}_{k|k-1})]. \tag{D.24}$$

$\phi_k$ follows a $\chi^2$ distribution with $s$ DoFs, where $s$ is the dimension of vector $\boldsymbol{\mu}_k = \boldsymbol{z}_k - h(\overline{x}_{k|k-1})$ ($s = 3$ in the case of Equation (6.1) wind vector). To detect a fault with reliability $1 - \sigma$ (where $\sigma$ is a preset value), a threshold $\chi_{s,\sigma}^2$ is set, such that

$$P(\phi_k > \chi_{s,\sigma}^2) = \sigma. \tag{D.25}$$

With these settings, a fault is detected with reliability $1 - \sigma$ when $\phi_k > \chi_{s,\sigma}^2$, which means that covariance matrices $\boldsymbol{R}$ and $\boldsymbol{Q}$ must be re-adjusted. $\chi_{s,\sigma}^2$ defines the error detection reliability (e.g., for 90% reliability, set $\sigma = 0.1$). If $s = 3$ DoF (as is the case here) then $\chi_{3,0.1}^2$ must be set to 6.36. The variables $\sigma$ and $\chi_{s,\sigma}^2$ indicate the confidence we have in the system model and the related noise covariance matrices. Thus, the higher the threshold $\chi_{s,\sigma}^2$, the lower the probability that an error is interpreted as a model fault.

# Bibliography


Agency, I. E. (2021). World energy outlook 2021. Technical report, International Energy Agency.

Al-Khalidy, N. (2018). Building generated wind shear and turbulence prediction utilising computational fluid dynamics. *WSEAS Transactions on Fluid Mechanics*, 13, 126–135.

Araújo da Silva, M. P., Rocadenbosch, F., Farré-Guarné, J., Salcedo-Bosch, A., González-Marco, D., & Peña, A. (2022a). Assessing obukhov length and friction velocity from floating lidar observations: A data screening and sensitivity computation approach. *Remote Sensing*, 14(6). https://doi.org/10.3390/rs14061394

Araújo da Silva, M. P., Rocadenbosch, F., Tanamachi, R. L., & Saeed, U. (2022b). Motivating a synergistic mixing-layer height retrieval method using backscatter lidar returns and microwave-radiometer temperature observations. *IEEE Transactions on Geoscience and Remote Sensing*, 60, 1–18. https://doi.org/10.1109/TGRS.2022.3158401

Ardhuin, F., Stopa, J. E., Chapron, B., Collard, F., Husson, R., Jensen, R. E., Johannessen, J., Mouche, A., Passaro, M., Quartly, G. D., Swail, V., & Young, I. (2019). Observing sea states. *Front. Mar. Sci.*, 6, 124. https://doi.org/10.3389/fmars.2019.00124

Atlas, D., Srivastava, R. C., & Sekhon, R. S. (1973). Doppler radar characteristics of precipitation at vertical incidence. *Reviews of Geophysics*, 11, 1–35. https://doi.org/10.1029/RG011i001p00001

AXYS Technologies (2015). *TRIAXIS sensor*. http://axystechnologies.com/products/triaxys-next-wave-ii-sensors/

Barlow, R. J. (1989). *Statistics: a guide to the use of statistical methods in the physical sciences*. Manchester physics series. Wiley. https://cds.cern.ch/record/213033

Barstow, S. F., Bidlot, J.-R., Caires, S., Donelan, M., & Drennan, W. (2005). *Measuring and analysing the directional spectra of ocean waves*. EUR 21367. COST Office. hal-00529755.

Barthelmie, R. & Pryor, S. (2003). Can satellite sampling of offshore wind speeds realistically represent wind speed distributions? *Journal of Applied Meteorology*, 42(1), 83–94. https://doi.org/10.1175/1520-0450(2003)042<0083:CSSOOW>2.0.CO;2

Bingöl, F., Mann, J., & Foussekis, D. (2009). Conically scanning lidar error in complex terrain. *Meteorologische Zeitschrift*, 18(2), 189–195. https://doi.org/10.1127/0941-2948/2009/0368

Bischoff, O., Schlipf, D., Würth, I., & Cheng, P. (2015). Dynamic motion effects and compensation methods of a floating lidar buoy. *EERA DeepWind 2015 Deep Sea Offshore Wind Conference*.

Bischoff, O., Würth, I., Cheng, P., Tiana-Alsina, J., & Gutiérrez, M. (2014). Motion effects on lidar wind measurement data of the EOLOS buoy. *Renewable Energies Offshore - 1st International Conference on Renewable Energies Offshore*, 197–203.

Bischoff, O., Yu, W., Gottschall, J., & Cheng, P. W. (2018). Validating a simulation environment for floating lidar systems. *Journal of Physics: Conference Series*, 1037, 052036. https://doi.org/10.1088/1742-6596/1037/5/052036

BP (2022). bp statistical review of world energy 2021. Technical report, BP p.l.c.

Bracewell, R. (2000). *The Fourier Transform and Its Applications*. Circuits and systems. McGraw Hill. https://books.google.es/books?id=ecH2KgAACAAJ

Brillouin, L. & Massey, H. (2013). *Wave Propagation and Group Velocity*, volume 8 of *Pure and applied physics*. Elsevier Science. https://books.google.es/books?id=gdQ3BQAAQBAJ

Brown, B. G., Katz, R. W., & Murphy, A. H. (1984). Time series models to simulate and forecast wind speed and wind power. *Journal of Applied Meteorology and Climatology*, 23(8), 1184–1195.

C., H. & S., K.-D. (2018). Estimation of significant wave period from wave spectrum. *J. Ocean Eng. Technol.*, 163, 609 – 616. https://doi.org/https://doi.org/10.1016/j.oceaneng.2018.06.043

Carbon Trust (2013). Carbon trust offshore wind accelerator roadmap for the commercial acceptance of floating LIDAR technology. Technical report, Carbon Trust.

Carbon Trust (2018). Carbon Trust Offshore Wind Accelerator Roadmap for the commercial acceptance of floating LiDAR technology. Technical report, Carbon Trust.

Center, N. D. B. (1996). Nondirectional and directional wave data analysis procedures. Technical report, National Oceanic and Atmospheric Administration.

Chang, R., Zhu, R., Badger, M., Hasager, C. B., Zhou, R., Ye, D., & Zhang, X. (2014). Applicability of synthetic aperture radar wind retrievals on offshore wind resources assessment in hangzhou bay, china. *Energies*, 7(5), 3339–3354.

Courtney, M. S. & Hasager, C. B. (2016). *Remote sensing technologies for measuring offshore wind*, (Chapter 4, 59–82). Elsevier.

Davari, N. & Gholami, A. (2017). An asynchronous adaptive direct kalman filter algorithm to improve underwater navigation system performance. *IEEE Sensors Journal*, 17(4), 1061–1068. https://doi.org/10.1109/JSEN.2016.2637402

Doviak, R. J. & Zrnic, D. S. (1984). 8 - rain measurements. *Doppler Radar and Weather Observations*, 179–239. Academic Press. https://doi.org/https://doi.org/10.1016/B978-0-12-221420-2.50013-2

Désert, T., Knapp, G., & Aubrun, S. (2021). Quantification and correction of wave-induced turbulence intensity bias for a floating lidar system. *Remote Sensing*, 13(15). https://doi.org/10.3390/rs13152973

EOLOS (2023). *Eolos - floating lidar solutions — home*. https://www.eolossolutions.com/. (Accessed on 02/08/2023)

Faltinsen, O. (1993). *Sea loads on ships and offshore structures*, volume 1. Cambridge university press.

Gao, Z., Feng, X., Zhang, Z., Liu, Z., Gao, X., Zhang, L., Li, S., & Li, Y. (2022). A brief discussion on offshore wind turbine hydrodynamics problem. *Journal of Hydrodynamics*, 34(1), 15–30. https://doi.org/10.1007/s42241-022-0002-y

Gottschall, J. (2020). *Wake Measurements with Lidar*, 1–18. Springer International Publishing. https://doi.org/10.1007/978-3-030-05455-7_55-1

Gottschall, J., Catalano, E., Dörenkämper, M., & Witha, B. (2018). The newa ferry lidar experiment: Measuring mesoscale winds in the southern baltic sea. *Remote Sensing*, 10(10). https://doi.org/10.3390/rs10101620

Gottschall, J., Courtney, M. S., Wagner, R., Jørgensen, H. E., & Antoniou, I. (2012a). Lidar profilers in the context of wind energy – a verification procedure for traceable measurements. *Wind Energy*, 15(1), 147–159. https://doi.org/10.1002/we.518

Gottschall, J., Gribben, B., Stein, D., & Würth, I. (2017a). Floating lidar as an advanced offshore wind speed measurement technique: current technology status and gap analysis in regard to full maturity. *Wiley Interdisciplinary Reviews: Energy and Environment*, 6(5), n/a–n/a. https://doi.org/10.1002/wene.250

Gottschall, J., Gribben, B., Stein, D., & Würth, I. (2017b). Floating lidar as an advanced offshore wind speed measurement technique: current technology status and gap analysis in regard to full maturity. *WIREs Energy and Environment*, 6(5), e250. https://doi.org/https://doi.org/10.1002/wene.250

Gottschall, J., Lilov, H., Wolken-Möhlmann, G., & Lange, B. (2012b). Lidars on floating offshore platforms; about the correction of motion-induced lidar measurement errors. *EWEA 2012 proceedings*.

Gottschall, J., Wolken-Möhlmann, G., Viergutz, T., & Lange, B. (2014a). Results and conclusions of a floating-lidar offshore test. *Energy Procedia*, 53, 156 – 161.

Gottschall, J., Wolken-Möhlmann, G., & Lange, B. (2014b). About offshore resource assessment with floating lidars with special respect to turbulence and extreme events. *Journal of Physics: Conference Series*, 555(1), 12–43. http://stacks.iop.org/1742-6596/555/i=1/a=012043

Goyer, G. G. & Watson, R. (1963). The laser and its application to meteorology. *Bulletin of the American Meteorological Society*, 44(9), 564 – 570. https://doi.org/10.1175/1520-0477-44.9.564

Gunn, R. & Kintzer, G. (1949). The terminal velocity of fall for water droplets in stagnant air. *Journal of Atmospheric Sciences*, 6, 243–248. https://doi.org/10.1175/1520-0469(1949)006<0243:TTVOFF>2.0.CO;2

Gutiérrez-Antuñano, M., Tiana-Alsina, J., Salcedo, A., & Rocadenbosch, F. (2018). Estimation of the Motion-Induced Horizontal-Wind-Speed Standard Deviation in an Offshore Doppler Lidar. *Remote Sens.*, 10(12), 2037. https://doi.org/10.3390/rs10122037

Gutierrez-Antunano, M. A., Tiana-Alsina, J., Rocadenbosch, F., Sospedra, J., Aghabi, R., & Gonzalez-Marco, D. (2017). A wind-lidar buoy for offshore wind measurements: First commissioning test-phase results. *2017 IEEE International Geoscience and Remote Sensing Symposium (IGARSS-2017)*, 1607–1610. https://doi.org/10.1109/igarss.2017.8127280

Gutiérrez, M. A., Tiana-Alsina, J., Bischoff, O., Cateura, J., & Rocadenbosch, F. (2015). Performance evaluation of a floating doppler wind lidar buoy in mediterranean near-shore conditions. *2015 IEEE International Geoscience and Remote Sensing Symposium (IGARSS-2015)*, 2147–2150. https://doi.org/10.1109/IGARSS.2015.7326228

Gutiérrez Antuñano, M. (2019). *Doppler wind LIDAR systems data processing and applications : an overview towards developing the new generation of wind remote-sensing sensors for off-shore wind farms*. UPC. http://hdl.handle.net/2117/166465

Gutiérrez-Antuñano, M. A., Tiana-Alsina, J., & Rocadenbosch, F. (2017). Performance evaluation of a floating lidar buoy in nearshore conditions. *Wind. Energy*, 20(10), 1711–1726. https://doi.org/10.1002/we.2118

Hajiyev, C. & Soken, H. E. (2014). Robust adaptive unscented kalman filter for attitude estimation of pico satellites. *International Journal of Adaptive Control and Signal Processing*, 28(2), 107–120. https://doi.org/https://doi.org/10.1002/acs.2393

Hardesty, R. M. & Weber, B. F. (1987). Lidar measurement of turbulence encountered by horizontal-axis wind turbines. *Journal of Atmospheric and Oceanic Technology*, 4(1), 191–203. https://doi.org/10.1175/1520-0426(1987)004<0191:LMOTEB>2.0.CO;2

Hasager, C. B., Stein, D., Courtney, M., Peña, A., Mikkelsen, T., Stickland, M., & Oldroyd, A. (2013). Hub height ocean winds over the north sea observed by the norsewind lidar array: Measuring techniques, quality control and data management. *Remote Sensing*, 5(9), 4280–4303. https://doi.org/10.3390/rs5094280

Hauser, D. & Amayenc, P. (1981). A New Method for Deducing Hydrometeor-Size Distributions and Vertical Air Motions from Doppler Radar Measurements at Vertical Incidence. *Journal of Applied Meteorology and Climatology*, 20(5), 547 – 555. https://doi.org/10.1175/1520-0450(1981)020<0547:ANMFDH>2.0.CO;2

He, Y., Fu, J., Chan, P. W., Li, Q., Shu, Z., & Zhou, K. (2021). Reduced sea-surface roughness length at a coastal site. *Atmosphere*, 12(8). https://doi.org/10.3390/atmos12080991

He, Y., Fu, J., Shu, Z., Chan, P., Wu, J., & Li, Q. (2019). A comparison of micrometeorological methods for marine roughness estimation at a coastal area. *Journal of Wind Engineering and Industrial Aerodynamics*, 195, 104010. https://doi.org/https://doi.org/10.1016/j.jweia.2019.104010

Hirth, B. D., Schroeder, J. L., Gunter, W. S., & Guynes, J. G. (2012). Measuring a utility-scale turbine wake using the TTUKa mobile research radars. *Journal of Atmospheric and Oceanic Technology*, 29(6), 765–771.

International Energy Association (2007). State of the art of remote wind speed sensing techniques using sodar, lidar and satellites. Technical report, International Energy Association.

Jash, D., Resmi, E., Unnikrishnan, C., Sumesh, R., Sreekanth, T., Sukumar, N., & Ramachandran, K. (2019). Variation in rain drop size distribution and rain integral parameters during south-west monsoon over a tropical station: An inter-comparison of disdrometer and micro rain radar. *Atmospheric Research*, 217, 24–36. https://doi.org/10.1016/j.atmosres.2018.10.014

Jeffreys, H. & Taylor, G. I. (1925). On the formation of water waves by wind. *Proceedings of the Royal Society of London. Series A, Containing Papers of a Mathematical and Physical Character*, 107(742), 189–206. https://doi.org/10.1098/rspa.1925.0015

Jelalian, A. (1992). *Laser Radar Systems*. Artech House radar library. Artech House. https://books.google.es/books?id=OuMOngEACAAJ

Joyce Lee and Feng Zhao (2019). Global wind report 2018. Technical report, Global Wind Energy Council.

Julier, S. J. & Uhlmann, J. K. (1997). New extension of the Kalman filter to nonlinear systems. *Signal Processing, Sensor Fusion, and Target Recognition VI*, volume 3068, 182 – 193. https://doi.org/10.1117/12.280797

Kelberlau, F. & Mann, J. (2022). Quantification of motion-induced measurement error on floating lidar systems. *Atmospheric Measurement Techniques Discussions*, 2022, 1–31. https://doi.org/10.5194/amt-2022-138

Kelberlau, F., Neshaug, V., Lønseth, L., Bracchi, T., & Mann, J. (2020). Taking the motion out of floating lidar: Turbulence intensity estimates with a continuous-wave wind lidar. *Remote Sensing*, 12(5). https://doi.org/10.3390/rs12050898

KIC InnoEnnergy (2015). Neptune Project Leaflet. Technical report, KIC InnoEnergy.

Kim, D.-K. & Lee, D.-I. (2016). Raindrop size distribution properties associated with vertical air motion in the stratiform region of a springtime rain event from 1290 mhz wind profiler, micro rain radar and parsivel disdrometer measurements. *Meteorol. Appl.*, 23(1), 40–49. https://doi.org/https://doi.org/10.1002/met.1518

Kindler, D., Courtney, M., & Oldroyd, A. (2009). Testing and calibration of various lidar remote sensing devices for a 2 year offshore wind measurement campaign. *EWEC 2009 Scientific proceedings*, 141–143. http://proceedings.ewea.org/ewec2009/proceedings/. 2009 European Wind Energy Conference and Exhibition, EWEC 2009 ; Conference date: 16-03-2009 Through 19-03-2009

Knoop, S., Bosveld, F. C., de Haij, M. J., & Apituley, A. (2021). A 2-year intercomparison of continuous-wave focusing wind lidar and tall mast wind measurements at cabauw. *Atmospheric Measurement Techniques*, 14, 2219–2235.

Kogaki, T., Sakurai, K., Shimada, S., Kawabata, H., Otake, Y., Kondo, K., & Fujita, E. (2020). Field measurements of wind characteristics using lidar on a wind farm with downwind turbines installed in a complex terrain region. *Energies*, 13(19). https://doi.org/10.3390/en13195135

Koivisto, M., Seppänen, J., Mellin, I., Ekström, J., Millar, J., Mammarella, I., Komppula, M., & Lehtonen, M. (2016). Wind speed modeling using a vector autoregressive process with a time-dependent intercept term. *International Journal of Electrical Power  Energy Systems*, 77, 91–99. https://doi.org/https://doi.org/10.1016/j.ijepes.2015.11.027

Kuik, A. J., van Vledder, G. P., & Holthuijsen, L. H. (1988). A Method for the Routine Analysis of Pitch-and-Roll Buoy Wave Data. *J. Phys. Oceanogr.*, 18(7), 1020–1034. https://doi.org/10.1175/1520-0485(1988)018<1020:AMFTRA>2.0.CO;2

Lang, S. & McKeogh, E. (2011). LIDAR and SODAR measurements of wind speed and direction in upland terrain for wind energy purposes. *Remote Sensing*, 3(9), 1871–1901. https://doi.org/10.3390/rs3091871

Lange, B., Larsen, S., Højstrup, J., & Barthelmie, R. (2004). Importance of thermal effects and sea surface roughness for offshore wind resource assessment. *Journal of Wind Engineering and Industrial Aerodynamics*, 92(11), 959–988. https://doi.org/https://doi.org/10.1016/j.jweia.2004.05.005

Lange, D., Rocadenbosch, F., Tiana-Alsina, J., & Frasier, S. (2015). Atmospheric boundary layer height estimation using a kalman filter and a frequency-modulated continuous-wave radar. *IEEE Transactions on Geoscience and Remote Sensing*, 53(6), 3338–3349. https://doi.org/10.1109/TGRS.2014.2374233

Lee, J. & Zhao, F. (2022). Global wind report 2022. Technical report, Global Wind Energy Council.

Lencer (2008). *Location map of the netherlands*. https://upload.wikimedia.org/wikipedia/commons/4/48/Netherlands_location_map.svg

Lhermitte, R. M. (1988). Observation of rain at vertical incidence with a 94 ghz doppler radar: An insight on mie scattering. *Geophysical Research Letters*, 15(10), 1125–1128. https://doi.org/10.1029/GL015i010p01125

Li, W., Sun, S., Jia, Y., & Du, J. (2016). Robust unscented kalman filter with adaptation of process and measurement noise covariances. *Digital Signal Processing*, 48, 93–103. https://doi.org/https://doi.org/10.1016/j.dsp.2015.09.004

M. Pitter, E. B. d. R., Medley, J., Mangat, M., Slinger, C., & Harris, M. (2014). Performance stability of zephir in high motion enviroments: floating and turbine mounted. Technical report, ZephIR.

MacEachern, C. & İlhami Yıldız (2018). 1.16 wind energy. *Comprehensive Energy Systems*, 665–701. Elsevier. https://doi.org/https://doi.org/10.1016/B978-0-12-809597-3.00118-8

MacIsaac, C. & Naeth, S. (2013). Triaxys next wave ii directional wave sensor the evolution of wave measurements. *2013 OCEANS - San Diego*, 1–8.

Mangat, M., des Roziers, E. B., Medley, J., Pitter, M., Barker, W., & Harris, M. (2014). The impact of tilt and inflow angle on ground based lidar wind measurements. *EWEA 2014 proceedings*.

Mann, J. (1998). Wind field simulation. *Probabilistic Engineering Mechanics*, 13(4), 269–282. https://doi.org/https://doi.org/10.1016/S0266-8920(97)00036-2

Massel, S. R. (2017). *Ocean surface waves: their physics and prediction*, volume 45. World Scientific Publishing Company.

Mathisen, J. P. (2013). Measurement of wind profile with a buoy mounted lidar. *Energy Procedia*, 00(00), 12.

Micallef, D. & Rezaeiha, A. (2021). Floating offshore wind turbine aerodynamics: Trends and future challenges. *Renewable and Sustainable Energy Reviews*, 152, 111696. https://doi.org/https://doi.org/10.1016/j.rser.2021.111696

Monin, A. S. & Obukhov, A. M. (1954). Basic laws of turbulent mixing in the surface layer of the atmosphere. *Contrib. Geophys. Inst. Acad. Sci. USSR*, 151(163), e187.

Moré, J. J. & Sorensen, D. C. (1983). Computing a trust region step. *SIAM Journal on scientific and statistical computing*, 4(3), 553–572.

Mücke, T., Kleinhans, D., & Peinke, J. (2011). Atmospheric turbulence and its influence on the alternating loads on wind turbines. *Wind Energy*, 14(2), 301–316. https://doi.org/https://doi.org/10.1002/we.422

Palais, B., Palais, R., & Rodi, S. (2009). A disorienting look at euler's theorem on the axis of a rotation. *The American Mathematical Monthly*, 116(10), 892–909. https://doi.org/10.4169/000298909X477014

Peña, A., Hasager, C., Merete, B., Barthelmie, R., Ferhat, B., Jean-Pierre, C., Stefan, E., Frandsen, S., Michael, H., Ioanna, K., Larsen, S., Jakob, M., Torben, M., Mark, P., Sara, P., Ameya, S., David, S., Chris, S., & Rozenn, W. (2015). *Remote Sensing for Wind Energy*. DTU Wind Energy.

Pichugina, Y., Banta, R., Brewer, W., Sandberg, S., & Hardesty, R. (2012). Doppler lidar–based wind-profile measurement system for offshore wind-energy and other marine boundary layer applications. *J. Appl. Meteorol. Climatol*, 51(2), 327–349. https://doi.org/10.1175/JAMC-D-11-040.1

Plancherel, M. & Leffler, M. (1910). Contribution à l'étude de la représentation d'une fonction arbitraire par des intégrales définies. *Rendiconti del Circolo Matematico di Palermo (1884-1940)*, 30(1), 289–335. https://doi.org/10.1007/BF03014877

Proakis, J. & Manolakis, D. (2006). *Digital Signal Processing (4th Edition)* (4 ed.). Prentice Hall.

Ramírez, L., Fraile, D., & Brindley, G. (2021). Offshore wind in Europe key trends and statistics 2020. Technical report, WindEurope, Brussels, Belgium.

Ricci, A. & Blocken, B. (2020). On the reliability of the 3d steady rans approach in predicting microscale wind conditions in seaport areas: The case of the ijmuiden sea lock. *Journal of Wind Engineering and Industrial Aerodynamics*, 207, 104437. https://doi.org/https://doi.org/10.1016/j.jweia.2020.104437

Robert Grover, R. & Y.C. Hwang, P. (2012). *Introduction to Random Signals and Kalman Filtering: with MATLAB exercises* (4 ed.). Wiley.

Rocadenbosch, F., Barragán, R., Frasier, S. J., Waldinger, J., Turner, D. D., Tanamachi, R. L., & Dawson, D. T. (2020). Ceilometer-based rain-rate estimation: A case-study comparison with s-band radar and disdrometer retrievals in the context of vortex-se. *IEEE Trans. Geosci. Remote Sens.*, 58(12), 8268–8284. https://doi.org/10.1109/TGRS.2020.2984458

Rocadenbosch, F., Soriano, C., Comerón, A., & Baldasano, J.-M. (1999). Lidar inversion of atmospheric backscatter and extinction-to-backscatter ratios by use of a kalman filter. *Appl. Opt.*, 38(15), 3175–3189. https://doi.org/10.1364/AO.38.003175

Rodgers, C. D. (2004). *Inverse methods for atmospheric sounding: theory and practice*, volume 2 of *Series on Atmospheric, Oceanic and Planetary Physics*. World scientific.

Rogers, R. R. (1984). A review of multiparameter radar observations of precipitation. *Radio Science*, 19(01), 23–36. https://doi.org/10.1029/RS019i001p00023

Roithmayr, C. M. & Hodges, D. H. (2016). *Dynamics: theory and application of Kane's method*. American Society of Mechanical Engineers Digital Collection.

Salcedo, A., Rocadenbosch, F., Frasier, S., & Domínguez, P. (2022). *Forward method for vertical air motion estimation from frequency modulated continuous wave radar rain measurements*, 104–111. MeteoSwiss (Bundesamt für Meteorologie und Klimatologie MeteoSchweiz).

Salcedo-Bosch, A., Domínguez-Pla, P., , Rocadenbosch, F., & Frasier, S. (2022a). Numerical Solver for Vertical Air Motion Estimation. *2022 IEEE Int. Geo. Rem. Sens. Symp. (IGARSS-2022)*. Presented.

Salcedo-Bosch, A., Farré-Guarné, J., Araújo da Silva, M. P., & Rocadenbosch, F. (2023). A unified formulation for the computation of the six-degrees-of-freedom-motion-induced errors in floating doppler wind lidars. *Remote Sensing*, 15(6). https://doi.org/10.3390/rs15061478

Salcedo-Bosch, A., Farré-Guarné, J., Sala-Álvarez, J., Villares-Piera, J., Tanamachi, R., & Rocadenbosch, F. (2021a). Floating doppler wind lidar motion simulator for horizontal wind speed measurement error assessment. *2021 IEEE International Geoscience and Remote Sensing Symposium IGARSS*, 7716–7719. https://doi.org/10.1109/IGARSS47720.2021.9555023

Salcedo-Bosch, A., Gutierrez-Antunano, M. A., Tiana-Alsina, J., & Rocadenbosch, F. (2020a). Floating doppler wind lidar measurement of wind turbulence: A cluster analysis. *IGARSS 2020 - 2020 IEEE International Geoscience and Remote Sensing Symposium*, 6077–6080. https://doi.org/10.1109/IGARSS39084.2020.9323578

Salcedo-Bosch, A., Rocadenbosch, F., Gutierrez-Antunano, M., & Tiana-Alsina, J. (2020b). Motional behavior estimation using simple spectral estimation: Application to the off-shore wind lidar. *IGARSS 2020 - 2020 IEEE International Geoscience and Remote Sensing Symposium*, 5682–5685. https://doi.org/10.1109/IGARSS39084.2020.9323801

Salcedo-Bosch, A., Rocadenbosch, F., Gutiérrez-Antuñano, M. A., & Tiana-Alsina, J. (2021b). Estimation of wave period from pitch and roll of a lidar buoy. *Sensors*, 21(4). https://doi.org/10.3390/s21041310

Salcedo-Bosch, A., Rocadenbosch, F., & Sospedra, J. (2021c). A robust adaptive unscented kalman filter for floating doppler wind-lidar motion correction. *Remote Sensing*, 13(20). https://doi.org/10.3390/rs13204167

Salcedo-Bosch, A., Rocadenbosch, F., & Sospedra, J. (2022b). Enhanced dual filter for floating wind lidar motion correction: The impact of wind and initial scan phase models. *Remote Sensing*, 14(19). https://doi.org/10.3390/rs14194704

Salcedo-Bosch, A., Rocadenbosch, F., & Sospedra, J. (2022c). On Adaptive Unscented Kalman Filtering for Floating Doppler Wind-Lidar Motion Correction: Effect of the Number of Lidar Measurement Heights. *2022 IEEE International Geoscience and Remote Sensing Symposium (IGARSS)*. Presented.

Schlipf, D., Rettenmeier, A., Haizmann, F., Hofsäß, M., Courtney, M., & Cheng, P. W. (2012). Model based wind vector field reconstruction from lidar data. *Proceedings of the 11th German Wind Energy Conference DEWEK 2012*.

Schuon, F., González, D., Rocadenbosch, F., Bischoff, O., & Jané, R. (2012). KIC InnoEnergy Project Neptune: Development of a Floating LiDAR Buoy for Wind, Wave and Current Measurements. *Proceedings DEWEK 2012 German Wind Energy Conference*.

Scientific, C. (2016). Zephir 300. Technical report, Campbell Scientific, 14532 131 Avenue NW, Edmonton AB T5L 4X4. https://s.campbellsci.com/documents/ca/product-brochures/zephir300_br.pdf. (Accessed on 04/15/2020)

Sempreviva, A. M., Barthelmie, R. J., & Pryor, S. C. (2008). Review of methodologies for offshore wind resource assessment in european seas. *Surveys in Geophysics*, 29(6), 471–497. https://doi.org/10.1007/s10712-008-9050-2

Shannon, C. (1949). Communication in the presence of noise. *Proceedings of the IRE*, 37(1), 10–21. https://doi.org/10.1109/JRPROC.1949.232969

Silva, M. P. A. d., Rocadenbosch, F., Farré-Guarné, J., Salcedo-Bosch, A., González-Marco, D., & Peña, A. (2022). Assessing obukhov length and friction velocity from floating lidar observations: A data screening and sensitivity computation approach. *Remote Sensing*, 14(6). https://doi.org/10.3390/rs14061394

Slinger, C. & Harris, M. (2012). Introduction to continuous-wave Doppler lidar.

Smith, D. A. & Mehta, K. C. (1993). Investigation of stationary and nonstationary wind data using classical box-jenkins models. *Journal of Wind Engineering and Industrial Aerodynamics*, 49(1), 319–328. https://doi.org/https://doi.org/10.1016/0167-6105(93)90027-L

Smullin, L. D. & Fiocco, G. (1962). Optical echoes from the moon. *Nature*, 194(4835), 1267–1267. https://doi.org/10.1038/1941267a0

Sospedra, J., Cateura, J., & Puigdefàbregas, J. (2015). Novel multipurpose buoy for offshore wind profile measurements eolos platform faces validation at ijmuiden offshore metmast. *Sea Technol.*, 56(7), 25–28.

Stade, E. (2015). *Fourier Analysis* (1st ed.). Wiley-Interscience.

Stearns, S. D. & Hush, D. R. (2011). *Digital Signal Processing with Examples in MATLAB* (2 ed.). Taylor & Francis Inc.

Stull, R. B. (1988). *An introduction to boundary layer meteorology*. Kluwer Academic Publishers.

Suh, K.-D., Kwon, H.-D., & Lee, D.-Y. (2010). Some statistical characteristics of large deepwater waves around the korean peninsula. *Coast. Eng.*, 57(4), 375 – 384. https://doi.org/https://doi.org/10.1016/j.coastaleng.2009.10.016

Sweitzer, K. A., Bishop, N. W., & Genberg, V. L. (2004). Efficient computation of spectral moments for determination of random response statistics. *Proceedings of ISMA*, 2677–2692. https://eprints.soton.ac.uk/28167/. Signal processing and instrumentation - SP1

Tanamachi, R. L., Frasier, S. J., Waldinger, J., LaFleur, A., Turner, D. D., & Rocadenbosch, F. (2019). Progress toward Characterization of the Atmospheric Boundary Layer over Northern Alabama Using Observations by a Vertically Pointing, S-Band Profiling Radar during VORTEX-Southeast. *J. Atmos. Ocean. Technol*, 36(11), 2221–2246. https://doi.org/10.1175/JTECH-D-18-0224.1

Tannuri, E., Sparano, J., Simos, A., & Cruz, J. D. (2003). Estimating directional wave spectrum based on stationary ship motion measurements. *Appl. Ocean Res.*, 25(5), 243 – 261. https://doi.org/https://doi.org/10.1016/j.apor.2004.01.003

Taylor, G. I. (1938). The spectrum of turbulence. *Proceedings of the Royal Society of London. Series A, Mathematical and Physical Sciences*, 164(919), 476 – 490.

Taylor, M., Ralon, P., & Al-Zoghoul, S. (2022). Renewable power generation costs in 2021. Technical report, International Renewable Energy Agency IRENA.

Tiana-Alsina, J., Gutiérrez, M. A., Würth, I., Puigdefàbregas, J., & Rocadenbosch, F. (2015). Motion compensation study for a floating doppler wind lidar. *2015 IEEE International Geoscience and Remote Sensing Symposium (IGARSS-2015)*, 5379–5382.

Tiana-Alsina, J., Rocadenbosch, F., & Gutierrez-Antunano, M. A. (2017). Vertical Azimuth Display simulator for wind-Doppler lidar error assessment. *2017 IEEE International Geoscience and Remote Sensing Symposium (IGARSS)*, 1614–1617. https://doi.org/10.1109/igarss.2017.8127282

Tokay, A. & Short, D. A. (1996). Evidence from tropical raindrop spectra of the origin of rain from stratiform versus convective clouds. *Journal of Applied Meteorology and Climatology*, 35(3), 355 – 371. https://doi.org/10.1175/1520-0450(1996)035<0355:EFTRSO>2.0.CO;2

Tokay, A., Wolff, D. B., & Petersen, W. A. (2014). Evaluation of the new version of the laser-optical disdrometer, ott parsivel2. *Journal of Atmospheric and Oceanic Technology*, 31(6), 1276 – 1288. https://doi.org/10.1175/JTECH-D-13-00174.1

Tolstov, G. P. (1976). *Fourier Series*. Prentice-Hall.

Tridon, F., Van Baelen, J., & Pointin, Y. (2011). Aliasing in micro rain radar data due to strong vertical winds. *Geophysical Research Letters - GEOPHYS RES LETT*, 38. https://doi.org/10.1029/2010GL046018

Türk, M. & Emeis, S. (2010). The dependence of offshore turbulence intensity on wind speed. *Journal of Wind Engineering and Industrial Aerodynamics*, 98(8), 466–471. https://doi.org/https://doi.org/10.1016/j.jweia.2010.02.005

Vaughan, J. & Forrester, P. (1989). Laser Doppler velocimetry applied to the measurement of local and global wind. *Wind Engineering*, 13(1), 1–15. http://www.jstor.org/stable/43749359

Vogt, S. & Thomas, P. (1995). Sodar—a useful remote sounder to measure wind and turbulence. *Journal of wind engineering and industrial aerodynamics*, 54, 163–172.

Wagner, R., Mikkelsen, T., & Courtney, M. (2009). Investigation of turbulence measurements with a continuous wave, conically scanning lidar. Technical report, DTU.

Waldinger, J., Hartley, T., Heberling, W., Frasier, S., & Tanamachi, R. (2017). S-band fmcw boundary layer profiler: System upgrades and results. *2017 IEEE International Geoscience and Remote Sensing Symposium (IGARSS)*, 4526–4529. https://doi.org/10.1109/IGARSS.2017.8128008

Wan, B., Wu, X., Yue, X., Zhang, L., & Wang, L. (2022). Calibration of phased-array high-frequency radar on an anchored floating platform. *Remote Sensing*, 14(9). https://doi.org/10.3390/rs14092174

Wan, E. A. & Van Der Merwe, R. (2000). The unscented kalman filter for nonlinear estimation. *Proceedings of the IEEE 2000 Adaptive Systems for Signal Processing, Communications, and Control Symposium (Cat. No.00EX373)*, 153–158. https://doi.org/10.1109/ASSPCC.2000.882463

WANG, J. (1999). Stochastic modeling for real-time kinematic gps/glonass positioning. *NAVIGATION*, 46(4), 297–305. https://doi.org/https://doi.org/10.1002/j.2161-4296.1999.tb02416.x

Werkhoven, E. J. & Verhoef, J. P. (2012). Offshore meteorological mast Ijmuiden abstract of instrumentation report. Technical report, Energy Research Centre of the Netherlands (ECN).

Wolken-Möhlmann, G., Lilov, H., & Lange, B. (2010). Simulation of motion induced measurement errors for wind measurements using lidar on floating platforms. *Proceedings 15th International Symposium for the Advancement of Boundary-layer Remote Sensing (ISARS)*, 28–30.

Yao, G., Xie, J., & Huang, W. (2021). Hf radar ocean surface cross section for the case of floating platform incorporating a six-dof oscillation motion model. *IEEE Journal of Oceanic Engineering*, 46(1), 156–171. https://doi.org/10.1109/JOE.2019.2959289

Zheng, B., Fu, P., Li, B., & Yuan, X. (2018). A robust adaptive unscented kalman filter for nonlinear estimation with uncertain noise covariance. *Sensors*, 18(3). https://doi.org/10.3390/s18030808

Øyvind F. Auestad, Gravdahl, J. T., & Fossen, T. I. (2013). Heave motion estimation on a craft using a strapdown inertial measurement unit. *9th IFAC Conference on Control Applications in Marine Systems*, volume 46, 298 – 303. https://doi.org/https://doi.org/10.3182/20130918-4-JP-3022.00033. 9th IFAC Conference on Control Applications in Marine Systems

İnce, T., Frasier, S. J., Muschinski, A., & Pazmany, A. L. (2003). An s-band frequency-modulated continuous-wave boundary layer profiler: Description and initial results. *Radio Science*, 38(4). https://doi.org/https://doi.org/10.1029/2002RS002753